Growth of (In, Ga)N/GaN short period superlattices using substrate strain engineering

D I S S E R T A T I O N

zur Erlangung des akademischen Grades

Dr. rer. nat.
im Fach Physik
Spezialisierung: Experimentalphysik

eingereicht an der
Mathematisch-Naturwissenschaftliche Fakultät
Humboldt-Universität zu Berlin

von
M.Sc. Torsten Ernst

Präsident der Humboldt-Universität zu Berlin:
Prof. Dr.-Ing. Dr. Sabine Kunst

Dekan der Mathematisch-Naturwissenschaftliche Fakultät:
Prof. Dr. Elmar Kulke

Gutachter:

(i) Prof. Dr. Henning Riechert

(ii) Prof. Dr. W. Ted Masselink

(iii) Prof. Dr. Martin Eickhoff

(iv) Prof. Dr. Christoph Koch

(v) Prof. Dr. Igor Sokolov

eingereicht am: 25.10.2019
Tag der mündlichen Prüfung: 24.11.2020

To my Family

Abstract

Several thin InN and GaN/InN films and (In, Ga)N heterostructures were grown using molecular beam epitaxy to investigate their growth mode. InN and GaN/InN films were grown on ZnO substrates and (In, Ga)N heterostructures were grown on (In, Ga)N buffers and ZnO substrates. Fabricating the heterostructures on two different types of substrates was a means of strain engineering to possibly increase the indium content in the (In, Ga)N layers.

An annealing procedure was established to treat ZnO substrate to gain smooth, stepped surfaces suitable for ML thin heterostructure devices. Smooth stepped surfaces were found with annealing at 1050 °C, under oxygen atmosphere of 1 bar, for 1 hour for both Zn-ZnO and O-ZnO surfaces.

Reflection high energy electron diffraction was used to investigate in situ the growth mechanism and evolution of the *a*-lattice spacing. The critical layer thickness for growth mode transition of InN from smooth to rough is below 2 MLs and fairly coincides with the onset of main relaxation. The deposition of GaN on ML thin InN/ZnO shows that at best a few MLs can be deposited before relaxation and/or intermixing into (In, GaN) takes place.

Investigations by X-ray diffraction and Raman spectroscopy indicate that the deposition of a nominal structure of 100x(1 ML InN/2 MLs GaN) seems to result in the growth of (In, Ga)N instead. The average chemical composition was similar for all samples with an indium content close to x: 0.36 and a degree of relaxation between R: 65% to R: 73% for samples grown on ZnO and R: 95% for the sample grown on 300 nm $In_{0.19}Ga_{0.81}N$/GaN pseudo-substrate. The surface was probed with atomic force microscopy and showed that starting with smooth surfaces with root mean square roughness around 0.2 nm there was a considerable roughening during growth and surfaces with grain like morphology and a roughness around 2 to 3 nm was produced. Unintentional differences in V/III ratio during growth of (In, Ga)N heterostructures, indicated by the presence of droplets on some of the sample surfaces, were possible, impacting on the sample relaxation behavior and the surface roughness.

Zusammenfassung

Das Wachstum von monolagen dünnen Schichten von InN und GaN/InN auf ZnO wurde untersucht. Ebenso der Einfluss der Verspannung, welche durch das Substrat bedingt ist, auf den indium Gehalt von (In, Ga)N Heterostrukturen, welche auf GaN und ZnO gewachsen wurden. Alle Proben wurden mittels Molekularstrahlepitaxy gewachsen. Es wurde eine Prozedur entwickelt zum Glühen von ZnO Substraten, um glatte Oberflächen mit Stufenfluss-Morphologie zu erhalten, welche sich für das Wachstum von monolagedünnen Heterostrukturen eignen. Solche Zn-ZnO und O-ZnO Oberflächen konnten produziert werden, wenn die Proben bei 1050 °C in einer O_2 Atmosphäre bei 1 bar für eine Stunde geglüht wurden.

Reflection high energy diffraction wurde eingesetzt, um in situ den Wachstumsmodus und die Entwicklung des a-Gitterabstandes zu untersuchen. Die kritische Schichtdicke, ab welcher ein Übergang im Wachstumsmodus von glattem zu rauhem Wachstum statt findet, war für das Wachstum von InN auf ZnO geringer als 2 ML und setzt gemeinsam mit dem Beginn der Relaxation ein. Für das Wachstum von GaN auf monolagen-dünnem InN/ZnO konnte gezeigt werden, dass höchstens wenige ML abgeschieden werden können, bevor Relaxation eintritt und/oder eine Vermischung zu (In, Ga)N stattfindet.

Untersuchungen durch Röntgenbeugung und Raman Spektroskopie geben Hinweise darauf, dass das Abscheidung der nominalen Struktur 100x(1 ML InN/2 MLs GaN) vermutlich zum Wachstum von (In, Ga)N führte. Die chemische Zusammensetzung war für alle Proben sehr ähnlich mit einem indium Gehält von etwa x: 0.36 und einem Relaxationsgrad von R: 65% bis R: 73% für Proben, die auf ZnO gewachsen wurde und R: 95% für Wachstum auf 300 nm $In_{0.19}Ga_{0.81}N$/GaN.

Ein unbeabsichtigter Unterschied im V/III-Verhältnis während des Wachstums von (In, Ga)N Heterostrukturen, auf welchen die Anwesenheit von Metalltröpchen auf manchen Proben hinwies, lies auf einen möglichen Einfluss auf das Relaxationsverhalten und die Oberflächenrauhigkeit schließen.

Selbständigkeitserklärung

Ich erkläre, dass ich die Dissertation selbständig und nur unter Verwendung der von mir gemäß §7 Abs. 3 der Promotionsordnung der Mathematisch-Naturwissenschaftlichen Fakultät, veröffentlicht im Amtlichen Mitteilungsblatt der Humboldt-Universität zu Berlin Nr. 126/2014 am 18.11.2014 angegebenen Hilfsmittel angefertigt habe.

Berlin, den Torsten Ernst

1 Conference presentations and disseminations

[SPRInG Meeting Sept., 2015 oral presentation] - **Nucleation studies of InN** T. Ernst, C. Chèze, R. Calarco

[SPRInG Meeting Feb., 2016 oral presentation] - **Growth of relaxed (In, Ga)N buffers and InN/GaN multi quantum wells** T. Ernst, M. Siekacz, G. Staszczak, E. Grzanka, J. Smalc-Koziorowska, J. Moneta and C. Skierbiszewski

[SPRInG Meeting Nov., 2016 oral presentation] - **Attempt to grow InN/GaN SPSL on ZnO** T. Ernst, C. Chèze, M. Ramsteiner, F. Feix, P. Wolny, R. Calarco, C. Skierbiszewski

[SPRInG Meeting Feb., 2017 oral presentation] - **Increase In-content in (In, Ga)N/GaN (SPSL) by means of strain engineering** T. Ernst, C. Chèze, M. Ramsteiner, F. Feix, M. Siekacz, G. Staszczak, E. Grzanka, R. Calarco, C. Skierbiszewski

[ICNS Aug., 2017 Poster presentation] - **The Impact of Barrier Width on Photoluminescence Wavelength in In(Ga)N/InGaN Short Period Superlattices Grown by Plasma Assisted MBE** T. Ernst, M. Siekacz, G. Staszczak, T. Suski, E. Grzanka, I. Gorczyca, H. Turski, M. Anikeeva, T. Schulz, M. Albrecht and C. Skierbiszewski

[SPRInG Meeting Nov., 2017 oral presentation] - **Growth of InN/GaN SPSLs on ZnO and partially relaxed InGaN buffers** T. Ernst, C. Chèze, M. Ramsteiner, R. Calarco

2 List of peer reviewed publications

InN and GaN/InN monolayers grown on ZnO(000$\bar{1}$) and ZnO(0001) T. Ernst, C. Chèze, R. Calarco; *Journal of applied physics*, 124, 115305 (2018);

Two more papers are in preparation.

3 Acknowledgment

Though this thesis has only one author many people have contributed to it and only with their help it was possible.

I want to thank Prof. Dr. Henning Riechert, director of the Paul-Drude Institute and Dr. Lutz Geelhaar, head of the epitaxy department for giving me the opportunity to work at the institute as a PhD student.

I want to thank Dr. Raffaella Calarco, coordinator of the SPRInG project that I had the luck to be part of, for her frequent and inspiring scientific input, her understanding and patient leadership and her honesty, which helped me not only to develop as a scientist but also as a person and especially for encouraging me to finish my PhD. I want to thank her for investing so much time in proof reading my thesis and helping me improving it.

I want to thank Prof. Dr. Henning Riechert, Prof. Dr. W. Ted Masselink, Prof. Dr. Martin Eickhoff, Prof. Dr. Christoph Koch, and Prof. Dr. Igor Sokolov for being part of the thesis review committee. Thank you for your time.

I want to thank Dr. Caroline Chèze for teaching me how to operate the MBE system and several other devices that were used to manufacture and investigate the samples for this study. I want to thank her for continuous discussion that helped me improve my understanding of semiconductor physics, for advising me in many instances on my way to the PhD and for her incredible patience while doing so.

It has been a stimulating experience to work with Dr. Manfred Ramsteiner, Dr. Bernd Jenichen and Dr. Oliver Brandt and to be able to benefit of their knowledge. Furthermore, Dr. Manfred Ramsteiner conducted the Raman measurements and Dr. Bernd Jenichen kept the XRD diffractometer operational. I am grateful to the technicians Hans-Peter Schönherr for keeping the MBE system operational and Claudia Herrmann for caring for the AFM setup.

I am thankful to the administration of the Paul-Drude Institute for their contribution.

My fellow students contributed through scientific and technical knowledge that they happily shared and by welcoming me in their midst. I especially want to thank Erdi Kuşdemir for going out if his way and participating in RHEED measurements that had to be conducted during night time. I want to thank Melanie Budde for interesting conversations and in general contributing to the very pleasant atmosphere here at the Paul-

Drude institute, and Dr. Rui Ning Wang for helping me to analyze the RHEED data. My gratitude goes to Dr. Valeria Bragaglia and Dr. Lauren Aranha Galves for contributing to this work.

Besides the Paul-Drude institute I had the pleasure to work half of the time at TopGaN lasers. I am greatly thankful to Dr. Andrzej Kasprowiak, president of TopGaN, Dr. Krzysztof Węgrzyn, CEO of TopGaN, Prof. Dr. Piotr Perlin, CTO of TopGaN and Prof. Dr. Czesław Skierbiszewski, head of the MBE laboratory group for the great opportunity to work at TopGaN lasers.

I'm largely indebted to Dr. Marta Sawicka for helping me in various ways to organize my life in Poland and being a very pleasant person to work with. I want to thank Dr. Marcin Siekacz for patiently teaching me how to use the MBE system and helping me with the growth of the samples as well as understanding the process and the physics behind it. I am thankful to Dr. Ewa Grzanka for sharing her knowledge regarding XRD spectroscopy with me, and M.Sc. Ania Feduniewicz-Zmuda for teaching me how to use the AFM setup, Dr. Szymon Grzanka and Dr. Grzesiek Staszczak for conducting photoluminescence measurements and providing insight in their analysis and M.Sc. Krzesimir Nowakowski-Szkudlarek for pre-growth preparation of the GaN-templates.

I wish to thank Prof. Dr. Tadeusz Suski, Dr. Grzegorz Muził, Dr. Henryk Turski, Dr. Julita Smalc-Koziorowska and M.Sc. Joanna Moneta for sharing their knowledge with me and improving my understanding of physics.

I am especially thankful to Paweł Wolny who welcomed me to stay at his home during my time in Poland and helped with so many things, both scientifically and organizationally.

I am thankful to the administration of TopGaN lasers for their contribution.

Thank you to our collaborators at the Institut für Kristallzüchtung, Dr. Martin Albrecht, Dr. Tobias Schulz, and M.Sc. Mariia Anikeeva for their insightful contributions.

Funding of this work by the European Union's Horizon 2020 research and innovation program (Marie Skłodowska-Curie Actions) under Grant Agreement "SPRInG" No. 642574 is gratefully acknowledged.

Contents

1 Introduction and motivation

Ternary (In, Ga)N alloys are widely used in optoelectronic devices like Light Emitting Diodes (LEDs) or Laser Diodes (LDs) [1],[2],[3]. The band gap of (In, Ga)N alloys covers a wide spectral range from 0.64 eV for InN [4] to (3.4 – 3.5) eV for GaN [5],[6]. Over the last three decades there have been considerable improvements in growing these alloys, especially (In, Ga)N with low indium content. In contrast, the fabrication of high In-content (In, Ga)N alloys is still challenging.

First of all, InN and GaN are grown at different temperatures for optimal electronic and optical properties, which presents a challenge, especially for the realization of high indium content (In, Ga)N or (In, Ga)N/GaN heterostructures. This difference in optimal growth temperature is caused by the different strength of In-N and Ga-N bonds. The first is weaker than the latter, which reflects in the activation energy for decomposition and desorption. Some literature values for the activation energy for decomposition of InN are 1.69 eV [7] - 1.92 eV [8] and for desorption 2.5 eV [9]. For GaN instead, the activation energy for decomposition is reported to be 3.1 eV [10] – 3.6 eV [11], and for desorption 2.2 eV - 2.8 eV [12], [13]. As a consequence, decomposition of InN starts to increase strongly above temperatures of about 480 °C [14], whereas for GaN, it is rather negligible up to a temperature of about 700 °C [15].

Second, phase separation (binodal and spinodal), occurs for (In, Ga)N over a wide range of compositions and results in nanoscale inhomogeneities. This issue is also referred to as the miscibility gap [16],[17],[18].

Third, (In, Ga)N inhomogeneities in indium content as well as QW thickness fluctuations produce changes in the wavelength of the emitted light and the radiative decay time [7], [19], [20]. This complicates the establishment of population inversion of charge carriers needed for the operation of LDs [7].

Fourth, the high difference in lattice spacing of InN and GaN limits the thickness of InN or (In, Ga)N layers that can be pseudomorphically grown on GaN [21] prior to elastical or plastical relaxation [20],[22],[23],[24],[25]. The growth of (In, Ga)N on GaN is further complicated by the so called composition pulling effect [26], [27], which refers to a strain induced compositional gradient along the growth direction.

All of this effects are detrimental for LEDs and LDs, as for example defects can act as sites for non-radiative recombination of charge carriers, which decrease the efficiency of optoelectronic devices. To solve these issues, Yoshikawa *et al.* proposed InN/GaN heterostructures, consisting of an integer number n of monolayers (MLs) of InN and m MLs of GaN (n InN/ m GaN) [28], called digital or rational alloys. The latter differ from conventional random alloys, where In and Ga atoms are randomly distributed within the (In, Ga)N layer. These digital alloys are also referred to as Short Period Superlattices (SPSLs) if the period thickness is short so that the wave functions of electrons and holes extend from one period into the next one.

Yoshikawa *et al.* fabricated such SPSL structures composed of 1-2 MLs (and sub monolayer) InN with 14 nm thick GaN barriers [28], [29] and reported a number of improvements over random alloys. The growth temperature on Ga-polar GaN was 650 °C-700 °C, exceeding the onset of InN decomposition and desorption by more than 150 °C. This effect was attributed to the larger occurrence of Ga-N bonds (stronger than In-N) within the GaN matrix surrounding the InN monolayer. This would increase the temperature for decomposition of InN by keeping the nitrogen atoms in place. At the same time the crystalline quality was improved as indicated by the appearance of additional orders of satellite peaks in X-Ray Diffraction (XRD) 2θ-ω scans [28], [29]. In-situ Reflection High-Energy Electron Diffraction (RHEED) measurements showed pseudomorphic growth up to 1 ML InN on GaN and full relaxation before the second ML was completed [29]. Based on this observation it was concluded that 1 ML InN embedded within a GaN matrix can be grown without the formation of misfit dislocations at the heterointerface. ML-thin QWs would also mitigate the effect of the quantum confined Stark effect (QCSE), as some groups reported that the emission wavelength did not change when the injection current was increased [30],[31],[32]. The realization of InN/GaN SPSLs with sharp interfaces for opto-electronic devices, circumventing (In, Ga)N inhomogeneities, would therefore be advantageous.

In order to tune the emission wavelength, either the quantum barrier or well thickness was varied in integer multiples m of (1 ML InN)/(m MLs GaN). Theoretical calculations by Gorczyca *et al.* predicted the PL emission of such structures with m= 1-40 MLs to be 1.3 eV to 2.1 eV [33]. Miao *et al.* instead predicted the PL emission of (1 ML InN)/(23

MLs GaN) to be 2.17 eV [34]. To explain the discrepancy between the theoretical emission energies and the experimental findings it was suggested that (In, Ga)N instead of InN formed [34],[35]. Alternatively, it was considered that the radiative recombination might be due to excitons located partially in the InN well and the GaN barrier [28], [34]. Furthermore, the discrepancy was suggested to be caused by carrier screening due to defects which give rise to free carriers [33]. However, recently Suski *et al.* used transmission electron microscopy (TEM) to investigate such SPSLs structures and revealed that the QWs are not composed of pure InN but (In, Ga)N with an indium composition below 33% [36].

Duff *et al.* performed theoretical calculations to investigate the growth of thin film InN on GaN and found that InN does not form under these conditions [37]. Their calculations showed that for growth on a more lattice matched substrate there is a wider range of possible growth conditions. This result suggests, that strain plays a key role for the growth of thin film InN/GaN.

Objective of this thesis

The main objective of the thesis is the investigation of In incorporation in (InN/GaN) SPSLs by strain engineering via growth on relaxed (In,Ga)N buffers (grown on Ga-polar GaN templates) and on ZnO substrates. An epitaxial process adapted to the type of substrate will be developed.

2 Introduction to group-III Nitrides and ZnO

2.1 Crystal structure

GaN, InN, AlN and their ternary alloys (In, Ga)N and (Al, Ga)N belong to the group-III-nitrides. Those materials as well as ZnO can crystallize in a cubic zinc blende and a hexagonal wurtzite structure, the latter being the thermodynamic stable phase. In the frame of this work we restricted our studies to the wurtzite phase. A schematic of the wurtzite structure of group-III-nitrides and ZnO with in-plane (a) and out-of-plane (c) lattice constants is depicted in figure 2.1. Along the c-axis there is an alternation of layers that consist only of Zn or group III atoms and layers with N or O atoms. The atoms are arranged in the hexagonal closed-packed system (hcp). Alternating bi-layers are rotated by 30° relative to each other around the c-axis with a distance of $c/2$ between them. The stacking sequence along the c-axis is (aAbBaAbB...) where a (b) corresponds to one group III (Zn) atom and A (B) to one N (O) atom. The ideal wurtzite structure consists thus of two hcp sub-lattices offset by $5/8$ of the c-lattice constant along the c-direction. This offset provides a charge imbalance. Thus, a spontaneous electrical polarization field arises along the c-axis (as indicated in figure 2.1). This anisotropy reflects in the space symmetry group $P6_3mc$ (Hermann-Mauguin notation). Every atom and its four nearest neighbors form a tetrahedral structure because of sp^3-hybridization. In c-direction (c) every group-III atom is bond to three N atoms in the underlaying layer (cf. 2.1). In -c-direction (-c) group-III atoms have only one bond to underlaying N atoms, but N atoms have three bonds to the underlaying group-III atoms. Thus the c-axis direction determines the polarity or face. The same structure is found for ZnO. Properties like chemical and thermal stability as well as growth kinetics depend on the polarity of the growth surface.

In order to exploit the symmetry of the hexagonal lattice, there is a modified Miller-Bravais notation used to describe it, the (*hkil*) notation, where $i = -(h+k)$. Figure 2.2 a) shows the (0001) (c) and the $(000\bar{1})$ (-c) planes. These planes are called the polar planes

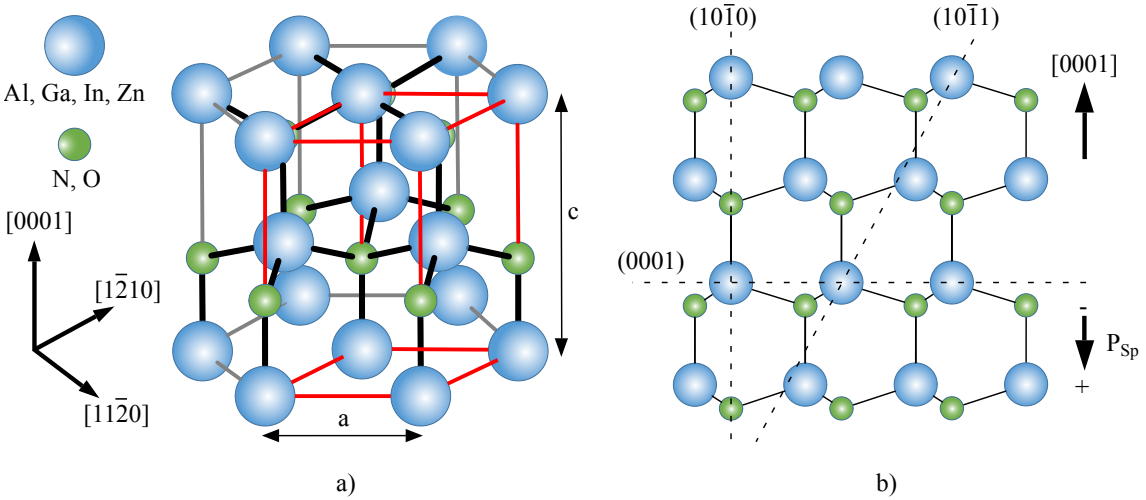

Figure 2.1: a) Wurtzite structure: blue spheres: Zn or Group-III elements like Al, Ga, In; green spheres: N or O; gray lines mark the hexagonal structure; black lines mark chemical bonds; red lines combined with some black lines mark unit cell. b) Wurtzite structure, guides to the eye are added to indicate (0001), (10$\bar{1}$0) and (10$\bar{1}$1) planes as well as the direction of spontaneous polarization field P_{Sp}.

of the wurtzite crystal since the spontaneous electric field (P_{Sp}) points along the [000$\bar{1}$] direction as indicated in figure 2.1. The angle between the (0001), (000$\bar{1}$) planes and the spontaneous electric field P_{Sp} is 90°. All families of planes with $l \neq 0$ and either $h \neq 0$ or $k \neq 0$, are called semi-polar planes because the angle between this planes and P_{Sp} is between zero and 90° (cf. figure 2.2 b). Finally, for families of non-polar planes $l = 0$ and either $h \neq 0$ or $k \neq 0$, as depicted in figure 2.2 c), the angle between these planes and P_{Sp} is 0° and thus the spontaneous electric field orthogonal to those planes is zero.

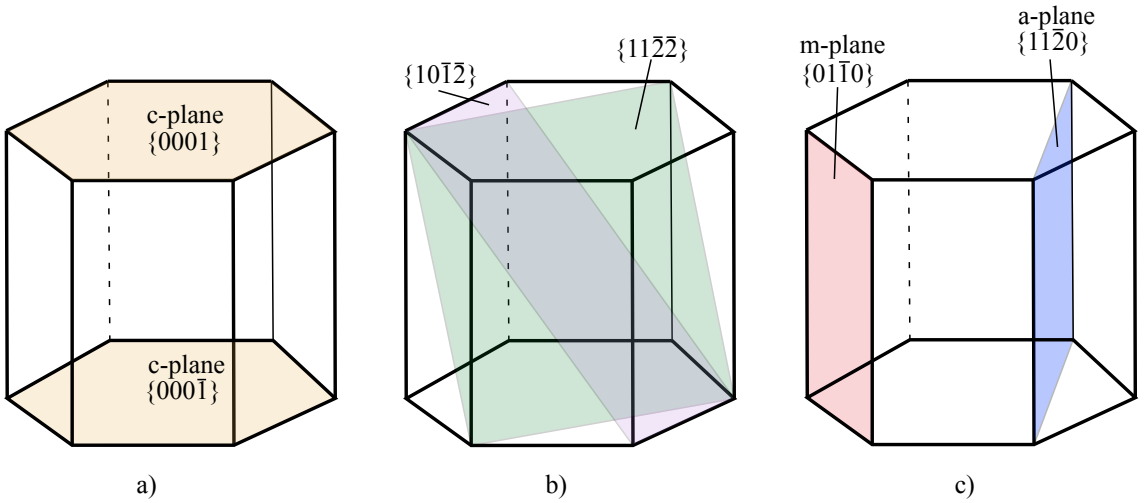

Figure 2.2: a) Polar c-planes {0001} and {000$\bar{1}$}. b) Two semi-polar planes {10$\bar{1}\bar{2}$} and {11$\bar{2}\bar{2}$}. c) Non-polar m- and a-plane.

Material	*a-lattice parameter* in Å	*c-lattice parameter* in Å
ZnO	3.25 [38], [39], [40]	5.20 [38], [39], [40]
InN	(3.52-3.54) [41], 3.54 [42]	5.70 [43], [41], 5.72 [42]
GaN	3.19 [44], (3.18 - 3.19) [45], 3.18 [46]	5.18 [45], 5.19 [44],[46]

Table 2.1: a- and c- lattice parameters of ZnO, InN and GaN.

Table 2.1 presents the a- and c- lattice parameters of ZnO, InN and GaN. If the lattice parameters of two compounds are known, than the lattice parameters of their ternary alloy can be approximated using Vegard's law. In case of InN and GaN and their ternary alloy (In, Ga)N, Vegard's law takes the form:

$$a_{In_xGa_{1-x}N}(x) = a_{InN}x + a_{GaN}(1-x) \tag{2.1}$$

With a_{InN}, a_{GaN} and $a_{In_xGa_{1-x}N}(x)$ the a-lattice parameter of InN, GaN and (In, Ga)N with indium content x. The same relationship is valid for the c-lattice parameter.

2.2 Physical properties of III-nitrides

2.2.1 Thermal stability

Though III-nitrides have all the same thermodynamic stable wurtzite structure, they differ for example in the strengths of their bonds. The bonds between Ga-N are stronger than the bonds between In-N. Averbeck *et al.* proposed an Arrhenius-like behavior for the decomposition and desorption process dependent on the In content x of (In, Ga)N [47]:

$$R = C \cdot x \cdot e^{\frac{-E_A(x)}{k \cdot T}} \tag{2.2}$$

With R the rate of decomposition or desorption, x the indium content, C a constant, E_A the activation energy for decomposition or desorption, k the Boltzmann constant and T the temperature. For $x = 1$, equation 2.2 describes the rate of decomposition of InN.

In addition to the difference in E_A between InN and GaN, there is a difference in temperature for the onset of decomposition (480 °C for InN [30], [8] and 700 °C for GaN [11], [10]). This difference in optimal growth temperature poses a challenge for the growth

of high quality InN/GaN structures. If the growth temperature is below the optimal growth temperature for GaN, then the crystal quality of the (In, Ga)N heterostructure deteriorates. If the growth temperature is above the optimal growth temperature of InN, then the layer starts to decompose and the incorporation of indium decreases. The activation energy for desorption of In on Ga-GaN is $E_A = 2.49$ eV [8] and therefore higher than the activation energy for decomposition (1.69 eV [7] - 1.92 eV [8]). Thus, when (In, Ga)N starts to decompose, there is accumulation of liquid indium on the surface. This has to be taken into account during the growth process, since indium droplets influence the surface morphology.

The thermal stability of the growing layer is also depending on the polarity of the crystal. Indium desorption measurements during the growth of thin film InN on N- and Ga-polar GaN showed a considerable indium desorption above 480 °C for growth on Ga-GaN [8], [48] compared to 590 °C for growth on N-GaN [48]. This is due to the difference in bond-configuration for both polarities. In N-polarity the nitrogen atoms that are incorporated into the growing layer have 3 bonds to the underlaying group-III atoms, compared to only 1 bond in case of group-III polarity. This impedes the decomposition of InN and enables thus the growth at higher temperatures.

2.2.2 Optical properties

InN, GaN and their ternary alloys can cover the whole visible spectral range [4], [5],[6], [49], [50]. This makes them interesting material systems for use in opto-electronic devices like LEDs and LDs, because the band gaps of (In, Ga)N ternary alloys can be tailored to emit light over the whole visible spectrum and beyond, by changing the indium content in the (In, Ga)N alloy.

These materials have a direct band gap, thus electrons and holes can recombine with high efficiency through a two-particle process. This is necessary for usage in LED technology.

The band gap value of (In, Ga)N ternary alloys can be approximated using Vegard's law:

$$E_{In_xGa_{1-x}N}(x) = E_{InN}x + E_{GaN}(1-x) - x(1-x)b \tag{2.3}$$

With b a bowing parameter that accounts for the non-linear behavior of the (In, Ga)N band gap as a function of the indium content. The electric fields (spontaneous and piezo-electric) present in group-III nitrides and ZnO force electrons and holes into opposite directions inside a QW. This decreases the overlap of the wave functions of electrons and holes and following Fermi's golden rule this leads to an increase in the radiative decay time. This increase scales not only with the electric field strength but also with the QW width. Additionally the energy band gaps are bent by these electric fields which cause an emission red-shift [51],[52]. These two effects are referred to as the Stark effect. The energy levels within the QW depend on the well thickness, this is called the confinement effect, Stark effect and confinement effect are often combined and called QCSE [53].

2.2.3 Electrical properties

InN posses a series of properties that makes it an interesting material for optoelectronic devices, among them the lowest effective electron masses of all group-III nitrides. For example the longitudinal effective electron mass $m_e^{||}$ in InN has values ranging from 0.04 m_0 to 0.085 m_0 [[54], [55], [56], [57]], compared to 0.20 m_0 to 0.29 m_0 in GaN [[58], [59]] and 0.29 m_0 to 0.45 m_0 in AlN [60]. Theoretical predictions for band parameters of all three mentioned materials can be found in a report by Rinke *et al.* [61]. This low effective electron mass of InN gives rise to a high electron mobility up to 2370 cm^2/Vs [62] and a high steady-state peak drift velocity of 4.2×10^7 cm/s at an applied electric field of 65 kV/cm, compared to 1150 cm^2/Vs [63] and 2.9×10^7 cm/s at 140 kV/cm [64] for GaN, respectively. This high steady-state peak drift velocity at a comparable small applied electric field qualifies InN for the use in high performance heterojunction field-effect transistors.

As grown InN, meaning without intentional doping, is always n-type doped due to the presence of several possible impurities [65].

The charge carrier density of unintentionally doped GaN exhibits a wide range with some examplary reported values of 1.2×10^{16} cm^{-3} [63], 2.3×10^{18} - 1.0×10^{19} cm^{-3} [66], 2.0×10^{17} cm^{-3} [67]. This is attributed to the incorporation of impurities, primarily O. Unintentional p-doping on the other hand was attributed to carbon impurities [68], the latter cause the well known yellow luminescence in GaN [69], [70].

3 Experimental methods: Theory and praxis

3.1 Heteroepitaxy of group-III nitrides

3.1.1 Epitaxial growth modes

Epitaxy refers to the growth of a crystal (epitaxial layer or epilayer) on another crystalline material (substrate), where the grown epilayer assumes some of the crystalline orientation and properties of the underlying substrate. There are two different forms of epitaxy: Homo- and heteroepitaxy. If the epitaxial layer and the substrate consist of the same (different) material it is the first (second) case.

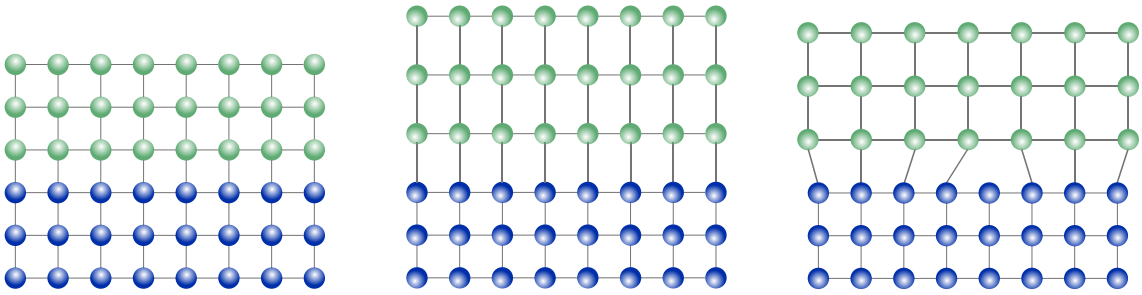

Figure 3.1: a) Homoepitaxy or lattice matched heteroepitaxy b) Heteroepitaxy, pseudomorphic growth c) Heteroepitaxy with misfit dislocation. Blue atoms belong to the substrate, green atoms belong to the epitaxial layer.

There are combinations of material systems that match in lattice parameter, for example $In_{0.18}Ga_{0.82}N$ on ZnO. In this case the growth of one on the other is called lattice-matched. If in case of heteroepitaxy the epitaxial layer assumes the in-plane lattice parameter a of the substrate, it is called pseudomorphic growth. By matching the in-plane lattice parameter a, the out-of-plane lattice parameter c changes and the relation between the change in a- and c- lattice parameter is described by the Poisson ratio ν. Since the lattice parameter of the epitaxial layer deviates from its natural value, strain occurs. Lattice strain is defined as $\epsilon = \frac{a_{Sub} - a_{Epi}}{a_{Epi}}$. Strain within a crystal can be partially or fully relaxed by glide,

bending, or formation of lattice defects or surface undulations. If the *a*-lattice parameter of the substrate is smaller then the *a*-lattice parameter of the epitaxial layer, the epitaxial layer is tensily strained in case of pseudomorphic growth. If it is the other way around, the epitaxial layer is compressively strained. With the introduction of strain, strain energy $E_{strain} = \frac{1}{2}\lambda\epsilon^2 V$, with λ the elastic modulus and V the volume of the strained layer increases with volume of the strained layer. As the strain energy increases, the formation of defects or surface undulations becomes energetically more favorable [71]. Since the surface area is fixed by the substrate, the critical layer thickness for the formation of defects is stated instead. In figure 3.1 homo- and heteroepitaxy (with and without lattice defects) is depicted. Besides strain, the surface has to be considered too. Surface energy can be visualized by cutting a crystal in two halfs, thus two new surfaces would be created. The energy necessary to cut all chemical bonds is equivalent to the surface energy of the two new surfaces. This also explains why different crystal facets have different surface energy densities - it is because they exhibit different densities of dangling bonds [71]. The growing crystal will take a form that minimizes the total energy. One of the components of the total energy is the surface energy. This means that the growth mode and the shape of the crystal will depend among other things on the relation of the surface energy density of all possible facets of the crystal [72] and can be influenced by introducing surfactants that change the relations of the surface energy densities of different surfaces [73], [74], [75], or by changing the V/III ratio in case of growth of group-III nitrides [76], [77], [78], [13]. By saturating unsaturated bonds, for example through surfactants, the surface energy of this specific surface will always be reduced.

Neglecting the strain energy, theoretical growth models suggest that the growth mode is governed by the surface free energy of the substrate σ_s, the epitaxial layer σ_e and the substrate-epilayer interface σ_i [73]. The surface free energy is the energy that is needed to create a surface of a specific material. Three different growth modes are traditionally distinguished and related to these surface free energies. Figure 3.2 illustrates the relationship between these surface free energies using the example of a surface wet by a fluid under a contact angle α.

Balancing the surface free energies depicted in figure 3.2 gives the equation:

$$\sigma_s = \sigma_e \cos(\alpha) + \sigma_i \tag{3.1}$$

In general three different growth modes are distinguished. The first is two dimensional layer-by-layer growth, also called Frank van der Merwe (FvdM) growth, during which the substrate surface is completely overgrown with a ML thick epitaxial layer before the

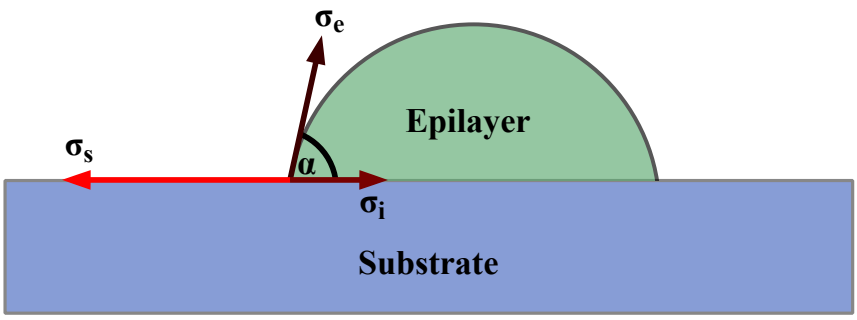

Figure 3.2: Wetting of a substrate surface by a "epilayer" fluid. σ_s, σ_e and σ_i need to be balanced.

next layer starts to nucleate on top of the previous epilayer. This is the case of complete surface wetting (see figure 3.3 a) and yields smooth layers. The condition for this growth mode is $\cos(0^\circ) = 1$:

$$\sigma_s > \sigma_e + \sigma_i \tag{3.2}$$

In this case the total surface energy is minimized by minimizing the substrate/surface energy, which results in a complete wetting of the substrate surface.

The second growth mode is governed by island nucleation and growth. This growth mode produces rather rough surfaces and is called Volmer Weber (VW) growth (figure 3.3 b). At its extremum the fluid does not wet the surface at all but forms a spherical droplet on top of the surface, the condition for this translates to $\cos(180^\circ) = -1$ [79]:

$$\sigma_s < \sigma_e + \sigma_i \tag{3.3}$$

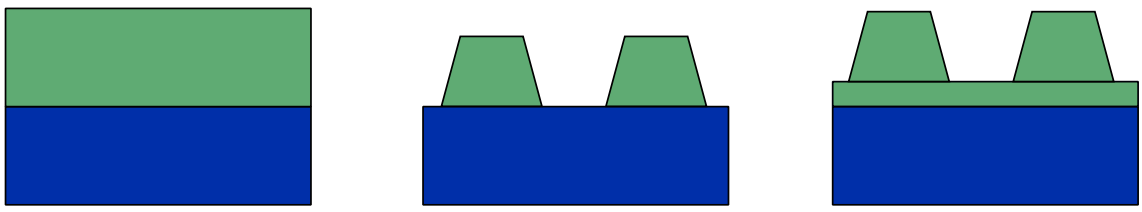

Figure 3.3: Growth modes: a) Two dimensional FvdM b) Three dimensional VW c) SK transition between 2D and 3D growth mode beyond critical layer thickness. Blue and green layers depict the substrate and the epitaxial layer, respectively.

The third growth mode is called Stranski-Krastanov (SK) growth (figure 3.3 c). Initially a two dimensional layer builds until a critical layer thickness is reached and the formation of 3D islands takes place. The relation of the surface energies favors wetting of the substrate, but the accumulation of strain energy initiates at some layer thickness a transition from 2D layer to 3D island growth to release some of the strain energy. The condition for this growth is:

$$\sigma_s \approx \sigma_e + \sigma_i \tag{3.4}$$

The conditions for crystal growth are more complex than just considering surface energies and wetting conditions. Strain and its relief play a crucial role and should not be neglected. There is a complex interplay between surface energies and strain energies [80], [81], [82]. FvdM growth is usually observed for rather small values of strain around $\epsilon < 2\%$. For intermediate values of strain SK growth is common. For high values of strain $\epsilon > 9\%$, VW growth is frequently encountered, but these are just rough indications. For a more detailed analysis see Daruka *et al.* [80].

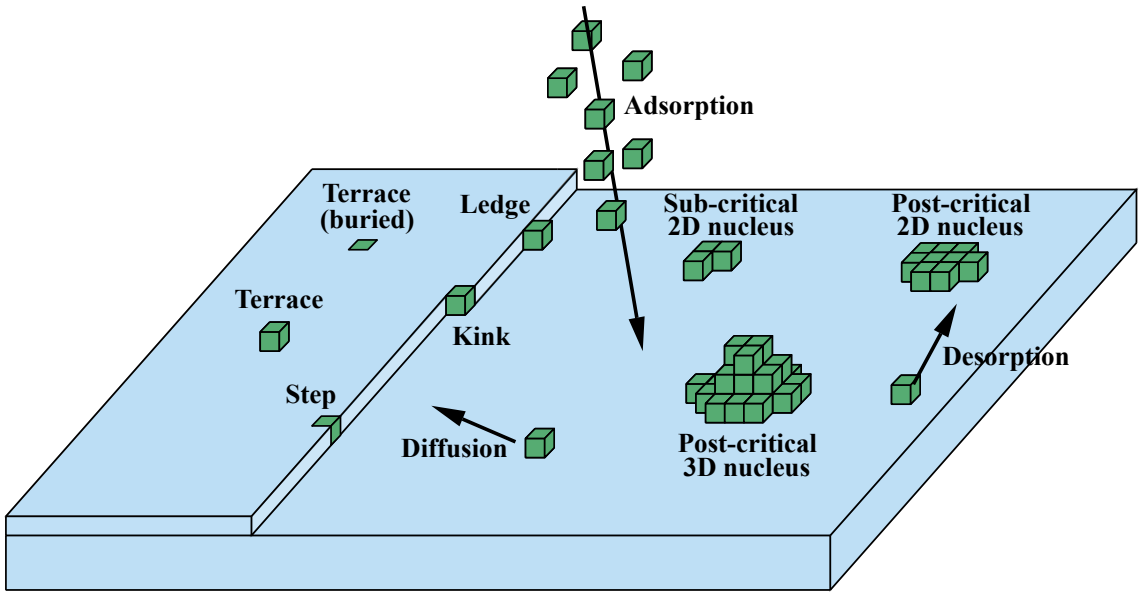

Figure 3.4: Illustration of adatom behavior on a surface during MBE growth applying the Kossel model.

The growth mode is not only determined by thermodynamic considerations but also by kinetic conditions, for example the diffusion length of adatoms. Figure 3.4 shows a schematic of the growth process with MBE. A beam of atoms, molecules or ions is the source of adatoms that impinge on the surface. Depending on conditions like substrate temperature and beam flux temperature, density of adatoms on the surface, aver-

age length of crystal terraces and possible presence of surfactants, the arriving adatoms will have a certain diffusion length - an average length of diffusion after which they either get incorporated into the growing crystal or desorb again into the ambient. In figure 3.4 the so-called Kossel model is sketched, it is a simplification, the building blocks of the crystal (atoms) are depicted as cubes which can form a maximum of six bonds to their neighbors - one bond per side of the cube. Several lattice sites are illustrated and numbered, the energetically most favorable site is the bulk site - a site within the bulk crystal where there are 6 bonds formed to the neighboring atoms. The less bonds are formed, the less energetically favorable the lattice site is (if strain is neglected). Every adatom diffusing over the surface has one bond to the crystal surface, if it interacts with another adatom, a second bond is formed, and so on. Two adatoms that bind together have together two bonds to the crystal surface, which makes this two-adatom-nucleus less mobile on the surface than a single adatom is. The more adatoms bind together the less mobile that nucleus becomes. Adatoms that are part of a nucleus can separate again from the nucleus and continue to diffuse. Whether the net flux to a nucleus is positive or negative is determined by thermodynamic considerations [71]. The Thompson-Gibbs equation states:

$$\Delta G = \mu_v dn_v + \mu_l dn_l + \sigma dS = 0 \tag{3.5}$$

Where ΔG is the change in the Gibbs free energy, μ_v and μ_l are the chemical potentials of the vapor and liquid phase, dn_v and dn_l are the change in atoms in the vapor and liquid phase, σ is the surface tension and dS is the change in surface. If we consider a closed system, then $dn_l = -dn_v$. This equation describes the energy that is either gained or needs to be invested if the liquid phase grows at the expense of the vapor phase while additional surface/interface is created.

$$\Delta G = (\mu_l - \mu_v) dn_l + \sigma dS = 0 \tag{3.6}$$

The first term scales with the volume ($\propto r^3$) of the vapor or the liquid phase with r being the radius of spherical volume, while the second term scales with the surface ($\propto r^2$) as depicted in figure 3.5. This illustrates that the formation of a liquid phase within a vapor ambient costs energy even if the chemical potential in the liquid phase is lower than in the vapor phase. This is due to the creation of a surface. But as the liquid phase (droplet) grows, the impact of the volume and the gain in energy due to a lower chemical potential of the liquid phase over the vapor phase grows compared to the impact of the surface and

the energetic costs that come with it. This change in the relationship of volume-energy to surface energy reflects in the change of slope of the Gibbs free energy as a function of droplet radius. After it initially rises until a critical droplet radius r_{crit} is reached, the slope of the Gibbs free energy turns negative, and ΔG decreases again. This means that energy is gained by adding further atoms to the liquid droplet for $r > r_{crit}$ [71].

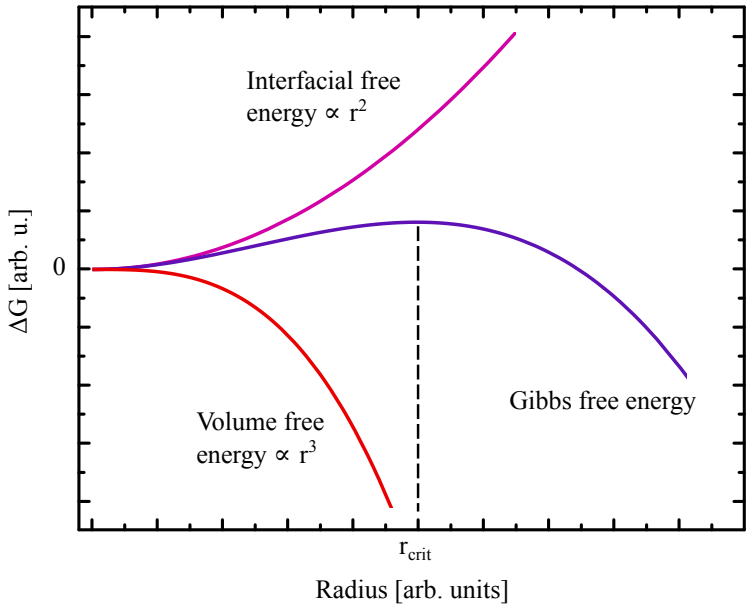

Figure 3.5: Changes in the Gibbs free energy (purple) due to changes in the volume free energy (red) and surface free energy (pink). r_{crit} denotes the critical radius at which the slope of the Gibbs free energy turns negative.

The same is true for growing a crystal phase from a beam of molecules, atoms or ions. Adatoms diffusing on the surface of the substrate can interact with each other and form a nucleus (2D or 3D) (see figure 3.4). This nucleus is initially unstable until it grows beyond the critical radius upon which it becomes stable. The critical radius is determined by thermodynamic parameters, like temperature, pressure, etc, as indicated by the fact that the Gibbs free energy, given by equation 3.5, contains a term for the chemical potential $[\mu(T, p, etc)]$.

Besides post-critical nuclei, there are other energetically favorable sites for adatoms to adsorb, for example step edges or kink positions [83]. The diffusion and interaction of adatoms is a stochastic process. The probability for incorporation either at a kink position or a nucleus can be influenced by factors like the miscut-angle of the crystal, which determines the length of the terraces, or by the substrate temperature and beam flux temperature, which determines the kinetic energy of the adatoms, and thus their diffusion length. Another important factor is the crystallographic orientation of the surface, which determines the types of dangling bonds, and whether it is rather stepped or kinked [71].

If adatoms preferentially incorporate into the growing crystal at the kink position, the crystal grows in a so-called step-flow mode, this happens when conditions are met for FvdM growth and the diffusion length of adatoms exceeds half the average length of terraces $l_T/2$. If conditions for FvdM growth are met and the diffusion length of adatoms is smaller than $l_T/2$, growth proceeds in layer-by-layer growth where two dimensional nuclei form all over the terraces and grow radially until they meet and coalesce. The more the diffusion length exceeds $l_T/2$, the more adatoms will reach the step edge and kink positions (reach 2D nuclei) and incorporate there into the growing layer. The diffusion length of adatoms is not only determined by growth conditions like substrate temperature, V/III ratio but also by substrate polarity and thermodynamic considerations, which determine for example the critical radius for nucleation of 2D structures (see discussion above). The smaller this critical radius is, the higher is the density of small nuclei able to capture adatoms and incorporate them into their growing structure. The boundaries of 2D nuclei are potential sites for defects. Therefore step-flow growth potentially yields higher quality crystals.

3.1.2 Molecular Beam Epitaxy

Molecular beam apitaxy (MBE) is a technique for crystal growth by which the materials are deposited on the heated substrate by means of one or more beams of molecules, ions or atoms. The source of this beam often originates from a so-called effusion cell (see figure 3.6) that contains the material in highly-purified, elementary form. Alternatively electron beam physical vapor deposition can be applied. When this effusion cell is heated up to an element-specific range of temperatures, the material first melts and then vaporizes causing the effusion cell to emit a temperature dependent flux of material. The temperature of the effusion cell and therefore the flux is controlled by proportional-integral-derivative parameters limiting the unwanted variation in flux to less then 1%. A shutter at the end of the effusion cell allows to open and close the cell. For the nitrogen supply for the growth of nitride-based crystals, we employed a radio frequency (RF) plasma cell. Purified N_2 is introduced in this cell and by heating up through a RF generator nitrogen radicals are created. The flux of emitted nitrogen radicals is controlled by the inflow of purified N_2 and the power applied to the RF source.

The ultra-high vacuum (UHV) in the growth chamber is produced by a system of different pumps, a rough pump creating an initial pressure of about 10^{-6} torr, after that an ion getter pump and cryo-pump take over decreasing the pressure to (10^{-10} - 10^{-11}) torr. Un-

der these conditions the rate of impinging atoms from the effusion cells is by many orders of magnitude higher then the rate of impinging atoms and molecules from the ambient within the growth chamber such as oxygen, hydrogen or carbon. The growth chamber is surrounded by a double wall that forms a cryopanel (see figure 3.6), that can be filled with liquid nitrogen further cooling down the growth chamber and thus decreasing the pressure within the chamber.

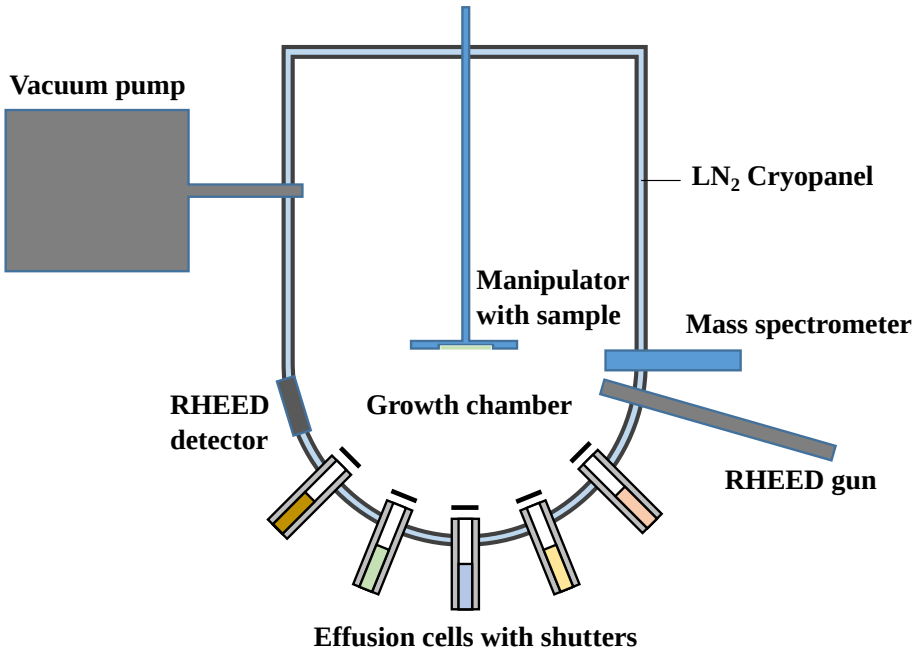

Figure 3.6: Schematic of MBE.

The UHV of the MBE system makes it possible to investigate the crystal growth *in-situ* with tools like RHEED, making MBE suitable for research and growth of high quality crystals.

The MBE system used for the growth of the samples investigated in this study is a DCA P600 plasma-assisted molecular beam epitaxy (PAMBE) system. It consists of 3 chambers. First, there is a so-called load lock, used to introduce the sample in the system. The pressure within the load lock is decreased to 10^{-8} torr and heated up for water outgassing. After that, the sample may be introduced into the preparation chamber ($p \sim 10^{-10}$ torr) that consists of a sample storage/annealing unit used to outgas/anneal samples. The growth chamber, as schematically illustrated in figure 3.6, is equipped with two nitrogen plasma cells, as well as two indium, two gallium, two aluminum cells, one magnesium and one silicon cell. Additionally, the MBE system is equipped with a RHEED system, a pyrometer, a laser combined with photo detector for laser reflectometry measurements, a beam flux monitor and a quadrupole mass spectrometer. The pyrometer is used to determine the substrate surface temperature within a certain temperature range. The laser

setup combined with the thermo-couple element is used for the same purpose. In addition, it is useful to calibrate the growth rate or to monitor changes on the surface due to a possible accumulation of a metal adlayer. The beam flux monitor is employed to measure the fluxes of the effusion cells. The quadrupole mass spectrometer helps to investigate the desorption of molecules, atoms and ions from the sample surface.

3.1.3 Growth of InN and ternary (In, Ga)N by Molecular Beam Epitaxy

Influence of the V/III ratio

The V/III ratio is a very important growth parameter for the growth of III-nitrides since it influences the surface reconstruction [84], [85], [86] but also the growth mode [87], [13], [14] by influencing the adatom mobility. Adatoms with a higher diffusion length will diffuse longer across the surface and their probability of being incorporated into the growing crystal at an energetically favorable site (for example a kink position) will be higher, which will favor the growth of smooth 2D surfaces, if thermodynamic conditions for 2D growth are met. The lower the adatom mobility is, the higher is the chance that the adatoms will incorporate into the growing crystal close to where they were adsorbed on the crystal surface. As these incorporation sites are not necessarily energetically favorable crystal sites, this will lead to a rough, grainlike morphology, with formation of new defects like stacking faults, grain boundaries, etc. The growth of SPSLs with ML-thin layers requires the fabrication of smooth, abrupt interfaces to prevent fluctuations in the quantum confinement potential. The control of the surface morphology is therefore a necessity. Gallinat *et al.* reported for the growth of InN on Ga-GaN that at 450 °C much smoother 2D surfaces were achieved for In-rich growth ($V/III = 0.8$) than for N-rich growth ($V/III = 1.2$) [9], [14]. The same dependence of the surface roughness on the V/III ratio was found for the growth of InN on N-GaN at 530 °C. N-rich growth with $V/III = 1.1$ resulted in a root mean square roughness (RMS) of $RMS = 54.1$ nm, whereas In-rich growth with $V/III = 0.7$ yielded a surface with $RMS = 6.6$ nm [62]. Furthermore, Wang *et al.* showed that InN grown at 500 °C with $V/III = 1.03$ exhibited large and deep pits with smooth step-flow morphology in between and an overall RMS roughness of 28 nm. InN grown at the same temperature but with $V/III = 0.95$ exhibited smaller and shallower pits as well as droplets on the surface with a smooth step-flow morphology in between and a RMS roughness of 2.8 nm [87]. This dependence of the surface morphology of InN on the V/III ratio was confirmed by other groups [88].

Heying *et al.* investigated this dependence for GaN growth and showed a similar behavior: N-rich growth ($V/III = 1.1$) leads to an overall rough surface with pits, growth near stochiometry ($V/III = 1$) resulted in rather smooth 2D surfaces that are interrupted by deep pits, and Ga-rich growth ($V/III = 0.9$) produced a smooth surface without pits ($V/III = 1.1$) [13]. The V/III ratio does not only influence the surface morphology and the defect density but the overall crystalline quality of the grown layer [89], [90], [88], the optical properties [89], [90] and the electrical properties [91], [88]. The surface morphology and the crystalline quality deteriorates when moving from group-III-rich growth to N-rich growth, which results in rough surfaces and crystals that are composed of a grain-like structure [89], [90]. The optical emission intensity measured by PL decreases for N-rich growth [89], which indicates a worsening of the optical properties for samples grown at 650 °C.

In order to understand the relation between surface reconstruction, polarity, adlayers and diffusion mechanisms, theoretical calculations were performed for GaN. Based on total energy calculations, applying density functional theory, the GaN(0001) and GaN(000$\bar{1}$) surface reconstructions were investigated. It was reported that for both polarities and all growth regimes (N-rich to Ga-rich) the surfaces would always be terminated by Ga-adatom reconstructions (for example 2x2 Ga-adatom layer, 1x1 Ga adlayer). Instead for extremely N-rich growth conditions on GaN(0001) a 2x2 N-adatom reconstruction was found to be the energetically most favorable one [84], [86]. The calculations by Northrup *et al.* yielded for very Ga-rich conditions a different GaN(0001) surface termination, a so-called laterally contracted bilayer, composed of one Ga-layer that shows the same gallium atom density than GaN followed by a laterally contracted gallium layer with a density 30% higher than in GaN [86]. The presence of a stable gallium adlayer of at least two MLs was confirmed by Mula *et al.* [92] and Koblmüller *et al.* [93]. RHEED and in some cases STM investigations conducted by several groups confirmed the presence of a 2x2 reconstruction under group-III-rich growth conditions on GaN(0001) [91] as well as under extreme N-rich conditions on GaN(0001) [90], 1x1 reconstructions were found under very group-III-rich conditions on GaN(0001) [92], [94] and on GaN(000$\bar{1}$)[84]. Depending on the coverage of the surface by gallium and the substrate temperature additional reconstructions were found like 3x3, 6x6 and 6x12 [84]. Ga-adatoms diffusing on gallium terminated surfaces (usually 1x1 or 2x2 reconstructions) of both polarities experience a considerably lower diffusion barrier [0.4 eV for GaN(0001), 0.2 eV for GaN(000$\bar{1}$)] than N-adatoms [1.4 eV for GaN(0001), 0.9 eV for GaN(000$\bar{1}$)] [95]. This is due to the rather weak metallic Ga-Ga bonds formed between surface reconstructions and the adlayer compared to the stronger Ga-N bonds. This means that group-III adatoms are more mobile than the rather immobile nitrogen atoms. When a nitrogen adatom forms a bond to a gallium

adatom, it creates a Ga-N compound that has two bonds to the underlying surface and is thus very immobile. The higher the concentration of nitrogen adatoms on the surface is, the higher is the probability of this process. The presence of more nitrogen atoms decreases thus the diffusion length of gallium adatoms. This was shown theoretically for extreme N-rich conditions (surface is terminated by N-atoms). In this case the diffusion barriers for Ga-adatoms increased from 0.4 eV to 1.8 eV for GaN(0001) and from 0.2 eV to 1.0 eV for GaN(000$\bar{1}$) [95]. The probability of an adatom to hop from one site to an adjacent one is proportional to $\exp(\frac{-(E_{DB}-E)}{k_B T})$, with E_{DB} the diffusion barrier or activation energy for diffusion, k_B the Boltzmann's constant and T the temperature. It can be shown that the probability of diffusion and thus the diffusion length of adatoms changes considerably even for moderate changes in E_{DB}, which explains the influence of the V/III ratio on the growth mode and the advantages of growing under group-III-rich conditions. This relationship between surface reconstruction or adlayer, diffusion length and surface morphology was explained for GaN, but a similar relationship is found for InN. In both cases the surface is terminated by group-III atoms. Calculations performed by C. K. Gan *et al.* [85] suggest that on InN(0001) an unreconstructed surface for N-rich conditions and an In-trimer reconstruction for In-rich conditions form, while on InN(000$\bar{1}$) the energetically most favorable surface termination is a ML-thick In-adlayer [85]. Theoretical calculations performed by Segev *et al.* [96] result in the same surface termination for InN(000$\bar{1}$), but suggest for InN(0001) a 2x2 In-adatom reconstruction (N-rich) and indium bilayer coverage (In-rich). This means that similar dependencies between V/III ratio and adatom mobility especially for indium atoms were found. For In-rich growth the indium adatoms are more mobile than the nitrogen atoms which from stronger, directional bonds to indium atoms.

There is a draw-back of group-III-rich growth conditions: If gallium or indium atoms accumulate at the surface, they can form droplets. It has been shown that gallium droplets on GaN(0001) cause changes to the surface morphology. For example, the terrace width of spiral hillocks underneath such droplets is decreased and voids can form at the droplet boundaries [97]. The growth of hillocks is not initiated by droplets, but by screw dislocations intersecting the growth surface. The decrease in hillock terrace width is caused by droplets [97]. Therefore, one should avoid the formation of droplets. It may not be necessary to grow continuously under group-III-rich conditions to reap the advantages associated with it. Based on total energy calculations, applying density functional theory, Neugebauer *et al.* predicted the diffusion barrier for Ga-adatoms on a GaN(0001) surface with 1x1 In-adlayer to be 0.12 eV compared to 0.7 eV for Ga-adatoms on a bare GaN(0001) surface. For nitrogen atoms, they found that the energetically most favorable site is in between the top gallium atoms of the GaN(0001) layer and the indium atoms of the 1x1

In-adlayer on top of it, therefore they conclude that nitrogen atoms diffuse beneath the indium adlayer and call that mechanism adlayer-enhanced lateral diffusion (AELD). The diffusion barrier for nitrogen atoms using AELD is 0.5 eV [98] compared to 1.3 eV [95] diffusing on the bare GaN(0001) surface. To activate this diffusion mechanism, it is necessary to have a group-III adlayer on top of the surface, and the actual growth can take place under stoichiometric conditions, though it might be difficult to find and maintain exact stoichiometric conditions.

The surface reconstruction encountered for the growth of (In, Ga)N on GaN(0001) in the smooth growth regime (group-III-rich) is a 1x1 or $\sqrt{3} \times \sqrt{3}$ reconstruction [99]. This reconstruction starts to form close to the transition from rough (N-rich) to smooth growth regime. RHEED measurements during growth can thus be used to determine the growth conditions for this transition point and ensure that growth will continue in the smooth growth regime. A polarity-dependent indium surfactant effect was found for the growth of (In, Ga)N. For (In, Ga)N grown on GaN(0001) the presence of indium showed a significant surfactant effect, if enough indium is supplied the Ga/N ratio can be decreased below stoichiometry ($Ga/N < 1$) and the growth will continue in the smooth growth regime. For (In, Ga)N grown on GaN($000\bar{1}$) no such surfuctant effect of In was found [99].

The real V/III ratio is not determined by the ratio of the impinging fluxes but the ratio of the group-V and group-III elements on the surface of the growing layer. This means that partial decomposition of the growing layer and desorption processes have to be taken into account. For the growth of (In, Ga)N:

$$V/III = \frac{N_{im} + N_{dec} - N_{inc} - N_{des}}{In_{im} + In_{dec} - In_{inc} - In_{des} + Ga_{im} + Ga_{dec} - Ga_{inc} - Ga_{des}} \tag{3.7}$$

E_{im} gives the rate of impinging adatoms of the specific element E (in our case N, In and Ga), E_{dec}, E_{inc} and E_{des} give the rates of decomposition, incorporation and desorption, respectively. Note that the temperature for onset of decomposition for InN, GaN or desorption of indium and gallium atoms differs. Decomposition and incorporation of new adatoms usually takes place at the same time, it is the net balance of this processes, which depends strongly on temperature, that determines whether the layer will overall grow or decompose. The process of partial decomposition is an additional source of adatoms on the surface, together with the adatoms from the Knudsen cells and nitrogen plasma cells respectively. They both determine the total rate of incoming adatoms on the surface. Both processes of desorption and incorporation of adatoms deplete this reservoir of adatoms on the surface.

The activation energy for decomposition is higher for GaN than the activation energy for desorption. In contrast, the situation is reversed for InN (as described in chapter 1). This means that at any given temperature, as long as InN is available to decompose, the rate of decomposition will be higher than the rate of In-adatom desorption, therefore the InN surface can not be thermally cleared of In-adatoms. The growth of structures consisting of alternating layers of different materials, like multi quantum wells (MQWs) or SPSLs makes it often necessary to desorb excess adatoms before resuming the growth, because otherwise intermixing would occur. This is the case for GaN and InN or (In, Ga)N. It is widely agreed on that due to the higher bond strength of Ga-N over In-N, gallium incorporates preferentially compared to indium into the growing (In, Ga)N layer [100], [101].

$$In_{inc} = N_{inc} - Ga_{inc} \tag{3.8}$$

The maximum incorporation rate of indium into the growing (In, Ga)N layer is limited by the excess nitrogen over gallium, and if the gallium flux exceeds the nitrogen flux, then there is no incorporation of indium [100]. Instead, the excess indium will accumulate on the surface forming liquid indium and some of it will desorb. If there is excess nitrogen over gallium adatoms, then the indium atoms are not replaced by gallium atoms and the incorporation into the growing (In, Ga)N layer is limited only by the decomposition of In-N bonds and the final indium content of the (In, Ga)N layer will be determined by equation 3.8.

To get rid of excess gallium before growing InN or (In, Ga)N a desorption step or growth interruption might be introduced, during which all cell shutters are closed and no deposition takes place, allowing for the excess gallium to be thermally desorbed from the surface. If needed, the substrate temperature can be increased to accelerate the process, but it will also increase the rate of decomposition and should be carefully monitored. An alternative to a desorption step is a nitridation step during which the surface is exposed to nitrogen only, in order to consume the excess of gallium (or indium) atoms and to form new GaN [InN, (In, Ga)N] in the process. This is called nitrogen radical beam irradiation by some authors [102], [103]. A third option is the intentional growth at stoichiometry or even slightly N-rich conditions. Even though it is well established that N-rich growth yields worse quality crystals than slightly group-III-rich growth [9], [14], [62], [13], [104]. Excess indium can not be thermally removed from an InN surface, as explained in the previous paragraph. The situation is different for (In, Ga)N because the In-N bonds are influenced by the configuration of their surrounding. The activation energy for decom-

position of In-N bonds in (In, Ga)N changes with the average indium content, the higher the indium content the lower the activation energy [100]. Yoshikawa *et al.* reported that the growth of 1 ML-thin InN on GaN can be achieved at higher temperatures than the growth of ML-thin InN on InN. They attributed this to a GaN matrix effect [29]. The presence of Ga-N bonds seem to stabilize the Ga-N-In-N compound. Therefore excess In-adatoms can be thermally removed from (In, Ga)N for low enough indium content.

Influence of the growth temperature

Besides the V/III ratio, the substrate temperature is the crucial growth parameter that determines the diffusion length and mobility of surface adatoms. The growth temperature influences all thermally activated processes. That includes decomposition, desorption, overcoming Schwoebel barriers and changing the thermodynamic conditions for the formation of phases (solid, liquid, vapor). Decomposition of InN and desorption of In is negligible for temperatures below 480 °C (on group-III-polar substrates) [14] and 580 °C (on N-polar substrates) [48], thus the V/III ratio can be approximated by comparing the flux ratios of indium and nitrogen. Smooth 2D layers with step-flow morphology is achieved by slightly In-rich growth (In/N>1) [14]. Above temperatures of 480 °C (580 °C) decomposition and desorption bgeins to matter and the indium lost needs to be compensated by an increased indium flux. The real V/III ratio of surface adatoms can no longer be approximated by comparing the impinging fluxes. The growth of InN with smooth 2D step-flow morphology was reported for MBE growth in a narrow temperature range from 450 °C [102], 480 °C [88], to 500 °C [87] and a growth diagram of InN depending on V/III ratio and temperature was established by Gallinat *et al.* [14] for In-polar InN.

Common substrate temperatures for MBE grown high quality Ga-GaN is in the range of 700 °C - 750 °C [90], [63], [67]. However, for temperatures above 700 °C, the decomposition and desorption of GaN is not negligible anymore and requires an increased gallium flux to keep a specific V/III ratio as shown in the GaN growth diagram, established by Adelmann *et al.* [15]. Thus, setting the growth temperature below the decomposition limit, smooth 2D layers with step-flow morphology can be achieved under slight In-excess, i.e. with the In- and N-flux such that $In/N > 1$.

Substrates for the growth of InN, GaN and (In, Ga)N

One of the obstacles for the epitaxial growth of InN, and (In, Ga)N is the lack of high quality, lattice-matched substrate, which are thermally compatible and not to expensive. $\alpha - Al_2O_3$ is commonly used as substrate for epitaxy of InN [57], GaN [105], [106] and ternary (In, Ga)N alloys [107]. When AlN or GaN is deposited directly on $\alpha - Al_2O_3$ they grow with their a-axis rotated by 30° relative to the $\alpha - Al_2O_3$ substrate due to the high lattice mismatch, and form $[10\bar{1}0]_{GaN,AlN} \parallel [11\bar{2}0]_{Al_2O_3}$. In contrast, InN on $\alpha - Al_2O_3$ forms with grains of mixed orientations, $[10\bar{1}0]_{InN} \parallel [11\bar{2}0]_{Al_2O_3}$ and $[11\bar{2}0]_{InN} \parallel [11\bar{2}0]_{Al_2O_3}$ [43], [108]. A Nitridation treatment of the $\alpha - Al_2O_3$ surface before the deposition of InN results in the growth of $[10\bar{1}0]_{InN} \parallel [11\bar{2}0]_{Al_2O_3}$ [108]. The structural and electrical properties of InN can be further improved by growing an AlN [109] or GaN [43] buffer layer on $\alpha - Al_2O_3$ before depositing InN. This technique has been frequently applied for GaN/Al_2O_3 [110], [111], [56], [103], [111] and AlN/Al_2O_3 [55], [56].

One of the factors determining the quality of a substrate is the defect density. (In, Ga)N layers are frequently grown on GaN/Al_2O_3 templates. Using Al_2O_3 as a substrate for the growth of an intermediate GaN buffer layer, usually using Metal Organic Chemical Vapor Deposition as a growth technique, results in a rather high defect density in the GaN layer of the order of $10^8 cm^{-2}$ [112] to $10^{10} cm^{-2}$. There are other techniques, like Hydride Vapor Phase Epitaxy, that produce better quality GaN, with defect densities of the order of $10^4 cm^{-2}$ [113] or $10^5 cm^{-2}$ [114], or solution growth techniques that resulted in defect densities of $10^5 cm^{-2}$ [112], but the GaN substrates produced by these techniques are rather expensive.

Less frequently used substrates are for example Si for the growth of InN [115], [116], [117], and GaN [118], [119], [120], SiC for InN growth [121], [122], [123], [124] and GaN growth [125], [126], [127], [128], ZnO for InN [129], [130], [131], GaN [132], [133] and (In, Ga)N [134], [135], [136].

Growth of ternary (In, Ga)N alloys

Growing high quality (In, Ga)N is still a challenging task, especially (In, Ga)N with high indium content. Due to the difference in bonding strengths as discussed in previous section (see paragraph 3.1.3), different optimum growth temperatures arise (see paragraph 3.1.3). The optimum growth temperature for MBE grown GaN is more than 200 °C above that of InN. This makes it problematic to grow high quality (In, Ga)N with a high in-

dium content. The indium content in the (In, Ga)N layer can be controlled by adjusting the growth temperature (see paragraph3.1.3) and the group-III and nitrogen fluxes (see paragraph3.1.3) [137], [100], [138], [139], [140], [141].

Strain related issues that arise from the lack of lattice matched substrate for most compositions of (In, Ga)N are an additional challenge. Complicating matters, strain gives rise to several relaxation mechanisms. Examples are dislocation networks [142], [143], [144], the composition pulling effect [26], [27], the formation of V-shaped pits [27], [145], [146], [147], or the formation of (In, Ga)N consisting of two sublayers with different indium content and strain state [148].

Bazioti *et al.* investigated the relaxation mechanisms at play for (In, Ga)N with various indium contents [140]. They found that for low indium content, an indium rich layer forms at the growth front (composition pulling effect) and threading dislocations with c-component open up into V-pits at the surface. In the vicinity of these V-pits, basal plane stacking faults (BSF) are formed. At intermediate indium contents, a so-called sequestration layer (SQL) forms at the substrate-epilayer interface and partially relaxes through formation of misfit dislocations (MD). Above the SQL, another (In, Ga)N layer forms with higher indium content and higher degrees of relaxation. This layer is mainly relaxed through BSF. At higher indium contents, the additional introduction of MDs and earlier onset of BSFs suppresses the SQL.

The (In, Ga)N buffer and (In, Ga)N heterostructures grown in this study will likely fall under "intermediate indium content" and "high indium content". So we can expect the formation of a SQL with MDs and BSFs that relax the epitaxial layer.

3.2 Reflection High-Energy Electron Diffraction

RHEED is a non-destructive tool for *in-situ* investigations, that can be used for example to determine the surface reconstruction, the surface morphology, growth mode, the growth rate and the lattice parameter. The RHEED setup consists of a fluorescence screen or a charge coupled device (CCD) camera and an electron gun that is driven at high voltage (20 kV in this study). The electron gun (see figure 3.7) emits a bundled beam of electrons that is focused on the sample surface at a grazing incidence angle by the use of magnetic lenses. The beam does not interact with molecules, atoms or ions on its path to the sample surface. Electrons focused on the sample surface interact with the electrons or nuclei of atoms of the surface layer and are being diffracted by them. These diffracted electrons

obey Bragg's law therefore creating regular diffraction patters on the detector. Because of the low angle of incidence of the electron beam on the sample (usually between 0.5° and 3°) and the high probability of interaction due to Coulomb interaction, these electrons penetrate only the upper most atomic monolayers of the surface. Therefore RHEED is a very surface-sensitive method of investigation.

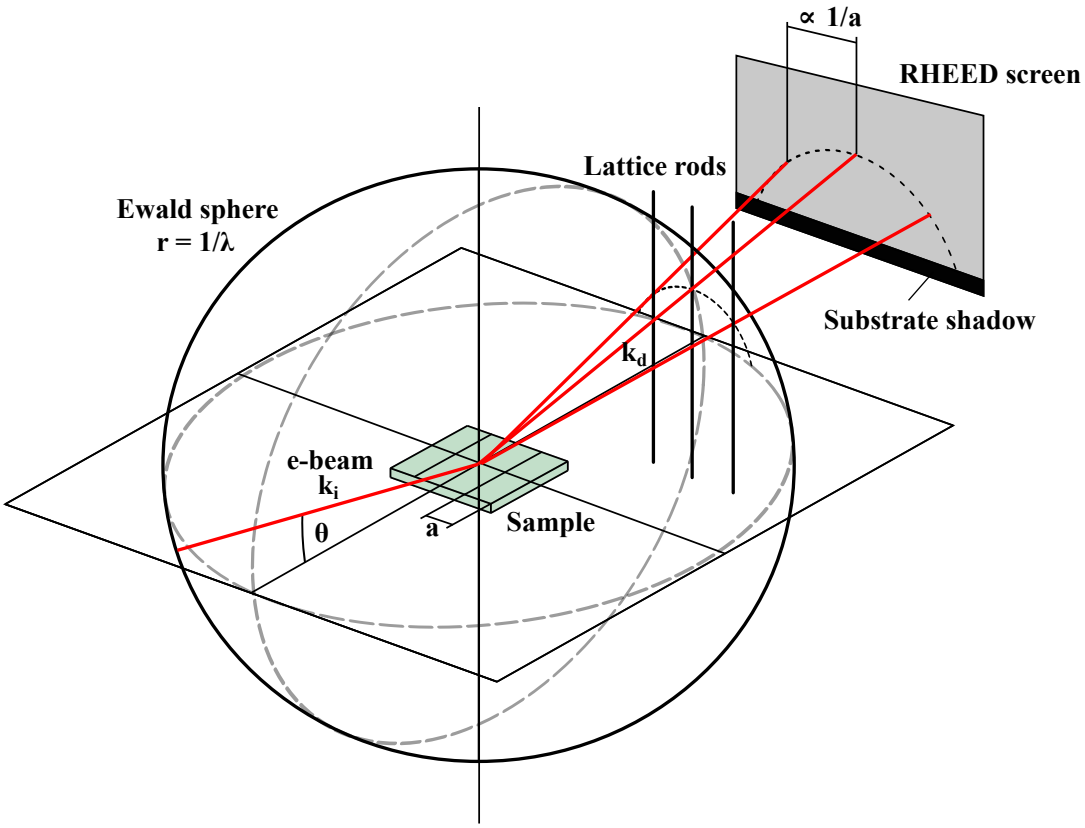

Figure 3.7: Schematic of RHEED geometry with the electron beam (red), the sample with lattice parameter a and the Ewald sphere with radius $r = 1/\lambda$, with λ the wavelength of the electrons. Guides to the eye are added, that show the intersection of the Ewald sphere with the x-y- and x-z-plane (grey, dotted lines).

Figure 3.7 illustrates the geometry of RHEED measurements. The electron beam (red) that impinges on the sample has the momentum $\vec{k_i}$. Assuming that only elastic scattering takes place, it gives rise to a diffracted electron beam with momentum $\vec{k_d}$. If one draws a sphere around the center of diffraction on the sample with radius $r = 1/\lambda$, with λ the wavelength of the electrons, than both vectors end on the surface of this sphere. The diffraction condition is given by Bragg's law:

$$2d\sin(\theta) = n\lambda \tag{3.9}$$

With d the distance between diffracting lattice planes, n an integer number, λ is the wavelength of the X-ray beam and θ the angle between the X-ray beam and the diffracting lattice plane.

Geometrically speaking, for diffraction on a bulk crystal, where the diffracting wave is penetrating into the bulk, this condition is satisfied if the resulting vector $\vec{k}_j - \vec{k}_i = \Delta\vec{K} = \vec{G}$ connects two lattice points in the reciprocal space (momentum space), where $\vec{G}$ is a reciprocal lattice vector.

For diffraction by a bulk crystal, the reciprocal space is composed of a 3D arrangement of lattice points due to constraints imposed by the Bragg's law in three dimensions. For diffraction at a very thin 2D-like layer (crystal, that has macroscopic extension in two dimensions, but is only 1 or a few MLs thick) Bragg's law imposes only constrains in two dimensions. Thus, a reciprocal lattice composed of rods forms instead of a reciprocal lattice composed of dots. The intersection of these rods with the Ewald sphere gives the geometrical diffraction condition (see figure 3.7). The projection of this intersection onto the RHEED screen gives the observed pattern. Each row of reciprocal lattice rods that lies within the Ewald sphere intersects with the Ewald sphere and gives rise to an elliptic line (dotted line in figure 3.7) that is called Laue zone 0, 1, 2, etc.

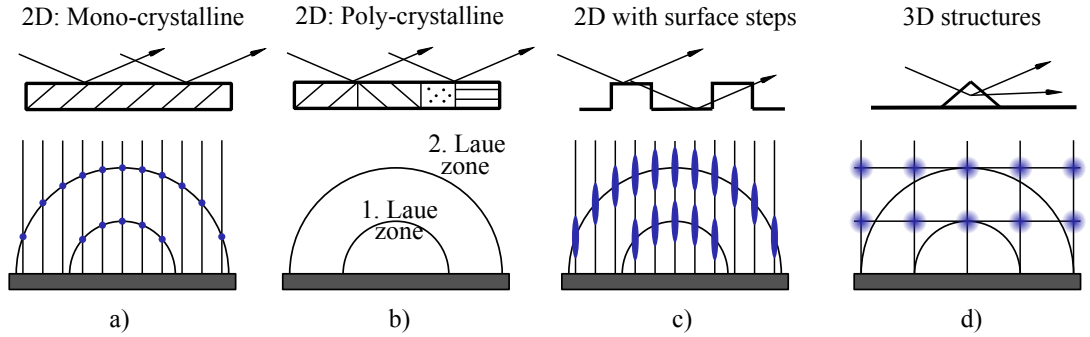

Figure 3.8: Schematics of RHEED diffraction patterns for diffraction at a) mono-crystalline, smooth 2D surface b) poly-crystalline, smooth 2D surface c) mono-crystalline stepped surface d) 3D structures.

Figure 3.8 shows exemplary schematics of four RHEED patterns and their correlating crystal structure or surface morphology. In case of a mono-crystalline, ideally perfect smooth 2D surface, infinitesimal thin reciprocal lattice rods will appear. If the electron beam of the RHEED system was perfectly monochromatic, the surface of the Ewald sphere would be infinitesimal thin, too. Thus the intersection of the reciprocal lattice rods and the Ewald sphere would be a dot. This is illustrated in figure 3.8 a). Though the surface of a high quality substrate is not perfect and the electron beam is not perfectly monochromatic, conditions are well enough to yield a spotty RHEED diffraction pattern

when a 2D surface of for example high quality silicon is investigated. For poly-crystalline perfectly smooth 2D surfaces the crystal is composed of crystallites with all kinds of orientations. Thus, the Bragg's condition is satisfied for a large number of angles, because for every angle there are crystallites with the right orientation that satisfy it. Thus, instead of reciprocal lattice rods there are reciprocal planes. The intersection of these planes with the Ewald sphere gives rise to elliptic line on the RHEED screen (figure 3.8 b). However, it is practically very challenging to produce a perfectly smooth un-stepped crystal surface, because there is always some miscut-angle with regards to the atomic planes. Therefore, every real crystal surface exhibits always some steps. Additional, at temperatures above absolute zero, there is always thermally activated surface roughening to some degree. In this case the electron beam is diffracted by all surfaces and there is interference of the different parts of the electron beam, this broadens the reciprocal lattice rods. Because of this broadening, the intersection of the reciprocal lattice rods and the Ewald sphere is not a dot anymore but an elliptic segment, as in figure 3.8 c. Such areas are often referred to as streaks. Thus, a streaky RHEED diffraction pattern is associated with a 2D surface. Finally, in case of 3D structures, the Bragg's law imposes constraints along three dimensions. Therefore, the reciprocal space is composed of dots instead of reciprocal lattice rods. These 3D structures have a very limited size L, usually in the order of 10^2 nm. This causes a broadening of the diffraction reflex. This phenomenon is described by Scherrer's equation [149], [150]:

$$\Delta(2\theta) = \frac{k\lambda}{L\cos(\theta)} \tag{3.10}$$

With L being the size of the 3D structure orthogonal to the lattice planes that cause the diffraction, λ the wavelength of the electrons of the probing electron beam and k is a form factor that is the Fourier transformed of the charge carrier distribution of the atoms of the material investigated. Diffraction spots of 3D structures are not just broadened compared to diffraction spots of a smooth, 2D surface, they are also more diffuse as is illustrated in figure 3.8 d. The diffraction spots of 3D structures are caused by a transmission of the electron beam through the 3D structures. Therefore, these diffraction spots do not lie on the Laue circle (see figure 3.8).

RHEED is a useful tool to investigate surface reconstructions as the diffraction patterns reflect the symmetry of the crystal or crystal surface in this case, since the RHEED electron beam penetrates only the upper most layers. For example, figure 3.9 shows the RHEED pattern of (In, Ga)N and GaN along the $\langle 1\bar{1}00\rangle$ azimuth. Figure 3.9 a) shows the

3x surface reconstruction of $In_{0.2}Ga_{0.8}N(0001)$ at 608 °C, figure 3.9 b) shows a 1x reconstruction of GaN(0001) at 690 °C. Pink and green arrows indicate integer and fractional order reflections, the blue arrow indicates the specular spot.

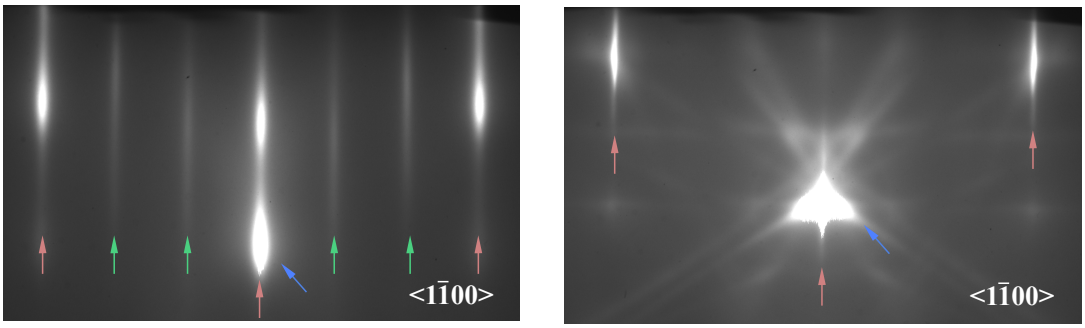

a) (In, Ga)N b) GaN

Figure 3.9: RHEED patterns along the $\langle 1\bar{1}00 \rangle$ azimuth of a) $In_{0.2}Ga_{0.8}N(0001)$ and b) GaN (0001). RHEED patterns showing a 1x reconstruction for GaN at 690 °C and a 3x reconstruction for $In_{0.2}Ga_{0.8}N$ at 608 °C. Pink and green arrows indicate integer and fractional order reflections, the blue arrow indicates the specular spot.

The relaxation behavior of the growing crystal can be analyzed by determining the evolution of the streak- or spot-distance, which is inversely proportional to the lattice parameter of the plane that is probed. This is very useful to determine whether the growth proceeds pseudomorphically or if and when relaxation starts.

Useful information can be derived from the shape of the RHEED diffraction patterns but also from the intensity evolution. Usually the intensity of the specular spot is also tracked, as it is the most intense signal. Increasing or decreasing spot intensity may indicate a smoothening or roughening of the surface [151]. If 3D structures form, an increasing spot intensity can also indicate an increase in total volume of these 3D structures, as the RHEED diffraction intensity is proportional to the diffracting volume. A special case is found for layer-by-layer growth, where the specular spot intensity exhibits a sinusoidal-like evolution with an intensity maximum for a fully closed 2D layer and a minimum for a half closed layer [152], [153], [154]. During layer-by-layer growth the surface periodically roughens, when 2D nuclei form and grow and then smooths again, when 2D nuclei coalesce to form a closed surface. This causes the sinusoidal-like evolution of the RHEED intensity.

3.3 X-ray Diffraction

XRD is a non destructive tool of investigation that can be used, for example, to determine the chemical composition, the crystal symmetry, the strain and to some extent the type and density of defects. The sample is probed with a collimated, coherent, monochromatic beam of X-rays. The X-ray system used in this study is a Panalytical X'Pert PRO MRD with triple-axis and Ge(220) monochromator, the X-rays are emitted through Cu-Kα1 transitions with a wavelength of 0.15406 nm.

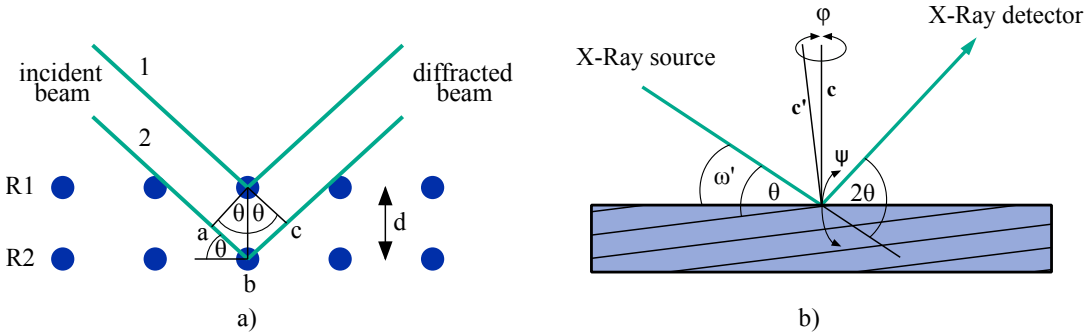

Figure 3.10: a) Geometrical conditions for diffraction b) Schematic of geometry of X-ray set-up with ω' the incident angle of the X-ray beam, θ the angle between the incident ray and lattice planes, 2θ the diffraction angle, c and c' are the normal to the surface and lattice planes, respectively. Additionally the direction of rotation for φ and ψ scans is indicated.

The electron cloud of atoms of the sample material scatters the electro-magnetic (EM) waves that probe the sample. The EM field produces oscillations in the electron cloud of the atoms it interacts with. As a result, an EM field is created through the change in dipole moment between the negatively charged electron cloud and the positively charged atomic core. Each atom emits EM fields in random directions, but due to the symmetry of the crystal, a constructive interference occurs only for specific directions. The condition for constructive interference is given by the Laue condition or equivalent to it the Bragg's law.

As illustrated in figure 3.10, the incident beam is scattered at different rows of atoms R1 and R2 giving rise to a diffracted beam. The path of part 2 of the incident beam is longer by a distance $\overline{ab} + \overline{bc} = 2d\sin(\theta)$ compared to the path of part 1 of the incident beam. For constructive interference to occur, both waves need to have the same phase, i.e. they can differ only in multiple integers of λ.

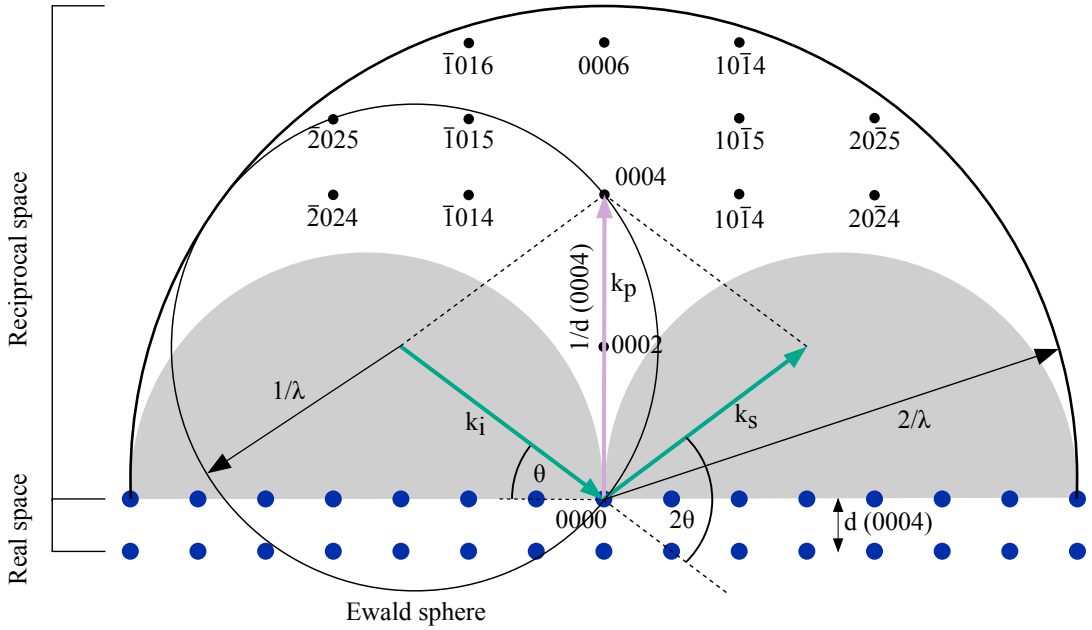

Figure 3.11: Schematic of XRD diffraction geometry for GaN (0001) [155]. The origin of axis for real space and reciprocal space is identical. Grey shaded areas indicate inaccessible areas, because for this measurement geometry the sample would hamper the incident beam $\vec{k_i}$. The Ewald sphere with $r = 1/\lambda$ around the origin. The incident beam $\vec{k_i}$ and the scattered beam $\vec{k_s}$ have length $r = 1/\lambda = 0.154$ nm. The probing vector $\vec{k_p}$ has length $1/d(0004)$. Blue spheres in real space indicate atoms, black dots in reciprocal space indicate reflexes, some spots/reflexes are missing since their intensity is zero [155] (material specific, cf. atomic form factor).

Figure 3.10 b) depicts the geometry of a X-ray setup. The incident beam from the X-ray source exhibits an angle ω' towards the sample surface, which is also called the incident angle, and an angle θ with the lattice planes at which it is diffracted. The difference between ω' and θ is due to a possible miscut angle. Before the actual XRD measurements are conducted, this discrepancy has to be accounted for by aligning the sample, so that the incident angle, that is called ω in the Panalytical software, is identical with θ in figure 3.10 b). With the Panalytical X'Pert PRO MRD the sample can additionally be rotated by an angle φ around the surface normal c in figure 3.10 or the normal c' on the lattice planes (after sample alignment). With the triple axis diffractometer, the sample can be skewed, in figure 3.10 b). This corresponds to a rotation ψ into or out of the image plane.

Figure 3.11 shows a schematic of the XRD diffraction geometry, including two atomic rows in real space and diffraction reflexes in reciprocal space. The incident beam $\vec{k_i}$ hits the sample surface at the origin under an angle θ, which is both the origin of real and reciprocal space, for reasons of simplicity a miscut angle of 0° was assumed. The scattering vector is indicated by $\vec{k_s}$. The Ewald sphere around the origin of the incident beam is determined by the wavelength of the incident beam $r = 1/\lambda$ that gives a constraint on the scattering vector for elastic scattering. Only lattice spots that are on the circle of the Ewald sphere are accessible by a given measurement condition. The probing vector $\vec{k_p} = \vec{k_i} + \vec{k_s}$ gives the place in reciprocal space that is probed. If $\vec{k_p} = \Delta G$, with ΔG being a reciprocal lattice vector connecting two reciprocal lattice spots, then a reflex is probed, which is equivalent to saying that the Laue condition is met or the Bragg's law is obeyed, respectively. Figure 3.11 shows that by probing the reflex (0004), the incident beam is reflected by the (0004) lattice planes, from which the distance d(0004) between these lattice planes can be derived. The area in reciprocal space that is accessible is limited by the sphere with $r = 2/\lambda$. Additionally, the grey shaded half circles are inaccessible because the sample hampers the incident beam under these measurement conditions. Again, for reasons of simplicity only two atomic rows are drawn in figure 3.11 but the X-rays penetrate the samples, depending on the angle of incidence, about 10 μm to 100 μm. The lateral spot size is about 100 μm, therefore X-ray measurements give average qualities of a crystal of a certain volume rather than a spot.

ω-2θ-scan

The sample is positioned so that the incident beam hits approximately the center of the sample with incident angle $\omega = \theta$ (see figure 3.11). For wurtzite structures it is common to use the (0002) reflex for alignment. During an ω-2θ-scan the sample or the X-ray

source is rotated by an angle ω and the detector is rotated by an angle $2\theta = 2\omega$. Therefore, the probing vector k_p keeps a constant direction while it is elongated or shortened along this direction. Given the measurements conditions illustrated in figure 3.11 an ω-2θ-scan would probe a line starting in the origin (0000) and passing through the reflexes (0002), (0004) and (0006). This is called a symmetric ω-2θ-scan and it probes only the out of plane direction or c-direction. This scan can be used for example to determine the chemical composition of the sample using databases. Periodic structures like MQWs or SL structures can be identified and software-based simulations applying kinematic or dynamic scattering theory can be performed to estimate for example the crystal symmetry, the *c*-lattice parameter, the layer thickness, the chemical composition, and the interface roughness of the sample.

Besides symmetrical reflexes like (0002), asymmetrical reflexes like $(10\bar{1}5)$ can be probed by choosing a corresponding angle ω. In figure 3.11 this would correspond to a probing vector k_p that connects the origin (0000) and the reflex $(10\bar{1}5)$. An ω-2θ-scan would elongate and shorten this vector along that direction. In case of an asymmetric scan not only the c-parameter but also the a-parameter of the lattice can be determined. Both symmetric and asymmetric scans can be used to estimate the dislocation density. a+c type dislocation can be determined by asymmetric scans and c-type dislocation by symmetric scans.

Reciprocal space map

This scan type consists of a series of ω-2θ-scans whereas in between each ω-2θ-scan, the ω-angle is changed slightly by $\Delta\omega$. Thus the probing vector k_p is tilted by the same angle $\Delta\omega$ with respect to the intersection between real and reciprocal space. With this procedure, an area of the reciprocal space is probed instead of probing along a line. This scan type can be used to determine the strain state of the epitaxial layers with respect to the substrate, to get information about inter-planar spacing [155], or defect-related broadening of peaks, and it is also useful to get a more complex image of the reflexes and satellite peaks (in case of periodic structures) compared to ω-2θ-scans.

3.4 Atomic Force Microscopy

AFM is a useful tool to investigate the surface morphology at a nano-scale. A thin tip is brought into close proximity to the surface that is to be measured. Tip and sample are moved relative to each other, so a line by line rastering of the surface occurs. A schematic of the AFM used in this study is illustrated in figure 3.12 b. A cantilever with a nm thin tip (for this study: 2 nm - 20 nm) is mounted on a scanner which uses piezo-crystals to move the cantilever. If a voltage is applied to piezo-crystals, they contract or elongate, depending on whether it is a negative or positive voltage. Through applying voltage at certain positions, the crystal can also be bent. This allows the movement in all three spatial directions. A piezo-crystal allows the control of movements in sub-nm regions, a precision which would be impossible with a conventional gearing mechanism. A laser beam focused on the cantilever tip is reflected and detected by a quadrode (a laser detector consisting of 4 photo-diodes). The deflection of the cantilever can be derived and with it, the surface morphology can be reconstructed. The signal from the quadrode is used as input for a feedback mechanism, which regulates the piezo-crystals that move the cantilever and, in case of tapping mode, maintains the tip oscillation.

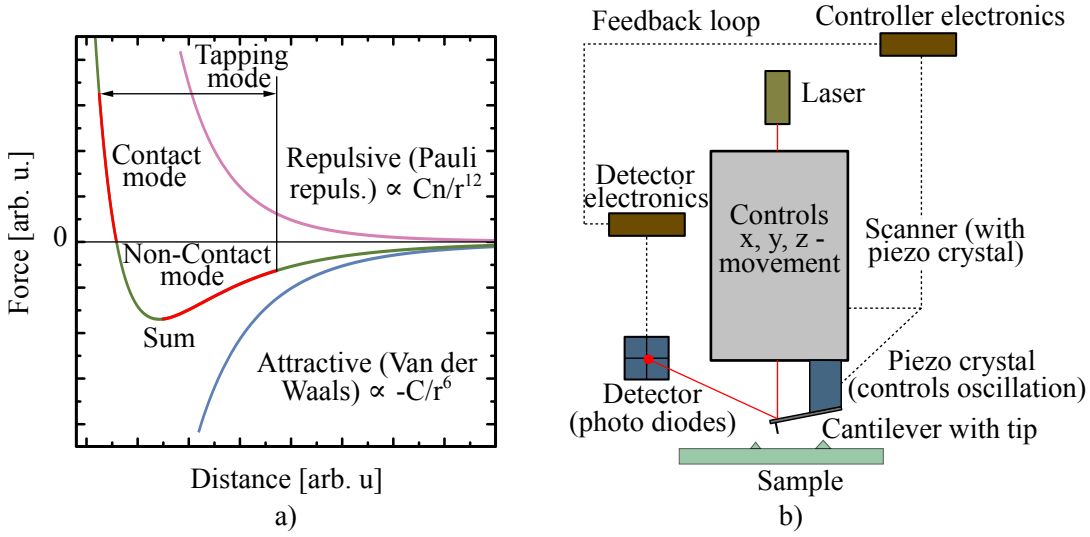

Figure 3.12: a) Plot of the interaction forces between the AFM tip and the sample surface: These forces are the repulsive Coulomb force, and the attractive van der Waals force. The range of forces within which specific AFM modes are operated are marked in red. b) Schematic of an AFM setup. The scanner (piezo-crystal) controls the x, y, z movement of the cantilever. The piezo-crystal maintains the cantilever oscillation (tapping mode). The laser with detector tracks the cantilever deflection and the controlling units form a feedback loop to control and maintain operations.

The AFM can be operated in 3 modes: That are the contact, non-contact and tapping mode. In contact mode, the tip is in contact with the surface, meaning there are short ranged repulsive Coulomb interactions between the tip and the surface atoms (see figure 3.12 a). The surface morphology is probed using one of two sub-modes of operation. There is the constant height mode, in which the cantilever is maintained at a constant height and the deflection of the cantilever tip, which is caused by interactions between the tip and the sample surface, is used as the input signal. This mode is simple (no feedback loop necessary) and suitable for rather smooth, 2D surfaces. However, the tip can be damaged if the variance in the height profile of the sample is to high. A more common application of the contact mode is the constant force mode, in which a feedback mechanism changes the height of the cantilever according to its deflection caused by the interaction with the sample surface. This feedback mechanism maintains a fairly constant force between tip and surface. This mode of operation is more gentle on the sample surface and the tip, also the signal to noise ratio is better. In both of these modes the wear-out of the tip is rather high and for rather soft sample materials, there is a danger of damaging the surface with the tip.

The most frequently used mode of operation is the so-called tapping mode. This mode was developed because in ambient conditions most surfaces develop a liquid surface layer (water condensates on the surface). This causes the tip to stick to the surface, which is detrimental to the signal to noise ratio. In tapping mode a piezo-crystal is used to drive the cantilever to oscillate at a frequency close to its resonance frequency. When the tip comes in proximity to the sample surface, interactions (Coulomb, van der Walls, dipole-dipole, cf. figure 3.12 a) between the tip and the sample surface cause the amplitude of the cantilever oscillation to change (usually to decrease). The tip touches the sample surface only intermittently. A feedback mechanism is used to maintain a specific frequency and amplitude by changing the height of the cantilever. This feedback signal to the piezo-crystal, needed to maintain a constant amplitude, is used as input signal from which the surface morphology is reconstructed. The overall damage to the tip and sample surface is considerable lower than in contact mode. This mode is used in this study.

In non-contact mode, the tip height above the sample is maintained within a range of about 1 nm to 10 nm, so there is no contact between the tip and the sample. In this range of distance to the sample, the van der Walls forces are dominant. Similar to tapping mode, the cantilever is driven to oscillate and a feedback mechanism maintains a constant frequency and amplitude by changing the tip height and thus compensating for the tip-sample-surface interactions. The sample surface is probed by using the driving signal of

the feedback loop as input signal. This mode of operation is most gentle to the tip and sample surface, but it does not allow for an accurate measurement, as the tip might be influenced more strongly by the liquid film than the actual surface.

All modes of operation do not give the actual height profile of the surface itself, but rather a convolution of the height profile and the tip profile, since in many cases the diameter of the tip is of the same order of magnitude than the structures that are to be measured. Thus the shape of the tip influences the results. A broken tip, for example, can cause the appearance of twin structures, where the sample exhibits one structure, or the size and shape of the sample structure is distorted. Furthermore, the settings of the feedback loop as well as external vibrations can cause periodic structures in the AFM height profile that do not correlate to any structure on the sample. A well-trained AFM operator is needed to recognize these measurement artifacts and change the measurement conditions accordingly.

3.5 Raman Spectroscopy

Raman spectroscopy is another non-destructive, non contact tool of investigation that does not require a special sample preparation. When light is scattered by molecules or atoms, the most probable case of scattering is elastic scattering (Rayleigh scattering), by which no energy is transferred from, or to the scattering molecules or atoms. This scattering takes place because the electron cloud oscillates upon the incidence of light. As a result of these oscillations, the molecules or atoms emit light, which has in most cases the same frequency (Rayleigh scattering) as the incident light. In about one in a million cases, light is scattered inelastically. This is called Raman scattering (see figure 3.13). In Raman spectroscopy the inelastically scattered part of the light is used to gather information about the molecule, atom or crystal [156]. Through inelastic scattering, energy can either be transferred from the incident light to the scattering target or from the scattering target to the light. The first case is called Stokes scattering and it leaves the scattering target in an excited state and the scattered light suffers a decrease in its frequency, so $\nu_s = \nu_i - \nu_{RS}$, where ν_s is the frequency of the scattered light, ν_i is the frequency of the incidence light (frequency of the probing laser light) and ν_{RS} is a so-called Raman shift in frequency corresponding to the transferred energy. The second case is called anti-Stokes scattering, which requires the scattering target to be in an excited state before the scattering takes place and leaves the scattering target in an energetically lower state but the frequency of the scattered light increases, $\nu_s = \nu_i + \nu_{RS}$. These energy states are either vibrational, rotational or electronic energy states, but most commonly the vibrational modes are probed

by Raman spectroscopy, therefore the bonds of molecules are investigated. The energy to excite vibrational states is specific to each molecule or crystal, and even specific to the surrounding of a molecule.

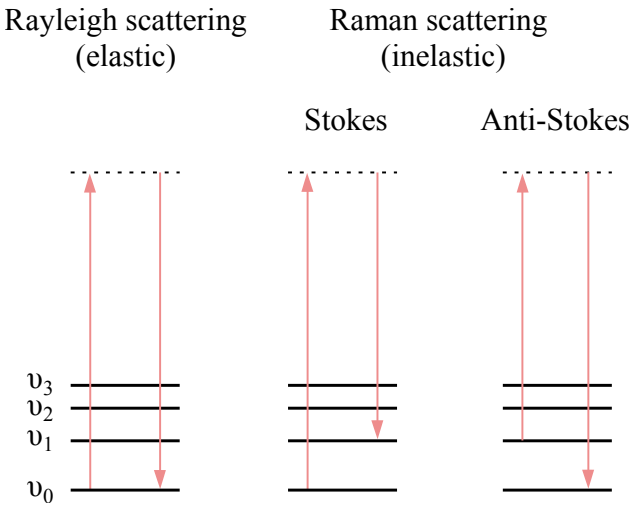

Figure 3.13: Schematic of elastic scattering (Rayleigh scattering) and inelastic scattering (Raman scattering), with distinction between Stokes and anti-Stokes scattering. Energy transitions are exemplified for transitions between vibrational modes.

Usually monochromatic laser light is used to illuminate the sample. Most of the light is scattered elastically and filtered out, for example with a holographic rejection filter, the inelastically scattered part is then analyzed. The laser spot can be focused to a lateral spot size of about 1 μm. The penetration depth depends on the used laser light frequency and the probed material. If the probed material is transparent for the used laser light, then the sample is penetrated all the way through. The penetration depth varies with the material only for materials that are not transparent for the used laser light. In this case, it is usually in the order of nano meters to a few micro meters. Raman spectroscopy probes the short range order: The bonds of molecules, as opposed to XRD, which probes the long range order. Therefore Raman spectroscopy can be used to investigate amorphous and crystalline materials. Molecules do not vibrate in arbitrary modes but only certain modes are possible, the so-called normal modes derived by Schrödinger equations. Not all of these modes are involved in the inelastic scattering of light, only the ones that involve a change of the polarizability of the molecule, which are called Raman active. The polarizability is a measure for the ease with which the electron cloud of a molecule or atom can be distorted.

The intensity of Raman scattering can be greatly increased if the incident photon energy is close to the energy of an electronic transition in the probed material. The chemical composition of a material can be determined by analyzing the scattering intensity as a function of wavenumbers and by comparing to values established in the literature. Additionally, the scattering intensities, correlated with certain phonon modes, can be compared and used to derive information about the relative scattering volume of one scattering phase with respect to others.

3.6 Photoluminescence Spectroscopy

Photoluminescence (PL) spectroscopy does not require special sample preparation and is a non destructive and non contact tool of investigation. It can be used to probe the electronic structure of a sample. Monochromatic laser light is used to excite the electrons of the sample and, in case of semiconductors, it creates electron-hole pairs. The energy of the photons of the laser light needs to exceed the band gap energy of the sample to be investigated in order to create electron-hole pairs. Electron excited from the valence band into the conduction band can participate in several processes. Some of them are radiative, meaning they involve the emission of photons and some are non-radiative, where no photon is emitted. In most cases electrons will first participate in non-radiative electron-phonon scattering. Through this process they will relax to the conduction band minimum or quantum states in case of quantum structures like quantum wells, quantum dots, etc, by transferring some of their excess energy to the crystal lattice (exciting phonons). Instead of electron-phonon scattering, there can be other interactions like Auger recombination. In Auger recombination the electron receives energy from another electron and is excited further up in the conduction band. After the electron is relaxed to the band gap minimum, it will recombine radiatively with a hole in the valence band by emitting a photon. This is the process that is used for the PL spectroscopy to derive information about the electronic band structure. An electron can non radiatively recombine with defect states in the band gap, so-called Shockley-Read-Hall-recombination, the excess energy is transferred to the lattice by creating phonons. The creation of the electron-hole pair and the recombination is not occurring simultaneously. This means that the charge carriers have a life-time τ, during which they diffuse or drift (if there is an electric field) in the sample. Therefore the probed volume is not only limited by the laser spot size but also the angle under which the re-emitted light is detected. The penetration depth of the laser light is described by the Lambert-Beer law. Carrier lifetimes can be probed by using time resolved PL in which a short laser pulse excites the sample and a fast camera mea-

sures PL spectra during consecutive, short-time intervals. Such measurements give a PL intensity decay curve which can be fitted applying theoretical models and information about the carrier life time and recombination mechanisms can be derived from that.

4 Results: Annealing study of ZnO substrates

This chapter presents the surface treatment procedure that was used in this study to obtain smooth, stepped ZnO surfaces. A resistance heat oven was used to anneal the ZnO substrates. The oven facilitates the use of special atmospheres like O_2. The dependence of the surface morphology on annealing parameters like annealing temperature, time, pressure and flux of the special atmosphere was investigated.

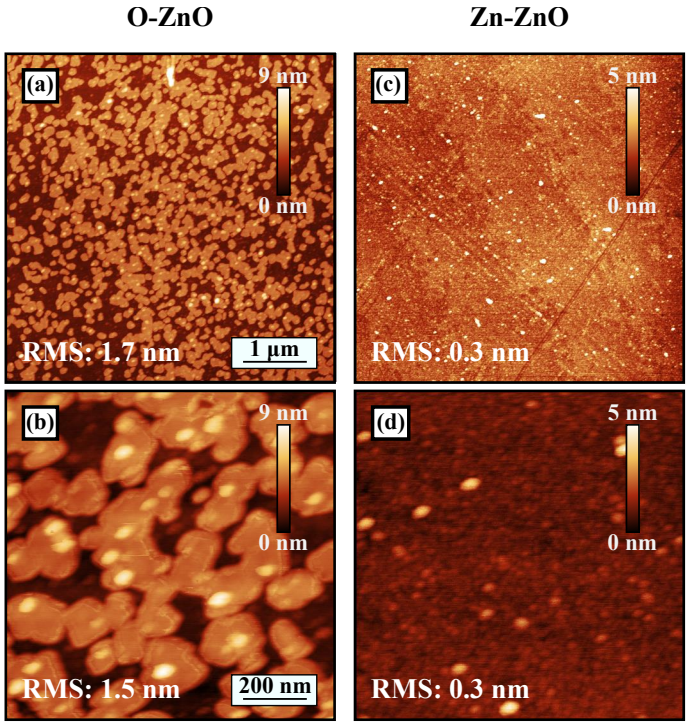

Figure 4.1: Surface morphology of ZnO substrates as delivered investigated by AFM. (a), (c): $5 \times 5\ \mu m^2$, (b), (d): $1 \times 1\ \mu m^2$. (a), (b): O-ZnO, (c), (d): Zn-ZnO.

Figure 4.1 shows exemplary the surface morphology of ZnO double side polished substrates as provided by CrysTec. The surface of O-ZnO faces are rough with RMS: 1.7 nm and covered with extended 3D structures. The surface of the Zn-ZnO faces are smoother with RMS: 0.3 nm. Neither of the polar surfaces exhibits atomic steps, which are favorable for the growth of high quality heterostructures.

4.1 Influence of annealing temperature

The starting point with regards to annealing parameters was a report by Graubner *et al.* [157], who investigated the preparation of ZnO substrates. They reported good quality ZnO for annealing temperatures around 1100 °C. Figure 4.2 shows the results of an annealing study with ZnO substrates, annealed at temperatures between 1000 °C and 1100 °C for 1h with O_2 atmosphere with 1 bar pressure and a flux rate of 150 sccm. The pressure varied slightly over time.

At a temperature of 1000 °C the O-ZnO surface [figure 4.2 (a), (b)] displays holes. Only faint, irregular fragments of steps can be distinguished with 3D structures on top of them. The Zn-ZnO surface [figure 4.2 (c), (d)] exhibits an even higher density of holes. The formation of steps with uneven terraces can be observed and they are covered with platelets. At 1050 °C the holes disappear [figure 4.2 (e)-(h)]. The O-ZnO surface is smooth and stepped [figure 4.2 (e),(f)], whereas the Zn-ZnO surface still shows only fragmented steps with 3D structures or platelets on top [figure 4.2 (g),(h)]. These 3D structures increase in density when the temperature is raised to 1100 °C on Zn-ZnO [figure 4.2 (k), (l)]. On O-ZnO [figure 4.2 (i), (j)] a low density of big 3D structures formed and the terraces look partially dissolved. Surfaces with the lowest RMS roughness were obtained for annealing at 1050 °C, therefore further experiments were conducted at this annealing temperature.

4.2 Influence of annealing time

Next, the influence of the annealing time was investigated. The samples were annealed at 1050 °C in O_2 atmosphere with 1 bar pressure and 150 sccm. The annealing time was varied between 30 minutes and 3 hours.

For O-ZnO, annealing for 30 minutes yielded stepped surfaces [figure 4.3 (a), (b)], but also shallow, large indentations. The Zn-ZnO surfaces [figure 4.3 (c), (d)] were covered with a high density of small 3D structures and step-bunching occurred. Annealing for one

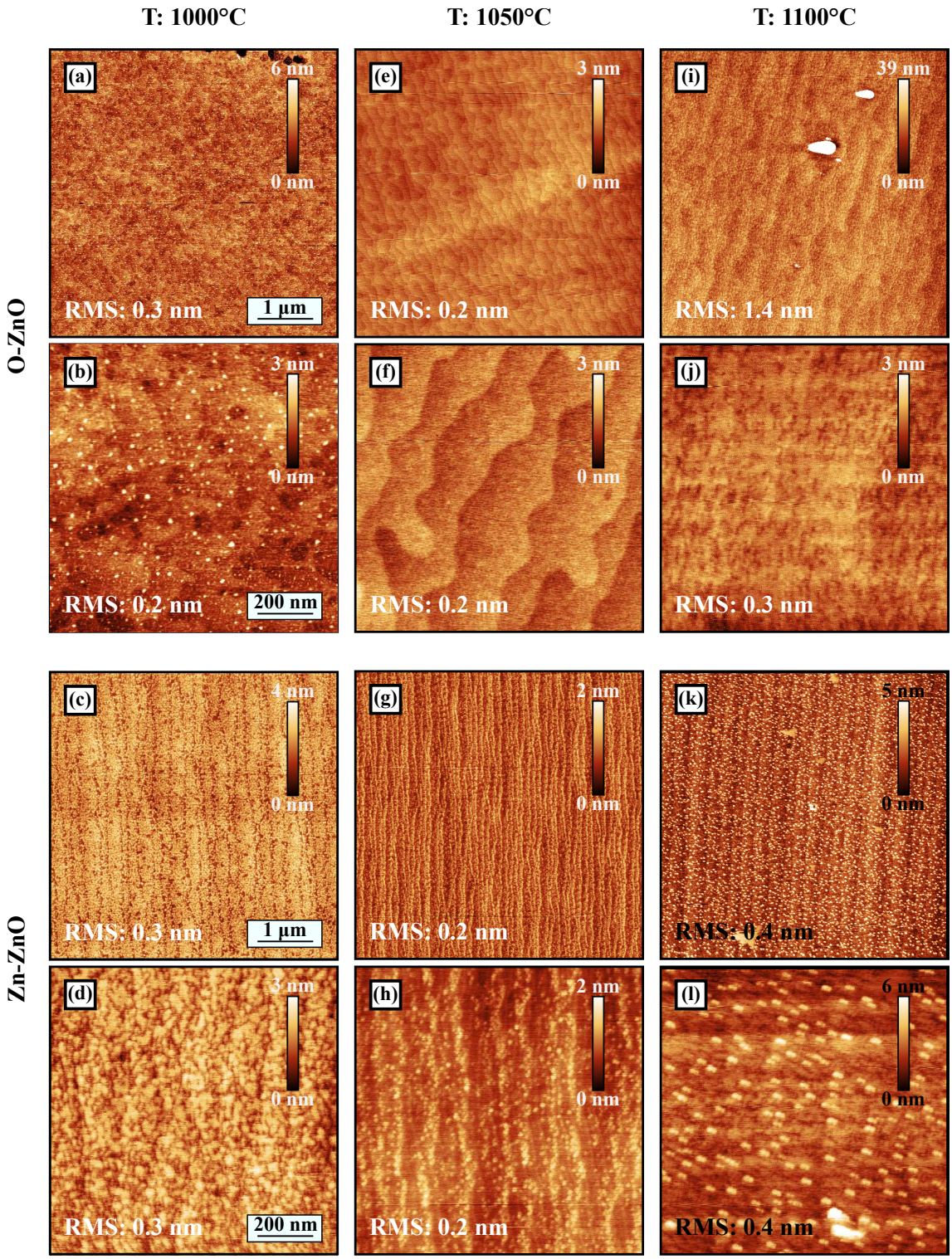

Figure 4.2: Influence of annealing temperature on the surface morphology of ZnO substrates investigated by AFM. [(a), (b), (e), (f), (i), (j)]: O-ZnO surfaces, [(c), (d), (g), (h), (k), (l)]: Zn-ZnO surfaces. The size of the AFM images is $5 \times 5\ \mu m^2$ [(a), (c), (e), (g), (i), (k)] and $1 \times 1\ \mu m^2$ [(b), (d), (f), (h), (j), (l)]. The annealing temperature was varied between 1000 °C and 1100 °C. The RMS roughness is indicated, as well as the height scale. The samples were annealed under O_2 atmosphere of 1 bar with a flux of 150 sccm for 1 hour.

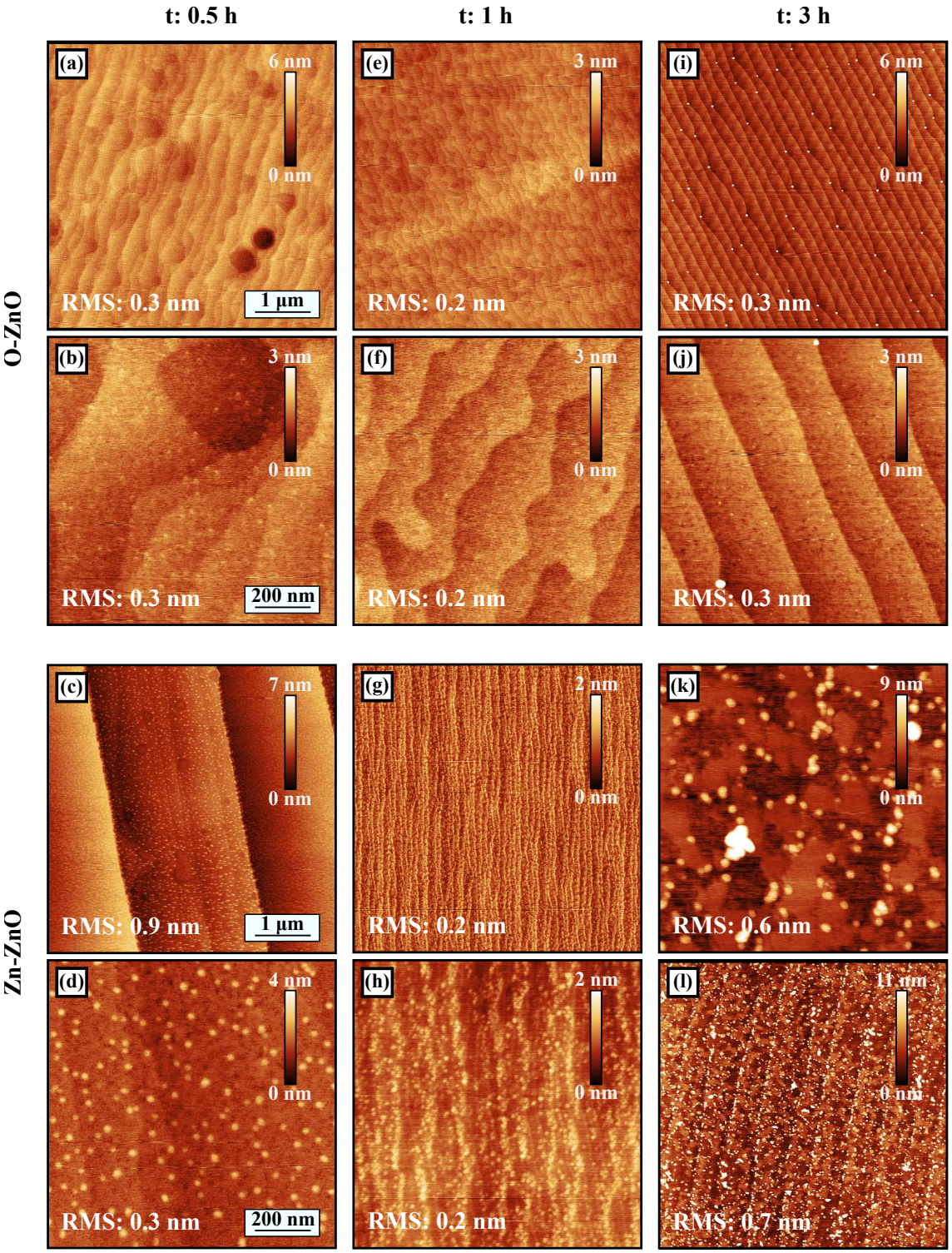

Figure 4.3: Influence of annealing time on the surface morphology of ZnO substrates investigated by AFM. [(a), (b), (e), (f), (i), (j)]: O-ZnO surfaces, [(c), (d), (g), (h), (k), (l)]: Zn-ZnO surfaces. The size of the AFM images is 5×5 μm^2 [(a), (c), (e), (g), (i), (k)] and 1×1 μm^2 [(b), (d), (f), (h), (j), (l)]. The annealing time was varied between 30 minutes and 3 h. The RMS roughness is indicated, as well as the height scale. The Samples were annealed under oxygen atmosphere of 1 bar with a flux of 150 sccm at 1050 °C.

hour led to smooth, stepped O-ZnO surfaces [figure 4.3 (e), (f)] without indentations. For Zn-ZnO, fragmented, stepped surfaces with 3D structures on top [figure 4.3 (g), (h)] were obtained instead. Annealing of the O-ZnO surfaces for three hours led to the formation of 3D structures at the step edges [figure 4.3 (i), (j)], this time with lower density. Figure 4.3 (j) shows that there are small holes in the terraces. This could mean that annealing for 3 hours leads to the dissolution of the terraces. This is even more pronounced for the Zn-ZnO surfaces [figure 4.3 (k), (l)]. Both figures show partially dissolved terraces. This might indicate that the prolonged exposure to 1050 °C damaged the surface. The density of the small 3D structures decreased and additional larger 3D structures formed. No step-bunching was observed under these conditions.

4.3 Influence of the oxygen flux

After establishing good annealing conditions for O-ZnO surfaces, the O_2 flux was varied to find annealing conditions that produce smooth, stepped Zn-ZnO surfaces. The O_2 flux was varied between 150 sccm and 400 sccm and the substrates were annealed at 1050 °C and 1 bar.

Using a O_2 flux of 150 sccm or 400 sccm yielded smooth, stepped O-ZnO surfaces [figure 4.4 (a), (b) and (i), (j)]. A flux of 300 sccm resulted in a surface composed of irregular formed steps with 3D structures on top [figure 4.4 (e), (f)]. This is probably due to the problem of only partial reproducibility, which will be discussed in the following chapter.

When increasing the O_2 flux from 150 sccm to 300 sccm, the steps on Zn-ZnO surfaces became more pronounced and the 3D structures became more distinct [figure 4.4 (c), (d) and (g), (h)]. A O_2 flux of 400 sccm finally yielded smooth, stepped Zn-ZnO surfaces [figure 4.4 (k), (l)].

4.4 Optimization procedures

Figure 4.5 shows nine different substrates. All three substrates shown in figure 4.5 were annealed under the same conditions: 1050 °C, 1 hour, 150 sccm, 1 bar. All six substrates shown in 2. and 3. row were annealed with parameters: 1050 °C, 1 hour, 400 sccm, 1 bar. Figure 4.5 shows that there is no 100% reproducibility. Nominal same annealing conditions can yield a smooth, stepped surface as shown in figure 4.5 (g), (h) or can

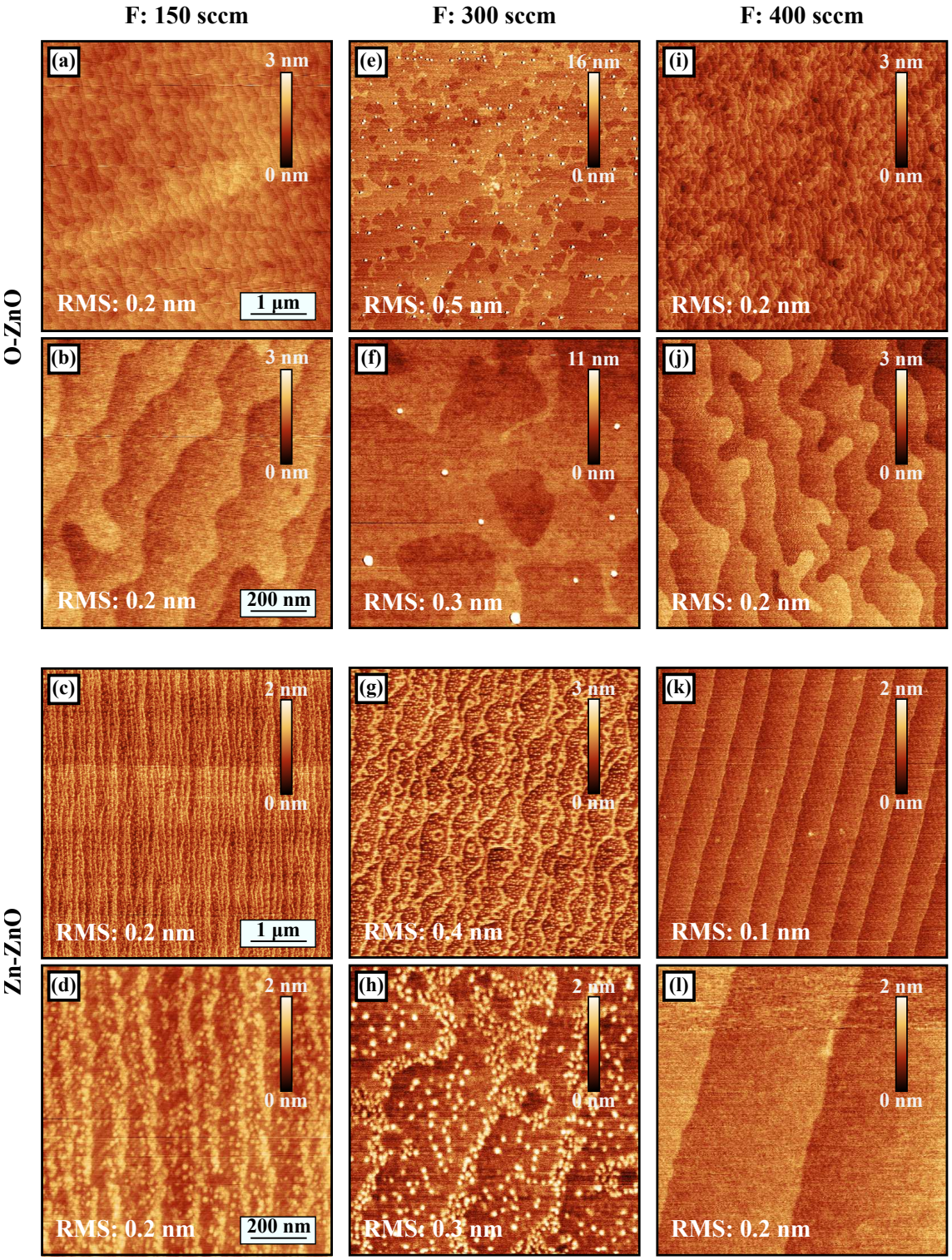

Figure 4.4: Influence of the atmosphere flux on the surface morphology of ZnO substrates investigated by AFM. [(a), (b), (e), (f), (i), (j)]: O-ZnO surfaces, [(c), (d), (g), (h), (k), (l)]: Zn-ZnO surfaces. The size of the AFM images is 5×5 μm^2 [(a), (c), (e), (g), (i), (k)] and 1×1 μm^2 [(b), (d), (f), (h), (j), (l)]. The atmosphere flux was varied between 150 sccm and 400 sccm. The RMS roughness is indicated as well as the height scale. The samples were annealed under oxygen atmosphere of 1 bar for 1 hour at 1050 °C.

yield a stepped surface with 3 D structures as shown in figure 4.5 (i). The reasons for that might be that the annealing conditions are not perfectly reproduceable or that the starting surface or miscut of the samples is not identical.

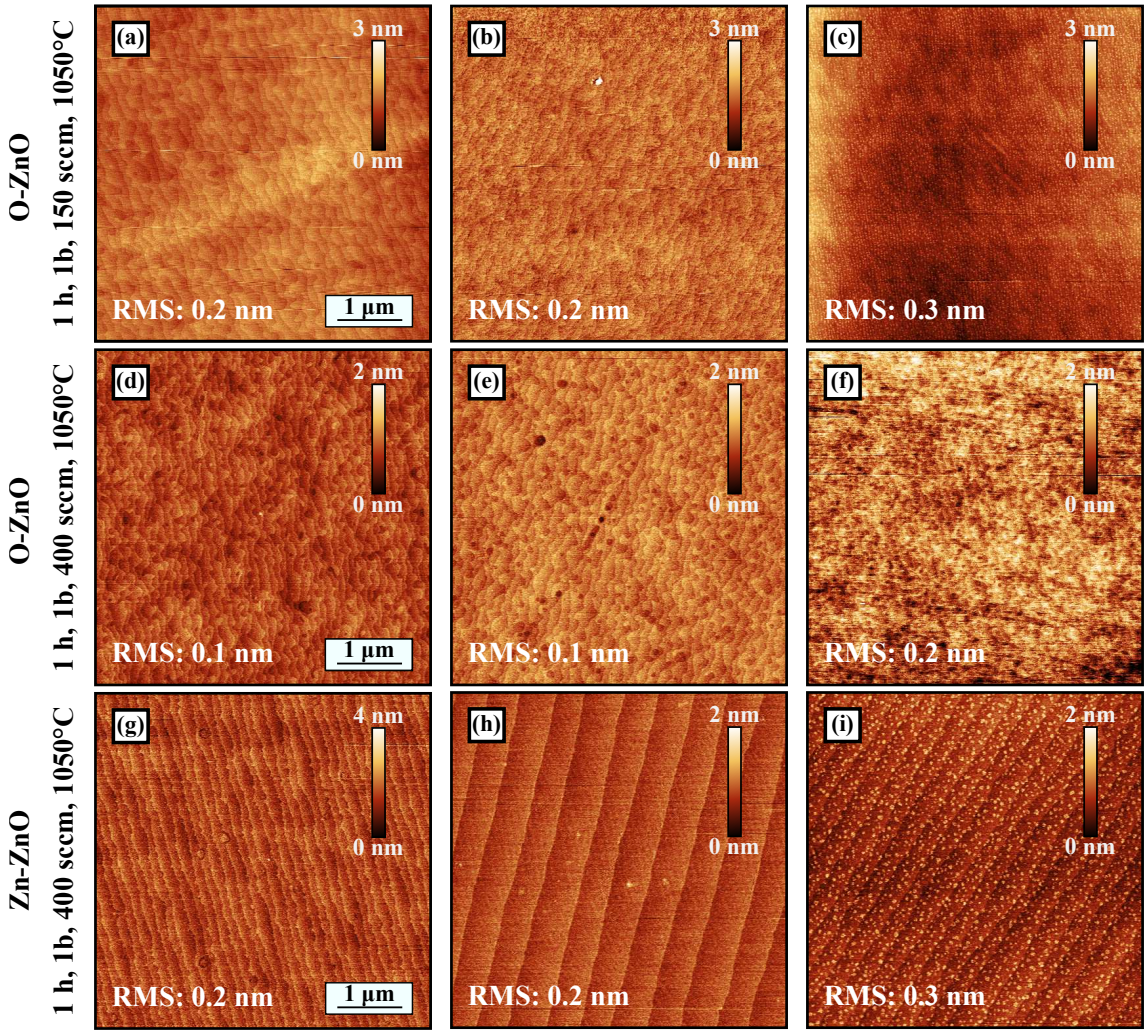

Figure 4.5: Reproducibility of ZnO surface annealed under the same annealing conditions. The size of the AFM images is $5 \times 5\ \mu m^2$. The RMS roughness is indicated as well as the height scale. (a)-(f): O-ZnO surfaces, (g)-(h): Zn-ZnO surfaces. (a)-(c): 3 samples were annealed under the same conditions: Oxygen atmosphere with 1 bar, 150 sccm flux for 1 hour at 1050 °C. (d)-(i): Samples were annealed with oxygen atmosphere with 1 bar, 400 sccm flux for 1 hour at 1050 °C.

As nominal same annealing conditions can yield different results, samples were re-annealed until their surface morphology was satisfactory. Figure 4.6 (a)-(f) shows the surface morphologies of one substrate after the first annealing and two successive re-annealing procedures. Figure 4.6 (a)-(c) shows the O-ZnO, figure 4.6 (d)-(f) the Zn-ZnO surfaces. Re-annealing the O-ZnO surface resulted first in an increase of the density of large hexagonal

pits [figure 4.6 (b)] and afterwards a decrease in their density [figure 4.6 (b)] but instead a high density of small pits appeared. The high density of 3D structures, that appeared after the first annealing, decreased considerably after the second annealing [figure 4.6 (b)] and the 3D structures vanished completely after the third annealing [figure 4.6 (c)]. The change in RMS roughness reflects this evolution of the surface morphology using re-annealing procedures with nominal identical annealing conditions.

The Zn-ZnO surface showed step-bunching with 3D structures [figure 4.6 (d)] after the first annealing. The second annealing procedure produced platelets instead of 3D structures [figure 4.6 (e)]. After the third annealing, both items vanished and a smooth, step bunched surface was obtained [figure 4.6 (f)]. This results show, that formerly inadequate surface morphologies can be improved through re-annealing. Even using the same re-annealing conditions.

Figure 4.6 (g)-(i) (O-ZnO) and (j)-(l) (Zn-ZnO) show the results from a second substrate that was annealed two times [figure 4.6 (g), (j)], producing a stepped surface with 3D structures on top for the O-face and an unstepped surface for Zn-ZnO-face. As the second annealing did not rid the O-ZnO surface of the 3D structures, the substrate was rinsed for 30 minutes in an ultrasonic bath with de-ionized water. Both the O-ZnO and Zn-ZnO surfaces looked partially dissolved or roughened after the rinsing. The O-ZnO surface exhibited pits but most of the 3D structures vanished. After the third annealing, the O-ZnO exhibited a smooth, stepped surface, the holes were filled and all the remaining 3D structures could be dissolved. The Zn-ZnO surface showed a very different morphology with step-bunching and platelets on the terraces.

These results show that rinsing ZnO substrates in an ultrasonic bath with de-ionized water may be a more aggressive treatment than annealing at temperatures around 1050 °C for one hour. This treatment can be used to rid the surface of 3D structures that do not vanish through re-annealing. After rinsing, the surface looks partially dissolved or etched. Therefore, it might be possible that surface layers are created that do not consist of ZnO. If such surface layers would be created and could not be removed by re-annealing afterwards, this could be a problem for growth purposes. Therefore, further investigations are necessary to investigate the effects of rinsing ZnO in ultrasonic baths on the chemical composition of the surface.

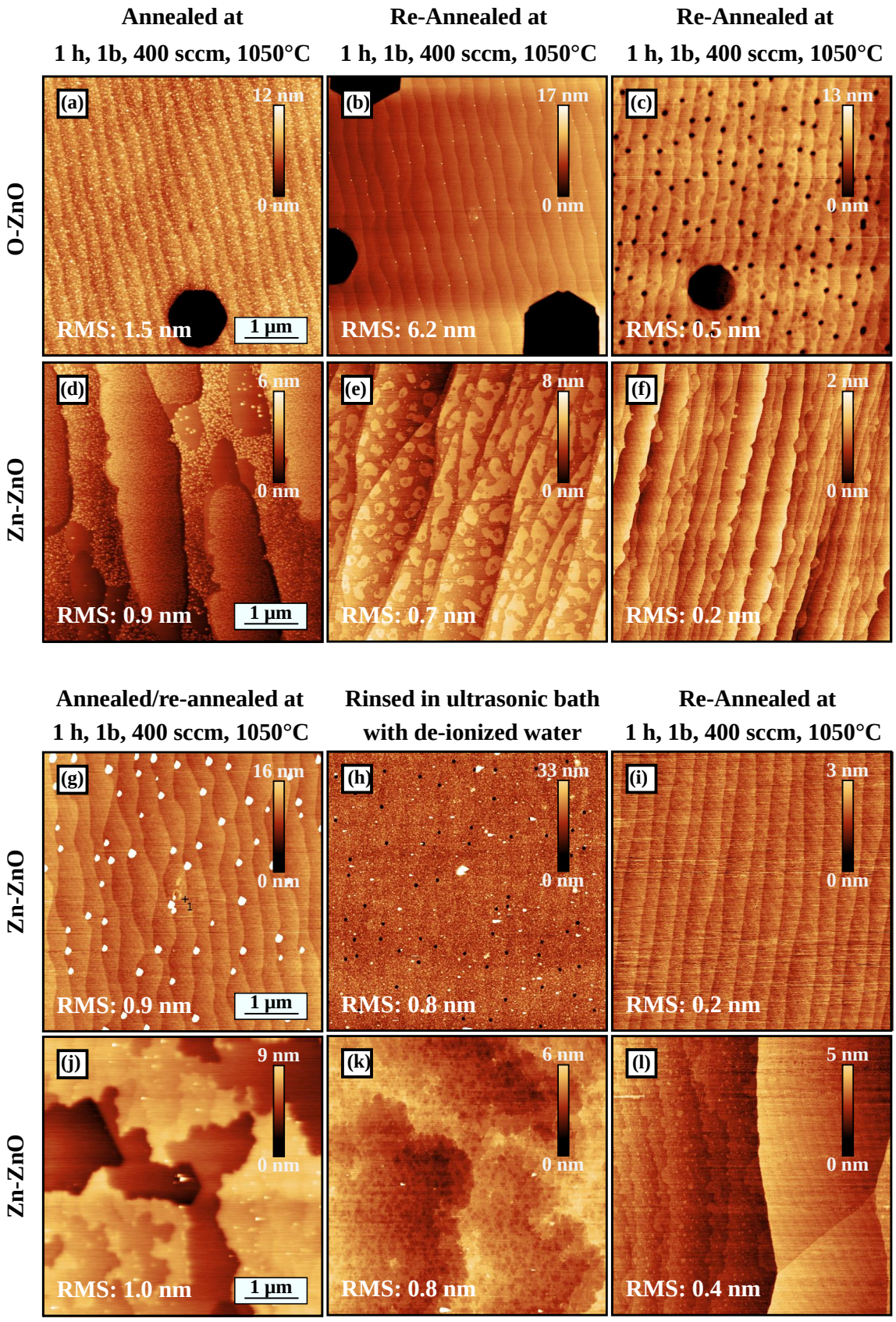

Figure 4.6: Re-annealing of ZnO surfaces. The size of the AFM images is $5 \times 5\ \mu m^2$. The RMS roughness is indicated as well as the height scale. (a)-(f) show O-ZnO and Zn-ZnO polar surfaces of a sample that was annealed and re-annealed 2 times at 1050 °C, 1h, 400 sccm, 1 bar. (g)-(l) show a sample that was rinsed in a ultrasonic bath with de-ionized water after annealing and re-annealed again at 1050 °C, 1h, 400 sccm, 1 bar.

4.5 Summary

Annealing conditions were established to produce smooth, stepped ZnO surfaces of both polarities. Such surfaces can be achieved by annealing ZnO substrates at 1050 °C for 1 hour at 1 bar with 400 sccm O_2 flux (Zn-ZnO) or 150 sccm and 400 sccm (O-ZnO).

Nominally similar annealing conditions do not yield always the same result. Substrates can be re-annealed until the surface morphology is suitable. Rinsing ZnO substrates in ultrasonic baths with de-ionized water can be used to rid the surface of 3D structures. However, additional annealing is necessary to obtain smooth, stepped surfaces.

5 Results: Growth of (In, Ga)N heterostructures on ZnO

Several reports suggest that there might be an upper limit for the indium content $x \leq 33\%$ for the fabrication of defect-free, ML-thin (In, Ga)N films [158], [36], [159], [160]. Additionally a self-limiting indium incorporation mechanism was reported for ML-thin (In, Ga)N layers [161]. It has been proposed that the maximum indium content in ML-thin (In, Ga)N layers might be limited by strain during hetero expitaxy [160]. The aim of this study is to increase the indium content in ML-thin (In, Ga)N layers by means of strain engineering. For that purpose, the growth on ZnO is explored. ZnO has an *a*-lattice parameter of 3.25 Å and it is lattice-matched to (In, Ga)N with $x = 0.18$.

In the first part of this chapter, the growth mode of thin InN films and GaN/InN heterostructures was studied to establish the limits for pseudomorphic growth and the transition between 2D and 3D growth mode. In the following, we utilize smooth thin InN layers as an intermediate protective layer for the growth of (In, Ga)N/GaN heterostructures in order to prevent chemical reactions between Ga and ZnO [129]. The dependence of the growth mode on the growth rate (GR) and the ZnO polarity is established. In the second part of this chapter, the growth of (In, Ga)N heterostructure SPSLs on ZnO is presented. The growth mode was analyzed *in-situ* by RHEED and the composition and strain were examined by XRD and Raman spectroscopy. The growth mode was confirmed by probing the surface morphology with AFM microscopy *ex-situ* and finally the optical emission was investigated by low temperature PL measurements.

5.1 Growth of thin InN films on ZnO

Prior to the growth of InN thin layers, ZnO substrates were prepared as described in chapter 4.

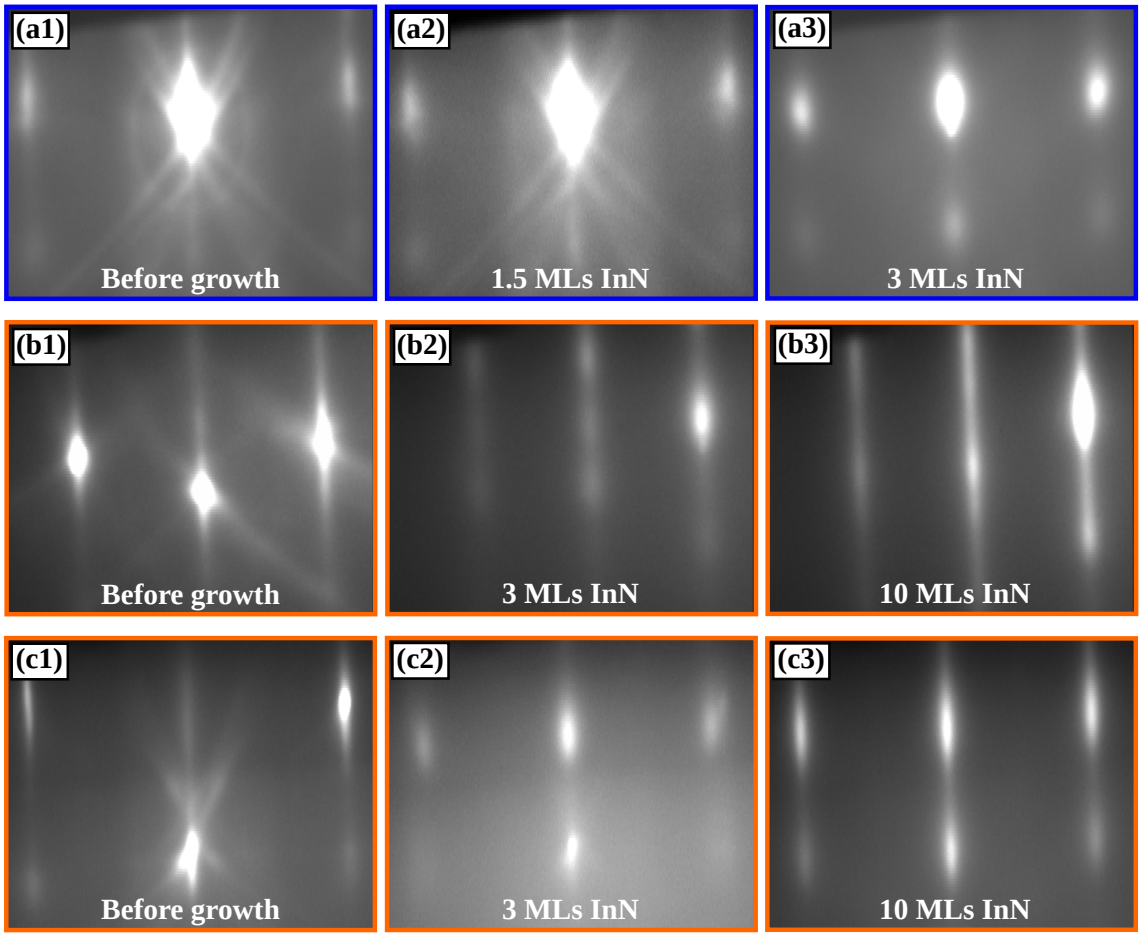

Figure 5.1: RHEED diffraction patterns of [(a1), (b1), (c1)] the bare ZnO substrate prior to the growth and [(a2), (a3), (b2), (b3), (c2), (c3)] ML-thin InN layers on (a) O-ZnO in $\langle 10\bar{1}0 \rangle$ and (b) $\langle 11\bar{2}0 \rangle$ azimuth, (c) Zn-ZnO in $\langle 10\bar{1}0 \rangle$ azimuth. The GR for InN was 0.2 ML/s for (a) and (c) and 0.5 ML/s for (b). Intensity and contrast was increased in image (c2).

For all samples the growth temperature was set to 450 °C, as measured by a thermocouple. Nitrogen-rich growth conditions during InN deposition ($N/In = 1.1$) were chosen to prevent the excess of metal which may etch the ZnO substrate surface [162]. In order to check for indication of unintended metal-rich growth, the surface of all InN/ZnO samples were investigated with OM and AFM and no indication of indium droplets was found after growth. In-fluxes of 0.2 ML/s, 0.5 ML/s, and 1.0 ML/s were used. The layers were deposited on both ZnO faces in separate experiments. Samples with 1 ML, 2 MLs, 3 MLs and 10 MLs of InN were grown on the smooth surfaces of the annealed ZnO substrates.

RHEED diffraction patterns were recorded in the $\langle 11\bar{2}0\rangle$ and the $\langle 10\bar{1}0\rangle$ azimuth during the growth of all samples. The streaky pattern at the start of the deposition evolved into a spotty one [figure 5.1 (a2), (b2), (c2)]. Figure 5.1 exemplary illustrates these patterns before the growth started (bare ZnO surface), after 1.5 MLs or 3 MLs, and at the end of the growth (3 MLs or 10 MLs, respectively).

Before all growth experiments, the investigation of the bare ZnO substrates by RHEED revealed a streaky pattern on both the Zn-ZnO and the O-ZnO polarities [figure 5.1 (a1), (b1), (c1)], which corresponds well to the smooth surface that we have prepared following our annealing procedures. Importantly, *in-situ* measurements by quadrupole mass spectrometry in the line of sight (not shown) revealed that metal desorption was negligible at the low growth temperature employed. In addition, no metal droplets were found on the surface after growth and the surface revealed by AFM was clear. Thus, we infer that all supplied In and Ga amounts were incorporated into the layers.

Next, we studied the evolution of the *a*-lattice spacing by measuring the streak spacing during the deposition of InN, as the in-plane lattice spacing, or *a*-lattice parameter, is inversely proportional to the streak or spot spacing. For the $\langle 11\bar{2}0\rangle$ azimuth:

$$a \propto \frac{k}{d_{11\bar{2}0}} \tag{5.1}$$

With $d_{11\bar{2}0}$ the spacing of the streaks or spots in $\langle 11\bar{2}0\rangle$ azimuth and k a constant. The constant k can be determined by comparison with the (a, $d_{11\bar{2}0}$) values of the ZnO substrate. To this end, we have measured the distance between the substrate streaks, whose positions were fitted by Gaussians.

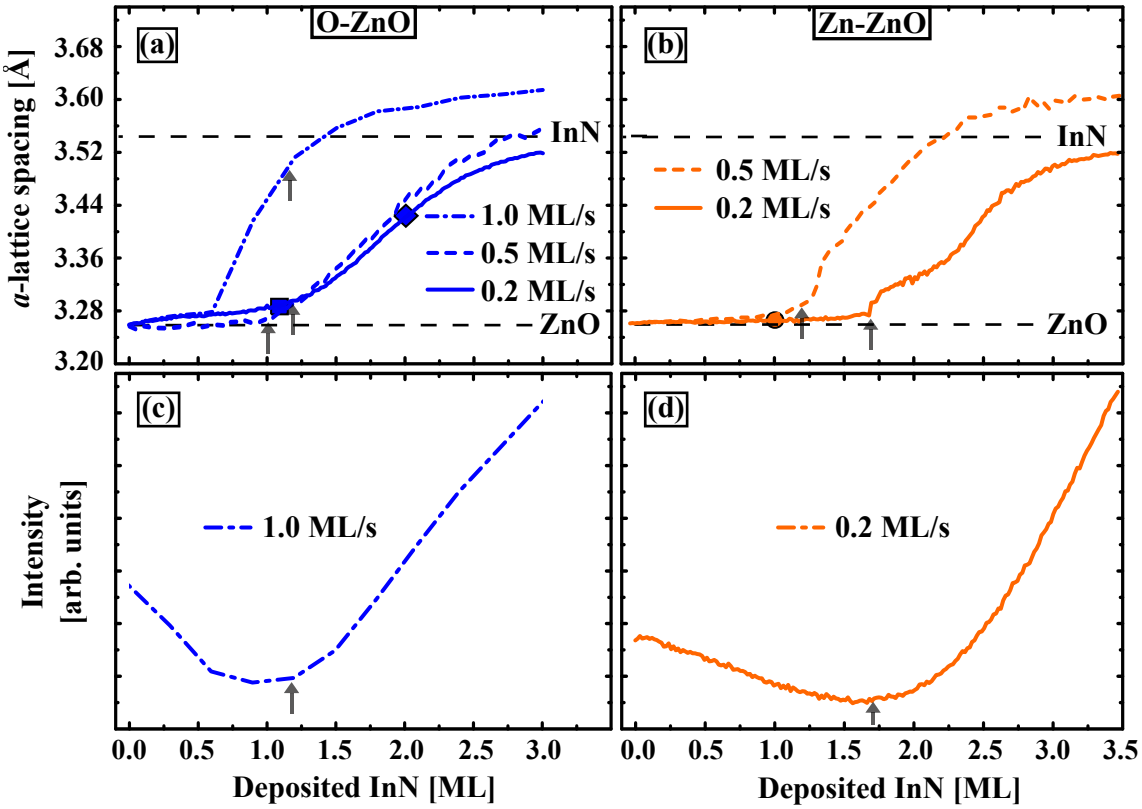

Figure 5.2: (a) and (b) show the evolution of *a*-lattice spacing derived from RHEED diffraction patterns during the deposition of InN at different GR on O-ZnO and Zn-ZnO, respectively. (c), (d) Intensity evolution of the RHEED specular reflection of InN/O-ZnO with GR 1.0 ML/s and InN/Zn-ZnO with GR 0.2 ML/s. The grey arrows highlight the transition from streaky to spotty RHEED patterns corresponding to h_{2D-3D}, while the dashed black lines indicate the unstrained lattice constants of InN and ZnO. Symbols in (a) and (b) recall figure 5.3 (c), (d) and figure 5.4 (a). Thermal expansion was taken into account when determining the lattice spacing.

GR [ML/s]	h_{crit}(O-ZnO)	h_{crit}(Zn-ZnO)	h_{2D-3D}(O-ZnO)	h_{2D-3D}(Zn-ZnO)
1.0 ML	0.6 ML		1.2	
0.5 ML	1.0 ML	1.2 MLs	1.0 ML	1.2 MLs
0.2 ML	1.2 MLs	1.7 MLs	1.2 MLs	1.7 MLs

Table 5.1: Critical layer thickness for relaxation (h_{crit}) and for the transition from 2D to 3D growth mode (h_{2D-3D}) of InN thin films on ZnO.

This procedure was used to obtain the evolution of the *a*-lattice parameter as a function of the InN layer thickness. All RHEED measurements were conducted at a substrate temperature of 450 °C. Therefore, thermal expansion of the material was taken into account when determining the lattice spacings. This was done for all samples in this study. The results are shown in figure 5.2 (a) and (b) for the growth on O-ZnO ($000\bar{1}$) and Zn-ZnO (0001), respectively. For all growth rates (GRs), as growth starts, the lattice spacing shows only a slight increase for the samples grown on O-ZnO while it remains unchanged for growth on Zn-ZnO. This observation indicates that InN grows at first nearly pseudomorphic to ZnO for both polarities. However, beyond a critical layer thickness (h_{crit}) the lattice spacing increases, i.e. relaxation sets in. On both polarities, h_{crit} increases with decreasing GR and is fairly comparable (cf. table 5.1). The largest h_{crit} measured for the lowest GR is 1.2 MLs on O-ZnO and 1.7 MLs on Zn-ZnO.

The roughening of the surface revealed by the emergence of the spotty patterns in RHEED occurs almost at the beginning of the relaxation process for all samples, except for the sample grown on O-ZnO at the highest GR. In this case the 2D to 3D transition occurs at 1.2 MLs, while the relaxation starts at 0.6 ML (see table 5.1 and figure 5.2). The observation of the surface roughening is confirmed by the evolution of the specular reflection intensity in RHEED as exemplarily shown in figure 5.2 (c) for the growth of InN on O-ZnO with GR 1.0 ML/s. After a slight intensity decrease, the signal increases for the rest of the growth. This increase in intensity coincides with the 2D to 3D growth mode transition. The same behavior is observed for the growth of InN on Zn-ZnO [figure 5.2 (d)].

This observation is also confirmed by the surface morphology of eight dedicated samples investigated by AFM [figure 5.3 (a) - (f) and figure 5.4 (a),(b)]. Six of the samples resulted from the deposition of 1.0 ML, 2.0 MLs, 3 MLs and 10 MLs of InN on O-ZnO and 1.0 ML and 10.0 MLs of InN on Zn-ZnO at a GR of 0.2 ML/s. In addition, the bare surfaces of two O-ZnO and Zn-ZnO substrates were examined for comparative purposes after annealing. The annealed ZnO substrates show a smooth, stepped surface with a RMS of 0.2 nm for O-ZnO and 0.1 nm for Zn-ZnO. After the deposition of 1.0 ML of InN on both O-ZnO

and Zn-ZnO, smooth surfaces covered by mono-atomic steps and a roughness of about 0.3 – 0.4 nm are obtained [figure 5.3 (c), (d)]. However, after the deposition of 2.0 MLs of InN on O-ZnO [figure 5.4 (a)], the surface roughness increases to 1.6 nm. Though mono-atomic steps are still observed, additional 3D structures formed on top with a density of $2.2 \times 10^8\ cm^{-2}$ and height and diameter of 17 nm and 64 nm, respectively. For thicknesses larger than 2 MLS, the density of 3D structures decreases to $6.8 \times 10^7\ cm^{-2}$ (3 MLs) and $3.7 \times 10^6\ cm^{-2}$ (10 MLs). While the height and diameter of these 3D structures was fairly constant for the 3 MLs sample with 16 nm and 59 nm, both increased to 23 nm and 138 nm, respectively, for 10 MLs of InN (cf. table 5.2). For the Zn-ZnO polarity, after the deposition of 10 MLs, 3D structures were revealed with a density of $5.7 \times 10^6\ cm^{-2}$ and height and diameter of 5 nm and 190 nm, respectively. Thus, these results clarify the streaky-spotty pattern transition observed in RHEED, and most importantly, they reveal that we can grow coherent and smooth InN layers with thickness of about 1.7 MLs and 1.2 MLs on Zn-ZnO and O-ZnO, respectively.

Sample	RMS [nm]	Height [nm]	Diameter [nm]	Density [$10^6\ cm^{-2}$]
2 MLs InN (O-ZnO)	1.6	17	64	220
3 MLs InN (O-ZnO)	1.6	16	59	68
10 MLs InN (O-ZnO)	0.3	23	138	3.7
10 MLs InN (Zn-ZnO)	0.4	5	196	5.7

Table 5.2: RMS surface roughness and height, diameter, and density of the 3D structures formed at the surface of InN/ZnO of both polarities investigation as measured by AFM.

RHEED investigations revealed a streaky-spotty transition between InN layer thicknesses of 1 ML to 2 MLs, which is confirmed by AFM and corresponds to a 2D-3D growth transition. Increasing further the InN layer thicknesses, the spotty diffraction pattern changes again into a more streaky pattern [figure 5.1 (b), (c)]. The total volume of the 3D structures, determined by AFM, decreases from 0.6 ML (2 MLs InN/O-ZnO) to 0.1 ML (3 MLs InN/O-ZnO) to below 0.1 ML (10 MLs InN/O-ZnO). This is in agreement with the RHEED pattern evolving from a spotty one into a more streaky pattern for the 10 MLs samples.

All 3D structures, that were investigated, where found to be located in hexagonal shaped pits [figures 5.3 (f), 5.4 (a), (b), 5.5 (a), (b), (f)]. The average pit depth increases with InN thickness up to 3 MLs InN and than decreases to 8.5 nm (2 MLs InN/O-ZnO) to 10.5 nm (3 MLs InN/O-ZnO) and to (2 - 3) nm (10 MLs InN/Zn-ZnO). Many of the 3D structures have a spiral form [figure 5.5 (b), (c), (d)] or double spiral form [figure 5.5 (e)]. This spiral growth mode might suggest the presence of a+c dislocations at their core [83]. The

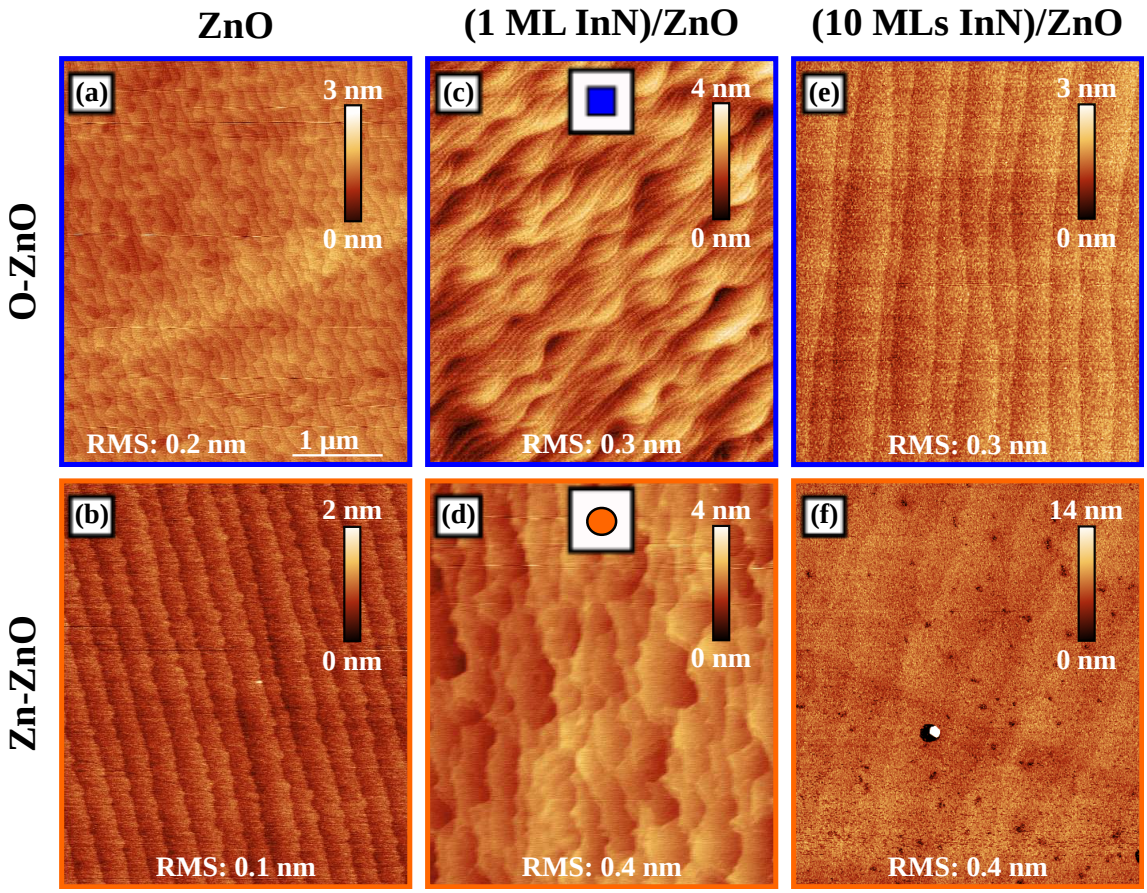

Figure 5.3: AFM images of $5 \times 5\ \mu m^2$ size of bare O-ZnO (a), Zn-ZnO (b), (1 ML InN)/O-ZnO (c), (1 ML InN)/Zn-ZnO (d), (10 ML InN)/O-ZnO (e) and (10 ML InN)/Zn-ZnO (f). The frames of the images are color coded, blue for O-ZnO and orange for Zn-ZnO. Symbols in (c), (d) recall figure 5.2 (a) and (b).

surface sites, where screw dislocations intersect the surface, are not only preferential sites for crystal growth, but also for etching, since these sites do not form a closed surface but a stepped one. This might be the case also for some of the 3D structures exhibiting a spiral shape. All hexagonal pits are decorated with 3D structures. Thus, we assume that the onset of 2D-3D transition at h_{2D-3D} is also the onset of formation of these pits. As the depth of these pits is 10 nm or more, it exceeds the thickness of the thin 0.26 nm to 2.6 nm InN layers. Thus, it indicates etching of the ZnO substrate. Such hexagonal pits were already reported in InN layers grown on O-ZnO and originate from the disturbed InN/ZnO interface where the ZnO substrate is severely etched down [129]. The islands were shown to have a crystal structure that matches the one of cubic In_2O_3 [129]. Thus, for layer thickness exceeding h_{crit} in the order of a ML, defects form in the InN adlayer and as relaxation occurs, the InN/ZnO interface is no longer protected towards back etching that might lead to the formation of In_2O_3 inclusions similarly to the step erosion mechanism occurring during InAs quantum dot formation on GaAs [163].

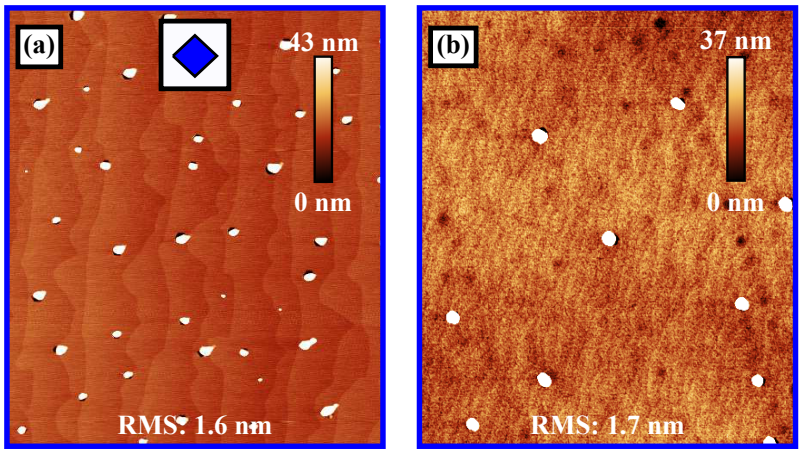

Figure 5.4: AFM images of 5×5 μm^2 size of (2 ML InN)/O-ZnO (a) and (3 ML InN)/O-ZnO (b). The Symbol in (a) recalls figure 5.2 (a).

For the deposition of InN layers, our results evidenced that the relaxation possibly followed the SK mechanism with h_{crit} that depends not only on the ZnO polarity but also on the GR. This last effect has not been reported so far for III-N. For InAs on InP, Nakayama *et al.* reported the increase of the critical thickness with increasing GR [164]. He attributed this finding to the slow transformation of a metastable 2D film, growing faster as the GR is increased, into stable 3D islands. In contrast, in the present case of InN on ZnO, we observe a slight delay of relaxation for lower GR. As shown above, whatever the ZnO polarity, an almost pseudomorphic 2D growth sets in at the start of the InN deposition. In RHEED, the intensity of the specular reflection decreases at the onset of InN deposition on both ZnO polar surfaces, which may result from the nucleation of platelets with

height 1 – 2 MLs similarly to the growth of GaN/AlN heterostructures [165]. This process develops until a specific h_{crit} that depends on the GR used for the InN deposition. Once h_{crit} is attained, the strain relaxation process initiates with an enlargement of the in-plane lattice parameter, as monitored by RHEED. However, it then proceeds differently for each ZnO polarity.

For growth of InN on both ZnO substrate polarities, the relaxation in almost all cases occurs close to the transition from 2D to 3D growth mode. Relaxation might occur first elastically and later on plastically with introduction of dislocations [166], or synchronously with dislocations. In contrast, for the case of growth of InN on O-ZnO with GR 1 ML/s, the relaxation occurs within the 2D growth mode. Therefore, the coalescence of the platelets should occur with the concomitant formation of dislocations as suggested by the simultaneous increase of the lattice parameter in RHEED for InN thickness above 0.6 ML [figure 5.2 (a)]. Such relaxation mechanisms might be due to the formation of dislocations at the junction of 2D platelets [165], however further investigations to elucidate the details of the process are necessary.

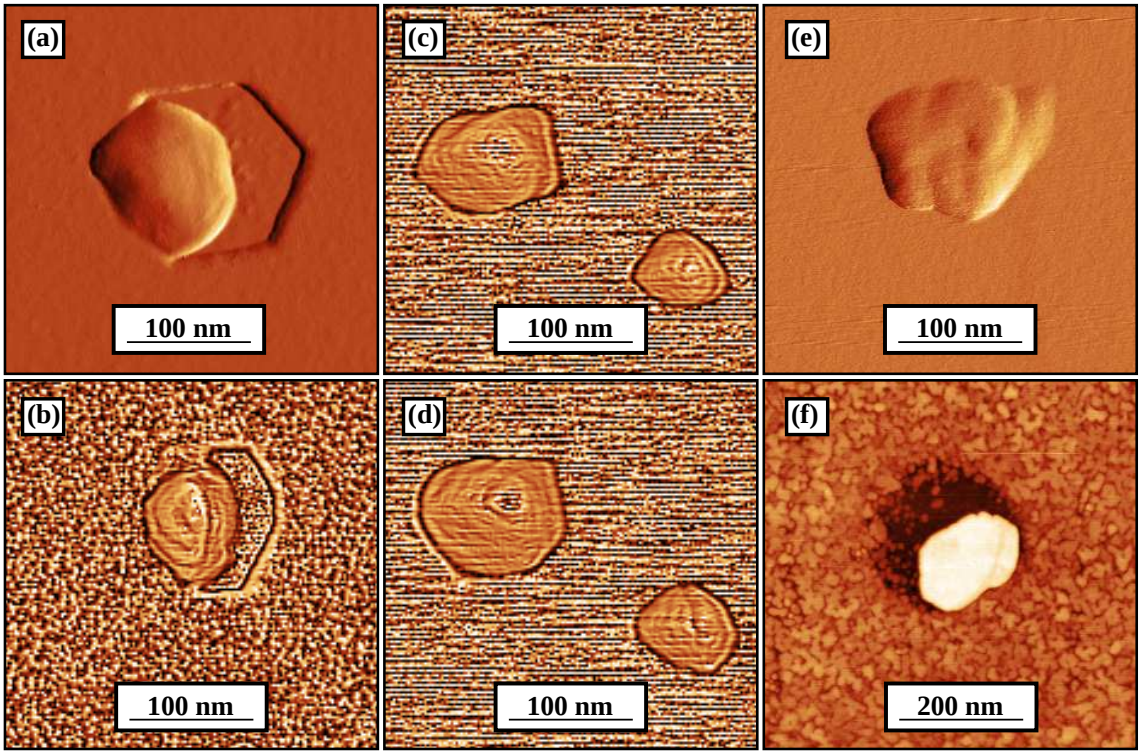

Figure 5.5: AFM images of (2 MLs InN/O-ZnO) (a), (3 MLs InN/O-ZnO) (b), (c), (d), (2 MLs InN/O-ZnO) (e), (10 MLs InN/Zn-ZnO) (f). Contrast filters were applied to figure (a)-(e).

The critical thickness h_{2D-3D} for the 2D – 3D growth mode transition is governed by a balance between the surface energy and the elastic energy [166]. As a consequence, depending on growth conditions, surface polarity, and / or growth techniques, h_{2D-3D} might vary. The observation that both h_{crit} and h_{2D-3D} depend on MBE growth parameters suggests a kinetic origin of the film growth mode with possible strong influences from film morphology [71].

It was demonstrated in this section that ML-thin InN of layer thicknesses below 2 MLs can be grown pseudomorphically on ZnO of both polarities. The exact onset of this 2D-3D transition at h_{2D-3D} depends on polarity. The onset of relaxation at h_{crit} depends not only on polarity but also on GR. The highest h_{crit} was obtained for the lowest growth rate of 0.2 ML/s on Zn-ZnO with 1.7 MLs, compared to 1.2 MLs on O-ZnO. Beyond h_{2D-3D} chemical etching takes place and hexagonal pits decorated with 3D structures are formed. In the following, a protective InN layer will be deposited on ZnO before growing GaN to prevent chemical etching between Ga and ZnO.

5.2 Growth of GaN on InN/ZnO

After establishing the limitations for pseudomophic growth of InN on ZnO, pseudo-substrates of (1.2 MLs InN/O-ZnO) and (1.5 MLs InN/Zn-ZnO) were grown. The protective layer as well as the ML-thin GaN were grown at the lowest GR that could be established, which was 0.2 ML/s. In order to check for indication of unintended metal-rich growth the surface of all GaN/InN/ZnO samples was investigated with OM and AFM and no indication of indium droplets was found.

In agreement with the results of the last section, [figure 5.6 (a2), (b2)] presents a streaky RHEED pattern, that was obtained after the deposition of InN layers at GR 0.2 ML/s with thickness 1.2 MLs on O-ZnO and 1.5 MLs on Zn-ZnO. However, the streaky pattern changes to a spotty one in the course of GaN deposition on both ZnO polarities [figure 5.6 (a3), (a4) and (b3), (b4)]. For growth on O-ZnO the intensity of the RHEED streaks decrease and simultaneously faint spots appeared [figure 5.6 (a3)]. This effect occurs at a total thickness of 1.3 MLs, i.e. it corresponds to the beginning of the GaN deposition. For growth of GaN on Zn-ZnO, the same intensity evolution is observed but the 2D – 3D transition is delayed to a total thickness of 4.6 MLs, i.e. it occurs after the deposition of 3.1 MLs GaN.

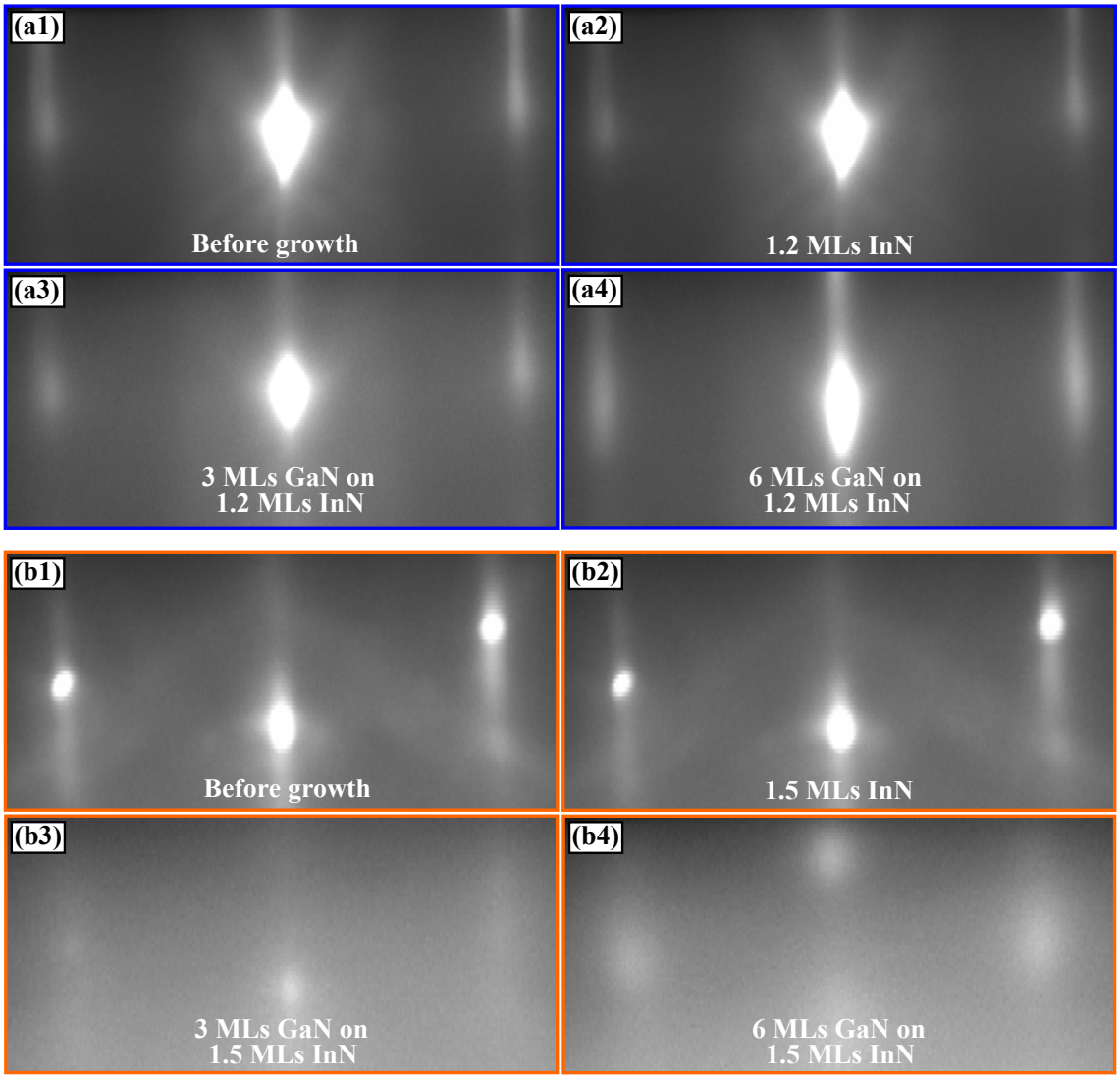

Figure 5.6: (a1)-(a4) and (b1)-(b4) RHEED diffraction patterns in the $\langle 10\bar{1}0 \rangle$ and in the $\langle 11\bar{2}0 \rangle$ azimuths after the deposition of 6.0 MLs GaN on 1.2 MLs InN/O-ZnO (blue frame) and 1.5 MLs InN/Zn-ZnO (orange frame), respectively. The intensity and the contrast were increased in images (b3), (b4). Thermal expansion was taken into account when determining the lattice spacing.

In-situ RHEED monitoring confirmed smooth surfaces of the protective InN layer, as the diffraction pattern at the end of the InN deposition was still streaky and the intensity did not decrease considerably. However, depending on polarity, very different changes in the diffraction pattern took place. In the course of the GaN deposition on InN/O-ZnO [figure 5.6 (a3), (a4)], the streaky diffraction pattern transitions temporarily into a spotty one and finally into a superposition of streaks and spots. For GaN deposition on InN/Zn-ZnO [figure 5.6 (b3), (b4)] the pattern is first streaky but decreases considerably in intensity. After the deposition of 3.1 MLs of GaN, faint spots appear. Due to the low overall intensity of the diffraction pattern, the intensity and contrast was increased in figure 5.6 (b3), (b4) to better distinguish the patterns.

The variation of the *a*-lattice spacing in dependence of the InN and GaN thicknesses deposited on O-ZnO and Zn-ZnO is presented in Figures 5.7 (a) and (b), respectively. Depending on the ZnO polarity, a very different evolution occurs.

On O-ZnO [figure 5.7 (a)], the lattice spacing increases during the deposition of 1.2 MLs of InN and gradually decreases immediately at the start of GaN deposition. Beyond the deposition of 1.3 MLs of GaN the lattice spacing even decreases further below the lattice spacing of ZnO, and it stabilizes at the value of 3.24 Å after the total deposition of about 5 MLs (1.2 MLs of InN + 3.8 MLs of GaN). This value corresponds to a remaining lattice mismatch of 1.3% for GaN. In order to understand this phenomenon, we have considered the possible alloying of the supplied InN and GaN as an (In, Ga)N layer. We considered two cases: unstrained and strained (In, Ga)N. Therefore, we also display in figure 5.7 (a) the evolution of the lattice spacing of an unstrained (In, Ga)N layer, that was calculated following Vegard's law. In that case, the calculated lattice spacing clearly does not follow the measured one. Nonetheless, in the case where the InN *a*-lattice spacing is strained to the experimental value attained just before the start of GaN deposition (equal to 3.31 Å), we obtain a satisfactory agreement between the experimental and calculated values up to a total layer thickness of 4.2 MLs (1.2 MLs InN + 3 MLs GaN). Beyond 4.2 MLs, the experimental lattice spacing decreases slower than the model. Hence, alloying does not seem to be the mechanism at play to explain the experimental data. Therefore, we examined a third case fitting the experimental data by an exponential decay law [dotted curve in figure 5.7 (a)] following a model introduced by Bourret *et al.* [165] to describe

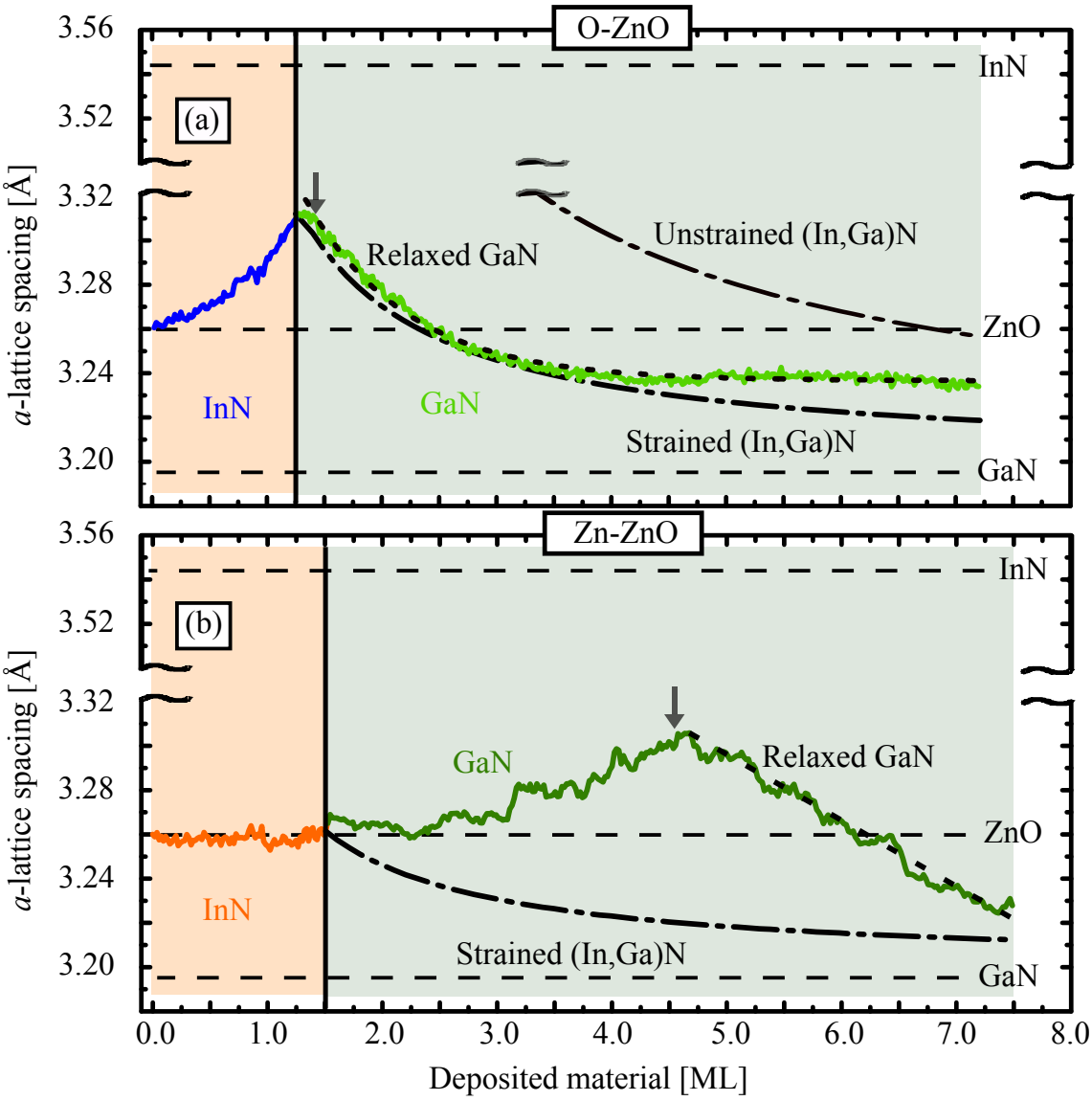

Figure 5.7: *a*-lattice spacing evolution during the deposition of 6 MLs GaN on (a) 1.2 ML thick InN on O-ZnO and (b) 1.5 ML thick InN on Zn-ZnO. The grey arrows indicate the transition between the streaky and spotty RHEED diffraction patterns (h_{2D-3D}), while the dashed black lines indicate the unstrained lattice constants of InN, GaN and ZnO. The grey dashed/dotted curves in (a) and (b) correspond to (In, Ga)N layers following Vegard's law. The grey dotted curve corresponds to partially relaxed GaN.

the evolution of the lattice strain in GaN/AlN heterostructures, measured by RHEED. This model is used in this work to describe the relaxation behavior of GaN/InN/ZnO heterostructures. This law reads:

$$a(h) = a_0 \exp\left(\frac{-(h - h_c)}{\Lambda}\right) + a_1 \tag{5.2}$$

where *a(h)* is the *a*-lattice spacing as a function of the layer thickness h, a_0 is the total amplitude of the lattice relaxation, h_c is a critical thickness, Λ is a characteristic thickness at which a fraction 1-1/e of the plastic relaxation has occurred and a_1 is the reference unstrained lattice parameter of the film. This model provides a satisfying fit of the experimental values for the parameters $a_0 = 0.07$ Å, $a_1 = 3.23$ Å, $h_c = 0.2$ ML and $\Lambda = 0.9$ ML.

In striking contrast, on Zn-ZnO [figure 5.7 (b)] the *a*-lattice spacing remains constant up to a total layer thickness of around 3.1 MLs (1.5 MLs InN + 1.6 MLs GaN). Thus, the thickness of 1.6 MLs can be assigned to the critical thickness of GaN on InN fully strained to Zn-ZnO. Beyond this thickness the *a*-lattice spacing increases, which indicates the formation of partially relaxed (In, Ga)N. However, after 4.6 MLs (1.5 MLs InN + 3.1 MLs GaN) the *a*-lattice spacing inverts its evolution and decreases. The streaky-spotty transition of the RHEED pattern occurs at around 4.6 MLs starting simultaneously to the onset of the decrease of the *a*-lattice spacing.

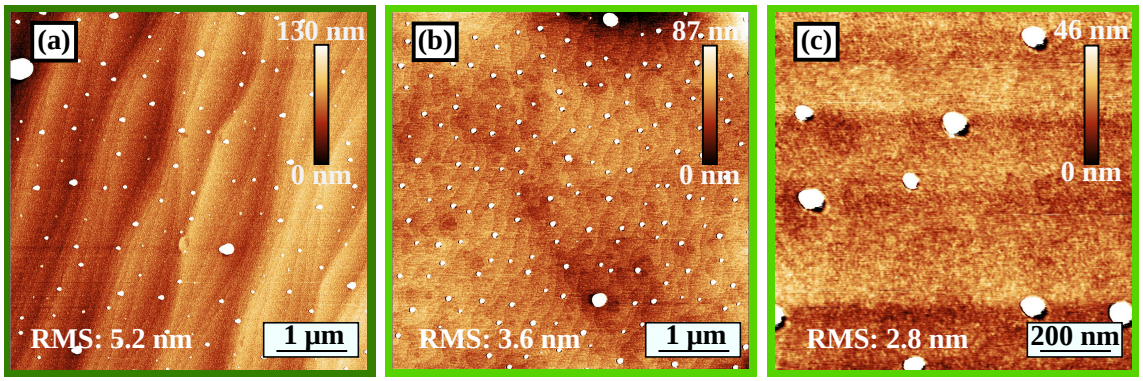

Figure 5.8: AFM images of (a) GaN(6.0 MLs)/InN(1.2 MLs)/Zn-ZnO ($5 \times 5\ \mu m^2$), (b) and (c) GaN(6.0 MLs)/InN(1.5 MLs)/O-ZnO of size ($5 \times 5\ \mu m^2$) and ($1 \times 1\ \mu m^2$), respectively.

As expected from the spotty RHEED patterns that emerged during both experiments, AFM measurements of these GaN/InN/ZnO heterostructures revealed the presence of 3D features at their surface [figure 5.8 (a), (b), (c)]. For growth on O-ZnO the density, average height, and diameter of these 3D features are $7.1 \times 10^8\ cm^{-2}$, 28 nm, and 44 nm,

respectively. The RMS roughness value for this sample is 5.2 nm. For growth on Zn-ZnO, the density, average height, and diameter of the 3D features are $5.6 \times 10^8\ cm^{-2}$, 10 nm, and 55 nm, respectively. The RMS roughness value for this sample is 3.6 nm. These values are reported in table 5.3. The total volume of these 3D features is for both samples similar with 1.4 MLs (Zn-ZnO) and 1.5 MLs (O-ZnO). However, in both cases the surface between them is still very smooth as atomic steps are observed [figure 5.8 (a), (b), (c)]. [Figure 5.8 (b), (c)] show that hexagonal etch pits formed regardless of the InN interlayer in the GaN/InN/ZnO structure. The average depth of these pits is 5 nm (O-ZnO) which proofs that the pits etch into the ZnO substrate, with all 3D structures residing within such pits.

For the deposition of GaN on InN pseudmorphic to ZnO, the relaxation process is also characteristic of the polarity of ZnO. On InN/O-ZnO the GaN lattice spacing immediately decreases and occurs simultaneously to the 2D-3D transition observed in RHEED. Therefore, at the low temperature of 450 °C, GaN growth seems to develop according to the Volmer-Weber mode on the 1 ML-thick InN layer. Nonetheless, the overgrowth of the unstable strained InN layer by the GaN cap layer could also possibly have triggered the sharp 2D-3D transition with increasing coverage [167]. Considering the formation and the relaxation of GaN 3D islands, we obtain a good fit to the *a*-lattice spacing evolution. However, the formation of strained or unstrained (In, Ga)N might also occur during capping by GaN [168], although the presence of (In, Ga)N alone does not allow to properly fit the data. Interestingly, the relaxation of the 6.0 ML-thick GaN layer is not full and the GaN *a*-lattice spacing reaches a steady-state *a*-lattice spacing around 3.24 Å that corresponds either to GaN with a residual strain of 1.3% or to fully relaxed $In_{0.12}Ga_{0.88}N$.

Sample	RMS [nm]	Height [nm]	Diameter [nm]	Density [$10^6\ cm^{-2}$]
2 MLs InN (O)	1.6	17	64	220
3 MLs InN (O)	1.6	16	59	68
10 MLs InN (O)	0.3	23	138	3.7
10 MLs InN (Zn)	0.4	5	196	5.7
1.2 MLs InN/6 MLs GaN (O)	5.2	28	44	710
1.5 MLs InN/6 MLs GaN (Zn)	3.6	10	55	560

Table 5.3: The RMS surface roughness, height, diameter and density of the 3D structures, formed at the surface of InN/ZnO and GaN/InN/ZnO of both polarities, measured by AFM. "O" refers to "O-ZnO" and "Zn" refers to "Zn-ZnO".

In contrast on InN/Zn-ZnO, the growth of GaN is pseudomorphic until a total layer thickness of about 3.1 MLs (1.5 MLs InN + 1.6 MLs GaN) is reached. Afterwards the *a*-lattice constant increases. Such a behavior is unexpected and might be due to composition pulling effect [26], [27] that allows the formation of (In, Ga)N with a higher In-content on the surface. In fact, RHEED describes transient of surface lattice spacing during growth. The relatively high strain state of the pseudomorphic layer allows for the composition pulling effect to appear. At a thickness of 4.6 MLs the *a*-lattice spacing starts to decrease and concomitantly, the 2D-3D transition occurs similarly to InN/ZnO.

A schematic of the growth process for InN/ZnO and GaN/InN/ZnO is shown in figure 5.9, summarizing all the obtained results.

In short, we have established that for growth on Zn-ZnO, templates consisting of 1.5 MLs InN and 1.6 MLs GaN can be pseudomorphically grown. For growth on O-ZnO no pseudomorphic growth of GaN on InN templates was found. In this case sub-ML InN already shows a slight relaxation with an increasing *a*-lattice constant, and for GaN grown on 1.2 MLs InN the *a*-lattice constant decreases right after the growth starts with an immediate streaky-spotty transition of the RHEED pattern.

5.3 Growth of (In, Ga)N heterostructures on ZnO

After establishing the limits of pseudomorphic growth of InN on ZnO and GaN on InN/ZnO pseudo-substrates the growth of InN/GaN SPSLs was investigated. The nominal GR for all samples was about 0.2 ML/s (3.4 nm/min), which was the metal flux. The nominal indium flux was 0.19 ML/s (3.25 nm/min), the nominal gallium flux was 0.2 ML/s (3.4 nm/min). The nominal nitrogen flux was 0.2 ML/s. The growth temperature was 450 °C. All samples were nominally grown under slightly nitrogen-rich conditions, though some samples unintentionally deviated from that, which will be discussed later. Three (1 ML InN/2 MLs GaN) SPSLs (nominal structure) were grown on ZnO, two on Zn-ZnO and one on O-ZnO: ten and hundred periods on Zn-ZnO, which will be referred to as SL^{Z}_{10x}, and SL^{Z}_{100x} and a hundred periods on O-ZnO, referred to as SL^{O}_{100x}.

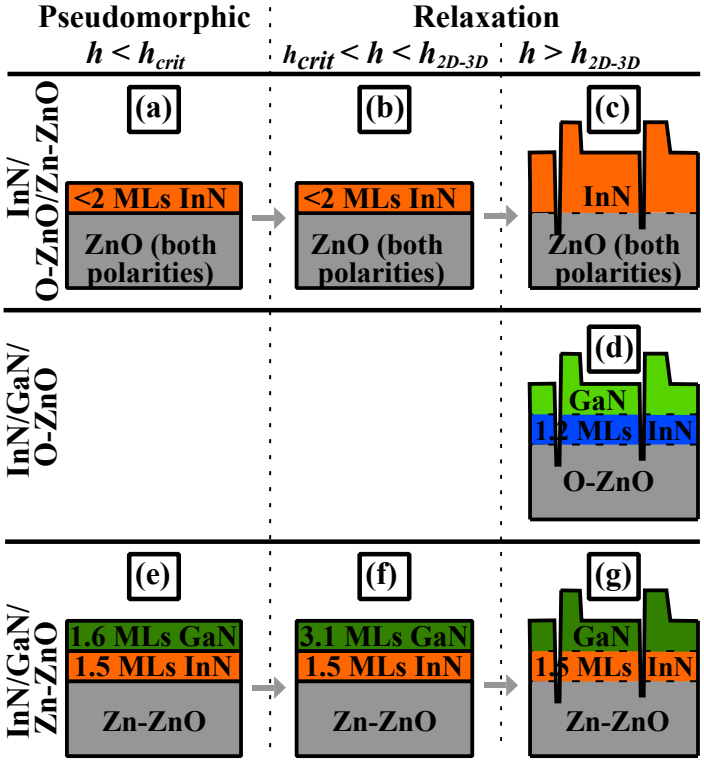

Figure 5.9: Schematic representation of the growth evolution of (a) - (c) InN on ZnO, and (d) - (g) GaN on InN/ZnO. In (a), the early formation of a pseudomorphic InN layer below the critical thickness is followed by (b) relaxation and (c) back etching and 3D structure formation on both ZnO polarities. For the growth of GaN on 1.2 MLs InN pseudomorphic to O-ZnO, relaxation with 2D-3D transition is immediate (d). On 1.5 MLs InN pseudomorphic to Zn-ZnO, the early formation of a GaN layer occurs below the critical thickness of 3.1 MLs (e). Above this thickness (f), relaxation, and (g) 2D-3D transition and back etching occur.

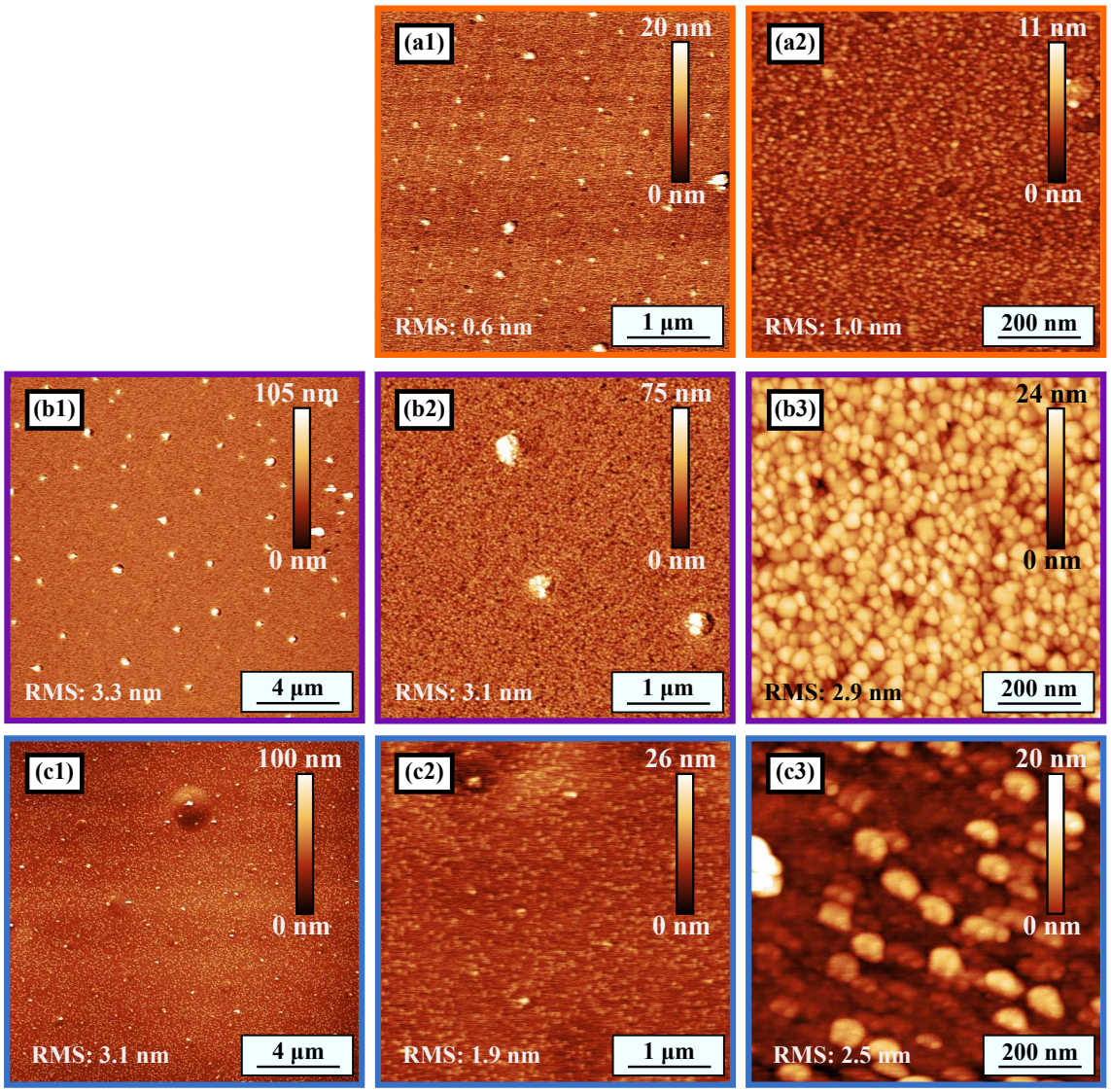

Figure 5.10: AFM height profiles of SL^{Z}_{10x} (a1)-(a2)($5 \times 5\ \mu m^2$, $1 \times 1\ \mu m^2$), SL^{Z}_{100x} (b1)-(b3)($20 \times 20\ \mu m^2$, $5 \times 5\ \mu m^2$, $1 \times 1\ \mu m^2$), SL^{O}_{100x} (c1)-(c3)($20 \times 20\ \mu m^2$, $5 \times 5\ \mu m^2$, $1 \times 1\ \mu m^2$).

5.3.1 Investigation of the surface morphology

The surface of the heterostructures were probed by AFM, the heterostructures grown on ZnO (SL^{Z}_{10x} and SL^{Z}_{100x}) [figure 5.10 (a) and (b)] exhibit a surface with faint steps with a high density of 3D structures that are only a few MLs high but cover nearly the complete surface. Since they can barely be distinguished from the surface it is not possible to determine their density, but comparing SL^{Z}_{10x} [figure 5.10 (a)] and SL^{Z}_{100x} [figure 5.10 (b)] it shows that the density of medium and large sized 3D structures decreases with increasing numbers of periods and a few large 3D structures grew in size.

The density, average height and diameter of these medium and large sized 3D structures is $3.2 \times 10^{8}\ cm^{-2}$, 0.7 nm and 23 nm for SL^{Z}_{10x} and $1.2 \times 10^{7}\ cm^{-2}$, 50.5 nm and 173 nm for SL^{Z}_{100x} respectively. The small ML-thin 3D structures increased in size so that the whole surface of SL^{Z}_{100x} consists of a grain like structure [figure 5.10 (b2)]. At the intersections of these platelets or grains, defects might form and facilitate the relaxation as described by Bourret *et al.* [165] for GaN/AlN heterostructures. The stepped morphology that is still well visible after 10 periods [figure 5.10 (a1)] can barely be distinguished anymore after 100 periods [figure 5.10 (b2)].

SL^{O}_{100x} does not exhibit a stepped surface morphology. Furthermore, the surface is covered with a high density of 3D structures of $7.9 \times 10^{9}\ cm^{-2}$. Figure 5.10 (c1) shows a large spherical object on the surface and several smaller ones, as their color indicates, they form depressions in the surface and not protrusions like the 3D structures. Therefore, they are probably traces of droplets of indium or gallium which are also present in figure 5.11 (c), which shows the surface of SL^{O}_{100x} magnified 20x by an optical microscope. Comparing figure 5.11 (b1), (b2) (SL^{Z}_{100x}) and (a1), (a2) (SL^{Z}_{10x}) to (c1), (c2) (SL^{O}_{100x}) shows that SL^{Z}_{100x} and SL^{Z}_{10x} were probably grown near stoichoimetry because there is only a low density of objects on the surface that may be droplets, whereas SL^{O}_{100x} exhibits a higher density of spherical objects, that may be droplets, and was probably grown with slightly group-III rich conditions.

Comparing RMS of all three samples shows that the RMS increased from 0.6 nm [figure 5.10 (a1)] to 3.1 nm [figure 5.10 (b2)] with increasing number of periods (SL^{Z}_{10x} compared to SL^{Z}_{100x}) and that SL^{O}_{100x} exhibits a lower RMS of 1.9 nm [figure 5.10 (c2)] compared to SL^{Z}_{100x} with 3.1 nm. The lower RMS of SL^{O}_{100x} compared to SL^{Z}_{100x} might be due to the metal-rich vs N-rich growth conditions, as explained in chapter 3.1.3.

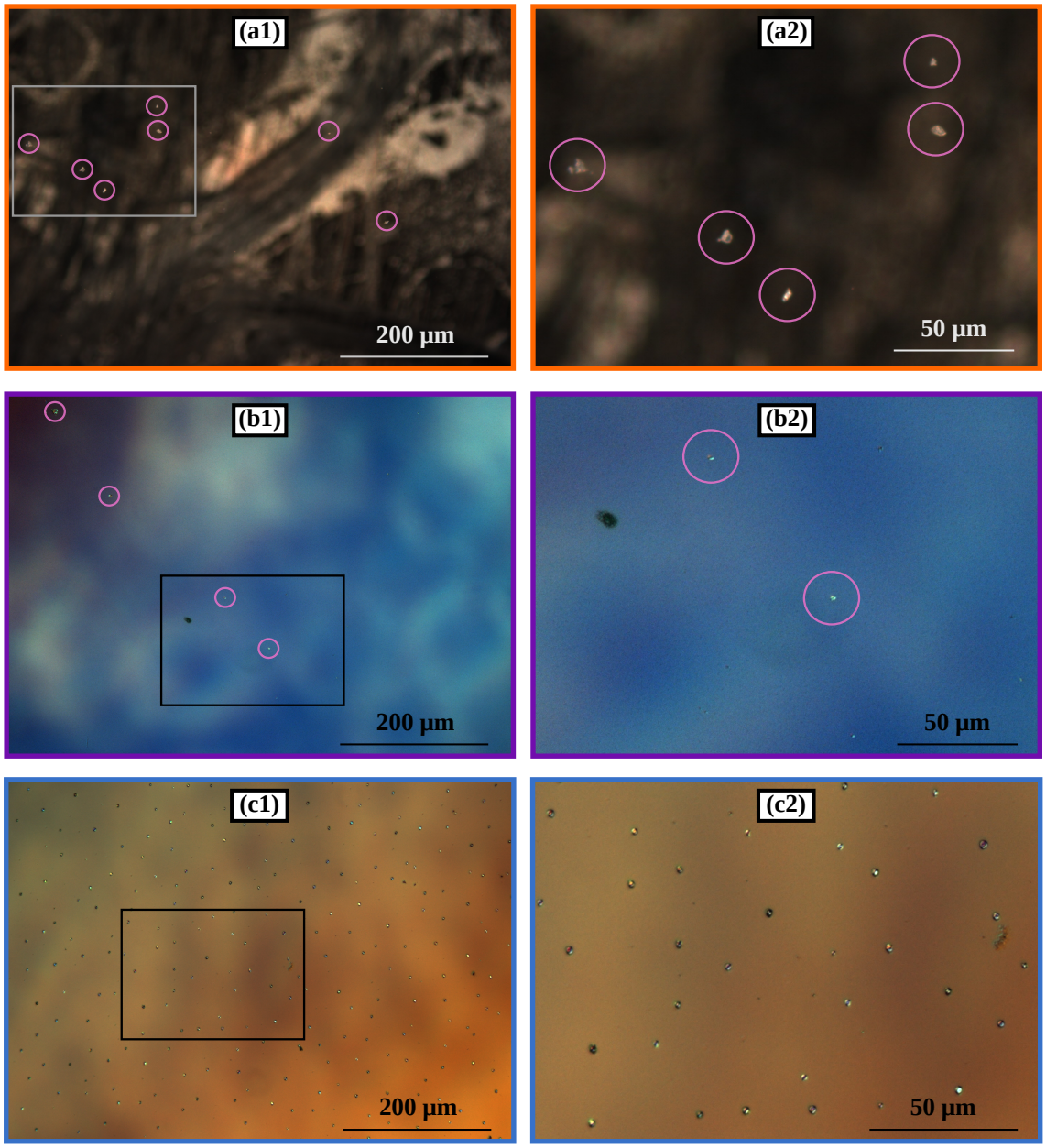

Figure 5.11: Surface of (a1), (a2) SL^{Z}_{10x}, (b1), (b2) SL^{Z}_{100x} and (c1), (c2) SL^{O}_{100x} magnified (20x) ((a1), (b1), (c1)) investigated with optical microscope. (a2), (b2), (c2) show enlarged area which is marked with black or grey rectangle in (a1), (b1), (c1). Spheres on the surface may be droplets (indium or gallium), pink circles in (a1), (a2), (b1), (b2)) mark possible droplets.

5.3.2 Investigation of the growth mode and surface morphology

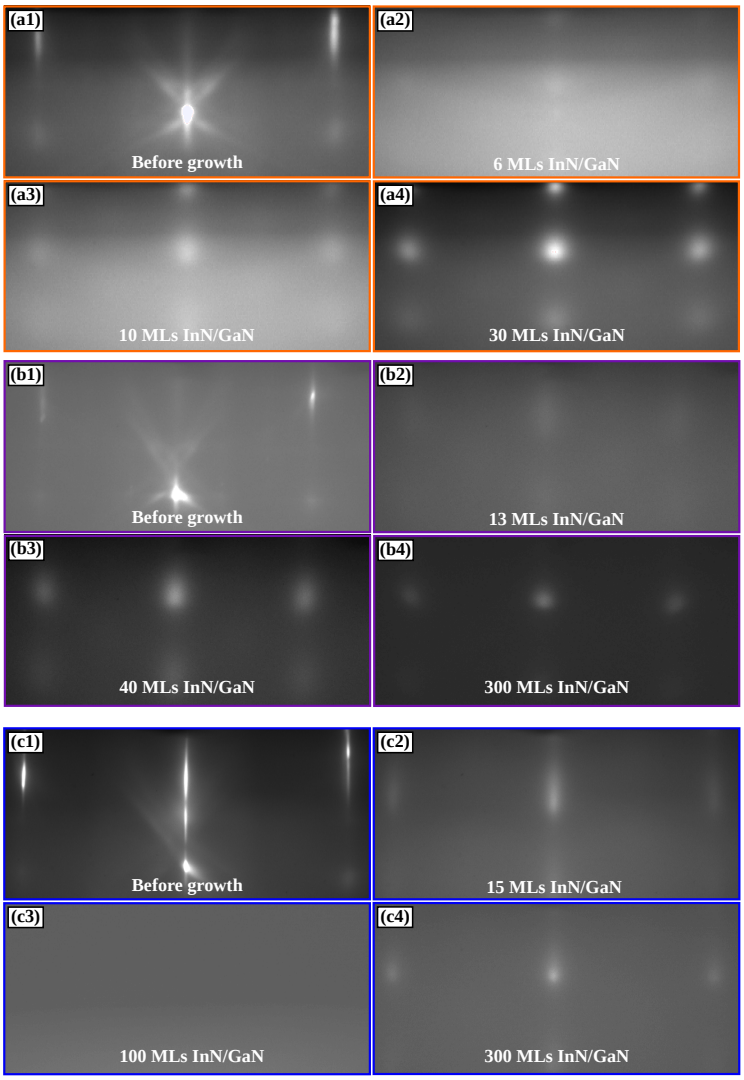

Figure 5.12: RHEED diffraction patterns in the $\langle 10\bar{1}0 \rangle$ azimuth of (a) SL^{Z}_{10x} (b) SL^{Z}_{100x} and (c) SL^{O}_{100x} . Intensity and contrast were increased in images (a2), (a3) and (b1), (b2).

For all heterostructures RHEED monitoring during growth revealed a streaky pattern at the beginning [figure 5.12 (a1), (b1), (c1)]. The intensity started to diminish after a few MLs of deposition [figure 5.13 (a2), (b2), (c2)]. For growth on Zn-ZnO the intensity almost vanished. Thus, the signal could not be displayed anymore (missing data points in figure 5.13 (a), (b) and 5.14). The intensity increases again beyond $h_{2D-3D} = 9$ MLs [figure 5.13 (b)] and a very faint spots start to appear in the RHEED diffraction pattern for SL^{O}_{100x} [figure 5.12 (c2)]. For SL^{Z}_{10x} [figure 5.12 (a3)] and SL^{Z}_{100x} [figure 5.12 (b3)] the exact layer thickness when the spotty diffraction pattern appears cannot be determined due to the low intensity of the signal. The initial decrease in RHEED specular intensity is an

indication of surface roughening, since it is combined with a streaky diffraction pattern below 9 MLs total thickness it is assumed that this roughening is due to formation of 2D platelets of 1 ML to 3 MLs thickness.

The evolution of the *a*-lattice spacing in figure 5.13 (a) and 5.14 shows a very different behavior of the *a*-lattice parameter for SL^{Z}_{10x} and SL^{O}_{100x}. For SL^{Z}_{10x} the *a*-lattice parameter increases during deposition of InN and decreases again during deposition of GaN (as indicated with guides to the eye within the range of 21 MLs to 27 MLs in figure 5.14) but the average *a*-lattice parameter increases up to a total layer thickness of about 12 MLs to a maximum value of 3.42 Å, which correlates to unstrained $In_{0.67}Ga_{0.33}N$. This could indicate a composition pulling effect [169], [170], [171]. Beyond the 12th ML the *a*-lattice spacing starts to decrease again. Due to compressive strain in the InN or (In, Ga)N layer (if InN and GaN mixes) there is initially a driving force that may decrease the indium content in the growing layer, gallium atoms may take the place of some of the indium atoms which then segregate to the growth surface and accumulate in the top layers or 3D structures, which increases the *a*-lattice spacing. Upon relaxation more indium may be incorporated into the (In, Ga)N layer, which could lower the indium content in the top layer or the 3D structures and therefore cause a decrease in the *a*-lattice spacing of the top layer. It must be noted at this point that beyond 9 MLs the RHEED pattern is spotty and we are possibly probing the *a*-lattice parameter of the 3D structures.

A similar behavior can be observed for SL^{Z}_{100x} in figure 5.13 (a), the maximum average value of the *a*-lattice parameter is 3.42 Å, determined for a total layer thickness of 20 MLs. After nearly 200 MLs of deposition, the intensity increases again and the *a*-lattice parameter shows a saw-tooth evolution around a stable average value of 3.33 Å.

In contrast, the SL^{O}_{100x} grown on O-ZnO [figure 5.13 (a)] shows a fairly constant *a*-lattice parameter up to the 2D-3D transition at $h_{2D-3D} = 9$ MLs. After this transition the *a*-lattice parameter slightly decreases and then recovers the average value of 3.30 Å, which stays constant for the rest of the growth. This value corresponds to $In_{0.37}Ga_{0.63}N$ ($R = 65\%$).

The change of *a*-lattice spacing beyond the 9th ML of deposited material is interpreted as the onset of relaxation. Therefore the fit of the $\omega - 2\theta$ scan was conducted accounting for relaxation between the 3rd and the 12th period (9-36 MLs) (see chapter 5.3.3).

The transition from 2D growth mode (streaky RHEED diffraction pattern) to 3D growth mode (spotty pattern) at a critical layer thickness $h_{2D-3D} = 9$ MLs that is observed for SL^{O}_{100x} and the simultaneous onset of RHEED specular intensity increase, that is observed for all 3 heterostructure samples at $h_{2D-3D} = 9$ MLs is indicative of Stranski-Krastanov

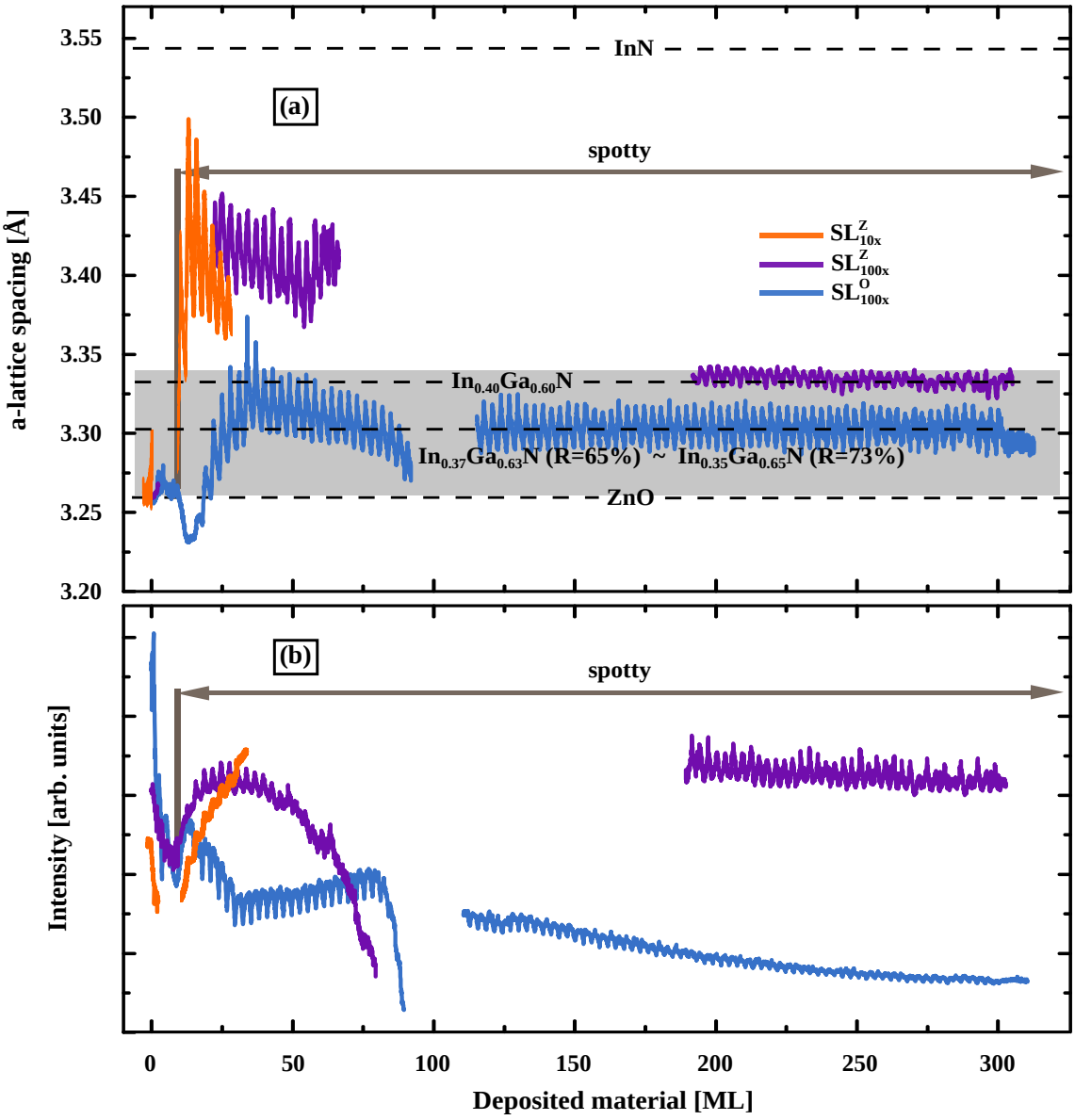

Figure 5.13: Evolution of (a) *a*-lattice spacing and (b) RHEED specular intensity during growth of SL^{Z}_{10x} (orange), SL^{Z}_{100x} (purple) and SL^{O}_{100x} (blue). Guides to the eye indicate *a*-lattice parameter of InN, ZnO, $In_{0.40}Ga_{0.60}N$, $In_{0.37}Ga_{0.63}N$ ($R = 65\%$) and $In_{0.35}Ga_{0.65}N$ ($R = 73\%$) as well as the transition from a streaky to a spotty RHEED diffraction pattern. A gray shaded area indicates the distribution of indium content in the (In, Ga)N heterostructures that correlates to RSM peak intensities within the $I_{2/3}$ range (see chapter 5.3.3). Thermal expansion was taken into account when determining the lattice spacing.

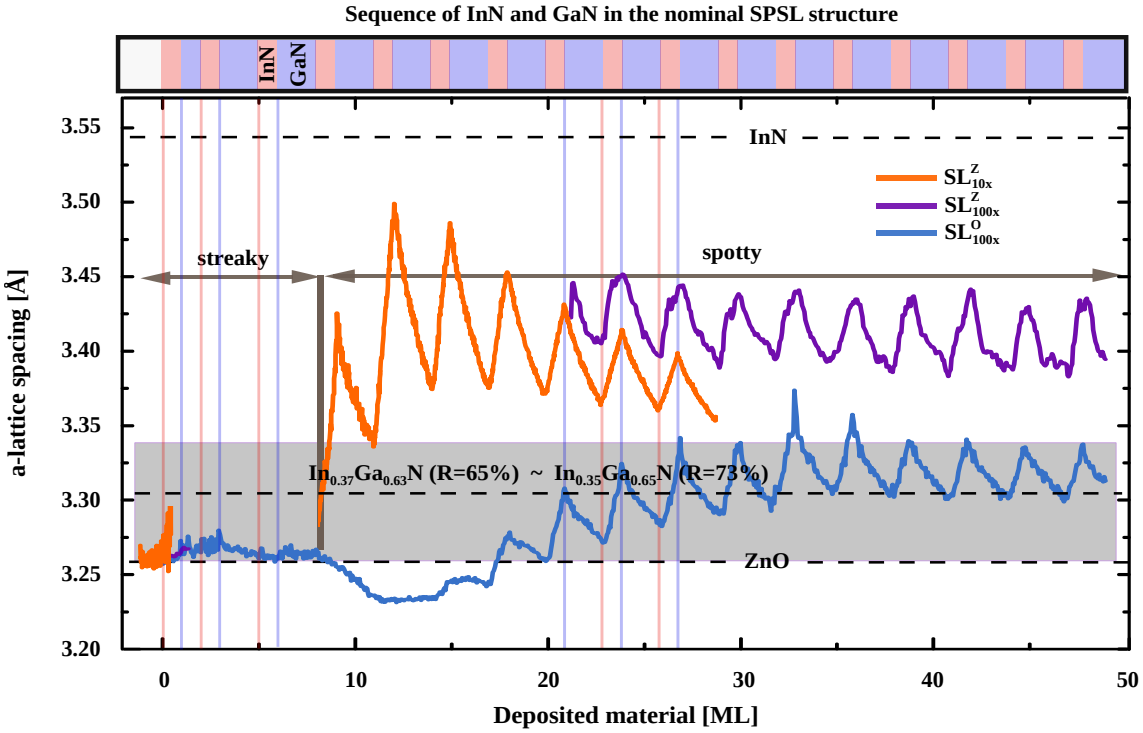

Figure 5.14: Evolution of a-lattice spacing during growth of SL^{Z}_{10x} (orange), SL^{Z}_{100x} (purple) and SL^{O}_{100x} (blue). Guides to the eye indicate a-lattice parameter of InN, ZnO, $In_{0.37}Ga_{0.63}N$ ($R = 65\%$) and $In_{0.35}Ga_{0.65}N$ ($R = 73\%$) as well as the transition from a streaky to a spotty RHEED diffraction pattern and indication of the onset of deposition of InN (light orange vertical lines) and GaN (light blue vertical lines). A gray shaded area indicates the distribution of indium content in the (In, Ga)N heterostructures that correlates to RSM peak intensities within the $I_{2/3}$ range (see chapter 5.3.3). Thermal expansion was taken into account when determining the lattice spacing.

growth mode, as already explained in chapter 5.2. It is interesting that h_{2D-3D} in this case is greater than that of GaN/InN/ZnO (see chapter 5.2). Furthermore, the rather constant *a*-lattice spacing of SL^{O}_{100x} up to a thickness of about 9 MLs shows a different behavior than the *a*-lattice spacing evolution found for the growth of GaN/InN on O-ZnO (see chapter 5.2), which shows an increase within the first ML of deposited InN. This difference might be due to the unintentional difference in V/III ratio (see chapter 5.3.1). Though both samples were nominally grown with V/III about 1.1 (N-rich), investigations with OM and AFM suggest that SL^{O}_{100x} was actually grown with metal-excess. Thus, this result suggests that pseudomorphic growth of thin InN/GaN layers on O-ZnO might be possible. The influence of the V/III ratio on growth will be further discussed in chapter 6.1.2.

5.3.3 Determination of indium content and degree of relaxation

The indium content and degree of relaxation of SL^{Z}_{100x} and SL^{O}_{100x} was determined by XRD reciprocal space maps (RSM).

Figure 5.15 shows the RSM of SL^{Z}_{100x} (5.15 (a)) and SL^{O}_{100x} (5.15 (b)) around the $(10\bar{1}5)$ reflex. The RSM of SL^{O}_{100x} (5.15 (b)) was acquired using a crystal analyzer. The RSM of SL^{Z}_{100x} (5.15 (a)) consists of two separate measurements. Measuring with a crystal analyzer no (In, Ga)N related peak could be distinguished with the used integration time due to its low intensity. Thus, a second scan without analyzer crystal but with a 1 mm slit in front of the detector was conducted and both scans are presented together. Since the detector setup as well as the scan parameters are not the same for both measurements the colors which indicate the intensity are not comparable between both measurements and therefore no color scale was added. The intensity values of all three RSM were logarithmized and displayed as a linear plot. The background was not displayed by setting the color of the intensity values below some threshold to white, except for the scan around the (In, Ga)N peak in figure 5.15 (a).

In figure 5.15 guides to the eye were added to mark the position of fully relaxed ZnO, GaN, InN, $In_{0.35}Ga_{0.65}N$ and $In_{0.37}Ga_{0.63}N$ (red dots). The vertical dash-dotted lines intersecting the ZnO peaks mark (In, Ga)N fully strained to ZnO. This vertical dash-dotted line will be referred to as the fully strained line. The maximum of the (In, Ga)N peak is marked with a black square. A black solid line connects unstrained GaN and InN. Fully relaxed (In, Ga)N layers of any composition will lie on this line, referred to as the composition line. The dashed black line that intersects the position of unstrained $In_{0.35}Ga_{0.65}N$ or $In_{0.37}Ga_{0.63}N$ (red dots) and the fully strained line is referred to as the relaxation line.

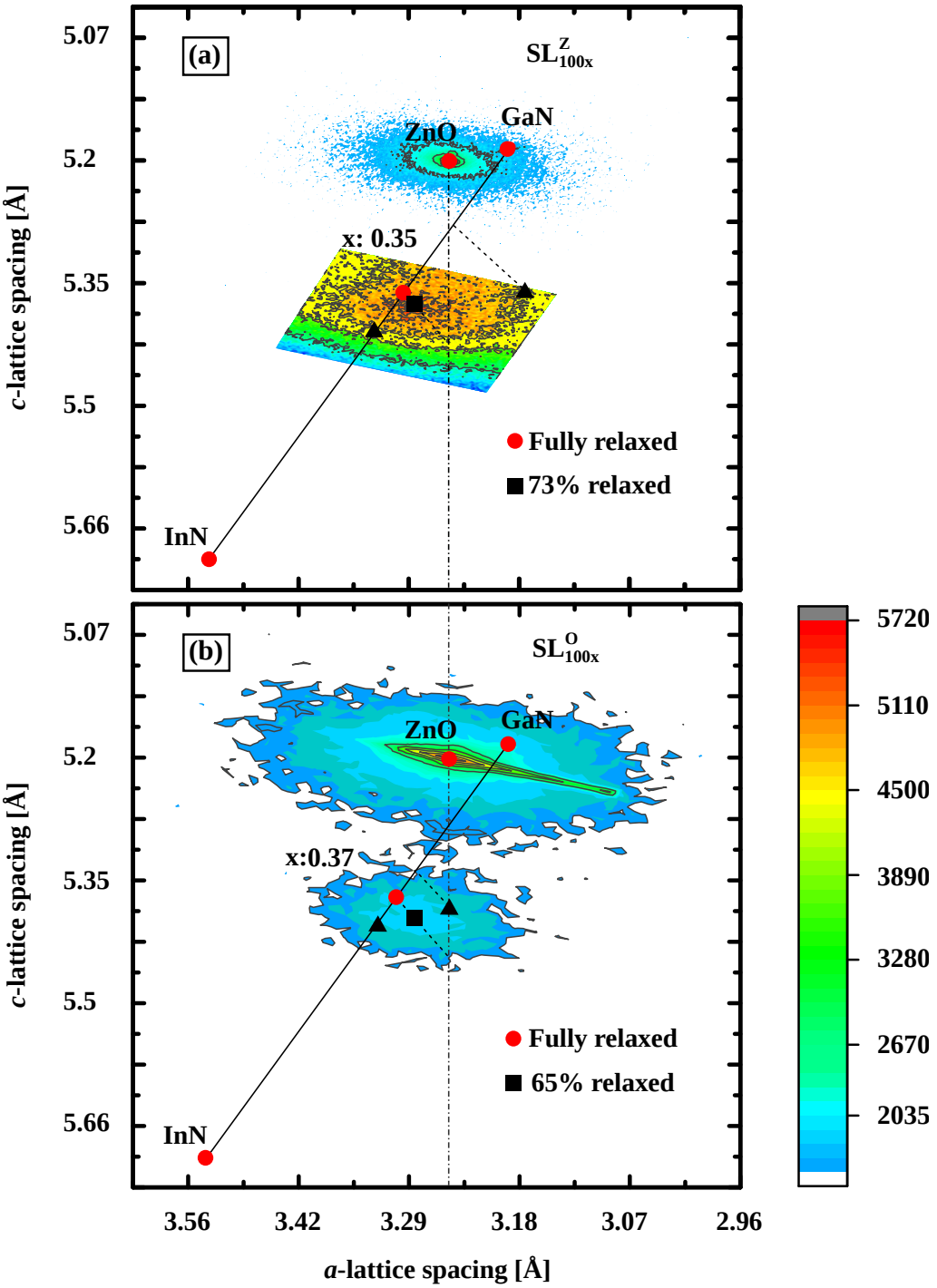

Figure 5.15: XRD: RSM of (In, Ga)N heterostructures on (a) Zn-ZnO and (b) O-ZnO around the $(10\bar{1}5)$ reflex. (a) shows the superposition of two separate maps (a) and (b). Red dots mark the position of fully relaxed ZnO, GaN, $In_{0.37}Ga_{0.63}N$, $In_{0.35}Ga_{0.65}N$ and InN. Black squares mark the position of the maximum intensity of the strained (In, Ga)N. Black dashed-dotted lines mark (In, Ga)N fully partially strained to the ZnO substrate, black dotted lines mark (In, Ga)N of a given indium content with varying degrees of relaxation. All fully relaxed (In, Ga)N layers lie on the black, solid line connecting InN and GaN. The intersection of these two lines corresponds to (In, Ga)N with In-content $x = 0.18$ that is lattice-matched to ZnO. Black triangles are discussed in the text.

Each such line represents (In, Ga)N with a specific composition but with varying degrees of relaxation, depending on its relative position between the position of fully strained and fully relaxed (In, Ga)N, which mark the end points of this line. Thus, this dashed line can be used to determine the degree of relaxation. The angle of the relaxation line was determined following a procedure explained below. The RSM of SL^{O}_{100x} and the composite RSM of SL^{Z}_{100x} both show a peak related to the ZnO substrate. This is the peak with highest intensity, and a second peak of lower intensity, which is attributed to the nominal (In, Ga)N heterostructure. The ZnO peak of SL^{Z}_{100x} sample shows an elliptical shape whereas the ZnO peak of the SL^{O}_{100x} sample has an elongated shape, which is a measurement artifact. Since significant differences in volume of the diffracting epitaxial structures is unlikely, the higher intensity of the heterostructure peak of sample SL^{O}_{100x} suggests that the crystal quality of the SL^{O}_{100x} structure is higher, meaning for example less crystal defects.

Analytical determination of the indium content and the degree of relaxation

The indium content and degree of relaxation can be determined analytically. The result of a reciprocal space map around a reflection (hkil) is usually given in reciprocal lattice units (rlu), they can be converted into *a*- and *c*- lattice spacings. The relation between the a- and c-lattice spacing and the distance $d_{(hkil)}$ of the scattering (hkil) planes, with hkil the Miller indices and $i = -(h + k)$ is given by [172], [173]:

$$\frac{1}{d^2_{(hkil)}} = \frac{4}{3} \cdot \frac{h^2 + h \cdot k + k^2}{a^2} + \frac{l^2}{c^2} \tag{5.3}$$

The relationship between the reciprocal lattice vector q_{hkil} and the distance d_{hkil} of diffracting planes (from which the *a*- and *c*-lattice spacings can be derived) is usually given by $q_{hkil} = \frac{1}{d_{hkil}}$ [174]. The X'Pert Epitaxy software used in this study uses:

$$q_{hkil} = \frac{\lambda}{2 \cdot d_{(hkil)}} \tag{5.4}$$

q_{hkil} is the reciprocal lattice vector in reciprocal lattice units (rlu), which gives:

$$1 = \frac{\lambda^2}{q^2_{hkil}} \left(\frac{h^2 + h \cdot k + k^2}{3 \cdot a^2} + \frac{l^2}{4 \cdot c^2} \right) \tag{5.5}$$

For $d_{(hki0)}$:

$$a_e(\lambda, h, k, q_x) = \frac{\lambda \cdot \sqrt{(h^2 + h \cdot k + k^2)}}{q_{hki0} \cdot \sqrt{3}} \tag{5.6}$$

For $d_{(000l)}$:

$$c_e(\lambda, l, q_z) = \frac{\lambda \cdot l}{q_{000l} \cdot 2} \tag{5.7}$$

With c_e, a_e the *a*- and *c*-lattice spacing measured with the RSM. q_{hki0}, q_{000l} are the reciprocal lattice vectors, sometimes also referred to as q_x, q_z, or $q_{parallel}$ and $q_{orthogonal}$ and λ the wavelength of the X-Ray beam. From the RSM peak positions, the *a*- and *c*-lattice spacings are derived using the Poisson ratio of the ZnO substrate or of the SL structures. The Poisson ratio of (In, Ga)N is interpolated linearly applying Vegard's law and using the values of the Poisson's ratio of GaN ($\nu_{GaN} = 0.183$)[173] and InN ($\nu_{InN} = 0.272$) [173].

$$\nu(x) = \nu_{InN} \cdot x + \nu_{GaN}(1 - x) \tag{5.8}$$

With x the indium content. Poissons ratio relates the unstrained *a*- and *c*-lattice spacing, that can be looked up in literature, to the *a*- and *c*-lattice spacing that are measured experimentally using the RSM. For biaxial strain:

$$\frac{c_e - c_0}{c_0} = \frac{-2\nu}{1 - \nu} \frac{a_e - a_0}{a_0} \tag{5.9}$$

With c_0, a_0 the *a*- and *c*-lattice spacing of unstrained (In, Ga)N. Vegard's law was used to calculate the unstrained *a*- and *c*-lattice spacings of (In, Ga)N neglecting bowing.

$$a(x) = a_{InN} \cdot x + a_{GaN}(1 - x) \tag{5.10}$$

$$c(x) = c_{InN} \cdot x + c_{GaN}(1 - x) \tag{5.11}$$

With $a_{InN} = 3.54$ Å, $c_{InN} = 5.70$ Å, $a_{GaN} = 3.19$ Å, $c_{GaN} = 5.19$ Å (see table 2.1 in chapter 2). Equation 5.9 is solved for c_e and equations 5.6, 5.7, 5.8, 5.10 and 5.11 are plugged in. An analytical solution can be found for the auxiliary function:

$$g(x, c_e, a_e) = c(x) - \frac{-c_e}{\frac{2\cdot\nu(x)}{1-\nu(x)}\frac{a_e - a(x)}{a(x)} - 1} = 0 \tag{5.12}$$

Solving this equation gives the indium content x, which can be used to derive the strain and degree of relaxation.

Using equation 5.12 the indium content and degree of relaxation was determined to be $x = 0.37$ and $R = 66\%$ for SL^{O}_{100x} and $x = 0.36$ and $R = 74\%$ for SL^{Z}_{100x}.

The degree of relaxation R can be calculated using:

$$R = \frac{P_{(In,Ga)N} - P_{ZnO-fs}}{P_{rc} - P_{ZnO-fs}} \times 100 \tag{5.13}$$

With $P_{(In,Ga)N}$ the position of the peak maximum of partially strained (In, Ga)N, and the intersection of the fully strained line with the relaxation line P_{ZnO-fs}. These relationships are exemplary explained for the case of (In, Ga)N grown on GaN in figure 5.16.

Determination of indium content and degree of relaxation graphically

Alternative to an analytic determination, the indium content and degree of relaxation can be determined by sliding the relaxation line along the composition line until the relaxation line intersects the (In, Ga)N peak maximum (see figure 5.16) [175]. This intersection of relaxation line and composition line is referred to as P_{rc}, the ratio:

$$x = \frac{P_{rc} - P_{GaN}}{P_{InN} - P_{GaN}} \tag{5.14}$$

gives the indium content x of the (In, Ga)N layer [175], with P_{rc} minus P_{GaN} the distance between P_{rc} and P_{GaN}, which marks the position of GaN using literature values ($a = 3.19$ Å, $a = 5.19$ Å, see table 2.1 in chapter 2)) and $P_{InN} - P_{GaN}$ the distance between the literature positions of InN marked with P_{InN} ($a = 3.54$ Å, $a = 5.70$ Å) and GaN.

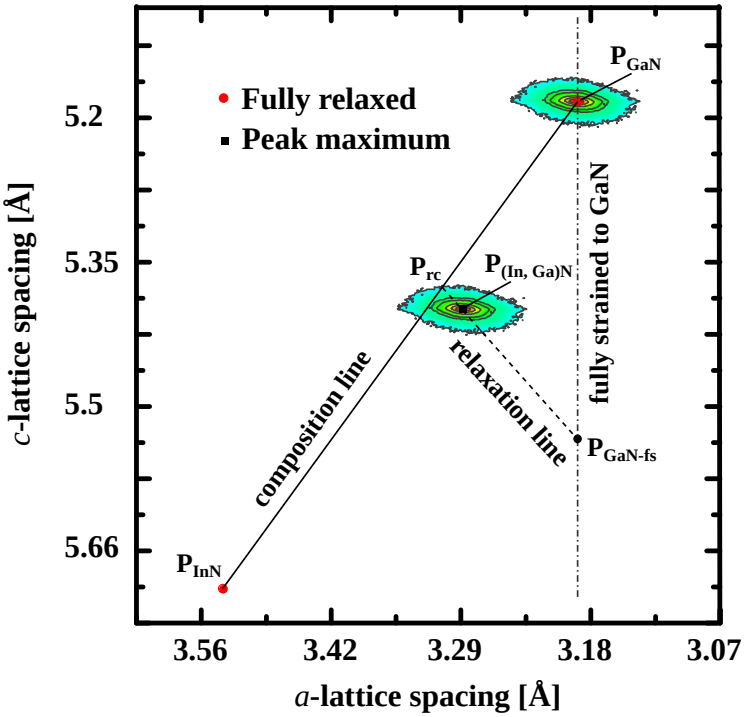

Figure 5.16: Schematic of XRD RSM of (In, Ga)N on GaN. Peak positions marked for GaN (P_{GaN}), InN (P_{InN}) and (In, Ga)N ($P_{(In,Ga)N}$), intersection of relaxation and composition line (P_{rc}) and the intersection of the relaxation line of (In, Ga)N with the line that marks (In, Ga)N that is fully strained to GaN (P_{GaN-fs}).

The angle α between the relaxation line and the fully strained line was determined using the following equation from Pereira *et al.* [176]:

$$\alpha(x) = \arctan\left(\frac{1}{\frac{2\cdot\nu(x)}{1-\nu(x)}}\right) \cdot \tan(\varphi) \cdot \frac{4(h^2+k^2)}{l\sqrt{\frac{4}{3}(h^2+hk+l^2)}} \tag{5.15}$$

This angle is depending on the indium content x. φ is the angle between the surface normal and the (hkl) planes with $\tan(\varphi) = \frac{c}{a}\sqrt{\frac{4}{3}\frac{(h^2+h\cdot k+l^2)}{l^2}}$. Pereira *et al.* derived that equation using equation 5.9.

The indium content of SL^{Z}_{100x} [figure 5.15 (a)] was determined to be $x = 0.35$ with a degree of relaxation of $R = 73\%$. The indium content of SL^{O}_{100x} [figure 5.15 (b)] was determined to be $x = 0.37$ with a degree of relaxation of $R = 65\%$. This results agree well with the results determined analytically and are compared in table 5.4.

Sample	Graphical Analysis		Analytic Analysis	
	x	R	x	R
SL^{Z}_{100x}	0.35	73%	0.36	74%
SL^{O}_{100x}	0.37	65%	0.37	66%

Table 5.4: Indium content x and strain ϵ of samples SL^{Z}_{100x} and SL^{O}_{100x} determined by XRD RSM.

Figure 5.15 (a) and (b) show that the ZnO(10$\bar{1}$5) peaks are more intense and have a smaller full width at have maximum (FWHM) than the heterostructure related peaks, which are rather broad and low in intensity. This broadening might indicate the presence of (In, Ga)N with varying indium contents and strain states. To compare the distribution of indium content between SL^{O}_{100x} and SL^{Z}_{100x} the following procedure was applied: The intensity of the peak maximum I_{SL-max} was determined, color coding was set in a way that the range $I_{SL-\frac{2}{3}max}$ - I_{SL-max} (hereafter referred to as $I_{2/3}$ range) could be distinguished. This range includes intensities between two thirds of the maximum and the maximum value. Black triangles in figure 5.15 (b) (SL^{O}_{100x}) mark the borders of the $I_{2/3}$ range. In case of SL^{Z}_{100x} [figure 5.15 (a)], the upper limit (highest indium content) was determined and marked but the lower limit could not be determined since the RSM does not extend far enough, only an upper estimate for the lower limit could be performed. The scan was not repeated with an increased scan range because the intensity of the peak was already very low (3 days measurement), bigger scan range that would require a smaller integration time would decrease the intensity further and make an analysis less accurate. It is noteworthy that this procedure is supposed to yield a measure for comparison, it is not

intended through this procedure to estimate the full distribution of indium contents. For the sample SL^{O}_{100x} this procedure yielded a range of indium contents and strain states between $x = 0.44$, fully relaxed and $x = 0.3$, fully strained. For SL^{Z}_{100x} the upper limit was determined to be $x = 0.44$, fully relaxed, and the upper estimate of the lower limit was $x = 0.19$ and tensile strained with $\epsilon = 0.02$. (In, Ga)N with $x = 0.19$ is close to being lattice-matched to ZnO. This suggests that the tensile strained (In, Ga)N with $x = 0.19$ is not located at the heterostructure/ZnO interface, because if it was, it would be lattice-matched and therefore not tensile strained. It is probably rather somewhere within the structure after the SL has already started to partially relax and therefore increased its lattice spacing.

Determination of indium content and degree of relaxation using $\omega - 2\theta$ scans

XRD $\omega - 2\theta$ scans around the (0002) reflex were conducted on samples SL^{O}_{100x} (blue), SL^{Z}_{100x} (purple) and bare ZnO (black) to further elucidate their structure (see figure 5.17).

The most intense peak in figure 5.17 is the ZnO (0002) reflex. To its left, at an angle of 33.2 ° there is the (In, Ga)N peak with 35% (SL^{Z}_{100x}) and 37% (SL^{O}_{100x}) indium content of the nominal InN/GaN SL structure. It is reported in literature that enough indium on the surface causes the In(101) reflex at 33 ° (indicated with dashed line in figure 5.17) [177], [178]. Though close to the peak maxima of what is judged to be the (In, Ga)N peak of SL^{O}_{100x} and SL^{Z}_{100x} it is clearly distinct from it. Possible indium on the surface may have contributed though to the lower angle flank of the (In, Ga)N peak. As discussed in chapter 5.3.1, a low density of objects were found on the surface of SL^{Z}_{100x} that may be assumed to be indium. SL^{Z}_{100x} shows clear signs of indium droplets on the surface. A comparison between the intensities of the (In, Ga)N peak of SL^{O}_{100x} (SL^{Z}_{100x}) and the ZnO(0002) peak shows that the intensity of ZnO(0002) is about 2 (4) orders of magnitude more intense. This difference in intensity of the (In, Ga)N peak of SL^{O}_{100x} (SL^{Z}_{100x}) was already addressed in the previous RSM section. One more feature can be distinguished at 22.2° that is in agreement with the expected position of the first satellite peak SL_{-1} of the SL^{O}_{100x} (SL^{Z}_{100x}) structure but also shows up in the measurement of bare ZnO. Superimposing all three measurement curves in a way, so that the intensity within the range 8° to 12° matches, shows that they all have a very similar intensity evolution (not shown here), therefore there may not be a satellite peak and no indication for a possible presence of a periodic structure in SL^{O}_{100x} (SL^{Z}_{100x}).

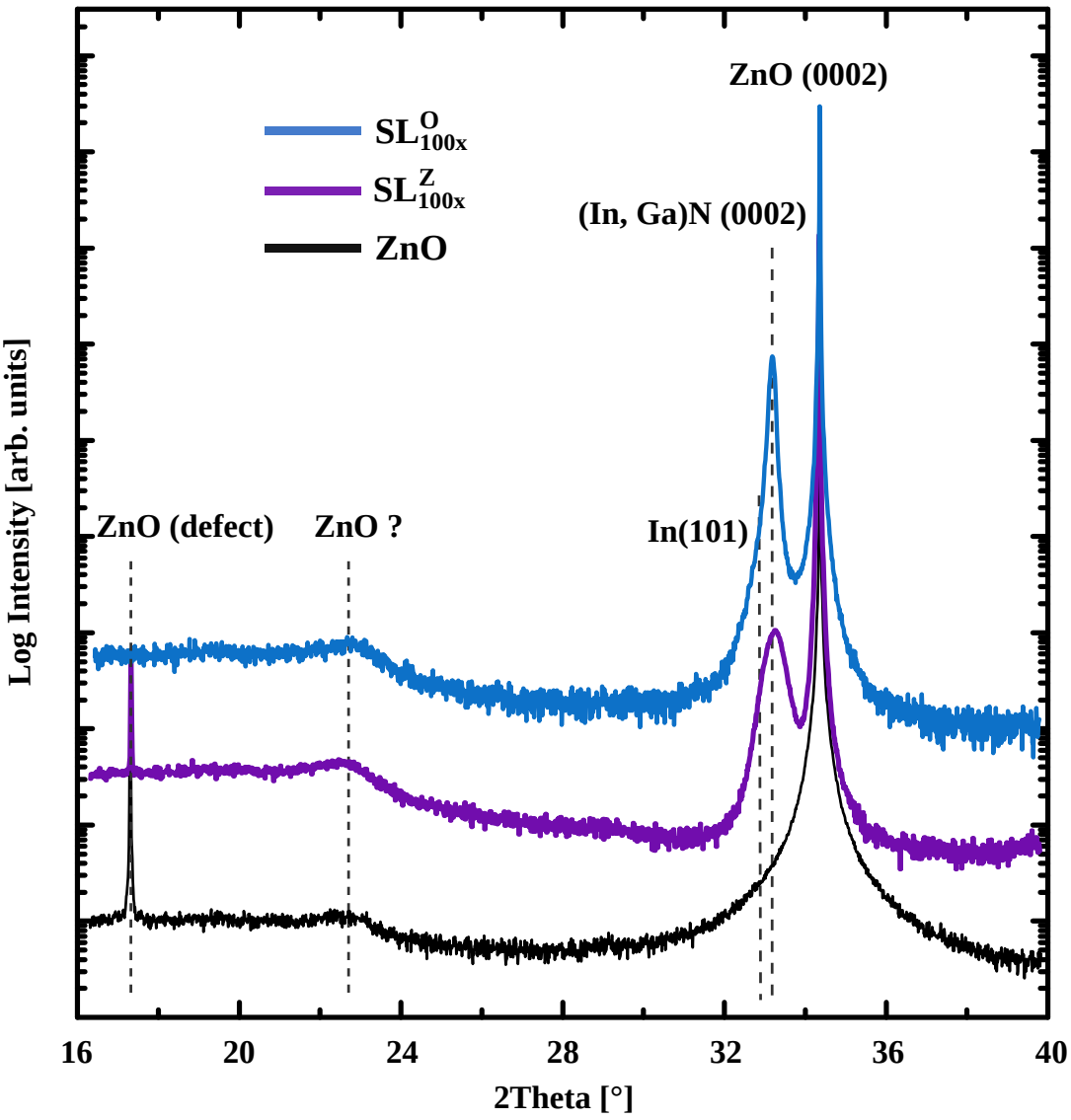

Figure 5.17: XRD $\omega - 2\theta$ scans around the (0002) reflex of SL^{O}_{100x} (blue), SL^{Z}_{100x} (purple) and bare ZnO (black). Guides to the eye were added to indicate In(101), (In, Ga)N peak and a broad ZnO related peak. Some of the XRD acquisition done by Dr- C. Chèze.

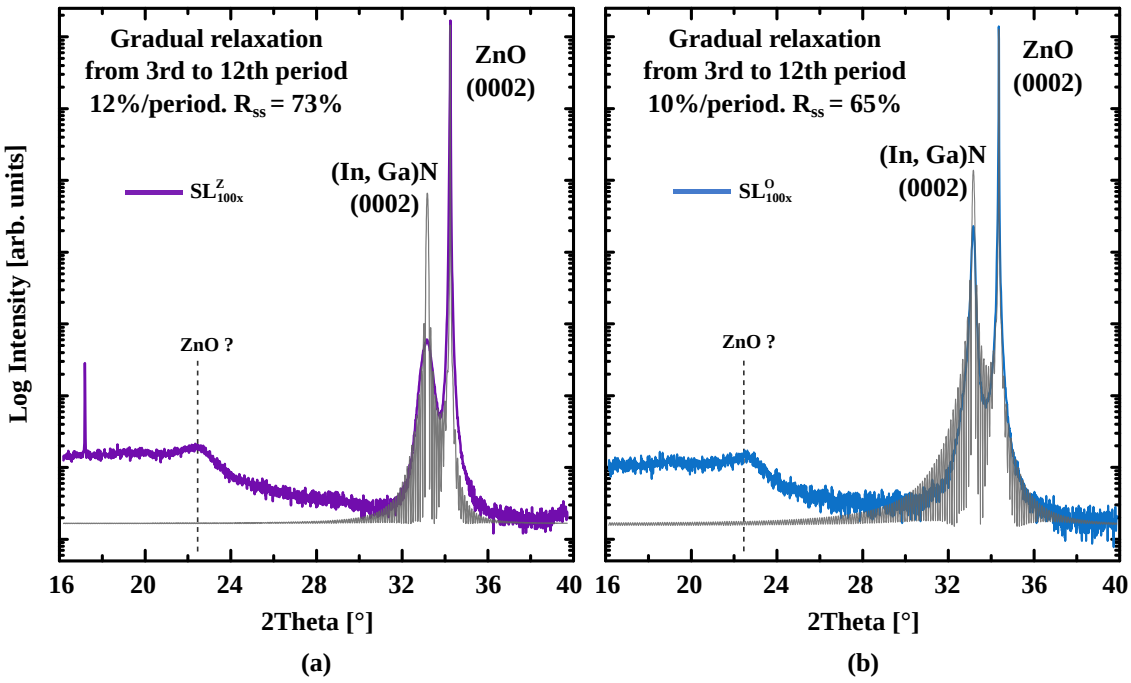

Figure 5.18: XRD $\omega - 2\theta$ scan around the (0002) reflex of (a) SL^{Z}_{100x} (purple) and (b) SL^{O}_{100x} (blue). Fitting curves are given in grey color. Using (In, Ga)N as a fitting structure for (a) SL^{Z}_{100x} with $x = 0.33$ and gradual relaxation of 12%/3 MLs of deposited material (referred to as 1 period) from 3rd period to the 12th period with final, steady state relaxation of $R_{ss} = 73\%$ and (b) SL^{O}_{100x} with $x = 0.35$ and gradual relaxation of 10%/period from 3rd period to the 12th period with final, steady state relaxation of $R_{ss} = 65\%$. XRD acquisition by Dr- C. Chèze.

The intensity of the fitting curves was normalized to fit the intensity of the measured ZnO (0002) peak. The structure of sample SL^{Z}_{100x} was fitted with (In, Ga)N with $x = 0.33$ [figure 5.18 (a)]. A gradual strain relaxation of 12% per 3 MLs of deposited material (referred to as 1 period) was assumed from the 3rd to the 12th period. Beyond the 12th period a steady state degree of relaxation of $R_{ss} = 73\%$ was assumed (further discussed in the RHEED section 5.3.2). The intensity of the simulated (In, Ga)N peak exceeds the experimental value by a factor of 100, which may indicate the imperfection of the structure, like interface roughness, defects, etc.

The SL^{O}_{100x} structure was fitted assuming (In, Ga)N with $x = 0.35$ (see figure 5.18 (b)). The experimental data was fitted with a gradual strain relaxation of 10% per period from the 3rd to the 12th period. Beyond the 12th period there was no more relaxation but instead a constant average lattice spacing and a final steady state relaxation $R_{ss} = 65\%$ was assumed. For SL^{O}_{100x} the intensity of the simulated (In, Ga)N peak exceeds the experimental value by a factor of 5, which is considerably lower than the value found for SL^{Z}_{100x}. Also the (In, Ga)N peak of SL^{O}_{100x} is narrower, both of these findings show that SL^{O}_{100x} might have a narrower range of composition (as already indicated by RSM) and an overall better crystalline quality.

5.3.4 Investigation of the chemical composition and strain by Raman spectroscopy

The measurements for this study were conducted with a HORIBA LabRAM HR Evolution in backscattering geometry. The scattered light was not analyzed for its polarization. A frequency doubled Ar-ion laser was used with a wavelength of 244 nm, a solid state laser was used for laser light of wavelength 405 nm. The scattered light was detected by a charge-coupled device that was cooled with LN_2.

Dependence of phonon frequency on strain and indium content in (In, Ga)N

Prior to presenting the findings of the Raman spectroscopy investigations it is necessary to recall how the phonon frequencies depend on the strain ϵ and indium content x. The frequency of A_1(LO) and E_2^H phonon modes shifts depending on the strain state and the indium content of the (In, Ga)N layer and can be approximated by [179], [180]:

$$\omega^{(In,Ga)N} = \omega_0^{GaN} + \Delta\omega_0(x) + \Delta\omega(\epsilon) \tag{5.16}$$

With ω_0^{GaN} the phonon frequency of unstrained GaN, $\Delta\omega_0(x)$ and $\Delta\omega(\epsilon)$ the shift in phonon frequency due to the alloying with indium and strain, respectively. The A_1(LO) phonon modes exhibit a linear dependence on the indium content x in unstrained (In, Ga)N [181], the E_2^H will be approximated to have a linear dependence on the indium content, even though its dependence shows a slight bowing [180]. Taking the values $A_1(LO)(GaN/InN)$ and $E_2(H)(GaN/InN)$ from Harima *et al.* [182], we estimated for both phonon modes the dependence of the frequency on the In content. A linear approximation is used:

$$\Delta\omega_0^{A_1}(x) = [A_1(LO)(GaN) - A_1(LO)(InN)] \cdot x\, cm^{-1} = -148 \cdot x\, cm^{-1} \tag{5.17}$$

$$\Delta\omega_0^{E_2}(x) = [E_2(H)(GaN) - E_2(H)(InN)] \cdot x\, cm^{-1} = -79.6 \cdot x\, cm^{-1} \tag{5.18}$$

The value $\Delta\omega_0^{A_1}(x)$ = -148 cm^{-1} is close to -149 cm^{-1}, which was calculated through a dynamical model by Correia *et al.*[181]. The value $\Delta\omega_0^{E_2}(x)$ = -79.6 cm^{-1} is similar to -77.9, which was derived from a plot of Oliva *et al.* [180]. The strain dependence of the A_1(LO) and E_2^H modes in case of biaxial strain can be approximated [183], [180] by:

$$\Delta\omega(\epsilon) = a(\epsilon_{xx} + \epsilon_{yy}) + b \cdot \epsilon_{zz} = 2 \cdot a \cdot \epsilon_{xx} - 2 \cdot b\frac{C_{13}}{C_{33}} \cdot \epsilon_{xx} = K_\perp \cdot \epsilon_{xx} \tag{5.19}$$

With a and b being phonon deformation potentials, ϵ_{xx}, ϵ_{yy} and ϵ_{zz} being the stress tensors, C_{13} and C_{33} being the elastic constants. With $K_\perp^{A_1}$ and $K_\perp^{E_2}$ being the $K_\perp$ for the A_1(LO) and E_2(H) of GaN [184]:

$$\Delta\omega^{A_1}(\epsilon) = -885 \cdot \epsilon_{xx}\, cm^{-1} \tag{5.20}$$

$$\Delta\omega^{E_2}(\epsilon) = -1115 \cdot \epsilon_{xx}\, cm^{-1} \tag{5.21}$$

The phonon frequency $\omega^{(In,Ga)N}$ in equation 5.16 can be determined experimentally through Raman spectroscopy. Using equations 5.16 to 5.21, we obtain two linear equations for two phonon modes A_1(LO) and E_2(H) according to equation 5.16. This gives two equations with two unknown variables, from which the strain ϵ and the indium content x can be determined.

Determination of strain and indium composition of (In, Ga)N heterostructures

Figure 5.19 presents the Raman spectra of SL^{Z}_{10x} [figure 5.19 (a), orange], SL^{Z}_{100x} [figure 5.19 (b), purple] and SL^{O}_{100x} [figure 5.19 (c), blue]. Guides to the eye were added to indicate the frequencies of several InN, GaN, ZnO and (In, Ga)N related phonon modes [182]. Measurements were conducted using two different laser excitation wavelengths λ_{405} and λ_{244}. Several features can be distinguished and are attributed to the A_1(LO) or E_2^H of ZnO or (In, Ga)N. The Raman spectra show a clear difference depending on the used wavelength of the laser light. Both samples SL^{O}_{100x} and SL^{Z}_{100x} (which amounts to approximately 80 nm thickness) do not show ZnO related phonon modes when laser light with λ_{244} was used, which indicates that the optical probing depth was smaller than d the thickness of the (In, Ga)N heterostructure. This is confirmed by calculations using the Lambert-Beer law, plotted in figure 5.20, and showing that for $2 \cdot d = 160$ nm path length (incoming and outgoing light) the light intensity has decreased by over 95%. In contrast to SL^{O}_{100x} and SL^{Z}_{100x}, SL^{Z}_{10x} shows a weakened A_1(LO) line from ZnO [see figure 5.19 (a)].

Using λ_{405}, all samples show the ZnO A_1(LO) mode and the ZnO E_2^H mode. Since laser light with λ_{405} penetrates deeper into the sample, measurements using this wavelength will give values for indium content x and strain ϵ that are closer to the average values of the (In, Ga)N heterostructure. Measurements using λ_{244} will emphasize more the upper parts of the (In, Ga)N heterostructures. If the indium content is higher for λ_{244} than for λ_{405} it would be an indication of composition pulling effect.

None of the Raman spectra in figure 5.19 exhibit a peak that can be assigned to the GaN A_1(LO) or E_2^H modes, which means that Raman spectroscopy does not give any indication of the existence of GaN in the (In, Ga)N heterostructure of these samples. This is true for all laser excitation energies used.

The phonon frequency was determined by fitting one or multiple Voigt curves to the Raman spectra. In the latter case several peak positions were extracted that are assumed to belong either to distinct (In, Ga)N phases with different indium composition and strain or in case of the A_1(LO) peak to a so-called S-peak [185], [186], [182]. Sample SL^{Z}_{10x}, probed with λ_{405}, does not show any indication of InN or (In, Ga)N (compare spectra of SL^{Z}_{10x} (orange) and bare ZnO (black) in figure 5.19 (a)), this might be due to the small scattering volume given by the small thickness of the epitaxial layer. Probing with λ_{244} reveals a peak that correlates with the A_1(LO) of (In, Ga)N, though no E_2^H peak was detected. Therefore, it is not possible to determine the chemical composition or the strain in this sample.

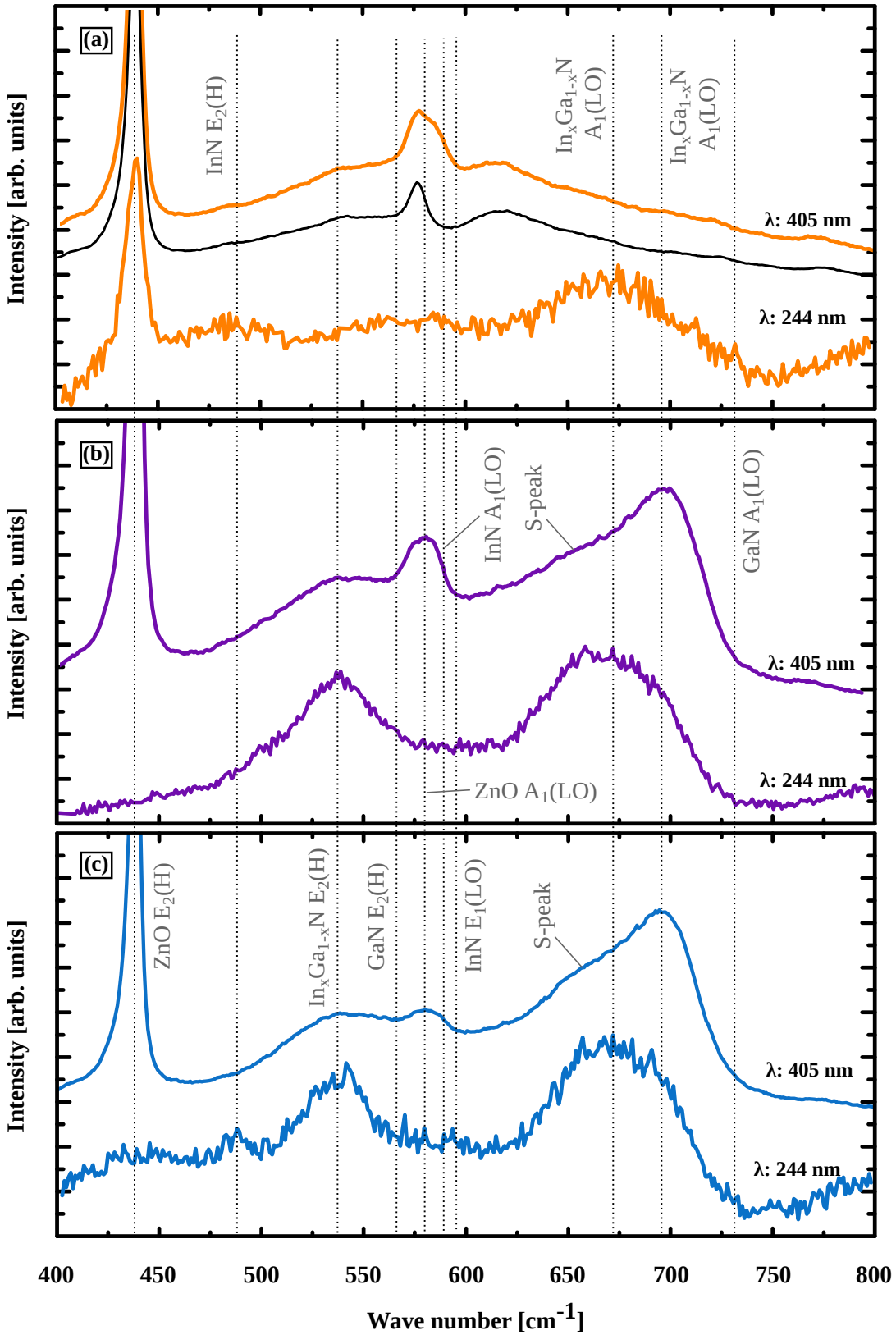

Figure 5.19: Raman spectra from samples a) SL^{Z}_{10x}, b) SL^{Z}_{100x}, c) SL^{O}_{100x}, using laser excitation wavelengths λ_{405}, and λ_{244}. The vertical dotted lines indicate literature values for InN, GaN and ZnO phonon frequencies. The Black curve in c) represents the Raman spectrum of a bare ZnO substrate. Raman spectroscopy measurements were conducted by Dr. Manfred Ramsteiner.

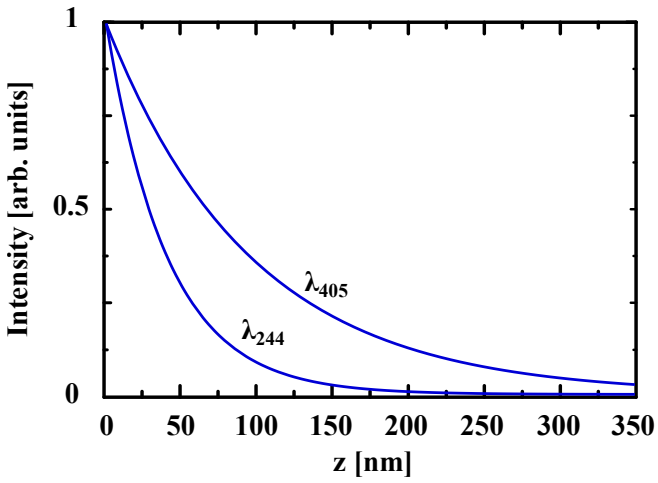

Figure 5.20: Attenuation of light in (In, Ga)N with $x = 0.35$ as a function of penetration depth z for two different wavelengths λ_{405} and λ_{244}. The absorption constant was taken from

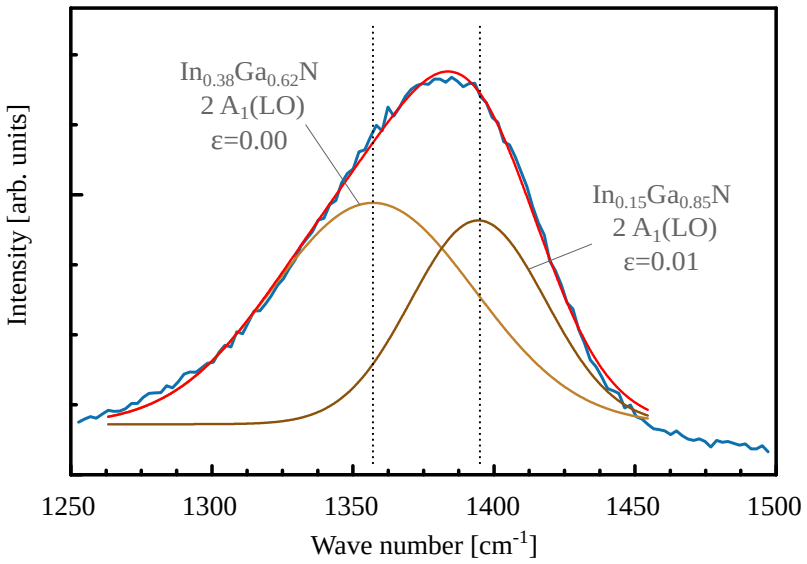

Figure 5.21: Raman spectrum of SL^{O}_{100x} for scattered laser light with excitation wavelength λ_{405} on SL^{O}_{100x}. The 2 A_1(LO) peak from second-order Raman scattering was fitted by two Voigt curves, their superposition is the red curve. The following color codes were used: 2 A_1(LO) of $In_{0.38}Ga_{0.62}N$ with average indium content of the sample in light brown and $In_{0.15}Ga_{0.85}N$ 2 A_1(LO) with low indium content and increased intensity by resonance effect in dark brown. Raman spectroscopy measurements were conducted by Dr. Manfred Ramsteiner.

Sample	E_{Exc}	E_2^H (average x)	S-peak	A_1(LO) (average x)	A_1(LO) (low x)
SL^Z_{100x}	244 nm	534 cm^{-1}		664 cm^{-1}	
SL^Z_{100x}	405 nm	545 cm^{-1}	656 cm^{-1}	688 cm^{-1}	708 cm^{-1}
SL^O_{100x}	244 nm	537 cm^{-1}		671 cm^{-1}	
SL^O_{100x}	405 nm	538 cm^{-1}	650 cm^{-1}	679 cm^{-1}	702 cm^{-1}

Table 5.5: Peak positions of Raman scattering modes E_2^H, A_1(LO) and S-peak of samples SL^Z_{100x} and SL^O_{100x} depending on used laser excitation wavelength E_{Exc}. "average x" refers to (In, Ga)N with average indium content and average strain of the sample; "low" refers to (In, Ga)N with low indium content.

The origin of the S-band is still under debate. Correia *et al.* link this S-peak to poor crystalline quality of the (In, Ga)N layer, and claim that defects in the (In, Ga)N layer induce disorder activated phonon scattering [181]. There are also reports that suggest that this S-peak may be related to regions near to the sample surface, since this peak vanishes after surface etching [188].

The S-peak intensity relative to the E_2^H intensity is highest when the degree of alloy disorder is maximum - which is for (In, Ga)N the case for intermediate indium contents. The Raman peak originating from second-order scattering by A_1(LO) phonon modes is not distorted by the superposition with the so-called S-peak, as exemplary shown for SL^O_{100x} in figure 5.21. The 2 A_1(LO) peak was fitted with two Voigt curves. One with a maximum at 1357 cm^{-1} [corresponding to 685 cm^{-1} for 1 A_1(LO)] represents the (In, Ga)N phase with average indium content and strain (light brown curve in figure 5.21) the other curve (dark brown) with a maximum at 1394 cm^{-1} (corresponding to 703 cm^{-1} for 1 A_1(LO)) represents a second (In, Ga)N phase with a lower indium content. The frequency of the 2 A_1(LO) mode is slightly more than twice the value of the 1 A_1(LO). This phenomenon was already reported for example for GaN [192], [193]. The existence of low indium content (In, Ga)N phases will be discussed later.

Figure 5.22 displays the first-order Raman spectra of SL^Z_{100x} and SL^O_{100x}. In order to extract the peak positions of the E_2^H and A_1(LO) phonon modes, the spectra were fitted by five Voigt curves for the following contributions: E_2^H of (In, Ga)N with average indium content of sample (light orange), A_1(LO) of ZnO (grey), S-peak (pink), A_1(LO) of (In, Ga)N with average indium content of sample (light brown), (In, Ga)N A_1(LO) with low indium content and increased intensity by resonance effect (dark brown). The resulting peak positions (see table 5.5) were used to determine the In content x and the strain ϵ in the (In, Ga)N layer using equations 5.16 to 5.21.

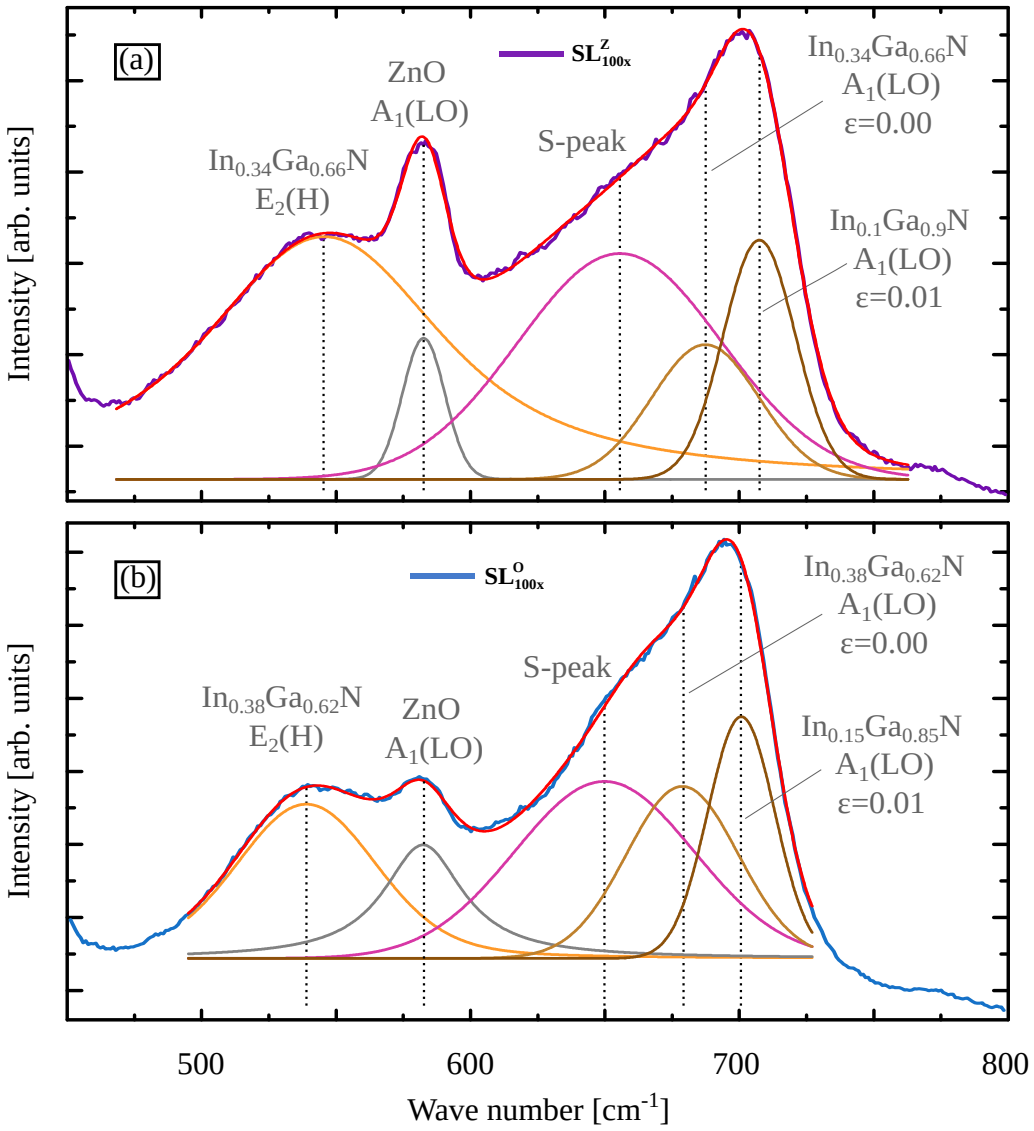

Figure 5.22: Raman spectra from samples (a) SL^{Z}_{100x} and (b) SL^{O}_{100x} with excitation wavelength λ_{405} on. Raman spectra were fitted with Voigt curves, the superposition of the Voigt fit curves is given as a red curve, guides to the eye were added for Voigt fit-curve maxima. The following color codes were used: E_2^H of (In, Ga)N with average indium content of sample (light orange), A_1(LO) of ZnO (grey), S-peak (pink), A_1(LO) of (In, Ga)N with average indium content of sample (light brown), (In, Ga)N A_1(LO) with low indium content and increased intensity by resonance effect (dark brown). Raman spectroscopy measurements were conducted by Dr. Manfred Ramsteiner.

Sample	Method	x	ϵ
SL^{Z}_{100x}	Raman (244 nm)	0.51	-0.01
SL^{Z}_{100x}	Raman (405 nm)	0.33	-0.00
SL^{Z}_{100x}	XRD	0.35	-0.01
SL^{O}_{100x}	Raman (244 nm)	0.47	-0.01
SL^{O}_{100x}	Raman (405 nm)	0.38	-0.00
SL^{O}_{100x}	XRD	0.37	-0.01

Table 5.6: Indium content x and strain ϵ of samples SL^{Z}_{100x} and SL^{O}_{100x} determined by Raman spectroscopy and XRD RSM.

For SL^{Z}_{100x} and laser excitation wavelength λ_{405} this resulted in $x = 0.33$ and $\epsilon = 0.00$, which compares well with the XRD RSM results $x = 0.35$ and $\epsilon = -0.01$ (see table 5.6).

Using laser excitation wavelength of λ_{405}, an indium content of $x = 0.38$ and strain $\epsilon = 0.00$ is found for sample SL^{O}_{100x}, which compares rather well with the XRD RSM results $x = 0.37$ and $\epsilon = -0.01$ (see table 5.6). It also fits to the *a*-lattice spacing evolution determined by RHEED which showed a final oscillation around the value of 3.3 Å, which corresponds to $x = 0.37$ and $\epsilon = -0.01$.

For both samples SL^{Z}_{100x} and SL^{O}_{100x} the A_1(LO) mode of ZnO was detected at 582 cm^{-1}.

Comparing the (In, Ga)N A_1(LO) peak shape in literature with the findings of this study, for λ_{405} it was found that there is a similarity of peak shape for $x = 0.36 - 0.60$ [191], $x = 0.37$ [190], $x = 0.33$ [180], $x = 0.30$ [189] and , $x = 0.24 - 0.29$ [189], most of these results compare rather well with the findings of the average indium content shown in table 5.6.

The frequencies of the A_1(LO) mode of 702 cm^{-1} (SL^{O}_{100x}) and 708 cm^{-1} (SL^{Z}_{100x}) (see figure 5.22 and table 5.5) are attributed to a low indium content (In, Ga)N phase for which the fundamental band gap energy is close to the photon energy of the incoming light when using excitation λ_{405}. In this case, Raman scattering by LO phonon modes is strongly enhanced via the so-called forbidden Fröhlich scattering mechanism [195], [191], [196], [197]. This resonant Raman scattering process leads to a selective enhancement of that (In, Ga)N fraction which approximately fulfills the resonance condition.

Using equation 5.16 the indium content and strain of these phases were estimated to be $x = 0.1$, $\epsilon = 0.01$ (SL^{Z}_{100x}) and $x = 0.15$, $\epsilon = 0.01$ (SL^{O}_{100x}). Their band gap depending on x and ϵ was determined using:

$$E_{gap}(x, \epsilon) = x \cdot E^{InN}_{gap} + (1 - x)E^{GaN}_{gap} - b \cdot x(1 - x) - s \cdot \epsilon \tag{5.22}$$

With the bowing parameter $b = 1.595$ eV [179], and the strain correction constant $s = 0.8$ eV [179]. This resulted in a band gap of $E_{gap} = 3.03$ eV (SL^{Z}_{100x}) which is very close to the laser excitation energy of 3.06 eV. For SL^{O}_{100x} a band gap of $E_{gap} = 2.83$ eV was determined. These results might substantiate the findings of the RSM investigations which showed, that within the $I_{2/3}$ range a distribution of indium contents was found ranging from $x = 0.30$ to $x = 0.44$ for SL^{O}_{100x} and from $x = 0.19$ to $x = 0.44$ for SL^{Z}_{100x}. This suggests that the relative volume of low indium content (In, Ga)N (relative to the total volume of the deposited (In, Ga)N heterostructure) might be greater in SL^{Z}_{100x} than in SL^{O}_{100x}. The contribution of the resonance effect may be evaluated using an approximation proposed by Oliva *et al.* [180].

For the intended growth of 1 ML InN embedded in a GaN matrix grown on a GaN(0001) templatete, it was reported that there is a discrepancy between the nominal structure and experiments. Instead of InN (In, Ga)N with a maximum indium content of $x = 0.33$ formed [36], [160]. It was proposed that strain, introduced by the GaN substrate might be the limiting factor. Duff *et al.* investigated the deposition of InN and (In, Ga)N on GaN via density functional theory calculations and found that there is no growth window for InN on GaN [37]. For growth of InN on $In_{0.25}Ga_{0.75}$N the window widened considerably and was closer to common growth conditions for InN and (In, Ga)N. This findings substantiate the possible role that strain plays when it comes to the incorporation of indium into (In, Ga)N. InN and GaN have a lattice mismatch of about 11%. In this study the role of strain on the incorporation of indium into (In, Ga)N was investigated and therefore nominal structures of InN/GaN were grown on ZnO. The lattice mismatch between InN and ZnO is about 9% and therefore slightly lower than the one between InN and GaN. There are no indications that either SL^{O}_{100x} or SL^{Z}_{100x} is composed of a SL-like structure as explained in section 5.3.3. The indium content of SL^{O}_{100x} was determined to be $x = 0.38$ (Raman, λ_{405}) to $x = 0.37$ (XRD RSM) at average. Due to a possible composition gradient along the growth direction this average indium content might even be as high as $x = 0.47$ (Raman, λ_{244}) in the upper part of the SL-structure. The probing of different volumes of the sample was possible due to the difference in penetration depth of light in matter depending on the excitation wavelength λ. Similar results were found for sample SL^{O}_{100x} for which the average indium content increased from $x = 0.33$ (Raman, λ_{405}), $x = 0.35$ (XRD RSM) to $x = 0.51$ ((Raman, λ_{244})). These results indicate that there might be a composition pulling effect that leads to a composition gradient along the growth direction. Results from XRD and Raman investigations further suggest that there is a wide range of distribution of indium content. Possibly the indium content does not only increase along the growth direction but also oscillates along the growth direction between higher indium content (In, Ga)N phases to lower indium content (In, Ga)N phases.

5.3.5 Investigation of the optical properties

As demonstrated above by means of XRD, RHEED and Raman spectroscopy the grown heterostructures are not fully strained but partially relaxed. This relaxation proceeds through glide or creation and introduction of new dislocations. Dislocations can act as non-radiative centers of recombination for electrons and holes. Thus, they can decrease the efficiency of optical emission. Therefore besides investigating the crystalline structure, chemical composition and strain, it is also important to probe the optical properties of the heterostructures. For this purpose photoluminescence spectroscopy was conducted on ZnO substrates and the heterostructures SL^{Z}_{100x}, SL^{Z}_{10x} and SL^{O}_{100x}. The results are shown in figure 5.23. All measurements were conducted at $T = 10$ K.

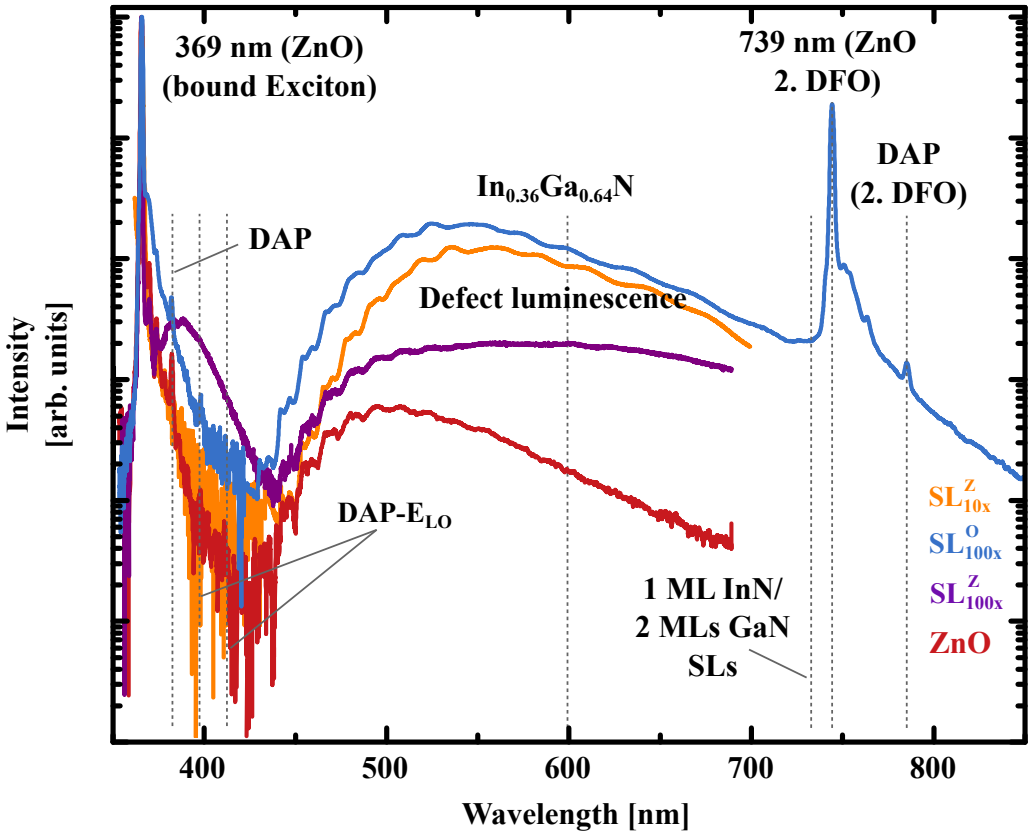

Figure 5.23: Photoluminescence emission spectra of ZnO (red), SL^{Z}_{100x} (purple), SL^{Z}_{10x} (orange) and SL^{O}_{100x} (blue). Guides to the eye were added to indicate the emission caused by donor acceptor pairs (DAP) and related phonon replica ($DAP - E_{LO}$), $In_{0.36}Ga_{0.64}N$, 1 ML InN/2 MLs GaN and the second diffraction orders of the ZnO bound exciton recombination and the DAP. PL measurements were conducted at $T = 10$ K by Dr. Felix Feix.

All samples exhibit an intense emission at 369 nm (3.36 eV) (figure 5.23) which is attributed to a bound exciton recombination [202]. It is still under debate whether the excitons in question are bound to donors or acceptors [203], [204], [205]. The second diffraction order (caused by the diffraction grading of the monochromator) of the emission at 369 nm is present at 739 nm. There is a wide emission band ranging from about 430 nm to 800 nm. Reynolds *et al.* investigated the so-called yellow emission band in GaN (430 nm to above 619 nm (end of measurement)) and the green emission band in ZnO (495 nm to above 619 nm (end of measurement)) [206]. Reshchikov *et al.* and Skirant *et al.* both found a yellow luminescence band in ZnO ranging from about 430 nm to 800 nm [203], [207]. Reshchikov *et al.* propose, that this green-yellow luminescence in ZnO is caused by Zn vacancies [203] similarly to Reynolds *et al.* who proposed that the yellow luminescence in GaN is caused by gallium vacancies [206] (in both cases metal vacancies). Comparing the broad emission bands of ZnO and SL^{Z}_{100x} and SL^{O}_{100x} shows that the band is red-shifted for SL^{Z}_{100x} and SL^{O}_{100x} compared to ZnO. This might indicate that the broad band of SL^{Z}_{100x} and SL^{O}_{100x} is composed of both the ZnO related green defect luminescence and the (In, Ga)N related yellow luminescence.

Figure 5.23 shows that for both samples SL^{Z}_{100x} and SL^{O}_{100x} there is emission between about 370 nm and 450 nm that differs from the emission spectrum of ZnO, whereas SL^{Z}_{10x} differs only in the defect related luminescence from the bare ZnO substrate. Within this broad band there is a narrow peak at 386 nm, which may be attributed to a donor-acceptor-pair (DAP) [202] of ZnO and correlates with a peak of higher intensity at the same position in the ZnO spectrum. There are faint peaks, that might possibly be noise, in the ZnO spectrum at 398 nm and 410 nm that correlate with the first and second phonon replica of the DAP emission. The energy of these phonon replicas is 72 meV in ZnO [202]. If that broad emission band was attributed to unstrained (In, Ga)N with various indium contents, the range of indium contents x would span from $x = 0.03$ to $x = 0.12$. Guides to the eye were added in figure 5.23 to indicate the emission wavelength of bulk $In_{0.36}Ga_{0.64}N$ and predicted 1 ML InN/2 MLs GaN SLs [33].

This would mean that no heterostructure related emission besides the possible defect related yellow luminescence was observed.

5.4 Summary

It was demonstrated that the critical layer thickness for relaxation of InN grown on ZnO is dependent on the GR (on O-ZnO) and the ZnO-polarity. Thin layers of InN can be grown pseudomorphically on Zn-ZnO up to a critical layer thickness of 1.7 MLs (GR: 0.2 ML/s). On O-ZnO no pseudomorphic growth was observed but up to a total thickness of 1.2 MLs (with GR: 0.2 MLs/s) InN can be grown with little relaxation. On O-ZnO there is a trend of increasing critical layer thickness with decreasing GR. The onset of formation of 3D structures is in all cases close to the onset of main relaxation. The formation of 3D structures comes with back etching of the ZnO substrate and creation of hexagonal pits that penetrate several nanometers into the ZnO substrate.

Pseudo-substrates composed of 1.2 MLs InN on O-ZnO and 1.5 MLs InN on Zn-ZnO were grown to investigate the deposition of GaN. Growing GaN on 1.2 MLs InN/O-ZnO led to immediate relaxation of GaN. Therefore no pseudomorphic growth could be established on this polarity. Simultaneously to the onset of GaN relaxation 3D structures formed. GaN deposited on 1.5 MLs InN/Zn-ZnO was grown pseudomorphically up to a thickness of 1.6 MLs GaN before it started to relax and possibly intermix with InN to form (In, Ga)N. The formation of 3D structures started at 3.1 MLs of deposited GaN.

The growth of (In, Ga)N heterostructures (nominally 100x(1 ML InN/2 MLs GaN)) was investigated. XRD $\omega - 2\theta$ scans did not indicated the presence of a periodic SL structure for SL^{O}_{100x} nor for SL^{Z}_{100x}, but instead (In, Ga)N. The best fit was reached assuming (In, Ga)N with $x = 0.33$ (SL^{Z}_{100x}) and $x = 0.35$ (SL^{O}_{100x}). The chemical composition and degree of relaxation was also determined by XRD RSM to be $x = 0.37$, $R = 65\%$ for SL^{O}_{100x} and $x = 0.35$, $R = 73\%$ for SL^{Z}_{100x}. Similar results were found using Raman spectroscopy, $x = 0.38$, $R = 95\%$ for SL^{O}_{100x} and $x = 0.34$, $R = 83\%$ for SL^{Z}_{100x}. RHEED investigations suggest that there might be progressive strain relaxation starting around the 3rd period and ending after the 12th period. Both the results from XRD RSM and Raman spectroscopy suggest that there is (In, Ga)N with a distribution of indium contents, with a greater variance for sample SL^{Z}_{100x}. Furthermore, there might be a composition gradient along the growth direction, as indicated by Raman spectroscopy conducted with two different laser excitation wavelengths λ_{244} and λ_{405}. No clear indication of heterostructure related PL emission besides the defect related yellow luminescence was observed.

6 Results: Growth of (In, Ga)N heterostructures on (In, Ga)N pseudo substrates

In the previous chapter strain engineering was attempted by using ZnO as a more lattice matched substrate to InN compared to GaN. In this chapter, partially relaxed (In, Ga)N pseudo-substrates are tested as substrate. This will not only show the effect of the strain on the indium incorporation into (In, Ga)N heterostructures, but also the effect of the chemical bonds at the substrate-epilayer interface when comparing the results of the SPSLs/ZnO with the ones of SPSLs/(In, Ga)N.

6.1 Growth of (In, Ga)N heterostructures on (In, Ga)N pseudo substrates

Prior to the growth of the (In, Ga)N buffer, 95 nm of GaN was deposited on the GaN/Sapphire substrate to overgrow possible surface defects. GaN was grown at 690 °C with gallium-rich conditions with a gallium flux of 13 nm/min and a nitrogen flux of 9.8 nm/min. Subsequently 300 nm (In, Ga)N buffer were grown at 608 °C under group-III rich conditions with a gallium flux of 6.3 nm/min and an indium flux of 8 nm/min. Subsequently, 100 periods of nominally 1 ML InN and 2 MLs GaN were deposited at 450 °C with a nitrogen flux of 2.85 nm/min, an indium flux of 2.6 nm/min and a gallium flux of 2.8 nm/min. This sample will be referred to as SP^{I}_{100x}.

6.1.1 Investigation of the surface morphology

Contrary to SL^{Z}_{100x} and SL^{O}_{100x} there was no indication of indium or gallium droplets on top of the surface of SL^{I}_{100x}, as it is demonstrated by investigations with optical microscope shown in figure 6.1 (a) and (b). Thus, SL^{I}_{100x} was not grown under indium-rich growth conditions, but probably N-rich conditions, close to stochiometry.

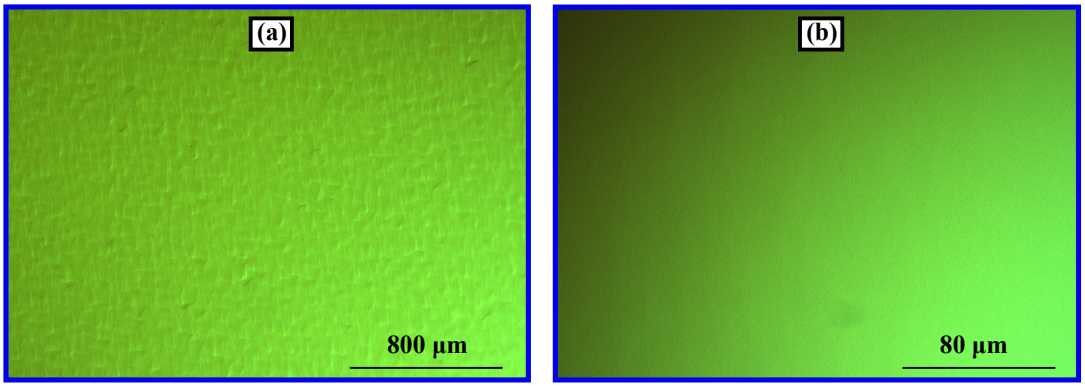

Figure 6.1: Surface of SL^{I}_{100x} investigated with optical microscope and magnification of (a) 5x and (b) 50x.

Figure 6.2 shows the results of AFM investigations of the surface of a Nanowin GaN/Al_2O_3 template [figure 6.2 (a2)], $In_{0.19}Ga_{0.81}N$ buffer layer [figure 6.2 (b1)-(b3)] and SL^{I}_{100x} [figure 6.2 (c1)-(c3)]. The Nanowin GaN/Al_2O_3 template exhibits a rather smooth, stepped surface with RMS: 0.4 nm [figure 6.2 (a2)], though a low density of holes, possibly originating in dislocations penetrating the surface, are visible. After the growth of 300 nm of $In_{0.19}Ga_{0.81}N$ buffer the surface is still free of 3D structures. The surface roughness has increased, demonstrated by RMS: 1.2 nm [figure 6.2 (b2)] compared to the 0.4 nm of the Nanowin template. Finally, after the growth of the (In, Ga)N heterostructure the surface roughness increased further to 3.0 nm [figure 6.2 (c2)] and the surface is now composed of a high density of small 3D structures [figure 6.2 (c3)]. This surface looks similar to the one of SL^{Z}_{100x} [see figure 5.10 (b3) in chapter 5.3.1].

Determination of indium content and degree of relaxation

The indium content x and strain ϵ were determined using XRD RSM.

The reciprocal space map (RSM) shown in figure 6.3 depicts the $(10\bar{1}5)$ reflex of GaN, the InGaN buffer layer and the (In, Ga)N heterostructure. Similar to SP^{Z}_{100x} (shown in figure 5.15) the RSM shown in figure 6.3 consists of two separate measurements, because the

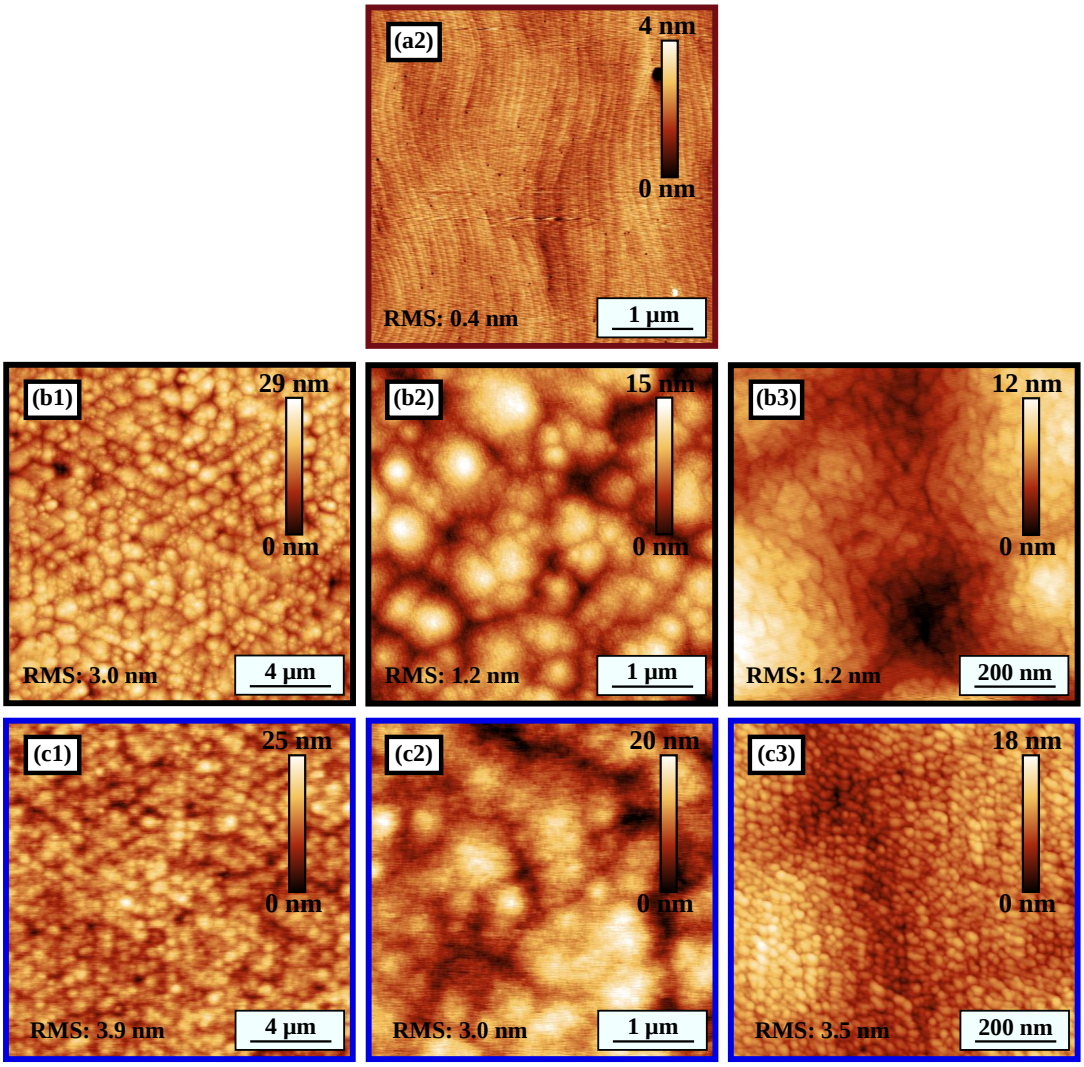

Figure 6.2: AFM height profiles of (a2) Nanowin GaN/Al_2O_3 template (wine red), (b1)-(b3) 400 nm $In_{0.19}Ga_{0.81}N$ buffer layer (black) and (c1)-(c3)SL^{I}_{100x} (blue) of size 20 $\times$ 20 μm^2 ((b1), (c1)), 5 $\times$ 5 μm^2 ((a2), (b2), (c2)), 1 $\times$ 1 μm^2 ((b3), (c3)).

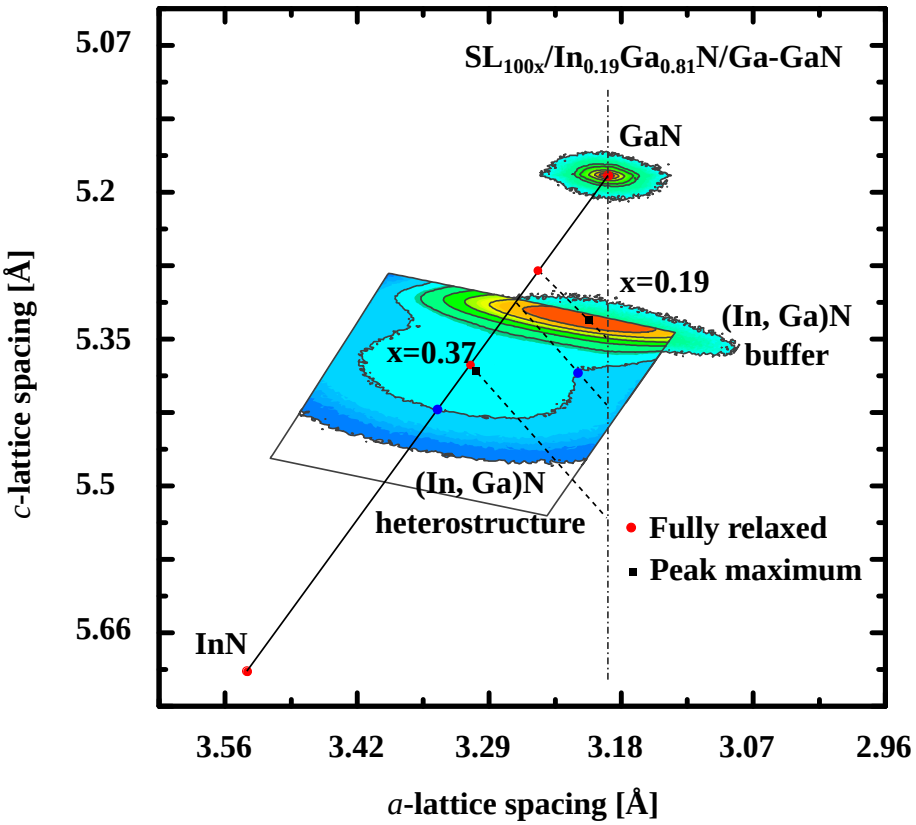

Figure 6.3: Superposition of two RSMs: SP^{I}_{100x} and (In, Ga)N buffer around the $(10\bar{1}5)$ reflex. Red dots mark the position of fully relaxed GaN, $In_{0.19}Ga_{0.81}N$ and InN, a black square marks the position of the maximum intensity of the (In, Ga)N buffer and the heterostructure. Black, dashed-dotted lines mark (In, Ga)N fully strained to the substrate, black dotted lines mark (In, Ga)N with a given indium content with varying degrees of relaxation. All fully relaxed (In, Ga)N layers lie on the black, solid line connecting InN and GaN.

intensity of the heterostructure peak was too low to be detected in a wide range scan with lower integration time per step. From this RSM, the indium content, the strain and degree of relaxation of the InGaN buffer layer and the (In, Ga)N heterostructure were determined as described in chapter 5.3. The results are listed in table 6.1.

Sample	Graphical Analysis		Analytic Analysis	
	x	R	x	R
(In, Ga)N buffer	0.19	25%	0.19	23%
(In, Ga)N heterostructure	0.37	95%	0.36	93%

Table 6.1: Indium content x and strain ϵ of (In, Ga)N buffer and (In, Ga)N heterostructure determined by XRD RSM.

The indium content x of the (In, Ga)N buffer was determined to be $x = 0.19$ with a degree of relaxation $R = 0.23\%$ (analytic analysis) to $R = 25\%$ (graphical analysis). It must be noted that the $(10\bar{1}5)$ reflex of the (In, Ga)N buffer is very broad. The intensity within the orange color coded area around the peak maximum of the (In, Ga)N buffer related reflex in figure 5.15 varies by less than 10%. This means within this narrow range of intensity there is a distribution of indium contents ranging from $x = 0.14$ to $x = 0.23$, the degree of relaxation ranges from unrelaxed (tensily strained) to $R = 86\%$. Within the $I_{2/3}$ range this distribution increases from $x = 0.11$ to $x = 0.25$ and degrees of relaxation ranging from $R = 0\%$ to $R = 100\%$. The indium content of the (In, Ga)N heterostructure was determined to be $x = 0.36$ with $R = 93\%$ (analytic analysis) to $x = 0.37$ with $R = 95\%$ (graphical analysis). The color coding in figure 6.3 was chosen to show the heterostructure peak intensity interval $I_{2/3}$ (see chapter 5.3.3 for more details). This interval is represented through light cyan color. Unfortunately this intensity intervals of the heterostructure overlaps with the reflex of the (In, Ga)N buffer. Therefore the lower limit of this interval for the heterostructure can not be determined precisely. This estimation gave an interval of $x = 0.26$, $R = 32\%$ to $x = 0.52$, $R = 100\%$. The results of the XRD RSM investigations of SP^{I}_{100x} are listed and compared to SP^{O}_{100x} and SP^{Z}_{100x} in table 6.2. The average indium content of all three SLs samples are very similar with $x = 0.35$ (SP^{Z}_{100x}) to $x = 0.37$ (SP^{O}_{100x}, SP^{I}_{100x}). Sample SP^{I}_{100x} shows a higher degree of relaxation with $R = 95\%$ compared to $R = 73\%$ (SP^{Z}_{100x}) and 65% (SP^{O}_{100x}) (possible reasons will be discussed later).

Sample	In-distribution x	x	ϵ
SP^{Z}_{100x}	0.19-0.44	0.35	-0.01
SP^{O}_{100x}	0.30-0.44	0.37	-0.01
SP^{I}_{100x}	0.26-0.52	0.37	-0.00

Table 6.2: Indium distribution x, indium content x and strain ϵ of samples SP^{Z}_{100x}, SP^{O}_{100x} and SP^{I}_{100x} determined by XRD RSM.

Determination of indium content and degree of relaxation using $\omega - 2\theta$ scans

Analogue to chapter 5.3 the structure of the sample was further investigated through an $\omega - 2\theta$ scan around the (0002) reflex [figure 6.4 (a)] and is shown together with the $\omega - 2\theta$ scans of SL^{O}_{100x} and SL^{Z}_{100x} in figure 6.4 (b). Since no indium droplets were found on the surface of sample SL^{I}_{100x}, as discussed in chapter 6.1.1, no In(101) reflex is expected.

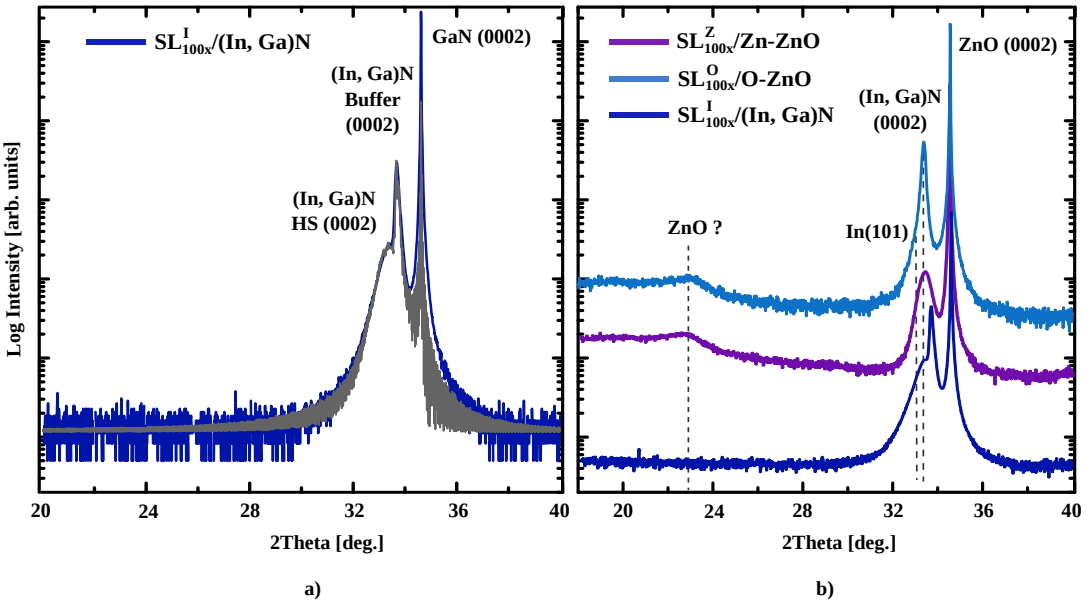

Figure 6.4: (a) XRD $\omega - 2\theta$ scan around the (0002) reflex of (In, Ga)N heterostructure (HS) (dark blue) grown on a $In_{0.19}Ga_{0.81}N$/GaN substrate, referred to as SL^{I}_{100x} and fitting curve (grey). Fitted with gradual changes in indium content and relaxation as described in the text and depicted in figure 6.5. (b) Comparison of XRD $\omega - 2\theta$ scans around the (0002) reflex of the SL^{I}_{100x}, the SL^{O}_{100x} and the SL^{Z}_{100x}. Guides to the eye were added to indicate the (In, Ga)N peak of the heterostructure and the ZnO related broad, low intensity peak.

The structure SL^{I}_{100x} was fitted with (In, Ga)N that exhibits a composition and strain grading along the growth direction. The structure of SL^{I}_{100x} is depicted in figure 6.5 (b). This layered structure was chosen to fit the left flank of the (In, Ga)N heterostructure and the right flank of the (In, Ga)N buffer. Both of them are extended and could not

be fitted with a structure without indium content grading. The width of the peaks gave the distribution of indium contents and the intensity evolution gave the layer thickness of each sublayer that was used to fit the structure. The indium content of the (In, Ga)N buffer ranged from $x = 0.11$ to $x = 0.23$, with an average indium content of $x = 0.20$. The relaxation was chosen to increase progressively with varying degrees as described in figure 6.5 (b) and which was found in RHEED data, too (see the next section 6.1.2). The average degree of relaxation is 53% and the final degree of relaxation of the upper part of the (In, Ga)N buffer is 65%. This further substantiates the findings of the XRD RSM which showed a wide range of indium contents and degrees of relaxation in the $I_{2/3}$ range of the (In, Ga)N heterostructure peak.

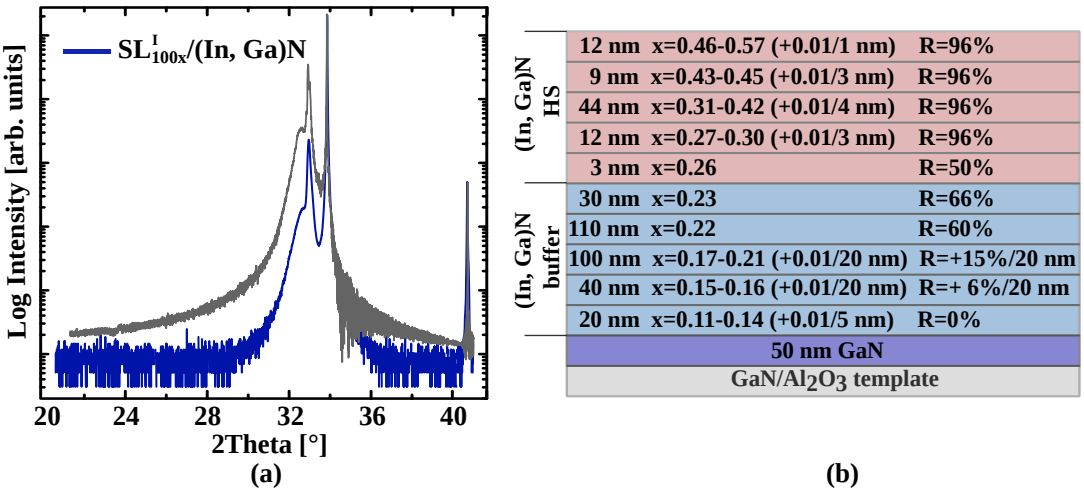

Figure 6.5: (a) XRD $\omega - 2\theta$ scans around the (0002) reflex of SL^{I}_{100x}, intensity was normalized to fit the GaN (0002) peak. (b) Structure of sample SL^{I}_{100x} fitted using $\omega - 2\theta$ scan. "40 nm $x = 0.15 - 0.16$ (+0.01/20 nm) R: +6%/20 nm" means that the layer is 40 nm thick, is subdivided into 2 layers of each 20 nms thickness and the indium content increases by 0.01 from sub-layer to sub-layer. The degree of relaxation increases by 6% relative to the underlying sub-layer.

There is no indication of a SL structure (no satellite peak around 22° where it would be expected). The indium content of the (In, Ga)N heterostructure was graded from $x = 0.26$ to $x = 0.57$ with $R = 96\%$ for the most part (for details see figure 6.5 (b)). The intensity of the fitting structure in figure 6.4 (a) was not normalized to fit the GaN (0002) peak but the $In_{0.19}Ga_{0.81}N$ (0002) buffer peak. This was done so because the XRD Epitaxy software, that was used to conduct the fitting, does not properly take the attenuation of diffracted X-Rays into account, that have to travel through a layer to exit the sample. Figure 6.5 (a) shows the fitting curve normalized to fit the GaN (0002) peak. It also shows the Sapphire

(0006) peak. The GaN layer thickness had to be overstated by a factor of 4 to fit both the GaN (0002) and the Sapphire (0002) peak intensities properly, therefore proofing the point that the attenuation by thick intermediate layers is not properly taken into account.

6.1.2 Investigation of the growth mode and surface morphology

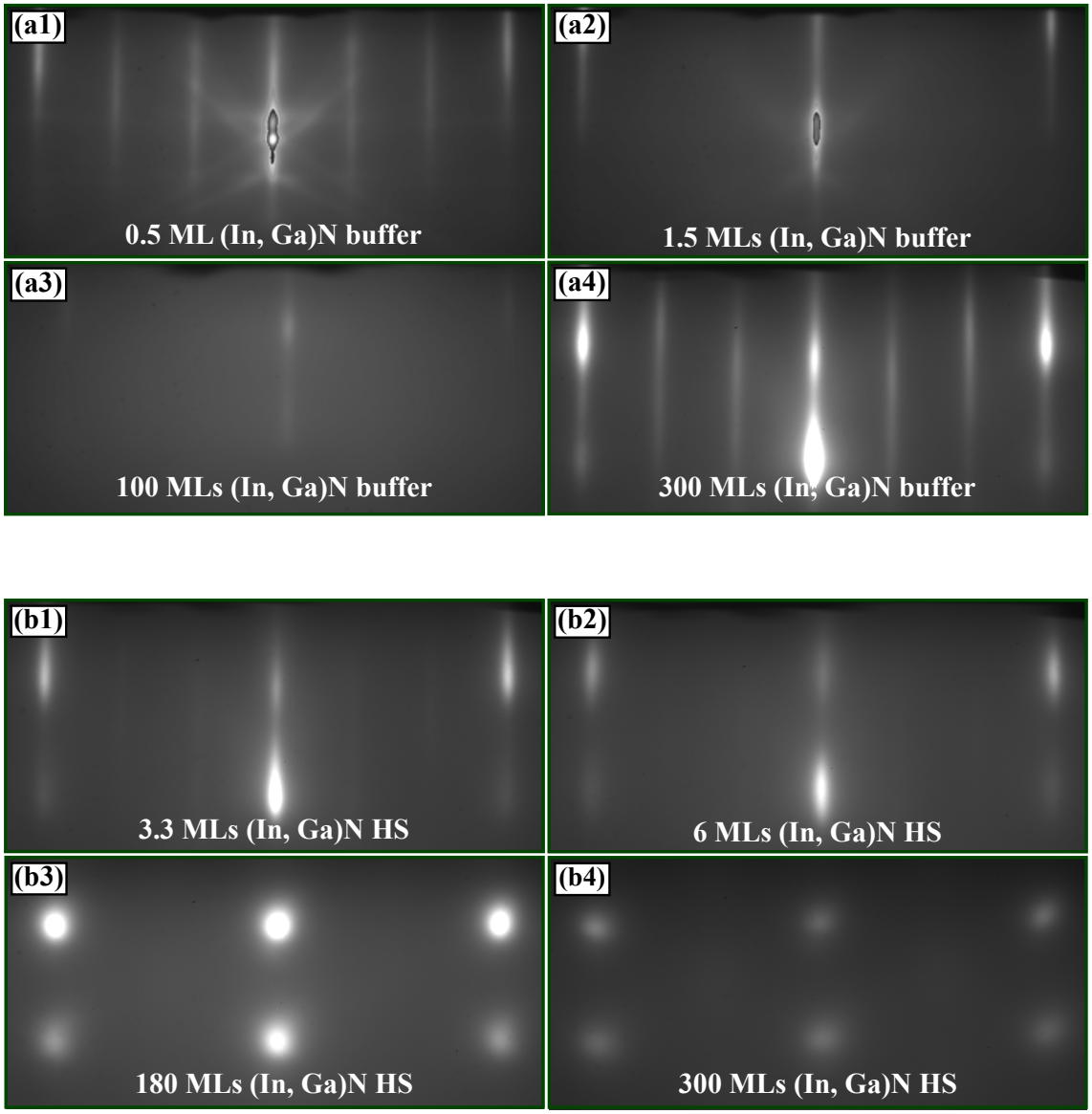

Figure 6.6: RHEED diffraction patterns along the $\langle 10\bar{1}0 \rangle$ azimuth of (a1)-(a4) (In, Ga)N buffer grown on GaN/Al_2O_3 (b1)-(b4) (IN, Ga)N heterostructure (HS) grown on $(In,Ga)N\ buffer/GaN/Al_2O_3$.

At the start of the growth of the (In, Ga)N buffer layer a (3x) reconstructions formed as demonstrated by the RHEED pattern shown in figure 6.6 (a1). The intensity of this RHEED pattern declined during growth quickly and vanished before 1.5 MLs of (In,

Ga)N was deposited [figure 6.6 (a2)]. Beyond 1.5 MLs of (In, Ga)N a very faint streaky (1x) RHEED pattern prevailed that decreased in intensity as can be seen in figure 6.6 (a3). This decrease is intensity is probably due to the accumulation of indium on the surface due to the indium rich growth conditions. After the growth of the (In, Ga)N buffer all shutters were closed and the surface was given time to desorb all excess indium. Due to this desorption step a (3x) reconstruction appeared again. After the deposition of 1 ML of InN and 2 MLs of GaN on top of the (In, Ga)N buffer, the RHEED pattern still indicated the presence of a (3x) reconstruction [see figure 6.6 (b1)]. After 6 MLs of (In, Ga)N heterostructure the faint (3x) pattern disappeared and transitioned into a streaky (1x) pattern [figure 6.6 (b2)].

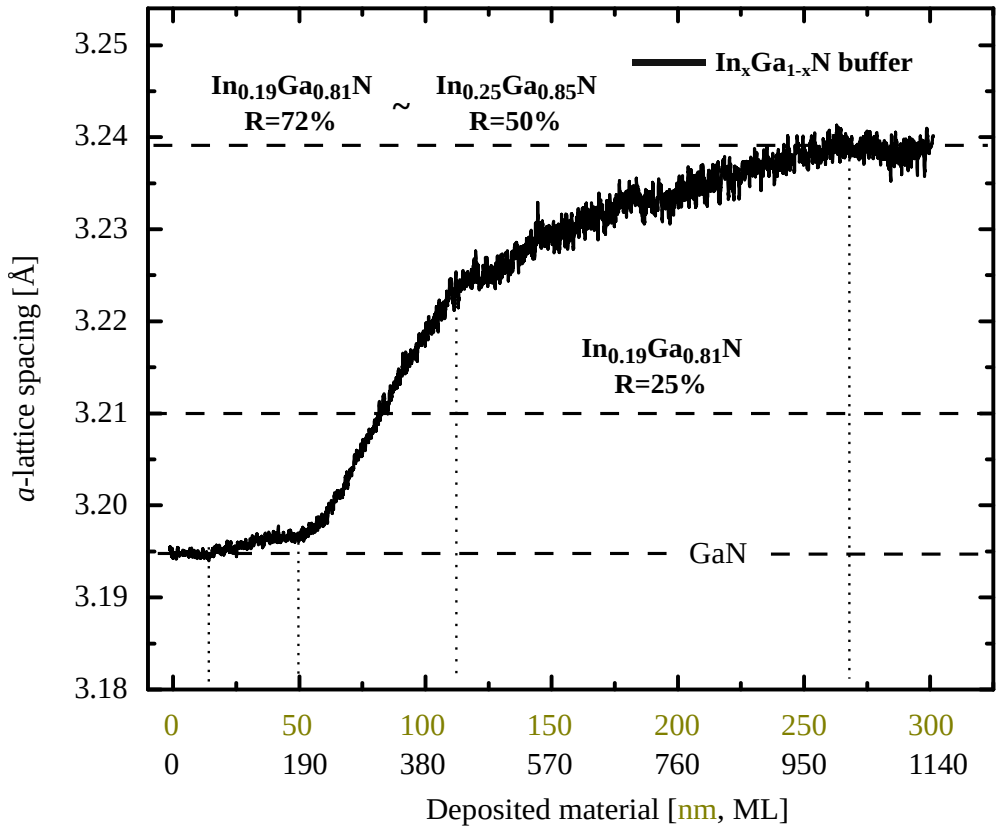

Figure 6.7: *a*-lattice spacing evolution during the growth of 300 nm (In, Ga)N buffer. Guides to the eye indicate *a*-lattice spacing of GaN, $In_{0.19}Ga_{0.81}N$ with $R = 25\%$, $R = 72\%$ and $In_{0.25}Ga_{0.85}N$ with $R = 50\%$. Thermal expansion was taken into account.

Due to the indium rich growth conditions during growth and the accumulation of indium atoms on the surface the *a*-lattice spacing derived by RHEED might not give an adequate picture of the lattice spacing of the investigated layers. The *a*-lattice spacing of the (In, Ga)N buffer shown in figure 6.7 stays constant for the first 17 nm and starts to slightly increase between 17 nm and 50 nm. The main relaxation takes place between 50 nm and

115 nm. Between 115 nm and 270 nm the slope decreased. Beyond 270 nm the a-lattice spacing stays constant, which was confirmed by additional measurements of a thicker sample (not shown here). These ranges of changing slopes, which may be correlated with changing degrees of relaxation, show some similarity to the structure determined by XRD $\omega - 2\theta$ scan (see figure 6.5 (b)). Guides to the eye in figure 6.7 indicate the a-lattice spacing of $In_{0.19}Ga_{0.81}N$ with $R = 25\%$ and $R = 72\%$, as well as $In_{0.25}Ga_{0.75}N$ with $R = 50\%$. This findings fit the results of the RSM and $\omega - 2\theta$ scan which showed that the (In, Ga)N buffer exhibits a wide range of indium contents and degrees of relaxation extending up to $R = 100\%$.

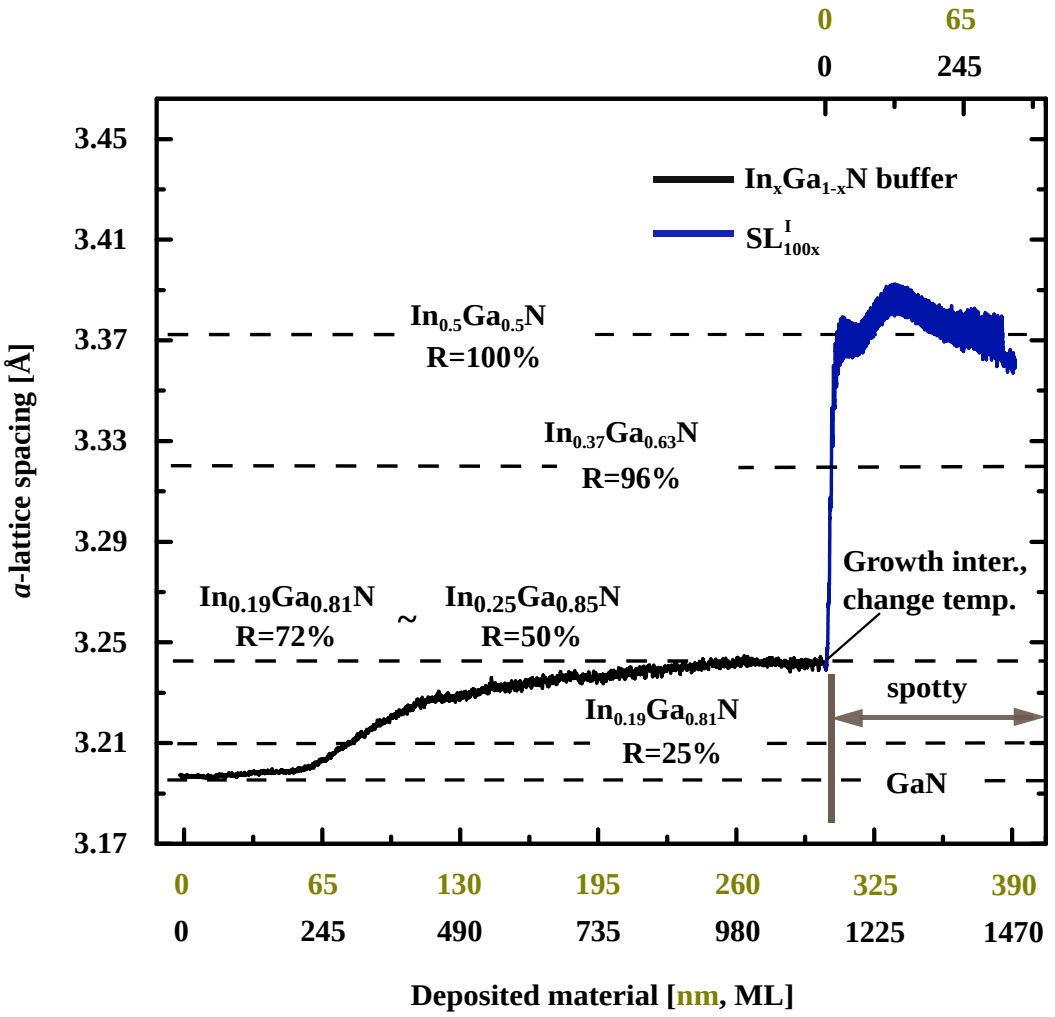

Figure 6.8: a-lattice spacing evolution during the growth of a 300 nm thick (In, Ga)N buffer layer and 80 nm (In, Ga)N heterostructure. Guides to the eye indicate a-lattice spacing of GaN and (In, Ga)N with different compositions and strain states. Thermal expansion was taken into account.

Figure 6.8 shows the *a*-lattice spacing evolution of the (In, Ga)N buffer and the (In, Ga)N heterostructure. There was a growth interruption after the growth of the (In, Ga)N buffer to desorb excess indium and cool down the heater from 608 °C to 450 °C. The slight change in *a*-lattice spacing due to a change in temperature was taken into account. The *a*-lattice spacing of the (In, Ga)N heterostructure does not reach a final steady state value that correlates with the average indium content and degree of relaxation determined by RSM. A steady state value is not reached at all but an oscillatory behavior around a steady state value of 3.37 Å can be observed.

Figure 6.6 (b1)-(b4) shows excerpts of the evolution of the RHEED diffraction pattern during growth of the heterostructure. The (3x) reconstruction, which is shown in figure 6.6 (a4) at the end of the growth of the (In, Ga)N buffer decreased in intensity during growth of the heterostructure and vanished completely during the 3rd and 4th deposited ML. A faint streaky pattern appeared [figure 6.6 (a2)], which evolved slowly into a spotty pattern, which is exemplary shown in figure 6.6 (a3). This observation is in line with Stranski-Krastanov growth. It was not possible to determine an exact layer thickness for the transition between streaky and spotty pattern, since this evolution was continuous and slow. It was estimated that this transition was close to 9 MLs. The spotty pattern decreased in intensity but remained until the end of the growth. The spotty RHEED pattern corresponds to a transmission pattern, which means that the *a*-lattice spacing is correlated with the 3D structures. Figure 6.9 shows the evolution of the *a*-lattice spacing of three heterostructure samples, SL^{O}_{100x}, SL^{Z}_{100x} and SL^{I}_{100x}. The layer thickness for the streaky-spotty transition of the RHEED diffraction pattern is similar for all three samples. The samples SL^{O}_{100x}, SL^{Z}_{100x} grown on ZnO show an initial increase in *a*-lattice spacing and a decrease afterwards towards a final steady-state *a*-lattice spacing. The *a*-lattice spacing of sample SL^{I}_{100x} increases directly towards an average final value around which the *a*-lattice spacing oscillates. The greatest increase in *a*-lattice spacing, both initial increase and final *a*-lattice spacing, is observed for SL^{Z}_{100x} and SL^{I}_{100x}, both grown on the metal-polar face (Ga-polar or Zn-polar). The final steady state *a*-lattice spacing of SL^{O}_{100x}, SL^{Z}_{100x} and SL^{I}_{100x} is correlated with the average degree of relaxation determined through RSM and the V/III ratio as shown in table 6.3.

Table 6.3 shows that there is a correlation between the V/III ratio and the average *a*-lattice spacing and degree of relaxation. SL^{O}_{100x} was probably unintentionally grown with slightly metal-rich conditions, which is evidenced by droplets on the surface, observed by optical microscope (see figure 5.11). This sample has the lowest degree of relaxation $R = 65\%$ and the lowest average *a*-lattice spacing of 3.3 Å. Sample SL^{Z}_{100x} has barely any droplets on the surface (see figure 5.11). Thus, it was probably grown very close

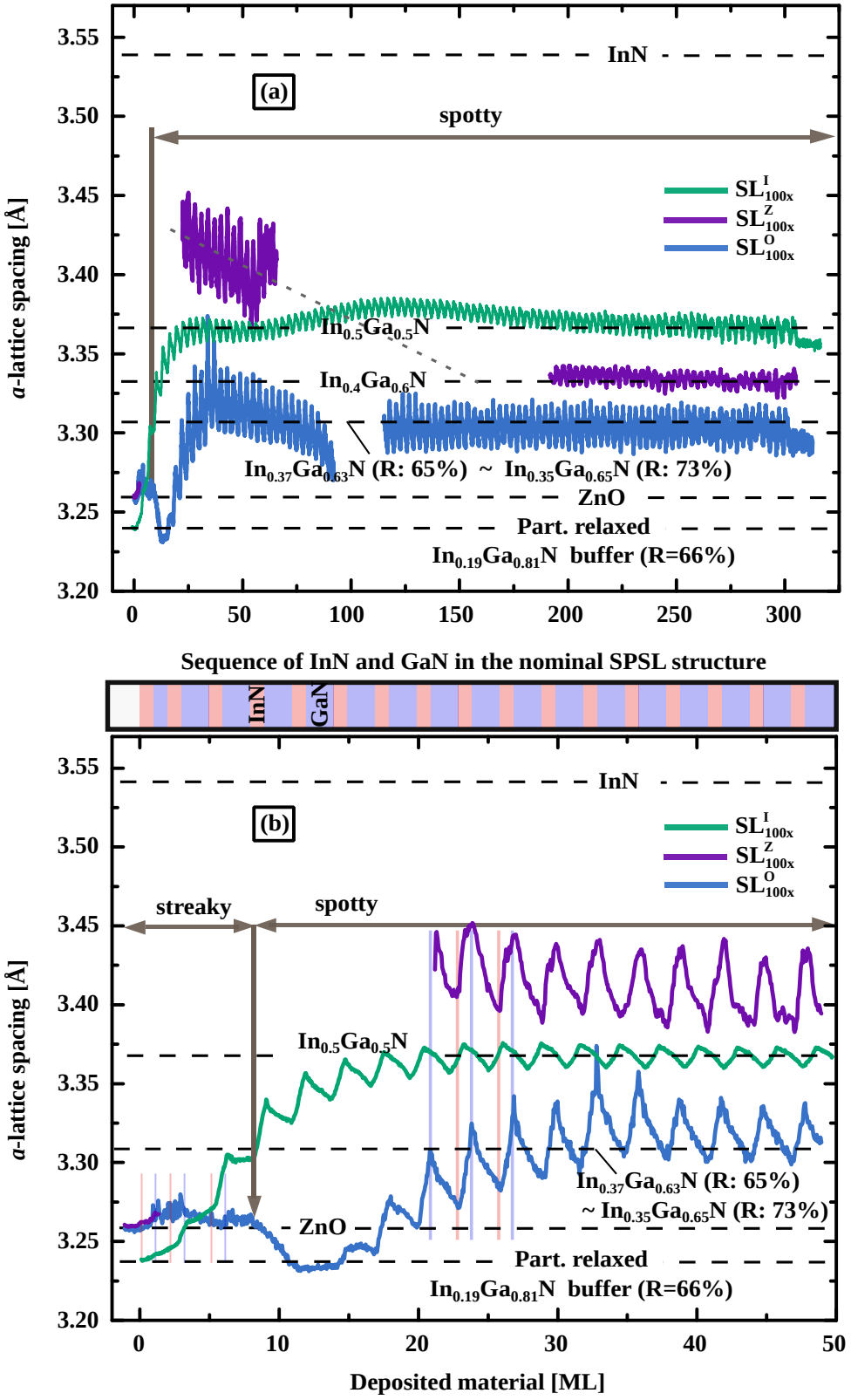

Figure 6.9: *a*-lattice spacing evolution during the growth of SL^{O}_{100x}, SL^{Z}_{100x} and SL^{I}_{100x}. Guides to the eye indicate *a*-lattice spacing of GaN and (In, Ga)N with different compositions and strain states, grey dotted line indicates possible slope of decrease of *a*-lattice spacing of SL^{Z}_{100x}. Thermal expansion was taken into account.

to stoichiometric conditions. This sample has a higher degree of relaxation $R = 73\%$ and average a-lattice spacing of 3.33 Å. Finally for sample SL^{I}_{100x} no droplets could be detected on the surface. Thus, it was probably grown under slightly N-rich conditions. This sample exhibits the highest degree of relaxation $R = 95\%$ and the highest average a-lattice spacing of 3.37 Å.

Bourret *et al.* reported on the strain relaxation mechanism in AlN/GaN heterostructures [165]. They found that there is an elastic strain component, which can be reversible. This elastic, reversible component is due to the formation of 2D platelets, which can relax, or in case of coalescence be strained again - this gives the elastic component. They found that there is no coalescence of 2D platelets and no reversible, elastic strain in case of N-rich growth. They further noted that even under metal-rich growth conditions it takes some time until the metal-adlayer build up and the advantages of metal-rich growth can be reaped (increased surface diffusion length of adatoms [98]). For only slightly metal-rich growth conditions it could take therefore several dozen MLs of deposited material before even 1 ML metal-ad-layer was accumulated. Figure 6.9 shows that for SL^{O}_{100x} and SL^{Z}_{100x} the initial increase in a-lattice spacing reverses after about 25 MLs of deposited material. But SL^{O}_{100x}, which was grown with slightly metal-rich conditions, does not only exhibit a smaller initial increase in a-lattice spacing but also reaches the final steady-state a-lattice spacing of 3.33 Å after about 75 MLs. SL^{Z}_{100x} however, which was grown closer to stoichiometry shows a much stronger initial increase in a-lattice spacing. It can not be determined exactly when the a-lattice spacing of SL^{Z}_{100x} reaches its steady-state value due to low intensity between about 75 MLs and 190 MLs. The a-lattice spacing of SL^{Z}_{100x} was fitted with a linear fit between 25 MLs and 75 MLs, the fit is indicated as a grey, dotted line in figure 6.9. If the actual decrease of the a-lattice spacing of SL^{Z}_{100x} was similar to what the linear fit suggested, it would mean that the final a-lattice spacing was reached around 160 MLs. This would be in line with the assumption, that under a smaller metal-surplus (closer to stoichiometric growth conditions) it takes longer to form a metal ad-layer, which in turn could lead to a (partial) coalescence of the 2D platelets and (smaller) 3D structures and therefore could lead to a decrease in the a-lattice spacing. Lastly, SL^{I}_{100x} was grown under slightly N-rich conditions and exhibits an a-lattice spacing that increases straight towards its final 'steady-state' value (oscillates around it).

This might suggest that the degree of relaxation and therefore the average a-lattice spacing can be influenced by the surface stoichiometry of adatoms during growth. It was already reported in literature that N-rich growth of GaN on GaN with MBE results in a defective, columnar growth [89] with stacking faults [90], whereas Ga-rich growth did not lead to the formation of such defects and the GaN epilayer was comparable to GaN

Sample	In-content x	*Relaxation [%]*	*a-lattice spacing [Å]*	V/III ratio	RSM [nm]
SP^{I}_{100x}	0.37	95	3.37	slightly N-rich	3.0
SP^{Z}_{100x}	0.35	73	3.33	stoichiometry	3.1
SP^{O}_{100x}	0.37	65	3.3	slightly metal-rich	1.9

Table 6.3: Indium content x, average degree of relaxation, 'steady state' *a*-lattice spacing, V/III ratio during growth and RSM of samples SP^{Z}_{100x}, SP^{O}_{100x} and SP^{I}_{100x} determined by XRD RSM and RHEED.

templates grown with metal organic vapor phase epitaxy. It may not even be necessary to conduct the whole growth under metal-rich conditions. Neugebauer *et al.* investigated the surface diffusion on GaN (0001) and (000$\bar{1}$) through density functional theory (DFT) and found that a metal bi-layer (In adlayer or Ga bi-layer) facilitates a diffusion mechanism they coined AELD (see chapter 3.1.3). This means that the deposition of indium or gallium atoms that form such a metal bi-layer would be sufficient and the rest of the growth could be conducted in stoichiometric conditions. Since gallium atoms incorporate into (In, Ga)N strongly preferentially over indium atoms, it would probably be advantageous to deposit an indium adlayer instead of an gallium adlayer. In the latter case this surplus gallium adatoms would incorporate into InN/(In, Ga)N during the deposition of InN.

Further investigations are required to understand if such a metal adlayer can be deposited without etching the ZnO substrate. The assumption that the presence of the metal adlayer and not flux ratios during growth is responsible for the difference in surface morphology, crystal quality, defect creation, etc. might explain why there is only a slightly smoother surface for SP^{O}_{100x} (grown with slightly metal-rich conditions) compared to SP^{Z}_{100x} and SP^{I}_{100x} (see table 6.3). Before such an adlayer could be formed on SP^{O}_{100x}, the diffusion of adatoms was lower, which probably lead to the roughening of the surface during growth. After the metal adlayer was formed surface diffusion was enhanced but could not smooth the initial roughening, it may have decreased the roughening compared to the stoichiometric growth of SP^{Z}_{100x} or the N-rich growth of SP^{I}_{100x}.

6.1.3 Investigation of the chemical composition and strain

Sample SL^{I}_{100x} as well as an $In_{0.19}Ga_{0.81}N$ buffer and a GaN/AlN/Al_2O_3 template were investigated by Raman spectroscopy. The analysis was conducted following the procedures described in chapter 5.3.4. Figure 6.10 shows the Raman spectra of SL^{I}_{100x} and the $In_{0.19}Ga_{0.81}N$ buffer excited with λ_{405} and λ_{244}.

Figure 6.11 (a) shows the results of Raman spectroscopy measurements of a GaN/AlN/Al_2O_3 template, the 3 peaks are attributed to GaN A_1(LO) at 735 cm^{-1}, E_2^H at 569 cm^{-1} and E_1(TO) at 560 cm^{-1} (listed in table 6.4). These peak positions correlate nicely with literature values reported by Harima *et al.* [182]. Guides to the eye were added to indicate the peak maxima.

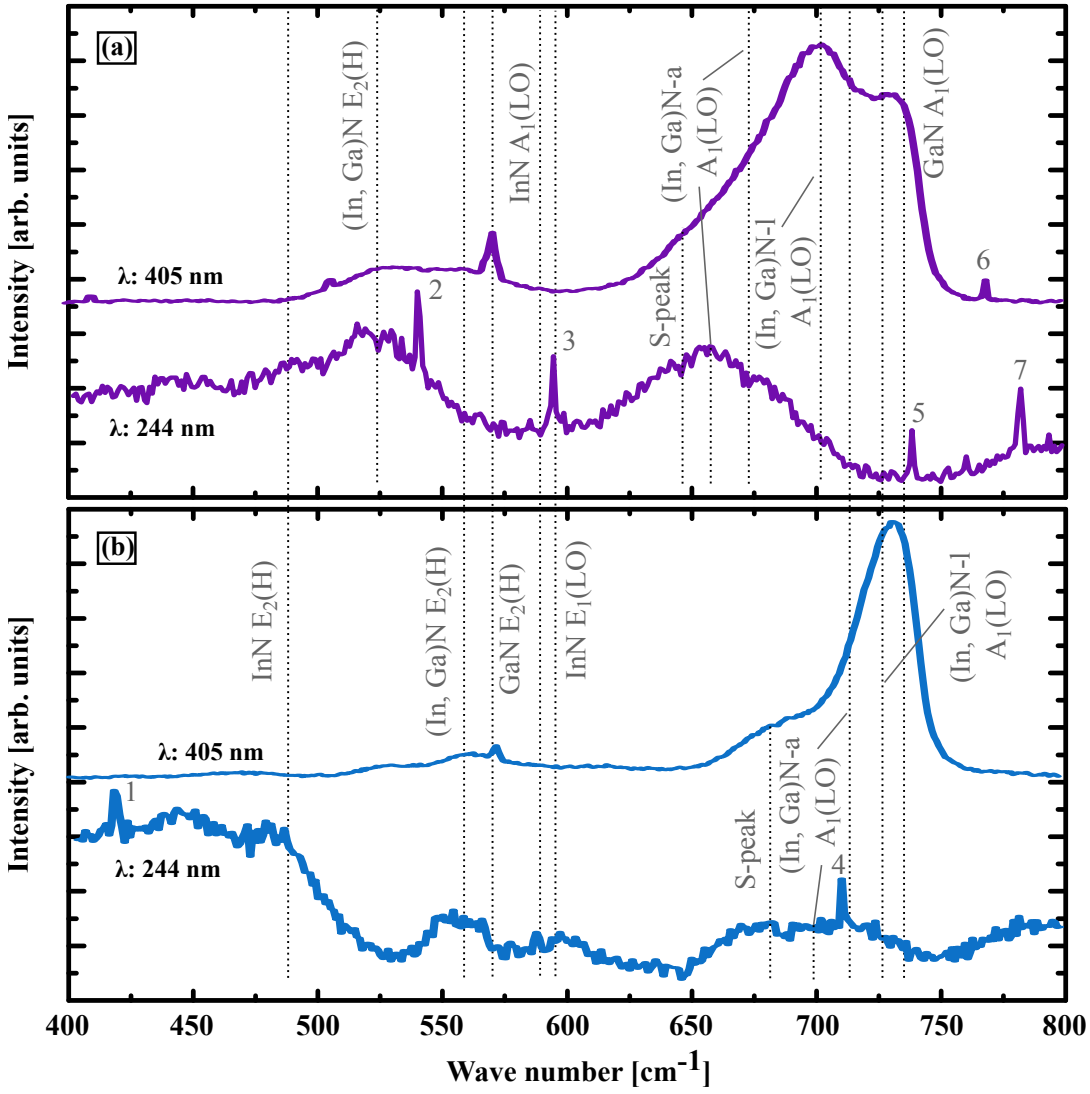

Figure 6.10: Raman spectra of samples a) SL^I_{100x} and b) $In_{0.19}Ga_{0.81}N$ using laser excitation wavelength λ_{405}, and λ_{244}. The vertical dotted lines indicate literature values for InN and GaN phonon frequencies. "$(In, Ga)N$-a/l" means (In, Ga)N with average/low indium content. Raman spectroscopy measurements were conducted by Dr. Manfred Ramsteiner at the Paul Drude Institut, Berlin.

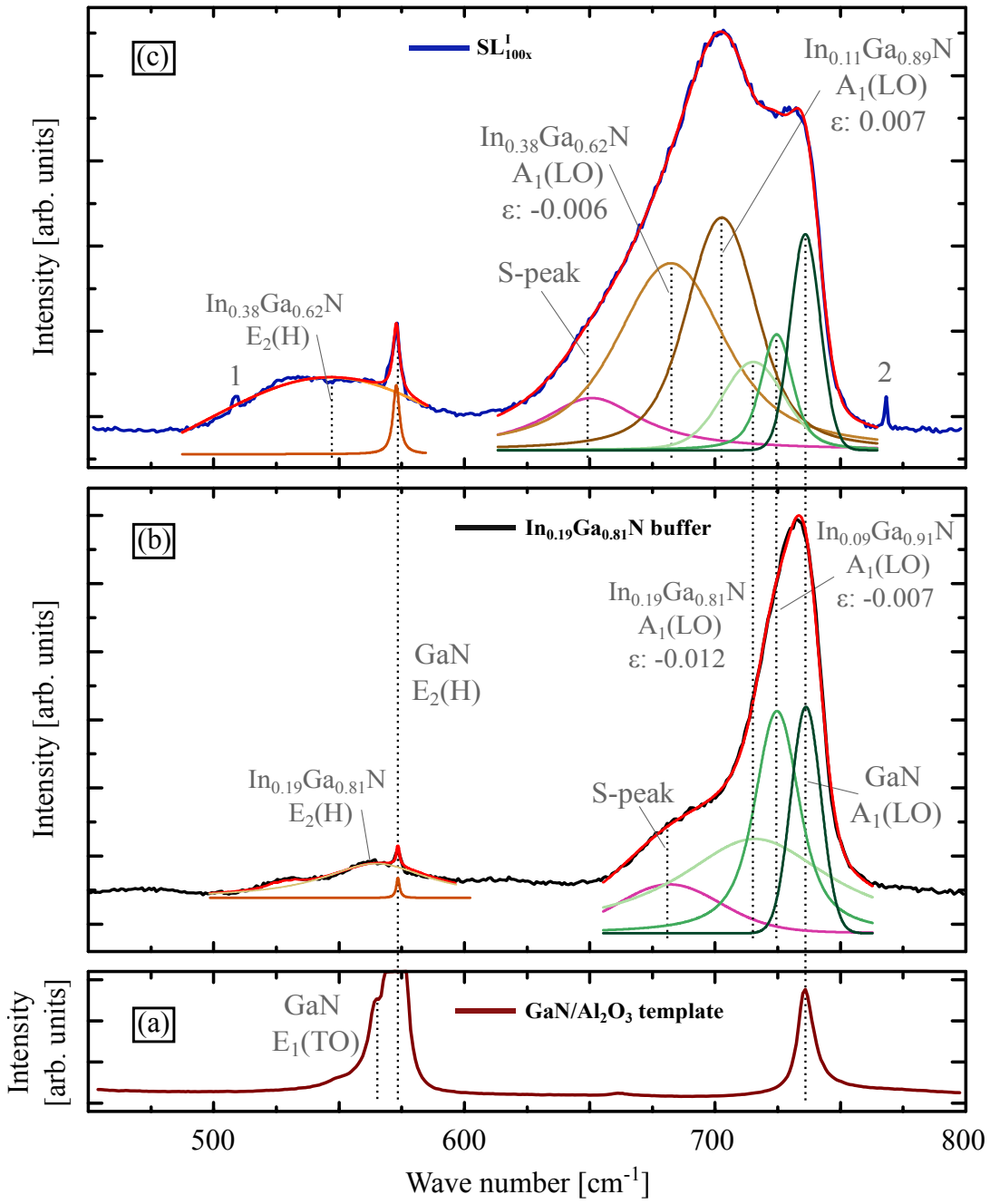

Figure 6.11: Raman spectra of samples (a) GaN/AlN/Al_2O_3 template (wine red); (b) 300 nm $In_{0.19}Ga_{0.81}N$ (black) on GaN/Al_2O3 template; (c) SL^{I}_{100x} (blue) using laser excitation wavelength λ_{405}. The Raman spectra were fitted with Voigt curves, the convolution of the Voigt fit curves is given as a red curve. The vertical dotted lines indicate the peak positions of the individual Voigt curves. The following color codes were used: E_2^H of $In_{0.38}Ga_{0.62}N$ (light orange), GaN (dark orange), $In_{0.19}Ga_{0.81}N$ (beige); $A_1(LO)$: $In_{0.38}Ga_{0.62}N$ (light brown), $In_{0.19}Ga_{0.81}N$ (light green), $In_{0.09}Ga_{0.91}N$ (green), $In_{0.11}Ga_{0.89}N$ (brown), GaN (dark green), S-peak (pink). Raman spectroscopy measurements were conducted by Dr. Manfred Ramsteiner.

Raman Mode [cm^{-1}]	SL^{Z}_{100x}	SL^{O}_{100x}	SL^{I}_{100x}	$In_{0.19}Ga_{0.81}N$	GaN templ.
$E_{Exc} = 405$ nm					
E_2^H	545	538	545	566	569
S-peak	656	650	651	682	
A_1(LO) (In, Ga)N (a) or GaN	688	679	683	716	735
A_1(LO) (In, Ga)N (l)	708	702	704	726	
E_1(TO) GaN					560
$E_{Exc} = 244$ nm					
E_2^H	534	537	523	554	
A_1(LO) (In, Ga)N (a)	664	671	654	699	

Table 6.4: Peak positions of Raman scattering modes E_2^H, A_1(LO), E_1(TO) and S-peak of samples SL^{Z}_{100x}, SL^{O}_{100x}, SL^{I}_{100x}, $In_{0.19}Ga_{0.81}N$ and GaN template depending on used laser excitation wavelength E_{Exc}. "(a)" refers to (In, Ga)N with average indium content and average strain of the sample; "(l)" refers to (In, Ga)N with low indium content

Figure 6.11 (b) shows the results of Raman spectroscopy measurements of an $In_{0.19}Ga_{0.81}N$ buffer. The peaks were fitted with Voigt curves which are displayed together with their convolution and guides to the eye to indicate peak maxima. A broad band of peaks between 650 cm^{-1} and about 770 cm^{-1} was fitted with 4 peaks.

Comparing the spectra stemming from the GaN template [figure 6.11 (a)] and from the $In_{0.19}Ga_{0.81}N$ buffer [figure 6.11 (b)] shows that the peak at 735 cm^{-1} (dark green) correlates with the A_1(LO) of GaN. The peak at 726 cm^{-1} (green) is attributed to the A_1(LO) of low indium content (In, Ga)N which causes an increased scattering intensity through the resonance effect. The indium content and strain was estimated to be $x = 0.09$ and $\epsilon = -0.01$ (listed in table 6.5), using both equation 5.16 and 5.22. This phase exhibits compressive strain, due to the GaN template. Peaks at 716 cm^{-1} (green) and 566 cm^{-1} (beige) are attributed to the A_1(LO) and E_2^H of (In, Ga)N with an average indium content of $x = 0.19$ and strain $\epsilon = -0.01$ and correlate nicely with the findings derived from RSM (see table 6.5). The peak at 566 cm^{-1} was attributed to the E_2^H of the (In, Ga)N phase with average indium content and not with low indium content because the E_2^H mode does not experience an increased intensity through the resonance effect as the A_1(LO) does. Therefore the E_2^H mode of the (In, Ga)N phase with low indium content should not be visible due to the probably small volume. The peak at 682 cm^{-1} (pink) is the S-peak (see section 5.3.4) and at 569 cm^{-1} (orange) is a low intensity peak that correlates with the E_2^H of GaN.

Finally the spectrum of SL^{I}_{100x} was fitted using 8 peaks [figure 6.11 (c)], 4 of which correlate with the already described A_1(LO) of GaN (dark green), low indium content and average indium content (In, Ga)N phase of the $In_{0.19}Ga_{0.81}N$ buffer (green and light green)

Sample	Method	x	ϵ
SL^{Z}_{100x}	Raman (244 nm)	0.51	-0.01
SL^{Z}_{100x}	Raman (405 nm)	0.33	0.00
SL^{Z}_{100x}	XRD	0.35	-0.01
SL^{O}_{100x}	Raman (244 nm)	0.47	-0.01
SL^{O}_{100x}	Raman (405 nm)	0.38	0.00
SL^{O}_{100x}	XRD	0.37	-0.01
SL^{I}_{100x}	Raman (244 nm)	0.53	≈ 0
SL^{I}_{100x}	Raman (405 nm)	0.39	-0.01
SL^{I}_{100x}	XRD	0.37	≈ 0
(In, Ga)N buffer	Raman (244 nm)	0.27	-0.01
(In, Ga)N buffer	Raman (405 nm)	0.19	-0.01
(In, Ga)N buffer	XRD	0.19	-0.02

Table 6.5: Indium content x and strain ϵ of samples SL^{Z}_{100x}, SL^{O}_{100x}, SL^{I}_{100x} and $In_{0.19}Ga_{0.81}N$ buffer determined by Raman spectroscopy and XRD RSM.

and the E_2^H of GaN (orange). Two of the additional peaks are correlated with the A_1(LO) of the low indium content and average indium content phase (brown and light brown) at 704 cm^{-1} and 683 cm^{-1}. The last two are the S-peak (pink) at 651 cm^{-1} and the E_2^H of the average indium content phase at 545 cm^{-1}. The indium content and strain state of the average indium content phase was determined to be $x = 0.39$ and $\epsilon = -0.01$, respectively. The indium content agrees well with the findings of the RSM, but the strain state differs significantly.

All narrow peaks in figure 6.10 (labeled "1" to "7") and 6.11 (labeled with "1" and "2") are probably due to cosmic radiation.

Comparing the Raman spectra for different excitation wavelengths shows that SL^{I}_{100x} and the (In, Ga)N buffer exhibit a higher average indium content for λ_{244} compared to λ_{405} (see table 6.5). All (In, Ga)N heterostructures investigated in this study showed this trend, that suggests the presence of the composition pulling effect (see section 5.3).

Comparing SL^{Z}_{100x}, SL^{O}_{100x} and SL^{I}_{100x} (see table 6.5) shows that they have similar average indium contents in the range of $x = 0.34$ to $x = 0.39$ measured by Raman spectroscopy, which agrees well with the results from the RSM.

6.1.4 Investigation of the optical properties

Figure 6.12 shows SL^{Z}_{100x} (purple), SL^{O}_{100x} (blue), SL^{I}_{100x} (dark blue) and $In_{0.19}Ga_{0.81}N$ buffer (black). The $In_{0.19}Ga_{0.81}N$ buffer shows emission at 471 nm. Using equation 5.22 this can be correlated with (IN, Ga)N with $x = 0.2$ and $R = 50\%$.

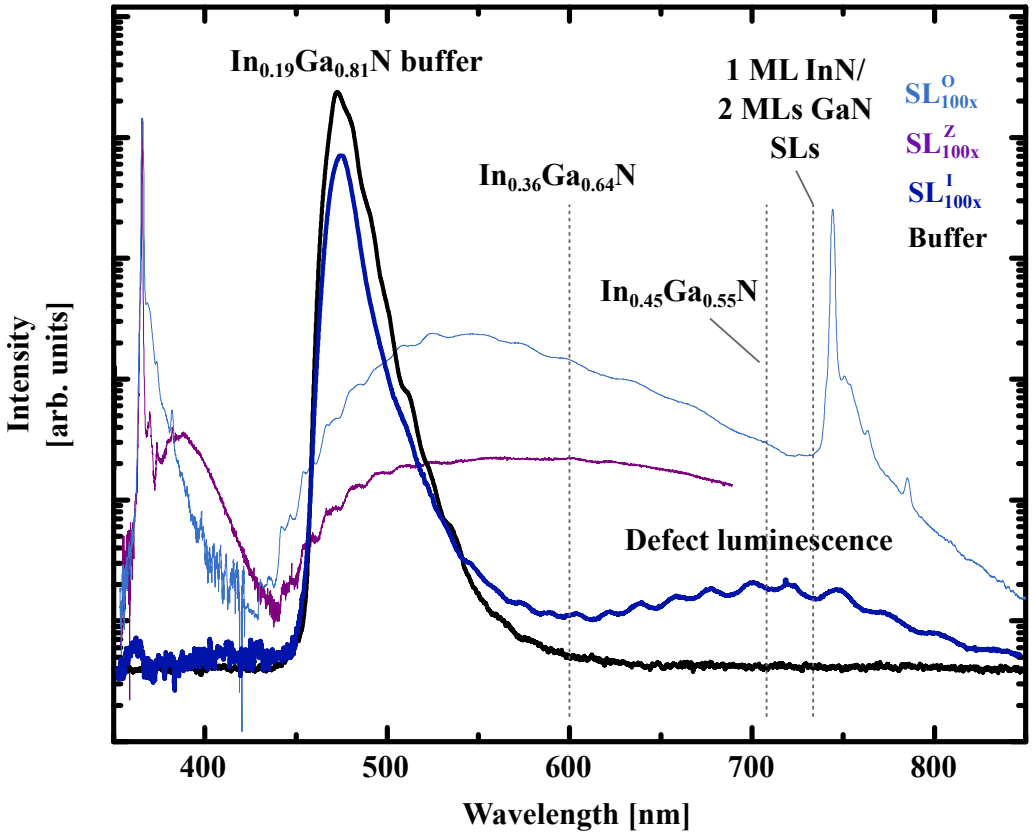

Figure 6.12: Photoluminescence emission spectra of SL^{Z}_{100x} (purple), SL^{O}_{100x} (blue), SL^{I}_{100x} (dark blue) and $In_{0.19}Ga_{0.81}N$ buffer (black). PL measurements were conducted at $T = 10$ K by Dr. Felix Feix.

A very similar emission can be observed at 472 nm for SL^{I}_{100x}, which proves that it does not originate in the (In, Ga)N heterostructure but in the (In, Ga)N buffer layer beneath. Additionally there is a broad peak from about 590 nm to 820 nm, with its center close to 700 nm. Reshchikov *et al.* reported on red defect related luminescence in GaN, with an emission band from 610 nm to 820 nm [208]. This luminescence was attributed to the presence of Mg [209], [210]. Mg was used in our MBE system 41 days prior to the growth of the $In_{0.19}Ga_{0.81}N$ buffer. No Mg related luminescence can be seen in figure 6.12 originating from the $In_{0.19}Ga_{0.81}N$ buffer. Sample SL^{I}_{100x} was grown 7 days after the usage of Mg and 3 days after to outgassing the manipulator. It is possible that Mg was unintentionally incorporated into SL^{I}_{100x} giving rise to the luminescence between 590 nm to 820 nm.

If this luminescence originated from (In, Ga)N band to band transitions, it would correlate with (In, Ga)N with indium contents ranging from $x = 0.38$ to $x = 0.74$, with the peak intensity correlating to $x = 0.45$. Guides to the eye in figure 6.12 indicate where emission from a 1 ML InN/2 MLs GaN SLs structure is expected to be [33], which is close to the broad emission band. But, as no indication for the presence of a periodic structure was found from XRD measurements, this is a less likely hypothesis.

6.2 Summary

In this chapter the growth of (In, Ga)N buffers and (In, Ga)N heterostructures was investigated. The (In, Ga)N buffers were grown on Nanowin GaN templates and XRD RSM as well as Raman spectroscopy showed them to have an average indium content around $x = 0.19$. They exhibit a wide range of distribution of indium contents ranging from $x = 0.11$ to $x = 0.25$ and degrees of relaxation from tensily strained to fully relaxed (within the $I_{2/3}$ range). The PL emission originating in the buffer correlates with (In, Ga)N with $x = 0.2$ and therefore agrees with the XRD and Raman findings.

This (In, Ga)N buffers were used as pseudo-substrates for the growth of [In, Ga)N heterostructures (nominally 100x(1 ML InN/2 MLs GaN)]. The average indium content was determined to be $x = 0.37$ (XRD RSM) - $x = 0.39$ (Raman). The degree of relaxation is 85% (Raman) to 95% (XRD). Within the $I_{2/3}$ range the distribution of indium content was determined to range from $x = 0.26$ to $x = 0.52$. Sample SL^{I}_{100x} shows a similar average indium content $x = 0.37$ than the other (In, Ga)N heterostructures grown on ZnO [$x = 0.35$ (SL^{Z}_{100x}) and $x = 0.37$ (SL^{O}_{100x})], but the highest degree of relaxation $R = 95\%$ [compared to $R = 66\%$ (SL^{O}_{100x}) and 74% (SL^{Z}_{100x})]. The difference in degree of relaxation as well as the difference in the evolution of the *a*-lattice spacing observed through RHEED were attributed in this study to the difference in surface stoichiometry of adatoms (metal-rich versus N-rich growth). The high degree of relaxation and the monotonic increase of the *a*-lattice spacing of SL^{I}_{100x} might be due to N-rich growth conditions, compared to close to stoichiometric (SL^{Z}_{100x}) and metal-rich growth conditions (SL^{O}_{100x}).

XRD RSM and $\omega - 2\theta$ scans indicated that all samples have a wide distribution of indium contents, but no indications for a periodic structure were found. The indium content determined within $I_{2/3}$ (see chapter 5.3.3), ranges for SL^{Z}_{100x} from $x = 0.19$ - $x = 0.44$, for SL^{O}_{100x} from $x = 0.3$ to $x = 0.44$, and for SL^{I}_{100x} from $x = 0.26$ - $x = 0.52$. Using

Raman spectroscopy with different excitation wavelengths λ_{244} and λ_{405} resulted in different indium contents of the probed volumes. This is interpreted as an indication for a compositional gradient along the growth direction - the composition pulling effect.

Low temperature PL measurements showed emission around 472 nm originating in the $In_{0.19}Ga_{0.81}N$ buffer and a broader band between 590 nm and 820 nm, which correlates with Mg doping related red-luminescence. No indication was found for a SLs related luminescence.

7 Conclusions and Outlook

The bandgap of (In,Ga)N alloys covers the whole visible spectrum. These alloys are widely used as the active region of optoelectronic devices like light-emitting diodes or laser diodes [1]. But still the fabrication of device grade (In, Ga)N with medium and high indium contents is allusive, because over a wide range of indium contents, In and Ga will not mix to form homogeneous (In, Ga)N, this is called the immicibility gap. The growth of (m InN)/(n GaN) SPSLs with m and n integer numbers of MLs was proposed as a solution, to circumvent the immicibility gap. Yoshikawa *et al.* reported on the successful growth of such structures [28], which probably consists, despite other claims, of (In, Ga)N/GaN instead [36].

The problem of unintended intermixing of thin film InN/GaN to form (In, Ga)N was thought to be a strain related problem [37]. Therefore, the solution would be to grow these InN/GaN SPSLs structures on a substrate with better lattice matching. This would reduce the strain in the SPSLs. This is the basic idea behind this thesis work. The growth of InN/GaN SPSLs was thus performed on ZnO and partially relaxed (In, Ga)N buffer.

The growth on ZnO was accompanied by the challenge of hampering the strong chemical reaction of Ga and ZnO, which required a protective layer to separate Ga and ZnO. Additionally, the ZnO substrate were not delivered epi-ready and thus had to undergo a surface treatment. For this purpose an annealing procedure by Graubner *et al.* was adapted [157] and further developed to produce epi-ready ZnO surfaces, which is explained in chapter 4.

The limits of 2D growth of InN and GaN/InN on ZnO was investigated, as well as the feasibility of fabricating a protective InN layer to prevent Ga etching the ZnO substrate [see section 5.1]. Following these studies, the growth of InN/GaN SPSLs was attempted on ZnO.

In chapter 4 the ZnO substrate preparation was investigated. It was demonstrated, that smooth, stepped surfaces can be obtained for both polarities. Such good conditions can be recovered, if one starts with a rough surface, through repeated processing. A more

aggressive surface treatment, comprised of rinsing the ZnO substrate with de-ionized water in an ultra-sonic bath, can be applied with subsequent re-annealing, if unfavorable ZnO surface conditions persist.

Investigating the growth of thin InN on ZnO [see section 5.1] showed that with the growth conditions applied in this study (T: 450 °C, slightly N-rich, GR: 0.2 ML/s - 1 ML/s), the critical layer thickness h_{2D-3D} for 2D-3D growth mode transition of InN is below 2 MLs. 2D growth of GaN on top of 1.2 MLs (O-ZnO) was not possible and on 1.5 MLs (Zn-ZnO) was only possible up to 3 MLs GaN thickness. Though after 2 MLs GaN there was already indication of intermixing of InN and GaN to form (In, Ga)N. If the limits of 2D growth for InN/ZnO and GaN/InN/ZnO can not be expanded it would limit the theoretically possible PL emission range to 1.3 eV - 1.7 eV [211]. It has to be noted that the experimentally found band gaps are higher than the theoretically calculated ones [211]. The onset of 2D-3D transition (h_{2D-3D}) coincides with the onset of main relaxation (h_{crit}), which suggest that surface undulations may play an important role in relieving strain in ML thin InN and GaN/InN layers grown on ZnO. These results indicate that the growth might proceed in a Stranski-Krastanov mode.

A feature frequently found for thin film InN on ZnO and GaN/InN/ZnO is 3D structures that reside in hexagonal pits [see section 5.1]. It is unclear what the exact mechanism of formation is. It may be, that the 3D structures form first, through a Stranski-Krastanov like mechanism, and cause then the etching of the ZnO substrate, possibly through a change in the stress field beneath the 3D structures, leading to the formation of hexagonal pits. Alternatively, the etching of the ZnO substrate and the formation of hexagonal pits might come first and is followed by material accumulating in these pits which then form the 3D structures.

After establishing the limitations for pseudomorphic growth of InN and GaN/InN on ZnO the growth of hundred periods of (1 ML InN)/(2 MLs GaN) heterostructures on both polarities of ZnO substrates was attempted. *In-situ* investigations of the growth using RHEED indicated a 2D-3D growth mode transition close to 9 MLs of heterostructure thickness for all heterostructures. The structural analysis using XRD $\omega - 2\theta$ and RSM showed that the (In, Ga)N heterostructures grown on ZnO (SL^{O}_{100x} and SL^{Z}_{100x}) exhibited no indication of a periodic structure. Fitting the $\omega - 2\theta$ was possible assuming an (In, Ga)N layer instead.

XRD RSM, $\omega - 2\theta$ and Raman spectroscopy were applied in combination to investigate the chemical composition, strain state and structure of the (In, Ga)N buffer and heterostructures (see section 5.3). All heterostructures investigated showed evidence of com-

positional inhomogeneity (see section 5.3.3) and composition pulling effect (see section 5.3.4), with an average indium content that was lower than the indium content found in the upper parts of the layer (see section 5.3.4). In addition, also strain inhomogeneities detrimental for opto-electronic devices were found (see section 5.3.3). This composition pulling along the growth direction makes it difficult to evaluate whether strain engineering, applied in this study, was successful in increasing the indium content of ML thin (In, Ga)N layers. Results from XRD RSM, $\omega - 2\theta$ and Raman spectroscopy suggest that the average indium content of the (In, Ga)N heterostructures is between $x = 0.35$ and $x = 0.37$ and between $x = 0.47$ and $x = 0.51$ in the upper parts of the samples (Raman). This suggests that the indium content in the part of the sample closer to the substrate/epilayer interface may be below $x = 0.35$ to $x = 0.37$.

A second type of pseudo-substrate was prepared, namely 300 nm thick $In_{0.19}Ga_{0.81}N$ buffers. XRD RSM and RHEED investigations indicate an indium composition of the upper part of the substrate close to $x = 0.19$ - $x = 0.25$. With degrees of relaxation, that depending on the assumed indium content range from $R = 25\%$ for $x = 0.19$ to nearly full relaxation for $x = 0.25$. RHEED patterns further indicated a 2D surface at the end of growth, which was confirmed by AFM.

The growth of hundred periods of (1 ML InN)/(2 MLs GaN) heterostructures was attempted on these 300 nm thick $In_{0.19}Ga_{0.81}N$ buffers. XRD RSM, $\omega - 2\theta$ and Raman spectroscopy showed results that are similar to the heterostructures grown on ZnO. No indication for a periodic structure was found. The average indium content is $x = 0.37$ (XRD RSM, see section 6.1.1) to $x = 0.39$ (Raman, see section 6.1.3). The average indium content in the upper parts of the sample is $x = 0.53$ (Raman, see section 6.1.3). The 2D-3D growth mode transition estimated through RHEED investigations was close to 9 MLs.

Comparing the results for all heterostructures it is possible to identify similarities (indium content, PL, possible composition pulling effect), but also differences. The average degree of relaxation determined by XRD RSM and the final *a*-lattice spacing determined by RHEED is $R = 65\%$, a= 3.30 Å (SL^{O}_{100x}), $R = 73\%$, a= 3.33 Å (SL^{Z}_{100x}) and $R = 95\%$, a= 3.37 Å (SL^{I}_{100x}). This might be explained by the possible unintentional difference in growth conditions. The surfaces of these three heterostructures were investigated with OM and AFM. SL^{O}_{100x} showed clear signs of metal droplets at the surface (see section 5.3.1), low density for SL^{Z}_{100x} (see section 5.3.1) and no droplets for SL^{I}_{100x} (see section 6.1.1). This might show that SL^{O}_{100x} was grown with slightly metal-rich conditions, SL^{Z}_{100x} close to stoichiometry and SL^{I}_{100x} slightly nitrogen-rich. This would explain the difference in relaxation behavior, since nitrogen-rich growth is associated with rougher, defect-richer layers that show higher degrees of relaxation compared to metal-rich grown layers.

These possible difference in growth condition was unintentional, all layers were intended to be grown with slightly nitrogen-rich conditions, to minimize the risk of chemical reactions between ZnO and In and Ga.

The surfaces of samples composed of thin film InN and GaN/InN on ZnO showed no indication for metal-rich growth (indium droplets). SL^{O}_{100x} on the other hand had droplets on the surface. The possible N-rich growth of InN/O-ZnO (Gr: 1 ML/s and 0.2 ML/s) and GaN/InN/O-ZnO might be the reason why no pseudomorphic growth of thin InN layers was found for these samples (see chapter 5.1). Comparing the growth of the first ML of SL^{O}_{100x} (see chapter 5.3) with the thin InN layers (Gr: 1 ML/s and 0.2 ML/s) and GaN/InN on O-ZnO shows that for metal-rich grown SL^{O}_{100x} pseudomorphic growth was found. Also InN/O-ZnO (GR: 0.5 ML/s) shows pseudomorphic growth up until 1 ML layer thickness. All InN/Zn-ZnO and GaN/InN/Zn-ZnO samples showed pseudomorphic growth during the first 1-3 MLs (for details see chapter 5.1). This results suggest that the polarity and the surface stoichiometry of adatoms might influence the growth mode and that pseudomorphic growth of ML thin InN on both polarities is possible.

All heterostructure samples grown on ZnO, as well as the InN/ZnO and GaN/InN/ZnO samples that exceeded the critical layer thickness showed ZnO etching (3D structures in hexagonal pits), even the one grown with possibly stoichiometric (SL^{Z}_{100x}) or nitrogen-rich conditions. Since stoichiometric and nitrogen-rich growth does not seem to prevent this etching and metal-rich growth seems to yield smoother surfaces and less relaxation, it might be advisable to grow slightly metal-rich. A possible compromise might be to grow a few MLs at stoichiometry and then open a second indium cell for a short duration, to deposit a metal adlayer and close the second indium cell again and continue growth under stoichiometry.

It was stressed already, that the possibly existing composition pulling effect makes it difficult to make a clear statement about the effects of the applied strain engineering by using substrates that are more lattice-matched to InN. The average indium content of the heterostructures was estimated to be close to $x = 0.35$ - $x = 0.37$, in the upper parts at average up to $x = 0.47$ - $x = 0.53$. This suggests, that the indium content close to the epi-layer/substrate interface is below $x = 0.35$ - $x = 0.37$. In fact, the fitting of the $\omega - 2\theta$ scan of SL^{I}_{100x} resulted in a layered structure for the (In, Ga)N heterostructure with a suggested indium content of $x = 0.26$ at the epi-layer/substrate interface. This would be in line with the findings of Lymperakis *et al.* [160]. Though as the growth continues and probably due to relaxation the indium incorporation into the (In, Ga)N heterostructures seems to increase, even up to above $x = 0.50$ as Raman investigations suggests for the upper parts of the samples. This is not necessarily contradicting the

findings of Lymperakis *et al.* since their proposed limit of 25% for indium incorporation into (In, Ga)N quantum wells concerns coherently strained layers, whereas the findings of this study suggest considerable relaxation up to $R = 100\%$ (see section 5.3 and 6.1.1).

The findings of this study suggest serious constraints for the possible growth of (In, Ga)N heterostructures suitable for optical devices. The small critical thickness for 2D-3D growth mode transition may challenge the possibility of periodic (In, Ga)N heterostructures by growing thicker wells or barriers. More research is necessary to determine the exact mechanism by which the 3D structures, residing in hexagonal pits, form.

Cho *et al.* reported on the growth of InN on O-ZnO and found that the crystalline quality depended strongly on the growth temperature [129]. Growth of bulk InN on O-ZnO at 350 °C resulted in three-dimensional growth, formation of hexagonal and cubic phases and a rough surface with RMS = 4 nm, combined with a rather broad FWHM of the InN (0002) peak in the XRD $\omega - 2\theta$ measurement. At 450 °C growth temperature, the growth was two-dimensional, the surface roughness decreased to 3.3 nm, only hexagonal phases formed, the FWHM of InN (0002) decreased, but some nano-scale protrusions formed at the InN/ZnO interface. Finally for 550 °C the surface was rather smooth with a RMS of 1 nm, the FWHM of InN (0002) was similar to the results found for growth at 450 °C, but large voids and In_2O_3 formed at the InN/ZnO interface. This indicates that growing InN on ZnO at 550 °C could yield smoother interfaces if chemical reactions between ZnO and InN (or GaN) could be prevented. If a protective layer could be established on ZnO that prevents that, it may open up the possibility to growth periodic (In, Ga)N heterostructures at higher temperatures and this potentially with a higher crystalline quality.

Bibliography

[1]S. Nakamura, M. Senoh, S. Nagahama, N. Iwasa, T. Yamada, T. Matsushita, H. Kiyoku, and Y. Sugimoto, "InGaN Multi-Quantum-Well-Structure Laser Diodes with Cleaved Mirror Cavity Facets", Jpn. J. Appl. Phys. **35**, L217–L220 (1996) 10.1143/JJAP.35.L217.

[2]K. Kojima, M. Funato, Y. Kawakami, S. Masui, S. Nagahama, and T. Mukai, "Stimulated emission at 474 nm from an InGaN laser diode structure grown on a (11$\bar{2}$2) GaN substrate", Appl. Phys. Lett. **91**, 251107 (2007) 10.1063/1.2799876.

[3]D. Queren, A. Avramescu, G. Brüderl, A. Breidenassel, M. Schillgalies, S. Lutgen, and U. Strauß, "500 nm electrically driven InGaN based laser diodes", Appl. Phys. Lett. **94**, 081119 (2009) 10.1063/1.3089573.

[4]Y. Ishitani, H. Masuyama, W. Terashima, M. Yoshitani, N. Hashimoto, S. Che, and A. Yoshikawa, "Bandgap energy of InN and its temperature dependence", Phys. status solidi **2**, 2276–2280 (2005) 10.1002/pssc.200461433.

[5]J. F. Muth, J. H. Lee, I. K. Shmagin, R. M. Kolbas, H. C. Casey, B. P. Keller, U. K. Mishra, and S. P. DenBaars, "Absorption coefficient, energy gap, exciton binding energy, and recombination lifetime of GaN obtained from transmission measurements", Appl. Phys. Lett. **71**, 2572–2574 (1997) 10.1063/1.120191.

[6]H. Teisseyre, P. Perlin, T. Suski, I. Grzegory, S. Porowski, J. Jun, A. Pietraszko, and T. D. Moustakas, "Temperature dependence of the energy gap in GaN bulk single crystals and epitaxial layer", J. Appl. Phys. **76**, 2429–2434 (1994) 10.1063/1.357592.

[7]M. Siekacz, M. Sawicka, H. Turski, G. Cywiński, A. Khachapuridze, P. Perlin, T. Suski, M. Boćkowski, J. Smalc-Koziorowska, M. Kryśko, R. Kudrawiec, M. Syperek, J. Misiewicz, Z. Wasilewski, S. Porowski, and C. Skierbiszewski, "Optically pumped 500 nm InGaN green lasers grown by plasma-assisted molecular beam epitaxy", J. Appl. Phys. **110**, 063110 (2011) 10.1063/1.3639292.

[8]C. S. Gallinat, G. Koblmüller, J. S. Brown, and J. S. Speck, "A growth diagram for plasma-assisted molecular beam epitaxy of In-face InN", J. Appl. Phys. **102**, 064907 (2007) 10.1063/1.2781319.

[9]C. S. Gallinat, G. Koblmüller, J. S. Brown, S. Bernardis, J. S. Speck, G. D. Chern, E. D. Readinger, H. Shen, and M. Wraback, "In-polar InN grown by plasma-assisted molecular beam epitaxy", Appl. Phys. Lett. **89**, 032109 (2006) 10.1063/1.2234274.

[10]S. Fernández-Garrido, G. Koblmüller, E. Calleja, and J. S. Speck, "In situ GaN decomposition analysis by quadrupole mass spectrometry and reflection high-energy electron diffraction", J. Appl. Phys. **104**, 033541 (2008) 10.1063/1.2968442.

[11]N. Grandjean, J. Massies, F. Semond, S. Y. Karpov, and R. A. Talalaev, "GaN evaporation in molecular-beam epitaxy environment", Appl. Phys. Lett. **74**, 1854–1856 (1999) 10.1063/1.123691.

[12]S. Guha, N. A. Bojarczuk, and D. W. Kisker, "Surface lifetimes of Ga and growth behavior on GaN (0001) surfaces during molecular beam epitaxy", Appl. Phys. Lett. **69**, 2879–2881 (1996) 10.1063/1.117349.

[13]B. Heying, R. Averbeck, L. F. Chen, E. Haus, H. Riechert, and J. S. Speck, "Control of GaN surface morphologies using plasma-assisted molecular beam epitaxy", J. Appl. Phys. **88**, 1855–1860 (2000) 10.1063/1.1305830.

[14]C. S. Gallinat, G. Koblmüller, J. S. Brown, and J. S. Speck, "A growth diagram for plasma-assisted molecular beam epitaxy of In-face InN", J. Appl. Phys. **102**, 064907 (2007) 10.1063/1.2781319.

[15]C. Adelmann, J. Brault, D. Jalabert, P. Gentile, H. Mariette, G. Mula, and B. Daudin, "Dynamically stable gallium surface coverages during plasma-assisted molecular-beam epitaxy of (0001) GaN", J. Appl. Phys. **91**, 9638 (2002) 10.1063/1.1471923.

[16]I. Ho and G. Stringfellow, "Solid phase immiscibility in GaInN", Appl. Phys. Lett. **69**, 2701 (1996) 10.1063/1.117683.

[17]J. Zheng and J. Kang, "Theoretical study of phase separation in wurtzite InGaN", Mater. Sci. Semicond. Process. **9**, 341–344 (2006) 10.1016/j.mssp.2006.01.014.

[18]D. Doppalapudi, S. N. Basu, K. F. Ludwig Jr., and T. D. Moustakas, "Phase Separation and Ordering in InGaN alloys", MRS Proc. **512**, 431 (1998) 10.1557/PROC-512-431.

[19]M. Gladysiewicz and R. Kudrawiec, "Theoretical studies of the influence of structural inhomogeneities on the radiative recombination time in polar InGaN quantum wells", Phys. status solidi **209**, 752–760 (2012) 10.1002/pssa.201127485.

[20]F. A. Ponce, S. Srinivasan, A. Bell, L. Geng, R. Liu, M. Stevens, J. Cai, H. Omiya, H. Marui, and S. Tanaka, "Microstructure and electronic properties of InGaN alloys", Phys. status solidi **240**, 273–284 (2003) 10.1002/pssb.200303527.

[21]D. Holec, P. Costa, M. Kappers, and C. Humphreys, "Critical thickness calculations for InGaN/GaN", J. Cryst. Growth **303**, 314–317 (2007) 10.1016/j.jcrysgro.2006.12.054.

[22]J. C. Zhang, D. S. Jiang, Q. Sun, J. F. Wang, Y. T. Wang, J. P. Liu, J. Chen, R. Q. Jin, J. J. Zhu, H. Yang, T. Dai, and Q. J. Jia, "Influence of dislocations on photoluminescence of InGaN/GaN multiple quantum wells", Appl. Phys. Lett. **87**, 071908 (2005) 10.1063/1.2012531.

[23]R. Liu, J. Mei, S. Srinivasan, H. Omiya, F. A. Ponce, D. Cherns, Y. Narukawa, and T. Mukai, "Misfit Dislocation Generation in InGaN Epilayers on Free-Standing GaN", Jpn. J. Appl. Phys. **45**, L549–L551 (2006) 10.1143/JJAP.45.L549.

[24]C. A. Parker, J. C. Roberts, S. M. Bedair, M. J. Reed, S. X. Liu, and N. A. El-Masry, "Determination of the critical layer thickness in the InGaN/GaN heterostructures", Appl. Phys. Lett. **75**, 2776 (1999) 10.1063/1.125146.

[25]C. Bazioti, E. Papadomanolaki, T. Kehagias, T. Walther, J. Smalc-Koziorowska, E. Pavlidou, P. Komninou, T. Karakostas, E. Iliopoulos, and G. P. Dimitrakopulos, "Defects, strain relaxation, and compositional grading in high indium content InGaN epilayers grown by molecular beam epitaxy", J. Appl. Phys. **118**, 155301 (2015) 10.1063/1.4933276.

[26]K. Hiramatsu, Y. Kawaguchi, M. Shimizu, N. Sawaki, T. Zheleva, R. F. Davis, H. Tsuda, W. Taki, N. Kuwano, and K. Oki, "The Composition Pulling Effect in MOVPE Grown InGaN on GaN and AlGaN and its TEM Characterization", MRS Internet J. Nitride Semicond. Res. **2**, e6 (1997) 10.1557/S1092578300001320.

[27]Y. Lin, K. Ma, C. Hsu, S. Feng, Y. Cheng, C. Liao, C. C. Yang, C. Chou, C. Lee, and J. Chyi, "Dependence of composition fluctuation on indium content in InGaN/GaN multiple quantum wells", Appl. Phys. Lett. **77**, 2988–2990 (2000) 10.1063/1.1323542.

[28]A. Yoshikawa, S. B. Che, W. Yamaguchi, H. Saito, X. Q. Wang, Y. Ishitani, and E. S. Hwang, "Proposal and achievement of novel structure InN/GaN multiple quantum wells consisting of 1 ML and fractional monolayer InN wells inserted in GaN matrix", Appl. Phys. Lett. **90**, 073101 (2007) 10.1063/1.2456132.

[29]A. Yoshikawa, S. B. Che, N. Hashimoto, H. Saito, Y. Ishitani, and X. Q. Wang, "Fabrication and characterization of novel monolayer InN quantum wells in a GaN matrix", J. Vac. Sci. Technol. B, Nanotechnol. Microelectron. Mater. Process. Meas. Phenom. **26**, 1551 (2008) 10.1116/1.2957620.

[30]E. Dimakis, A. Y. Nikiforov, C. Thomidis, L. Zhou, D. J. Smith, J. Abell, C.-K. Kao, and T. D. Moustakas, "Growth and properties of near-UV light emitting diodes based on InN/GaN quantum wells", Phys. Status Solidi **205**, 1070–1073 (2008) 10.1002/pssa.200778742.

[31]S. Ko, H. Kwack, C. Park, Y. Yoo, S. Kwon, H. Jin Kim, E. Yoon, L. Si Dang, and Y. Cho, "Strong carrier localization and diminished quantum-confined Stark effect in ultrathin high-indium-content InGaN quantum wells with violet light emission", Appl. Phys. Lett. **103**, 222104 (2013) 10.1063/1.4833917.

[32]J. Bai, T. Wang, and S. Sakai, "Influence of the quantum-well thickness on the radiative recombination of InGaN/GaN quantum well structures", J. Appl. Phys. **88**, 4729 (2000) 10.1063/1.1311831.

[33]I. Gorczyca, K. Skrobas, T. Suski, N. E. Christensen, and A. Svane, "Band gaps in InN/GaN superlattices: Nonpolar and polar growth directions", J. Appl. Phys. **114**, 223102 (2013) 10.1063/1.4843015.

[34]M. S. Miao, Q. M. Yan, and C. G. Van de Walle, "Electronic structure of a single-layer InN quantum well in a GaN matrix", Appl. Phys. Lett. **102**, 102103 (2013) 10.1063/1.4794986.

[35]G. Staszczak, I. Gorczyca, T. Suski, X. Q. Wang, N. E. Christensen, A. Svane, E. Dimakis, and T. D. Moustakas, "Photoluminescence and pressure effects in short period InN/nGaN superlattices", J. Appl. Phys. **113**, 123101 (2013) 10.1063/1.4796101.

[36]T. Suski, T. Schulz, M. Albrecht, X. Q. Wang, I. Gorczyca, K. Skrobas, N. E. Christensen, and A. Svane, "The discrepancies between theory and experiment in the optical emission of monolayer In(Ga)N quantum wells revisited by transmission electron microscopy", Appl. Phys. Lett. **104**, 182103 (2014) 10.1063/1.4875558.

[37]A. I. Duff, L. Lymperakis, and J. Neugebauer, "Understanding and controlling indium incorporation and surface segregation on $In_xGa_{1-x}N$ surfaces: ab initio approach", Phys. Rev. B **89**, 085307 (2014) 10.1103/PhysRevB.89.085307.

[38]R. Reeber, "Lattice parameters of ZnO from 4.2 to 296K", J. Appl. Phys. **41**, 5063–5066 (1970) 10.1063/1.1658600.

[39]E. H. Kisi and M. M. Elcombe, "u parameters for the wurtzite structure of ZnS and ZnO using powder neutron diffraction", Acta Crystallogr. Sect. C Cryst. Struct. Chem. **45**, 1867–1870 (1989) 10.1107/S0108270189004269.

[40]S. Desgreniers, "High-density phases of ZnO: Structural and compressive parameters", Phys. Rev. B **58**, 14102–14105 (1998) 10.1103/PhysRevB.58.14102.

[41]E. Dimakis, E. Iliopoulos, K. Tsagaraki, A. Adikimenakis, and A. Georgakilas, "Biaxial strain and lattice constants of InN (0001) films grown by plasma-assisted molecular beam epitaxy", Appl. Phys. Lett. **88**, 191918 (2006) 10.1063/1.2202136.

[42]X. Cai, K. Cheung, A. Djurišić, and M. Xie, "Growth of cubic and hexagonal InN nanorods", Mater. Lett. **61**, 1563–1566 (2007) 10.1016/j.matlet.2006.07.079.

[43]S. Yamaguchi, M. Kariya, S. Nitta, T. Takeuchi, C. Wetzel, H. Amano, and I. Akasaki, "Structural properties of InN on GaN grown by metalorganic vapor-phase epitaxy", J. Appl. Phys. **85**, 7682–7688 (1999) 10.1063/1.370571.

[44]H. Schulz and K. Thiemann, "Crystal structure refinement of AlN and GaN", Solid State Commun. **23**, 815–819 (1977) 10.1016/0038-1098(77)90959-0.

[45]V. Petkov, M. Gateshki, J. Choi, E. G. Gillan, and Y. Ren, "Structure of nanocrystalline GaN from X-ray diffraction, Rietveld and atomic pair distribution function analyses", J. Mater. Chem. **15**, 4654 (2005) 10.1039/b509577h.

[46]Z. K. Heiba, S. Ahmed, A. Abo-Shama, and K. El-Sayed, "The effect of Al and Gd doping on the structure, microstructure and thermal expansion of gallium nitride (GaN)", Zeitschrift für Krist. Suppl. **23**, 581–586 (2006) 10.1524/zksu.2006.suppl_23.581.

[47]R. Averbeck and H. Riechert, "Quantitative Model for the MBE-Growth of Ternary Nitrides", Phys. status solidi **176**, 301–305 (1999) 10.1002/(SICI)1521-396X(199911)176:1<301::AID-PSSA301>3.0.CO;2-H.

[48]K. Xu, W. Terashima, T. Hata, N. Hashimoto, M. Yoshitani, B. Cao, Y. Ishitani, and A. Yoshikawa, "Comparative study of InN growth on Ga- and N-polarity GaN templates by molecular-beam epitaxy", Phys. status solidi **2817**, 2814–2817 (2003) 10.1002/pssc.200303456.

[49]R. Dingle, D. D. Sell, S. E. Stokowski, and M. Ilegems, "Absorption, Reflectance, and Luminescence of GaN Epitaxial Layers", Phys. Rev. B **4**, 1211–1218 (1971) 10.1103/PhysRevB.4.1211.

[50]M. Ilegems, R. Dingle, and R. A. Logan, "Luminescence of Zn- and Cd-doped GaN", J. Appl. Phys. **43**, 3797–3800 (1972) 10.1063/1.1661813.

[51]R. Langer, J. Simon, V. Ortiz, N. T. Pelekanos, A. Barski, R. André, and M. Godlewski, "Giant electric fields in unstrained GaN single quantum wells", Appl. Phys. Lett. **74**, 3827–3829 (1999) 10.1063/1.124193.

[52]P. Lefebvre, J. Allègre, B. Gil, H. Mathieu, N. Grandjean, M. Leroux, J. Massies, and P. Bigenwald, "Time-resolved photoluminescence as a probe of internal electric fields in GaN-(GaAl)N quantum wells", Phys. Rev. B **59**, 15363–15367 (1999) 10.1103/PhysRevB.59.15363.

[53]A. Hangleiter, F. Hitzel, S. Lahmann, and U. Rossow, "Composition dependence of polarization fields in GaInN/GaN quantum wells", Appl. Phys. Lett. **83**, 1169–1171 (2003) 10.1063/1.1601310.

[54]T. Hofmann, T. Chavdarov, V. Darakchieva, H. Lu, W. J. Schaff, and M. Schubert, "Anisotropy of the Γ-point effective mass and mobility in hexagonal InN", Phys. status solidi **3**, 1854–1857 (2006) 10.1002/pssc.200565467.

[55]S. P. Fu and Y. F. Chen, "Effective mass of InN epilayers", Appl. Phys. Lett. **85**, 1523–1525 (2004) 10.1063/1.1787615.

[56]J. Wu, W. Walukiewicz, W. Shan, K. M. Yu, J. W. Ager, E. E. Haller, H. Lu, and W. J. Schaff, "Effects of the narrow band gap on the properties of InN", Phys. Rev. B **66**, 201403 (2002) 10.1103/PhysRevB.66.201403.

[57]T. Inushima, M. Higashiwaki, and T. Matsui, "Optical properties of Si-doped InN grown on sapphire (0001)", Phys. Rev. B **68**, 235204 (2003) 10.1103/PhysRevB.68.235204.

[58]I. Vurgaftman and J. R. Meyer, "Band parameters for nitrogen-containing semiconductors", J. Appl. Phys. **94**, 3675–3696 (2003) 10.1063/1.1600519.

[59]B. Rheinländer and H. Neumann, "Plasma Faraday Rotation in n-Type GaN", Phys. status solidi **64**, K123–K125 (1974) 10.1002/pssb.2220640254.

[60]E. Silveira, J. A. Freitas, M. Kneissl, D. W. Treat, N. M. Johnson, G. A. Slack, and L. J. Schowalter, "Near-bandedge cathodoluminescence of an AlN homoepitaxial film", Appl. Phys. Lett. **84**, 3501–3503 (2004) 10.1063/1.1738929.

[61]P. Rinke, M. Winkelnkemper, A. Qteish, D. Bimberg, J. Neugebauer, and M. Scheffler, "Consistent set of band parameters for the group-III nitrides AlN, GaN, and InN", Phys. Rev. B **77**, 075202 (2008) 10.1103/PhysRevB.77.075202.

[62]G. Koblmüller, C. S. Gallinat, S. Bernardis, J. S. Speck, G. D. Chern, E. D. Readinger, H. Shen, and M. Wraback, "Optimization of the surface and structural quality of N-face InN grown by molecular beam epitaxy", Appl. Phys. Lett. **89**, 071902 (2006) 10.1063/1.2335685.

[63]B. Heying, I. Smorchkova, C. Poblenz, C. Elsass, P. Fini, S. Den Baars, U. Mishra, and J. S. Speck, "Optimization of the surface morphologies and electron mobilities in GaN grown by plasma-assisted molecular beam epitaxy", Appl. Phys. Lett. **77**, 2885–2887 (2000) 10.1063/1.1322370.

[64]B. E. Foutz, S. K. O'Leary, M. S. Shur, and L. F. Eastman, "Transient electron transport in wurtzite GaN, InN, and AlN", J. Appl. Phys. **85**, 7727–7734 (1999) 10.1063/1.370577.

[65]A. G. Bhuiyan, A. Hashimoto, and A. Yamamoto, "Indium nitride (InN): A review on growth, characterization, and properties", J. Appl. Phys. **94**, 2779–2808 (2003) 10.1063/1.1595135.

[66]J. Sumner, S. D. Bakshi, R. A. Oliver, M. J. Kappers, and C. J. Humphreys, "Unintentional doping in GaN assessed by scanning capacitance microscopy", Phys. status solidi **245**, 896–898 (2008) 10.1002/pssb.200778567.

[67]Z. Yang, L. K. Li, and W. I. Wang, "GaN grown by molecular beam epitaxy at high growth rates using ammonia as the nitrogen source", Appl. Phys. Lett. **67**, 1686–1688 (1995) 10.1063/1.115057.

[68]T. Zhu and R. A. Oliver, "Unintentional doping in GaN", Phys. Chem. Chem. Phys. **14**, 9558–9573 (2012) 10.1039/c2cp40998d.

[69]J. L. Lyons, A. Janotti, and C. G. Van de Walle, "Carbon impurities and the yellow luminescence in GaN", Appl. Phys. Lett. **97**, 152108 (2010) 10.1063/1.3492841.

[70]R. Armitage, W. Hong, Q. Yang, H. Feick, J. Gebauer, E. R. Weber, S. Hautakangas, and K. Saarinen, "Contributions from gallium vacancies and carbon-related defects to the "yellow luminescence" in GaN", Appl. Phys. Lett. **82**, 3457–3459 (2003) 10.1063/1.1578169.

[71]I. V. Markoc, *Crystal growth for beginners - Fundamentals of Nucleation, Crystal Growth and Epitaxy*, 1 (World Scientific Publishing Co. Pte. Ltd., Singapore, Apr. 2003), 10.1107/S0021889803028358.

[72]I. Daruka, J. Tersoff, and A.-L. Barabási, "Shape Transition in Growth of Strained Islands", Phys. Rev. Lett. **82**, 2753–2756 (1999) 10.1103/PhysRevLett.82.2753.

[73]M. Copel, M. C. Reuter, E. Kaxiras, and R. M. Tromp, "Surfactants in epitaxial growth", Phys. Rev. Lett. **63**, 632–635 (1989) 10.1103/PhysRevLett.63.632.

[74]R. I. G. Uhrberg, R. D. Bringans, R. Z. Bachrach, and J. E. Northrup, "Symmetric arsenic dimers on the Si(100) surface", Phys. Rev. Lett. **56**, 520–523 (1986) 10.1103/PhysRevLett.56.520.

[75]B. Daudin, G. Feuillet, G. Mula, H. Mariette, J. L. Rouviére, N. Pelekanos, G. Fishman, C. Adelmann, and J. Simon, "Epitaxial Growth of GaN, AlN and InN: 2D/3D Transition and Surfactant Effects", Phys. status solidi **176**, 621–627 (1999) 10.1002/(SICI)1521-396X(199911)176:1<621::AID-PSSA621>3.0.CO;2-Y.

[76]T. Yang, K. Uchida, T. Mishima, J. Kasai, and J. Gotoh, "Control of Initial Nucleation by Reducing the V/III Ratio during the Early Stages of GaN Growth", Phys. status solidi **180**, 45–50 (2000) 10.1002/1521-396X(200007)180:1<45::AID-PSSA45>3.0.CO;2-5.

[77]R. A. Oliver, M. J. Kappers, C. J. Humphreys, and G. A. D. Briggs, "Growth modes in heteroepitaxy of InGaN on GaN", J. Appl. Phys. **97**, 013707 (2005) 10.1063/1.1823581.

[78]S. Kim, J. Oh, J. Kang, D. Kim, J. Won, J. Kim, and H. Cho, "Two-step growth of high quality GaN using V/III ratio variation in the initial growth stage", J. Cryst. Growth **262**, 7–13 (2004) 10.1016/j.jcrysgro.2003.10.009.

[79]I. Markov and R. Kaischew, "Influence of the supersaturation on the mode of thin film growth", Krist. und Tech. **11**, 685–697 (1976) 10.1002/crat.19760110702.

[80]I. Daruka and A. Barabási, "Dislocation-Free Island Formation in Heteroepitaxial Growth: A Study at Equilibrium", Phys. Rev. Lett. **79**, 3708–3711 (1997) 10.1103/PhysRevLett.79.3708.

[81]Y. F. Ng, Y. G. Cao, M. H. Xie, X. L. Wang, and S. Y. Tong, "Growth mode and strain evolution during InN growth on GaN(0001) by molecular-beam epitaxy", Appl. Phys. Lett. **81**, 3960–3962 (2002) 10.1063/1.1523638.

[82]P. Waltereit, O. Brandt, A. Trampert, M. Ramsteiner, M. Reiche, M. Qi, and K. H. Ploog, "Influence of AlN nucleation layers on growth mode and strain relief of GaN grown on 6H–SiC(0001)", Appl. Phys. Lett. **74**, 3660–3662 (1999) 10.1063/1.123214.

[83]W. K. Burton, N. Cabrera, and F. C. Frank, "The Growth of Crystals and the Equilibrium Structure of their Surfaces", Philos. Trans. R. Soc. A Math. Phys. Eng. Sci. **243**, 299–358 (1951) 10.1098/rsta.1951.0006.

[84]R. Smith, R. M. Feenstra, D. W. Greve, J. Neugebauer, and J. E. Northrup, "Reconstructions of the GaN(000-1) Surface", Phys. Rev. Lett. **79**, 3934–3937 (1997) 10.1103/PhysRevLett.79.3934.

[85]C. K. Gan and D. J. Srolovitz, "First-principles study of wurtzite InN (0001) and (000-1) surfaces", Phys. Rev. B **74**, 115319 (2006) 10.1103/PhysRevB.74.115319.

[86]J. E. Northrup, J. Neugebauer, R. M. Feenstra, and A. R. Smith, "Structure of GaN(0001): The laterally contracted Ga bilayer model", Phys. Rev. B **61**, 9932–9935 (2000) 10.1103/PhysRevB.61.9932.

[87]X. Wang, S.-B. Che, Y. Ishitani, and A. Yoshikawa, "Step-Flow Growth of In-Polar InN by Molecular Beam Epitaxy", Jpn. J. Appl. Phys. **45**, L730–L733 (2006) 10.1143/JJAP.45.L730.

[88]W. Yamaguchi, S. Che, N. Kikukawa, Y. Ishitani, and A. Yoshikawa, "Towards fabrication of In-polar InN films and InN/GaN MQWs", Phys. status solidi **3**, 1511–1514 (2006) 10.1002/pssc.200565353.

[89]E. J. Tarsa, B. Heying, X. H. Wu, P. Fini, S. P. DenBaars, and J. S. Speck, "Homoepitaxial growth of GaN under Ga-stable and N-stable conditions by plasma-assisted molecular beam epitaxy", J. Appl. Phys. **82**, 5472–5479 (1997) 10.1063/1.365575.

[90]F. Widmann, B. Daudin, G. Feuillet, N. Pelekanos, and J. L. Rouvière, "Improved quality GaN grown by molecular beam epitaxy using In as a surfactant", Appl. Phys. Lett. **73**, 2642–2644 (1998) 10.1063/1.122539.

[91]P. Hacke, G. Feuillet, H. Okumura, and S. Yoshida, "Monitoring surface stoichiometry with the (2x2) reconstruction during growth of hexagonal-phase GaN by molecular beam epitaxy", Appl. Phys. Lett. **69**, 2507–2509 (1996) 10.1063/1.117722.

[92]G. Mula, C. Adelmann, S. Moehl, J. Oullier, and B. Daudin, "Surfactant effect of gallium during molecular-beam epitaxy of GaN on AlN (0001)", Phys. Rev. B **64**, 195406 (2001) 10.1103/PhysRevB.64.195406.

[93]G. Koblmüller, R. Averbeck, H. Riechert, and P. Pongratz, "Direct observation of different equilibrium Ga adlayer coverages and their desorption kinetics on GaN (0001) and (000-1) surfaces", Phys. Rev. B **69**, 035325 (2004) 10.1103/PhysRevB.69.035325.

[94]C. Kruse, S. Einfeldt, T. Böttcher, and D. Hommel, "In as a surfactant for the growth of GaN (0001) by plasma-assisted molecular-beam epitaxy", Appl. Phys. Lett. **79**, 3425–3427 (2001) 10.1063/1.1419232.

[95]T. Zywietz, J. Neugebauer, and M. Scheffler, "Adatom diffusion at GaN (0001) and (000-1) surfaces", Appl. Phys. Lett. **73**, 487–489 (1998) 10.1063/1.121909.

[96]D. Segev and C. G. Van de Walle, "Surface reconstructions on InN and GaN polar and nonpolar surfaces", Surf. Sci. **601**, L15–L18 (2007) 10.1016/j.susc.2006.12.018.

[97]C. Kruse, S. Einfeldt, T. Böttcher, D. Hommel, D. Rudloff, and J. Christen, "Spatially modified layer properties related to the formation of gallium droplets on GaN(0001) surfaces during plasma-assisted molecular-beam epitaxy", Appl. Phys. Lett. **78**, 3827–3829 (2001) 10.1063/1.1377629.

[98]J. Neugebauer, T. K. Zywietz, M. Scheffler, J. E. Northrup, H. Chen, and R. M. Feenstra, "Adatom Kinetics On and Below the Surface: The Existence of a New Diffusion Channel", Phys. Rev. Lett. **90**, 056101 (2003) 10.1103/PhysRevLett.90.056101.

[99]H. Chen, R. M. Feenstra, J. E. Northrup, T. Zywietz, J. Neugebauer, and D. W. Greve, "Surface structures and growth kinetics of InGaN(0001) grown by molecular beam epitaxy", J. Vac. Sci. Technol. B Microelectron. Nanom. Struct. **18**, 2284 (2000) 10.1116/1.1306296.

[100]R. Averbeck and H. Riechert, "Quantitative Model for the MBE-Growth of Ternary Nitrides", Phys. status solidi **176**, 301–305 (1999) 10.1002/(SICI)1521-396X(199911)176:1<301::AID-PSSA301>3.0.CO;2-H.

[101]C. Adelmann, R. Langer, G. Feuillet, and B. Daudin, "Indium incorporation during the growth of InGaN by molecular-beam epitaxy studied by reflection high-energy electron diffraction intensity oscillations", Appl. Phys. Lett. **75**, 3518–3520 (1999) 10.1063/1.125374.

[102]T. Yamaguchi and Y. Nanishi, "Indium Droplet Elimination by Radical Beam Irradiation for Reproducible and High-Quality Growth of InN by RF Molecular Beam Epitaxy", Appl. Phys. Express **2**, 051001 (2009) 10.1143/APEX.2.051001.

[103]T. Yamaguchi and Y. Nanishi, "New MBE growth method for high quality InN and related alloys using in situ monitoring technology", Phys. Status Solidi **207**, 19–23 (2009) 10.1002/pssa.200982638.

[104]R. M. Feenstra, H. Chen, V. Ramachandran, C. D. Lee, A. R. Smith, J. E. Northrup, T. Zywietz, J. Neugebauer, and D. W. Greve, "SURFACE MORPHOLOGY OF GaN SURFACES DURING MOLECULAR BEAM EPITAXY", Surf. Rev. Lett. **07**, 601–606 (2000) 10.1142/S0218625X00000804.

[105]G. Yu, G. Wang, H. Ishikawa, M. Umeno, T. Soga, T. Egawa, J. Watanabe, and T. Jimbo, "Optical properties of wurtzite structure GaN on sapphire around fundamental absorption edge (0.78–4.77 eV) by spectroscopic ellipsometry and the optical transmission method", Appl. Phys. Lett. **70**, 3209–3211 (1997) 10.1063/1.119157.

[106]J. Paek, K. Kim, J. Lee, D. Kim, M. Yi, D. Noh, H. Kim, and S. Park, "Nitridation of sapphire substrate and its effect on the growth of GaN layer at low temperature", J. Cryst. Growth **200**, 55–62 (1999) 10.1016/S0022-0248(98)01253-6.

[107]M. Shimizu, Y. Kawaguchi, K. Hiramatsu, and N. Sawaki, "Metalorganic Vapor Phase Epitaxy of Thick InGaN on Sapphire Substrate", Jpn. J. Appl. Phys. **36**, 3381–3384 (1997) 10.1143/JJAP.36.3381.

[108]Y. Nanishi, Y. Saito, and T. Yamaguchi, "RF-Molecular Beam Epitaxy Growth and Properties of InN and Related Alloys", Jpn. J. Appl. Phys. **42**, 2549–2559 (2003) 10.1143/JJAP.42.2549.

[109]H. Lu, W. J. Schaff, J. Hwang, H. Wu, G. Koley, and L. F. Eastman, "Effect of an AlN buffer layer on the epitaxial growth of InN by molecular-beam epitaxy", Appl. Phys. Lett. **79**, 1489–1491 (2001) 10.1063/1.1402649.

[110]E. Dimakis, E. Iliopoulos, K. Tsagaraki, T. Kehagias, P. Komninou, and A. Georgakilas, "Heteroepitaxial growth of In-face InN on GaN (0001) by plasma-assisted molecular-beam epitaxy", J. Appl. Phys. **97**, 113520 (2005) 10.1063/1.1923166.

[111]I. Gherasoiu, M. O'Steen, T. Bird, D. Gotthold, A. Chandolu, D. Y. Song, S. X. Xu, M. Holtz, S. A. Nikishin, and W. J. Schaff, "Characterization of high quality InN grown on production-style plasma assisted molecular beam epitaxy system", J. Vac. Sci. Technol. A Vacuum, Surfaces, Film. **26**, 399–405 (2008) 10.1116/1.2899412.

[112]F. Kawamura, T. Iwahashi, M. Morishita, K. Omae, M. Yoshimura, Y. Mori, and T. Sasaki, "Growth of Transparent, Large Size GaN Single Crystal with Low Dislocations Using Ca-Na Flux System", Jpn. J. Appl. Phys. **42**, L729–L731 (2003) 10.1143/JJAP.42.L729.

[113]X. Xu, R. Vaudo, C. Loria, A. Salant, G. Brandes, and J. Chaudhuri, "Growth and characterization of low defect GaN by hydride vapor phase epitaxy", J. Cryst. Growth **246**, 223–229 (2002) 10.1016/S0022-0248(02)01745-1.

[114]B. Łucznik, B. Pastuszka, I. Grzegory, M. Boćkowski, G. Kamler, E. Litwin-Staszewska, and S. Porowski, "Deposition of thick GaN layers by HVPE on the pressure grown GaN substrates", J. Cryst. Growth **281**, 38–46 (2005) 10.1016/j.jcrysgro.2005.03.041.

[115]A. Ajagunna, A. Adikimenakis, E. Iliopoulos, K. Tsagaraki, M. Androulidaki, and A. Georgakilas, "InN films and nanostructures grown on Si (111) by RF-MBE", J. Cryst. Growth **311**, 2058–2062 (2009) 10.1016/j.jcrysgro.2008.12.012.

[116]X. Ji, S. Lau, H. Yang, and Q. Zhang, "Structural and optical properties of wurtzite InN grown on Si(111)", Thin Solid Films **515**, 4619–4623 (2007) 10.1016/j.tsf.2006.11.046.

[117]T. Yodo, H. Ando, D. Nosei, and Y. Harada, "Growth and Characterization of InN Heteroepitaxial Layers Grown on Si Substrates by ECR-Assisted MBE", Phys. status solidi **228**, 21–26 (2001) 10.1002/1521-3951(200111)228:1<21::AID-PSSB21>3.0.CO;2-R.

[118]S. A. Nikishin, N. N. Faleev, V. G. Antipov, S. Francoeur, L. Grave de Peralta, G. A. Seryogin, H. Temkin, T. I. Prokofyeva, M. Holtz, and S. N. G. Chu, "High quality GaN grown on Si(111) by gas source molecular beam epitaxy with ammonia", Appl. Phys. Lett. **75**, 2073–2075 (1999) 10.1063/1.124920.

[119]T. Takeuchi, H. Amano, K. Hiramatsu, N. Sawaki, and I. Akasaki, "Growth of single crystalline GaN film on Si substrate using 3C-SiC as an intermediate layer", J. Cryst. Growth **115**, 634–638 (1991) 10.1016/0022-0248(91)90817-O.

[120]A. Watanabe, T. Takeuchi, K. Hirosawa, H. Amano, K. Hiramatsu, and I. Akasaki, "The growth of single crystalline GaN on a Si substrate using AIN as an intermediate layer", J. Cryst. Growth **128**, 391–396 (1993) 10.1016/0022-0248(93)90354-Y.

[121]M. E. Sherwin and T. J. Drummond, "Predicted elastic constants and critical layer thicknesses for cubic phase AlN, GaN, and InN on β-SiC", J. Appl. Phys. **69**, 8423–8425 (1991) 10.1063/1.347412.

[122]T. Ive, O. Brandt, M. Ramsteiner, M. Giehler, H. Kostial, and K. H. Ploog, "Properties of InN layers grown on 6H–SiC(0001) by plasma-assisted molecular beam epitaxy", Appl. Phys. Lett. **84**, 1671–1673 (2004) 10.1063/1.1668318.

[123]M. Losurdo, M. M. Giangregorio, G. Bruno, T. Kim, P. Wu, S. Choi, A. Brown, F. Masia, M. Capizzi, and A. Polimeni, "Characteristics of InN grown on SiC under the In-rich regime by molecular beam heteroepitaxy", Appl. Phys. Lett. **90**, 011910 (2007) 10.1063/1.2424664.

[124]A. S. Brown, T. Kim, S. Choi, P. Wu, M. Morse, M. Losurdo, M. M. Giangregorio, G. Bruno, and A. Moto, "Growth of InN on 6H-SiC by plasma assisted molecular beam epitaxy", Phys. status solidi **3**, 1531–1535 (2006) 10.1002/pssc.200565150.

[125]M. E. Lin, B. Sverdlov, G. L. Zhou, and H. Morkoç, "A comparative study of GaN epilayers grown on sapphire and SiC substrates by plasma-assisted molecular-beam epitaxy", Appl. Phys. Lett. **62**, 3479–3481 (1993) 10.1063/1.109026.

[126]F. A. Ponce, B. S. Krusor, J. S. Major, W. E. Plano, and D. F. Welch, "Microstructure of GaN epitaxy on SiC using AlN buffer layers", Appl. Phys. Lett. **67**, 410–412 (1995) 10.1063/1.114645.

[127]T. Sasaki and T. Matsuoka, "Substrate-polarity dependence of metal-organic vapor-phase epitaxy-grown GaN on SiC", J. Appl. Phys. **64**, 4531–4535 (1988) 10.1063/1.341281.

[128]D. G. Zhao, S. J. Xu, M. H. Xie, S. Y. Tong, and H. Yang, "Stress and its effect on optical properties of GaN epilayers grown on Si(111), 6H-SiC(0001), and c -plane sapphire", Appl. Phys. Lett. **83**, 677–679 (2003) 10.1063/1.1592306.

[129]Y. Cho, O. Brandt, M. Korytov, M. Albrecht, V. M. Kaganer, M. Ramsteiner, and H. Riechert, "Structural properties of InN films grown on O-face ZnO(0001) by plasma-assisted molecular beam epitaxy", Appl. Phys. Lett. **100**, 152105 (2012) 10.1063/1.3702572.

[130]C. Shih, I. Lo, W. Pang, and C. Hiseh, "Growth of InN thin films on ZnO substrate by plasma-assisted molecular beam epitaxy", J. Phys. Chem. Solids **71**, 1664–1668 (2010) 10.1016/j.jpcs.2010.09.005.

[131]K. Ikuta, Y. Inoue, and O. Takai, "Optical and electrical properties of InN thin films grown on ZnO/α-Al2O3 by RF reactive magnetron sputtering", Thin Solid Films **334**, 49–53 (1998) 10.1016/S0040-6090(98)01115-8.

[132]F. Hamdani, A. Botchkarev, W. Kim, H. Morkoç, M. Yeadon, J. M. Gibson, S.-C. Y. Tsen, D. J. Smith, D. C. Reynolds, D. C. Look, K. Evans, C. W. Litton, W. C. Mitchel, and P. Hemenger, "Optical properties of GaN grown on ZnO by reactive molecular beam epitaxy", Appl. Phys. Lett. **70**, 467–469 (1997) 10.1063/1.118183.

[133]F. Hamdani, M. Yeadon, D. J. Smith, H. Tang, W. Kim, A. Salvador, A. E. Botchkarev, J. M. Gibson, A. Y. Polyakov, M. Skowronski, and H. Morkoç, "Microstructure and optical properties of epitaxial GaN on ZnO (0001) grown by reactive molecular beam epitaxy", J. Appl. Phys. **83**, 983–990 (1998) 10.1063/1.366786.

[134]S. Wang, N. Li, E. Park, S. Lien, Z. Feng, A. Valencia, J. Nause, and I. Ferguson, "Metalorganic chemical vapor deposition of InGaN layers on ZnO substrates", J. Appl. Phys. **102**, 106105 (2007) 10.1063/1.2817482.

[135]N. Li, S. Wang, E. Park, Z. Feng, H. Tsai, J. Yang, and I. Ferguson, "Suppression of phase separation in InGaN layers grown on lattice-matched ZnO substrates", J. Cryst. Growth **311**, 4628–4631 (2009) 10.1016/j.jcrysgro.2009.09.004.

[136]T. Matsuoka, N. Yoshimoto, T. Sasaki, and A. Katsui, "Wide-gap semiconductor InGaN and InGaAln grown by MOVPE", J. Electron. Mater. **21**, 157–163 (1992) 10.1007/BF02655831.

[137]E. Iliopoulos, A. Georgakilas, E. Dimakis, A. Adikimenakis, K. Tsagaraki, M. Androulidaki, and N. T. Pelekanos, "InGaN(0001) alloys grown in the entire composition range by plasma assisted molecular beam epitaxy", Phys. status solidi **203**, 102–105 (2006) 10.1002/pssa.200563509.

[138]S. Valdueza-Felip, E. Bellet-Amalric, A. Núñez-Cascajero, Y. Wang, M.-P. Chauvat, P. Ruterana, S. Pouget, K. Lorenz, E. Alves, and E. Monroy, "High In-content InGaN layers synthesized by plasma-assisted molecular-beam epitaxy: Growth conditions, strain relaxation, and In incorporation kinetics", J. Appl. Phys. **116**, 233504 (2014) 10.1063/1.4903944.

[139]M. Siekacz, M. Sawicka, H. Turski, G. Cywiński, A. Khachapuridze, P. Perlin, T. Suski, M. Boćkowski, J. Smalc-Koziorowska, M. Kryśko, R. Kudrawiec, M. Syperek, J. Misiewicz, Z. Wasilewski, S. Porowski, and C. Skierbiszewski, "Optically pumped 500 nm InGaN green lasers grown by plasma-assisted molecular beam epitaxy", J. Appl. Phys. **110**, 063110 (2011) 10.1063/1.3639292.

[140]C. Bazioti, E. Papadomanolaki, T. Kehagias, T. Walther, J. Smalc-Koziorowska, E. Pavlidou, P. Komninou, T. Karakostas, E. Iliopoulos, and G. P. Dimitrakopulos, "Defects, strain relaxation, and compositional grading in high indium content InGaN epilayers grown by molecular beam epitaxy", J. Appl. Phys. **118**, 155301 (2015) 10.1063/1.4933276.

[141]H. Turski, M. Siekacz, Z. Wasilewski, M. Sawicka, S. Porowski, and C. Skierbiszewski, "Nonequivalent atomic step edges—Role of gallium and nitrogen atoms in the growth of InGaN layers", J. Cryst. Growth **367**, 115–121 (2013) 10.1016/j.jcrysgro.2012.12.026.

[142]Y. Liu, Y. Cai, L. Zhang, M. H. Xie, N. Wang, S. B. Zhang, and H. S. Wu, "Dislocation network at InNGaN interface revealed by scanning tunneling microscopy", Appl. Phys. Lett. **92**, 231907 (2008) 10.1063/1.2944145.

[143]J. Moneta, M. Siekacz, E. Grzanka, T. Schulz, T. Markurt, M. Albrecht, and J. Smalc-Koziorowska, "Peculiarities of plastic relaxation of (0001) InGaN epilayers and their consequences for pseudo-substrate application", Appl. Phys. Lett. **113**, 031904 (2018) 10.1063/1.5030190.

[144]R. Liu, J. Mei, S. Srinivasan, H. Omiya, F. A. Ponce, D. Cherns, Y. Narukawa, and T. Mukai, "Misfit Dislocation Generation in InGaN Epilayers on Free-Standing GaN", Jpn. J. Appl. Phys. **45**, L549–L551 (2006) 10.1143/JJAP.45.L549.

[145]I. Kim, H. Park, Y. Park, and T. Kim, "Formation of V-shaped pits in InGaN/GaN multiquantum wells and bulk InGaN films", Appl. Phys. Lett. **73**, 1634–1636 (1998) 10.1063/1.122229.

[146]J. E. Northrup, L. T. Romano, and J. Neugebauer, "Surface energetics, pit formation, and chemical ordering in InGaN alloys", Appl. Phys. Lett. **74**, 2319–2321 (1999) 10.1063/1.123837.

[147]S. Han, D. Lee, H. Shim, J. Wook Lee, D. Kim, S. Yoon, Y. Sun Kim, and S. Kim, "Improvement of efficiency and electrical properties using intentionally formed V-shaped pits in InGaN/GaN multiple quantum well light-emitting diodes", Appl. Phys. Lett. **102**, 251123 (2013) 10.1063/1.4812810.

[148]Z. Liliental-Weber, M. Benamara, J. Washburn, J. Z. Domagala, J. Bak-Misiuk, E. L. Piner, J. C. Roberts, and S. M. Bedair, "Relaxation of InGaN thin layers observed by X-ray and transmission electron microscopy studies", J. Electron. Mater. **30**, 439–444 (2001) 10.1007/s11664-001-0056-5.

[149]A. Monshi, M. R. Foroughi, and M. R. Monshi, "Modified Scherrer Equation to Estimate More Accurately Nano-Crystallite Size Using XRD", World J. Nano Sci. Eng. **02**, 154–160 (2012) 10.4236/wjnse.2012.23020.

[150]J. I. Langford and A. J. C. Wilson, "Scherrer after sixty years: A survey and some new results in the determination of crystallite size", J. Appl. Crystallogr. **11**, 102–113 (1978) 10.1107/S0021889878012844.

[151]E. Chason, J. Y. Tsao, K. M. Horn, S. T. Picraux, and H. A. Atwater, "Surface roughening of Ge(001) during 200 eV Xe ion bombardment and Ge molecular beam epitaxy", J. Vac. Sci. Technol. A Vacuum, Surfaces, Film. **8**, 2507–2511 (1990) 10.1116/1.576724.

[152]N. Grandjean and J. Massies, "GaN and AlGaN molecular beam epitaxy monitored by reflection high-energy electron diffraction", Appl. Phys. Lett. **71**, 1816–1818 (1997) 10.1063/1.119408.

[153]B. Daudin and F. Widmann, "Layer-by-layer growth of AlN and GaN by molecular beam epitaxy", J. Cryst. Growth **182**, 1–5 (1997) 10.1016/S0022-0248(97)00339-4.

[154]L. Li, Z. Yang, and W. Wang, "High quality GaN grown at high growth rates by gas-source molecular beam epitaxy", Electron. Lett. **31**, 2127–2128 (1995) 10.1049/el:19951456.

[155]M. A. Moram and M. E. Vickers, "X-ray diffraction of III-nitrides", Reports Prog. Phys. **72**, 036502 (2009) 10.1088/0034-4885/72/3/036502.

[156]P. Y. Yu and M. Cardona, *Fundamentals of Semiconductors*, 4., Vol. 1, Graduate Texts in Physics (Springer Berlin Heidelberg, 2010), 10.1007/978-3-642-00710-1.

[157]S. Graubner, C. Neumann, N. Volbers, B. K. Meyer, J. Bläsing, and A. Krost, "Preparation of ZnO substrates for epitaxy: Structural, surface, and electrical properties", Appl. Phys. Lett. **90**, 042103 (2007) 10.1063/1.2434170.

[158]W. C. Yang, C. H. Wu, Y. T. Tseng, S. Y. Chiu, and K. Y. Cheng, "Growth mechanisms of plasma-assisted molecular beam epitaxy of green emission InGaN/GaN single quantum wells at high growth temperatures", J. Appl. Phys. **117**, 015306 (2015) 10.1063/1.4905419.

[159]C. Chèze, M. Siekacz, F. Isa, B. Jenichen, F. Feix, J. Buller, T. Schulz, M. Albrecht, C. Skierbiszewski, R. Calarco, and H. Riechert, "Investigation of interface abruptness and In content in (In,Ga)N/GaN superlattices", J. Appl. Phys. **120**, 125307 (2016) 10.1063/1.4963273.

[160]L. Lymperakis, T. Schulz, C. Freysoldt, M. Anikeeva, Z. Chen, X. Zheng, B. Shen, C. Chèze, M. Siekacz, X. Q. Wang, M. Albrecht, and J. Neugebauer, "Elastically frustrated rehybridization: Origin of chemical order and compositional limits in InGaN quantum wells", Phys. Rev. Mater. **2**, 011601 (2018) 10.1103/PhysRevMaterials.2.011601.

[161]C. Chèze, F. Feix, M. Anikeeva, T. Schulz, M. Albrecht, H. Riechert, O. Brandt, and R. Calarco, "In/GaN(0001)- (3 3) R 30 adsorbate structure as a template for embedded (In, Ga)N/GaN monolayers and short-period superlattices", Appl. Phys. Lett. **110**, 072104 (2017) 10.1063/1.4976198.

[162]Y. Cho, M. Korytov, M. Albrecht, H. Riechert, and O. Brandt, "Effects of Ga on the growth of InN on O-face ZnO(000-1) by plasma-assisted molecular beam epitaxy", Appl. Phys. Lett. **101**, 052103 (2012) 10.1063/1.4739941.

[163]E. Placidi, F. Arciprete, V. Sessi, M. Fanfoni, F. Patella, and A. Balzarotti, "Step erosion during nucleation of InAsGaAs(001) quantum dots", Appl. Phys. Lett. **86**, 241913 (2005) 10.1063/1.1946181.

[164]T. Nakayama and H. Miyamoto, "Dependence of critical thickness of strained InAs layer on growth rate", in Proc. 8th Int. Conf. Indium Phosphide Relat. Mater. (Mar. 2002), pp. 614–617, 10.1109/ICIPRM.1996.492323.

[165]A. Bourret, C. Adelmann, B. Daudin, J. Rouvière, G. Feuillet, and G. Mula, "Strain relaxation in (0001) AlN/GaN heterostructures", Phys. Rev. B **63**, 245307 (2001) 10.1103/PhysRevB.63.245307.

[166]J. Tersoff and R. M. Tromp, "Shape transition in growth of strained islands: Spontaneous formation of quantum wires", Phys. Rev. Lett. **70**, 2782–2785 (1993) 10.1103/PhysRevLett.70.2782.

[167]Y. Tu and J. Tersoff, "Origin of Apparent Critical Thickness for Island Formation in Heteroepitaxy", Phys. Rev. Lett. **93**, 216101 (2004) 10.1103/PhysRevLett.93.216101.

[168]F. Ivaldi, C. Meissner, J. Domagala, S. Kret, M. Pristovsek, M. Högele, and M. Kneissl, "Influence of a GaN Cap Layer on the Morphology and the Physical Properties of Embedded Self-Organized InN Quantum Dots on GaN(0001) Grown by Metal–Organic Vapour Phase Epitaxy", Jpn. J. Appl. Phys. **50**, 031004 (2011) 10.1143/JJAP.50.031004.

[169]S. Pereira, M. R. Correia, E. Pereira, K. P. O'Donnell, C. Trager-Cowan, F. Sweeney, and E. Alves, "Compositional pulling effects in InGaN/GaN layers: A combined depth-resolved cathodoluminescence and Rutherford backscattering/channeling study", Phys. Rev. B **64**, 205311 (2001) 10.1103/PhysRevB.64.205311.

[170]H. Y. Lin, Y. F. Chen, T. Y. Lin, C. F. Shih, K. S. Liu, and N. C. Chen, "Direct evidence of compositional pulling effect in AlGaN epilayers", J. Cryst. Growth **290**, 225–228 (2006) 10.1016/j.jcrysgro.2006.01.021.

[171]Y.-L. Tsai, C. Wang, P. Lin, W. Liao, and J. Gong, "Observation of compositional pulling phenomenon in AlGaN (0.4<x<1.0) films grown on (0001) sapphire substrates", Appl. Phys. Lett. **82**, 31–33 (2003) 10.1063/1.1533850.

[172]P. F. Fewster, *X-Ray Scattering from Semiconductors* (Imperial College Press, London, 2003).

[173]M. A. Moram, Z. H. Barber, and C. J. Humphreys, "Accurate experimental determination of the Poisson's ratio of GaN using high-resolution x-ray diffraction", J. Appl. Phys. **102**, 023505 (2007) 10.1063/1.2749484.

[174]A. Kadir, C. Huang, K. Kian Lee, E. Fitzgerald, and S. Chua, "Determination of alloy composition and strain in multiple AlGaN buffer layers in GaN/Si system", Appl. Phys. Lett. **105**, 232113 (2014) 10.1063/1.4904007.

[175]N. Herres, L. Kirste, H. Obloh, K. Köhler, J. Wagner, and P. Koidl, "X-ray determination of the composition of partially strained group-III nitride layers using the Extended Bond Method", Mater. Sci. Eng. B **91-92**, 425–432 (2002) 10.1016/S0921-5107(01)01036-4.

[176]S. Pereira, M. R. Correia, E. Pereira, K. P. O'Donnell, E. Alves, A. D. Sequeira, N. Franco, I. M. Watson, and C. J. Deatcher, "Strain and composition distributions in wurtzite InGaN/GaN layers extracted from x-ray reciprocal space mapping", Appl. Phys. Lett. **80**, 3913–3915 (2002) 10.1063/1.1481786.

[177]X. L. Zhu, L. W. Guo, B. H. Ge, M. Z. Peng, N. S. Yu, J. F. Yan, J. Zhang, H. Q. Jia, H. Chen, and J. M. Zhou, "Observation of metallic indium clusters in thick InGaN layer grown by metal organic chemical vapor deposition", Appl. Phys. Lett. **91**, 172110 (2007) 10.1063/1.2802073.

[178]H. F. Liu, W. Liu, S. B. Dolmanan, S. Tripathy, S. J. Chua, and D. Z. Chi, "Effects of doping and indium inclusions on the structural and optical properties of InN thin films grown by MOCVD", J. Phys. D. Appl. Phys. **45**, 195102 (2012) 10.1088/0022-3727/45/19/195102.

[179]M. Woelz, "Control of the emission wavelength of gallium nitride-based nanowire light-emitting diodes", PhD thesis (Humboldt-Universität zu Berlin, 2013).

[180]R. Oliva, J. Ibáñez, R. Cuscó, R. Kudrawiec, J. Serafinczuk, O. Martínez, J. Jiménez, M. Henini, C. Boney, A. Bensaoula, and L. Artús, "Raman scattering by the E2h and A1(LO) phonons of InGaN epilayers ($0.25 < x < 0.75$) grown by molecular beam epitaxy", J. Appl. Phys. **111**, 063502 (2012) 10.1063/1.3693579.

[181]M. R. Correia, S. Pereira, E. Pereira, J. Frandon, and E. Alves, "Raman study of the A1(LO) phonon in relaxed and pseudomorphic InGaN epilayers", Appl. Phys. Lett. **83**, 4761–4763 (2003) 10.1063/1.1627941.

[182]H. Harima, "Properties of GaN and related compounds studied by means of Raman scattering", J. Phys. Condens. Matter **14**, R967–R993 (2002) 10.1088/0953-8984/14/38/201.

[183]R. J. Briggs and A. K. Ramdas, "Piezospectroscopic study of the Raman spectrum of cadmium sulfide", Phys. Rev. B **13**, 5518–5529 (1976) 10.1103/PhysRevB.13.5518.

[184]J.-M. Wagner and F. Bechstedt, "Properties of strained wurtzite GaN and AlN: Ab initio studies", Phys. Rev. B **66**, 115202 (2002) 10.1103/PhysRevB.66.115202.

[185]M. R. Correia, S. Pereira, E. Pereira, J. Frandon, and E. Alves, "Raman study of the A1(LO) phonon in relaxed and pseudomorphic InGaN epilayers", Appl. Phys. Lett. **83**, 4761–4763 (2003) 10.1063/1.1627941.

[186]A. G. Kontos, Y. S. Raptis, N. T. Pelekanos, A. Georgakilas, E. Bellet-Amalric, and D. Jalabert, "Micro-Raman characterization of InGaN/Al2O3 heterostructures", Phys. Rev. B **72**, 155336 (2005) 10.1103/PhysRevB.72.155336.

[187]M. Correia, S. Pereira, J. Frandon, M. Renucci, E. Alves, A. Sequeira, and N. Franco, "Analysis of Strain Depth Variations in an In0.19Ga0.81N Layer by Raman Spectroscopy", Phys. status solidi **567**, 563–567 (2003) 10.1002/pssc.200390114.

[188]M. R. Correia, S. Pereira, E. Pereira, J. Frandon, I. M. Watson, C. Liu, E. Alves, A. D. Sequeira, and N. Franco, "Direct evidence for strain inhomogeneity in InxGa1xN epilayers by Raman spectroscopy", Appl. Phys. Lett. **85**, 2235–2237 (2004) 10.1063/1.1791324.

[189]D. Alexson, L. Bergman, R. J. Nemanich, M. Dutta, M. A. Stroscio, C. A. Parker, S. M. Bedair, N. A. El-Masry, and F. Adar, "Ultraviolet Raman study of A1(LO) and E2 phonons in InxGa1xN alloys", J. Appl. Phys. **89**, 798–800 (2001) 10.1063/1.1330760.

[190]S. Hernández, R. Cuscó, D. Pastor, L. Artús, K. P. O'Donnell, R. W. Martin, I. M. Watson, Y. Nanishi, and E. Calleja, "Raman-scattering study of the InGaN alloy over the whole composition range", J. Appl. Phys. **98** (2005) 10.1063/1.1940139.

[191]V. Y. Davydov, A. A. Klochikhin, V. V. Emtsev, A. N. Smirnov, I. N. Goncharuk, A. V. Sakharov, D. A. Kurdyukov, M. V. Baidakova, V. A. Vekshin, S. V. Ivanov, J. Aderhold, J. Graul, A. Hashimoto, and A. Yamamoto, "Photoluminescence and Raman study of hexagonal InN and In-rich InGaN alloys", Phys. status solidi **240**, 425–428 (2003) 10.1002/pssb.200303448.

[192]S. Murugkar, R. Merlin, A. Botchkarev, A. Salvador, and H. Morkoç, "Second order Raman spectroscopy of the wurtzite form of GaN", J. Appl. Phys. **77**, 6042–6043 (1995) 10.1063/1.359190.

[193]H. Siegle, G. Kaczmarczyk, L. Filippidis, A. P. Litvinchuk, A. Hoffmann, and C. Thomsen, "Zone-boundary phonons in hexagonal and cubic GaN", Phys. Rev. B **55**, 7000–7004 (1997) 10.1103/PhysRevB.55.7000.

[194]P. Manuel, G. A. Sai-Halasz, L. L. Chang, C.-A. Chang, and L. Esaki, "Resonant Raman Scattering in a Semiconductor Superlattice", Phys. Rev. Lett. **37**, 1701–1704 (1976) 10.1103/PhysRevLett.37.1701.

[195]H. Fröhlich, "Electrons in lattice fields", Adv. Phys. **3**, 325–361 (1954) 10.1080/00018735400101213.

[196]D. Behr, J. Wagner, A. Ramakrishnan, H. Obloh, and K.-H. Bachem, "Evidence for compositional inhomogeneity in low In content (InGa)N obtained by resonant Raman scattering", Appl. Phys. Lett. **73**, 241–243 (1998) 10.1063/1.121768.

[197]J. Wagner, A. Ramakrishnan, H. Obloh, and M. Maier, "Effect of strain and associated piezoelectric fields in InGaN/GaN quantum wells probed by resonant Raman scattering", Appl. Phys. Lett. **74**, 3863–3865 (1999) 10.1063/1.124205.

[198]A. Kar, D. Alexson, M. Dutta, and M. A. Stroscio, "Evidence of compositional inhomogeneity in InGaN alloys using ultraviolet and visible Raman spectroscopy.", J. Appl. Phys. **104**, 073502 (2008) 10.1063/1.2986140.

[199]D. Behr, J. Wagner, A. Ramakrishnan, H. Obloh, and K.-H. Bachem, "Evidence for compositional inhomogeneity in low In content (InGa)N obtained by resonant Raman scattering", Appl. Phys. Lett. **73**, 241–243 (1998) 10.1063/1.121768.

[200]N. Wieser, O. Ambacher, H.-P. Felsl, L. Görgens, and M. Stutzmann, "Compositional fluctuations in GaInN/GaN double heterostructures investigated by selectively excited photoluminescence and Raman spectroscopy", Appl. Phys. Lett. **74**, 3981–3983 (1999) 10.1063/1.124243.

[201] V. Y. Davydov, A. A. Klochikhin, I. N. Goncharuk, A. N. Smirnov, A. V. Sakharov, A. P. Skvortsov, M. A. Yagovkina, V. M. Lebedev, H. Lu, and W. J. Schaff, "Resonant Raman scattering in InGaN alloys", Phys. status solidi **243**, 1494–1498 (2006) 10.1002/pssb.200565350.

[202] B. K. Meyer, H. Alves, D. M. Hofmann, W. Kriegseis, D. Forster, F. Bertram, J. Christen, A. Hoffmann, M. Straßburg, M. Dworzak, U. Haboeck, and A. V. Rodina, "Bound exciton and donor–acceptor pair recombinations in ZnO", Phys. status solidi **241**, 231–260 (2004) 10.1002/pssb.200301962.

[203] M. A. Reshchikov, J. Q. Xie, B. Hertog, and A. Osinsky, "Yellow luminescence in ZnO layers grown on sapphire", J. Appl. Phys. **103**, 103514 (2008) 10.1063/1.2924437.

[204] J. Gutowski, N. Presser, and I. Broser, "Acceptor-exciton complexes in ZnO: A comprehensive analysis of their electronic states by high-resolution magnetooptics and excitation spectroscopy", Phys. Rev. B **38**, 9746–9758 (1988) 10.1103/PhysRevB.38.9746.

[205] P. Loose, M. Rosenzweig, and M. Wöhlecke, "Zeeman Effect of Bound Exciton Complexes in ZnO", Phys. status solidi **75**, 137–144 (1976) 10.1002/pssb.2220750113.

[206] D. Reynolds, D. Look, B. Jogai, J. Van Nostrand, R. Jones, and J. Jenny, "Source of the yellow luminescence band in GaN grown by gas-source molecular beam epitaxy and the green luminescence band in single crystal ZnO", Solid State Commun. **106**, 701–704 (1998) 10.1016/S0038-1098(98)00048-9.

[207] V. Srikant and D. R. Clarke, "On the optical band gap of zinc oxide", J. Appl. Phys. **83**, 5447–5451 (1998) 10.1063/1.367375.

[208] M. Reshchikov and H. Morkoç, "Luminescence properties of defects in GaN", J. Appl. Phys. **97**, 061301 (2005) 10.1063/1.1868059.

[209] E. R. Glaser, W. E. Carlos, G. C. B. Braga, J. A. Freitas, W. J. Moore, B. V. Shanabrook, R. L. Henry, A. E. Wickenden, D. D. Koleske, H. Obloh, P. Kozodoy, S. P. DenBaars, and U. K. Mishra, "Magnetic resonance studies of Mg-doped GaN epitaxial layers grown by organometallic chemical vapor deposition", Phys. Rev. B **65**, 085312 (2002) 10.1103/PhysRevB.65.085312.

[210] M. Bayerl, M. Brandt, T. Suski, I. Grzegory, S. Porowski, and M. Stutzmann, "ODMR of bound excitons in Mg-doped GaN", Phys. B Condens. Matter **273-274**, 120–123 (1999) 10.1016/S0921-4526(99)00421-4.

[211] I. Gorczyca, T. Suski, N. E. Christensen, and A. Svane, "Hydrostatic pressure and strain effects in short period InN/GaN superlattices", Appl. Phys. Lett. **101**, 092104 (2012) 10.1063/1.4748325.